

Design and Time-domain Analysis of Antenna Array for UWB Imaging Application



A thesis submitted to the University of London in partial fulfilment
of the requirements for the Degree of Doctor of Philosophy

By

Min Zhou

Supervisors: Prof. X. Chen and Prof. C. G. Parini

School of Electronic Engineering and Computer Science

Queen Mary, University of London

June 2014

*I hereby declare that the work presented
in this thesis is my own and all references
are cited accordingly.*

To My Family

ACKNOWLEDGEMENTS

I would like to express my sincere gratitude to my supervisors, Prof. Xiaodong Chen and Prof. Clive Parini for their strong support and great encouragement. Their deep understanding and immense knowledge help me to understand this project clearly and solve the problems.

I will give my thanks to my colleague Mr. Lei Li, who works in the same project with me. We always have discussions on this project together, which is helpful to me.

I will appreciate Dr. Massimo Candotti, Mr. Tony Stone and Dr. Max Ovidio Munoz Torrico for their help in fabricating the antennas and the cables. Thank Mr. John Dupuy for his help and advice on choosing the commercial RF components.

Furthermore, I would like to thank other colleagues in our antenna group for their help and support, especially Dr. Sheng Wang, Dr. Lu Guo and Dr. Xiaoming Liu. They all give me very constructive suggestions on antenna study.

Last but not least, I would like to extend my deepest love to my parents and my husband. They have always motivated me to continue my higher studies and given me their unconditional support.

ABSTRACT

UWB technology has been developing in imaging applications. For security imaging applications, it is vital to detect and image metallic targets concealed in bag at airports, subway stations or other public environments. To reduce the cost of the deployment of X-ray machines, a novel UWB imaging system has been developed, including the design of the UWB rotating antenna array, the design of RF circuits and the implementation of the two-dimensional delay-and-sum (DAS) image reconstruction method.

Two types of UWB antennas, the circular-edge antipodal Vivaldi antenna and the corrugated balanced antipodal Vivaldi antenna (BAVA) have been designed and studied in both frequency domain and time domain. Both of them can work across UWB frequency range from 3.1 GHz to 10.6 GHz, and have directional radiation patterns. The corrugated BAVA with smaller physical size has been improved to have a relative high gain around 7 dBi across the operating frequency range. It also causes less distortion to signals in the time domain. So the corrugated BAVA is used as the antenna element in the UWB rotating antenna array.

The UWB rotating antenna array comprises one central transmitting antenna and four receiving antennas. The receiving antennas, which rotate around the central transmitting antenna, are placed side-by-side on a straight arm. The equivalent antenna elements in space are increased by the rotation of the antenna array. The two-dimensional image reconstruction method has been developed based on DAS algorithm.

This UWB imaging system can detect and reconstruct the image of the single and pairs of metallic targets concealed in bag. The smallest single target with the size of 4 cm \times 4 cm \times 1 cm can be reconstructed in images at a maximum distance of 30 cm away from the system. It can achieve 6 cm in cross-range resolution and 15 cm in down-range resolution. Therefore, the feasibility of the proposed UWB imaging system has been proved.

Contents

ACKNOWLEDGEMENTS	- 4 -
ABSTRACT	- 5 -
ContentsList of Figures	- 6 -
List of Figures	- 10 -
List of Tables.....	- 22 -
Abbreviations and Glossary	- 23 -
Chapter 1 Introduction	- 25 -
1.1 Challenges, motivations and objectives	- 26 -
1.2 Contributions	- 28 -
1.3 Organization of the thesis	- 30 -
Reference	- 31 -
Chapter 2 UWB Imaging Technology	- 32 -
2.1 UWB Radar technology	- 32 -
2.1.1 UWB Radar detecting methods	- 32 -
2.1.2 UWB frequency domain imaging technique	- 34 -
2.1.3 UWB time domain imaging technique	- 35 -
2.2 UWB Imaging applications	- 37 -
2.2.1 Current Status of Medical imaging.....	- 37 -
2.2.2 Current Status of Ground Penetrating Radar	- 43 -
2.2.3 Current Status of See-through Wall imaging	- 47 -
2.3 Summary	- 50 -
References	- 50 -

Chapter 3 The Antenna for the Imaging System.....	- 61 -
3.1 Overview of the antennas in UWB imaging systems.....	- 62 -
3.2 Tapered Slot Antenna	- 64 -
3.2.1 Principle of operation	- 64 -
3.2.2 Feeding technique.....	- 66 -
3.3 The circular-edge antipodal Vivaldi antenna	- 69 -
3.3.1 Structure of the antenna.....	- 69 -
3.3.2 Simulated and measured results	- 72 -
3.4 The Corrugated Balanced Antipodal Vivaldi Antenna	- 72 -
3.4.1 Structure of the antenna	- 79 -
3.4.2 Simulated and measured results	- 81 -
3.5 Summary	- 88 -
Reference.....	- 89 -
Chapter 4 The Antenna's characteristics in the Time Domain	- 93 -
4.1 The input UWB pulse.....	- 93 -
4.1.1 Gaussian pulse	- 93 -
4.1.2 Modulated pulse	- 96 -
4.2 Impulse response	- 98 -
4.2.1 Fundamental analysis	- 98 -
4.2.2 Impulse response of the circular-edge antipodal Vivaldi antenna.....	- 102 -
4.2.3 Measurements for the circular-edge antipodal Vivaldi antenna.....	- 106 -
4.2.4 Impulse response of the corrugated balanced antipodal Vivaldi antenna.....	- 109 -
4.2.5 Measurements for the corrugated balanced antipodal Vivaldi antenna.	- 112 -

4.3 Fidelity analysis.....	- 114 -
4.3.1 Performances of current bow-tie antennas for GPR.....	- 114 -
4.3.2 Fundamental analysis	- 116 -
4.3.3 The results for the circular-edge antipodal Vivaldi antenna.....	- 116 -
4.3.4 The results for the corrugated balanced antipodal Vivaldi antenna	- 119 -
4.4 Summary	- 122 -
Reference.....	- 122 -
Chapter 5 UWB Imaging System.....	- 125 -
5.1 Reflections in UWB bag imaging application.....	- 125 -
5.2 Link budget.....	- 128 -
5.3 The UWB imaging system	- 135 -
5.3.1 Architecture of the system.....	- 135 -
5.3.2 The signal and RF circuit.....	- 136 -
5.3.3 The rotating antenna array	- 138 -
5.4 The Imaging Algorithm.....	- 143 -
5.4.1 The existing imaging algorithms	- 143 -
5.4.2 Two-dimensional image reconstruction method	- 145 -
5.5 Summary	- 150 -
Reference.....	- 150 -
Chapter 6 Imaging Measurements	- 153 -
6.1 Received signals	- 153 -
6.2 Images for the single concealed target	- 157 -
6.2.1 The results of the measurements	- 158 -
6.2.2 The analysis on imaging results.....	- 168 -

6.3 Images for pairs of concealed targets	- 171 -
6.3.1 Fundamental analysis on resolutions	- 171 -
6.3.2 The results of the measurements	- 173 -
6.3.3 The analysis on imaging results.....	- 181 -
6.4 Summary	- 184 -
Chapter 7 Summary and Future work	- 185 -
7.1 Summary	- 185 -
7.2 Future work	- 187 -
List of publications	- 189 -

List of Figures

Figure 2-1	UWB imaging system based on frequency domain measurement [21]. ...	- 34 -
Figure 2-2	UWB imaging system based on time domain measurement.	- 36 -
Figure 2-3	Microwave breast imaging system developed in Dartmouth College. (a) Illumination tank with antenna array during patient examination, (b) integration of electronics cart (top removed) with the illumination tank [25].	- 38 -
Figure 2-4	UWB mono-static imaging system developed in University of Wisconsin. (a) UWB horn antenna, (b) 3D FDTD model comprised of a breast phantom and an UWB antenna, (c) Schematic showing a cross-sectional side view of the experimental setup [30].	- 39 -
Figure 2-5	UWB mono-static imaging system developed in University of Wisconsin. (a) UWB horn antenna [32], (b) 3D FDTD model comprised of a breast phantom and an UWB antenna [35], (c) Schematic showing a cross-sectional side view of the experimental setup [35].	- 40 -
Figure 2-6	UWB mono-static imaging system developed in University of Queensland. (a) UWB tapered slot antenna, (b) Experimental setup [38].	- 41 -
Figure 2-7	The 2D FDTD simulation set up proposed in University of Liverpool; (a) 2D FDTD simulation set up; (b) circular array in this model [41].	- 41 -
Figure 2-8	The simulated phantom with the dipole antenna array and the skin layer [42].	- 41 -
Figure 2-9	Multi-static UWB Radar system for Breast Cancer from University of Bristol; (a) 60-element antenna array; (b) Completed 60-way TX/RX electromechanical switching interface; (c) The whole imaging system including switching interface (below) between VNA and array (top) [46].	- 42 -
Figure 2-10	ALIS system with the cavity spiral antenna [56]	- 44 -

Figure 2-11	ALIS system develop in Tohoku University. (a) The symmetrical CMP antenna array, (b) CMP antenna array GPR system mounted on MHV, (c) Disassemble CMP antenna GPR system [57].	- 45 -
Figure 2-12	The GPR system develop in Tohoku University. (a) the Vivaldi antenna, (b) the developed common-source GPR antenna array system [58].	- 45 -
Figure 2-13	IRCTR radar system, (a) The antenna array system [60], (b) Antenna system of the radar mounted at the TNO test platform [61], (c) TNO multi-sensor test trolley for landmine detection research [61].	- 46 -
Figure 2-14	The cavity-backed resistively loaded bow-tie antenna [64].	- 46 -
Figure 2-15	The Mickey Mouse monopole antenna developed in University of Liverpool [67].	- 47 -
Figure 2-16	The ARL UWB SIRE radar system integrated onto the vehicle [72].	- 48 -
Figure 2-17	UWB through-wall imaging system from University of Tennessee; (a) The first generation of the whole system; (b) 16×16 antenna array (first generation) [74]; (c) 8×8 antenna array (second generation) [76].	- 49 -
Figure 2-18	The dual-polarimetric antennas used in UWB imaging system from Universit ä Duisburg-Essen. (a) the model, (b) the manufacture [77].	- 49 -
Figure 2-19	UWB 3D Imager from Roke Manor Research Ltd., DTI and Thales Research & Technology (UK) Ltd; (a) The whole system; (b) Suitcase imaging; (c) People scanning [79].	- 50 -
Figure 3-1	Types of TSA: (a) Vivaldi, (b) Linear-Constant, (c) Tangent, (d) Vivaldi-Constant, (e) Parabolic, (f) Stepped-Constant, (g) Linear, (h) Broken-Linear [17].	- 65 -
Figure 3-2	Geometry of the tapered slot antenna.	- 65 -
Figure 3-3	Structure of the stripline-fed Vivaldi element (a) top view, (b) middle layer-stripline feed structure, (c) side view [22].	- 68 -

Figure 3-4 The antipodal Vivaldi antenna.	- 68 -
Figure 3-5 Balanced antipodal Vivaldi antenna [23].	- 69 -
Figure 3-6 The structure of the antipodal Vivaldi antenna; (a) the traditional one; (b) the circular-edge one.	- 71 -
Figure 3-7 The fabricated antipodal antenna; (a) the front view; (b) the back view.	- 71 -
Figure 3-8 S_{11} performance of the simulated and measured results for the circular-edge antipodal Vivaldi antenna.	- 73 -
Figure 3-9 The comparison of S_{11} simulated results between the traditional one and the proposed modified one.	- 73 -
Figure 3-10 The simulated S_{11} when varying the radius of circular edge.	- 74 -
Figure 3-11 The current distribution on the surface of the antenna; (a) the traditional antipodal Vivaldi antenna; (b) the circular-edge antipodal Vivaldi antenna.	- 74 -
Figure 3-12 The simulated result of gain.	- 75 -
Figure 3-13 3D simulated radiation patterns at different frequencies; (a) 4 GHz; (b) 5 GHz; (c) 6 GHz; (d) 7 GHz.	- 75 -
Figure 3-14 E-plane of simulated (blue) and measured (red) results at different frequencies; (a) 4 GHz, (b) 5 GHz, (c) 6 GHz, (d) 7 GHz.	- 76 -
Figure 3-15 H-plane of simulated (blue) and measured (red) results at different frequencies; (a) 4 GHz, (b) 5 GHz, (c) 6 GHz, (d) 7 GHz.	- 77 -
Figure 3-16 The simulated radiation pattern in E-plane of four elements array at different frequencies; (a) 4 GHz, (b) 5 GHz, (c) 6 GHz, (d) 7 GHz.	- 79 -
Figure 3-17 The physical structure of the corrugated BAVA; (a) the front layer view; (b) the middle layer view; (c) the back layer view.	- 80 -

Figure 3-18	The fabricated corrugated BAVA.	- 81 -
Figure 3-19	The simulated and measured S_{11} of corrugated BAVA.	- 81 -
Figure 3-20	The comparison of with and without corrugation in simulated S_{11} . -	83 -
Figure 3-21	The current distribution on the surface of the antenna at 4 GHz and 7 GHz for different BAVAs; (a) the BAVA without corrugation at 4 GHz; (b) the BAVA without corrugation at 7 GHz; (c) the corrugated BAVA at 4 GHz; (d) the corrugated BAVA at 7 GHz.	- 84 -
Figure 3-22	The comparison of gain for corrugated BAVA and the one without corrugated structure.	- 84 -
Figure 3-23	The comparison of gain for corrugated BAVA and circular-edge antipodal Vivaldi antenna.	- 85 -
Figure 3-24	3D simulated radiation patterns for Corrugated BAVA; (a) 4 GHz; (b) 5 GHz; (c) 6 GHz; (d) 7 GHz.	- 86 -
Figure 3-25	The simulated (blue) and measured (red) radiation patterns in E-plane; (a) At 4 GHz, (b) At 5 GHz, (c) At 6 GHz, (d) At 7 GHz.	- 87 -
Figure 3-26	The simulated (blue) and measured (red) radiation patterns in H-plane; (a) At 4 GHz, (b) At 5 GHz, (c) At 6 GHz, (d) At 7 GHz.	- 87 -
Figure 3-27	The simulated radiation pattern in E-plane of four elements array at different frequency; (a) 4 GHz, (b) 5 GHz, (c) 6 GHz, (d) 7 GHz.	- 88 -
Figure 4-1	The Gaussian pulse with different pulse width; (a) the pulse in the time domain; (b) PSD with FCC's regulation.	- 95 -
Figure 4-2	The different derivations of Gaussian pulse; (a) the pulse in the time domain; (b) the PSD with FCC's regulation.	- 95 -
Figure 4-3	The fourth order of Gaussian pulse; (a) the pulse in the time domain; (b) the PSD with FCC's regulation.	- 96 -

Figure 4-4	The modulated Gaussian pulse; (a) the pulse in the time domain; (b) the PSD with FCC's regulation.....	- 97 -
Figure 4-5	The modulated rectangular signal; (a) the signal of one period in the time domain; (b) the PSD of one period with FCC's regulation.	- 98 -
Figure 4-6	A simple communication UWB antenna system [1].	- 98 -
Figure 4-7	The model of antenna system in head-to-head orientation.....	- 102 -
Figure 4-8	The measured S_{21} of the head-to-head antenna system; (a) the amplitude of S_{21} ; (b) the phase of S_{21}	- 104 -
Figure 4-9	The simulated gain of Tx (blue) and Rx (red).....	- 104 -
Figure 4-10	The group delay of the head-to-head antenna system for different distances between the two antennas.....	- 105 -
Figure 4-11	The impulse responses for the head-to-head antenna system; (a) for the antenna system; (b) for the receiving antenna; (c) for the transmitting antenna.	- 105 -
Figure 4-12	The measurement for the transmission of the two antennas (head-to-head).....	- 106 -
Figure 4-13	The measured (solid curves) S_{21} of the head-to-head antennas in the frequency domain compared with the simulated (dash curves) result for $d=41$ cm (blue) and $d=20$ cm (red); (a) Amplitude of S_{21} ; (b) Phase of S_{21}	- 107 -
Figure 4-14	The simulated model with the wood behind each antenna in CST.	- 107 -
Figure 4-15	The simulated S_{11} for the model with the wood behind each antenna. ...	- 108 -
Figure 4-16	The simulated gain of the antipodal antenna in the models with and without woods.....	- 108 -
Figure 4-17	The measured (solid curves) and simulated (dash curves) group delay for the head-to-head antennas separated by 41 cm (blue) and 20 cm (red).	- 108 -

Figure 4-18 The impulse responses for the head-to-head antenna systems in situations of different distances between Tx and Rx; (a) for the antenna system; (b) for the receiving antenna; (c) for the transmitting antenna. - 109 -

Figure 4-19 The model of the head-to-head antenna system using BAVA. - 109 -

Figure 4-20 The transfer function of the antenna system in the frequency domain; (a) Amplitude of S_{21} ; (b) Phase of S_{21} - 110 -

Figure 4-21 The simulated gain of Tx (blue) and Rx (red). - 111 -

Figure 4-22 The group delay of the head-to-head antenna system when they are separated by 41 cm (blue) and 20 cm (red). - 111 -

Figure 4-23 The impulse responses for the head-to-head antenna system; (a) for the antenna system; (b) for the receiving antenna; (c) for the transmitting antenna. - 112 -

Figure 4-24 The measurement for the transmission of the two antennas (head-to-head). - 112 -

Figure 4-25 The measured S_{21} of the head-to-head antenna system in the frequency domain for different antenna spacing ranges; (a) Amplitude of S_{21} ; (b) Phase of S_{21} - 113 -

Figure 4-26 The measured group delay for the head-to-head antenna system; (a) the corrugated BAVA separated by 41 cm (blue solid curve) and 20 cm (red solid curve) compared with the simulated results (dash curves); (b) the comparison of the corrugated BAVA (solid curves) with the circular-edge antipodal antenna (dash curves). - 113 -

Figure 4-27 The measured impulse response for the head-to-head antenna system spacing at 41 cm (blue solid curve) and 20 cm (red solid curve) compared with simulated ones (dash curves); (a) for the antenna system; (b) for the receiving antenna; (c) for the transmitting antenna. - 114 -

Figure 4-28 The comparison of the signals; (a) the input Gaussian pulse VS the received signal; (b) the double differentiation of Gaussian pulse from Matlab VS the received signal from the antenna..... - 118 -

Figure 4-29 The comparison of the signals; (a) the input Modulated Gaussian pulse (b=250ps) VS the received signal; (b) the First-order of Modulated Gaussian pulse (b=250ps) from Matlab VS the received signal from the antenna. - 118 -

Figure 4-30 The comparison of the signals; (a) the input Modulated Gaussian pulse (b=350ps) VS the received signal; (b) the First-order of Modulated Gaussian pulse (b=350ps) from Matlab VS the received signal from the antenna. - 118 -

Figure 4-31 The comparison of the signals; (a) the input modulated rectangular signal VS the received signal; (b) the First-order of the modulated rectangular signal from Matlab VS the received signal from the antenna. - 119 -

Figure 4-32 The comparison of the signals; (a) the input Gaussian pulse VS the received signal; (b) the Third-order of Gaussian pulse from Matlab VS the received signal from the antenna. - 120 -

Figure 4-33 The comparison of the signals; (a) the input modulated Gaussian pulse (b=250ps) VS the received signal; (b) the inversed first-order of Modulated Gaussian pulse (b=250ps) from Matlab VS the received signal from the antenna. - 121 -

Figure 4-34 The comparison of the signals; (a) the input modulated Gaussian pulse (b=350ps) VS the received signal; (b) the inversed first-order of Modulated Gaussian pulse (b=350ps) from Matlab VS the received signal from the antenna. - 121 -

Figure 4-35 The comparison of the signals; (a) the input modulated rectangular signal VS the received signal; (b) the inversed first-order of the modulated rectangular signal from Matlab VS the received signal from the antenna..... - 121 -

Figure 5-1 The effect on the received signal introduced by the obstacle; (a) the simulation model in CST; (b) the received signals from Rx without (blue) and with (red) the obstacle..... - 126 -

Figure 5-2	The effect on the received signal introduced by obstacles; (a) Permittivity=2, thickness is chosen to be 1 cm , 2 cm and 5 cm; (b) Permittivity=4.6, thickness is chosen to be 1 cm , 2 cm and 5 cm; (c) Thickness=1 cm, permittivity is chosen to be 2 and 4.6.	- 127 -
Figure 5-3	Model of detecting metal block behind the obstacle.	- 131 -
Figure 5-4	The received reflected signals without metallic target (blue) and with metallic target (red); (a) the thickness of the obstacle is 1 cm; (b) the thickness of the obstacle is 2 cm.	- 131 -
Figure 5-5	The relationship between the antenna gain and SNR for different sizes of the detected target when $P_t=29$ dBm and $d=40$ cm; (a) Loss=40 dB; (b) Loss=50 dB.	- 133 -
Figure 5-6	The relationship between antenna gain and SNR for different sizes of the detected target when $P_t=24$ dBm and $d=40$ cm; (a) Loss=40 dB; (b) Loss=50 dB.	- 134 -
Figure 5-7	The relationship between the antenna gain and SNR for the target of 6 cm \times 6 cm in different detecting ranges when $P_t=29$ dBm; (a) Loss=40 dB; (b) Loss=50 dB.	- 134 -
Figure 5-8	The relationship between the antenna gain and SNR for the target of 10 cm \times 10 cm in different detecting ranges; (a) Loss=40 dB; (b) Loss=50 dB.	- 134 -
Figure 5-9	The UWB imaging system architecture.	- 135 -
Figure 5-10	The RF circuit in the UWB imaging system.	- 137 -
Figure 5-11	The transmitting and receiving antennas part.....	- 139 -
Figure 5-12	The operation principle of antenna part; (a) the measured order in each rotating position; (b) the rotating way of the receiving antenna array.	- 139 -
Figure 5-13	The UWB imaging system implemented in the lab.	- 140 -
Figure 5-14	The simulated S_{11} for each receiving antenna element.	- 141 -

Figure 5-15	The mutual coupling S_{21} between the receiving antenna elements.	- 141 -
Figure 5-16	The radiation pattern (a) the single receiving antenna, (b) four Rx elements array.	- 141 -
Figure 5-17	S_{21} between Tx and each Rx for different distances between them; (a) $d_{txrx}=8$ cm; (b) $d_{txrx}=11.5$ cm; (c) $d_{txrx}=15$ cm; (d) $d_{txrx}=18.5$ cm.	- 142 -
Figure 5-18	The detecting process.	- 146 -
Figure 5-19	The influence introduced by the bag.	- 146 -
Figure 5-20	Delay-and-summed received signal.	- 147 -
Figure 5-21	Time window for the received signal; (a) One target; (b) Two targets. .	- 148 -
Figure 5-22	The process of image reconstruction.....	- 149 -
Figure 5-23	The 2D image reconstruction method.	- 150 -
Figure 6-1	The input signal and received signal in one period.	- 153 -
Figure 6-2	Comparison of the direct signal transmitted from Tx to each Rx and the returned signal reflected from the target in one period of time; (a) Received by RXA, (b) Received by RXB, (c) Received by RXC, (d) Received by RXD.	- 155 -
Figure 6-3	The demodulated signal received from different receiving antenna in one rotating position; (a) The situation of one target; (b) The situation of two targets. .	- 156 -
Figure 6-4	The bag used in the following measurements.	- 157 -
Figure 6-5	The UWB imaging system in the measurement, (a) side view of the bag and the antenna array, (b) side view of the measurement when the antenna array is rotating, (c) the concealed metallic target in the bag.	- 157 -
Figure 6-6	The reconstructed image for the single metallic target with the size of 10 cm \times 10 cm \times 1 cm at $d_z=20$ cm, (a) 2D image of the target, (b) the reconstructed	

image of the target in XY plane, (c) side view of the reconstructed image in YZ plane.
..... - 160 -

Figure 6-7 The reconstructed image for the single metallic target with the size of 10 cm × 10 cm × 1 cm at $d_z=30$ cm, (a) 2D image of the target, (b) the reconstructed image of the target in XY plane, (c) side view of the reconstructed image in YZ plane.
..... - 160 -

Figure 6-8 The reconstructed image for the single metallic target with the size of 10 cm × 10 cm × 1 cm at $d_z =40$ cm, (a) 2D image of the target, (b) the reconstructed image of the target in XY plane, (c) side view of the reconstructed image in YZ plane.
..... - 161 -

Figure 6-9 The reconstructed image for the single metallic target with the size of 10 cm × 10 cm × 1 cm at $d_z =50$ cm, (a) 2D image of the target, (b) the reconstructed image of the target in XY plane, (c) side view of the reconstructed image in YZ plane.
..... - 162 -

Figure 6-10 The reconstructed image for the single metallic target with the size of 8 cm × 8 cm × 1 cm at $d_z =20$ cm, (a) 2D image of the target, (b) the reconstructed image of the target in XY plane, (c) side view of the reconstructed image in YZ plane.
..... - 163 -

Figure 6-11 The reconstructed image for the single metallic target with the size of 8 cm × 8 cm × 1 cm at $d_z =30$ cm, (a) 2D image of the target, (b) the reconstructed image of the target in XY plane, (c) side view of the reconstructed image in YZ plane.
..... - 164 -

Figure 6-12 The reconstructed image for the single metallic target with the size of 8 cm × 8 cm × 1 cm at $d_z =40$ cm, (a) 2D image of the target, (b) the reconstructed image of the target in XY plane, (c) side view of the reconstructed image in YZ plane.
..... - 164 -

Figure 6-13 The reconstructed image for the single metallic target with the size of 5 cm × 5 cm × 1 cm at $d_z =20$ cm, (a) 2D image of the target, (b) the reconstructed

image of the target in XY plane, (c) side view of the reconstructed image in YZ plane.
..... - 165 -

Figure 6-14 The reconstructed image for the single metallic target with the size of 5 cm × 5 cm × 1 cm at $d_z = 30$ cm, (a) 2D image of the target, (b) the reconstructed image of the target in XY plane, (c) side view of the reconstructed image in YZ plane.
..... - 166 -

Figure 6-15 The reconstructed image for the single metallic target with the size of 4 cm × 4 cm × 1 cm at $d_z = 20$ cm, (a) 2D image of the target, (b) the reconstructed image of the target in XY plane, (c) side view of the reconstructed image in YZ plane.
..... - 167 -

Figure 6-16 The reconstructed image for the single metallic target with the size of 4 cm × 4 cm × 1 cm at $d_z = 30$ cm, (a) 2D image of the target, (b) the reconstructed image of the target in XY plane, (c) side view of the reconstructed image in YZ plane.
..... - 168 -

Figure 6-17 The comparison of the reconstructed image with the real one, (a) in XY plane, (b) in YZ plane..... - 170 -

Figure 6-18 Range resolution; (a) pulse towards the target, (b) pulse reflected from the target, (c) two returned pulse FWHM. - 172 -

Figure 6-19 Cross-range resolution..... - 173 -

Figure 6-20 The two targets in one column concealed in bag, (a) front view of the two targets in the bag, (b) side view of the two targets in the bag. - 174 -

Figure 6-21 The reconstructed image for the two targets in one column at $d_z = 10$ cm, (a) 2D image of the target, (b) front view in XY plane, (c) side view in YZ plane.
..... - 175 -

Figure 6-22 The reconstructed image for the two targets in one column at $d_z = 15$ cm, (a) 2D image of the target, (b) front view in XY plane, (c) side view in YZ plane.
..... - 175 -

Figure 6-23 The two targets in one row concealed in bag, (a) front view of the two targets in the bag, (b) side view of the two targets in the bag..... - 176 -

Figure 6-24 The reconstructed image for the two targets in one row at $d_{x2}=4$ cm, (a) 2D image of the target, (b) front view in XY plane, (c) side view in YZ plane. - 177 -

Figure 6-25 The reconstructed image for the two targets in one row at $d_{x2}=6$ cm, (a) 2D image of the target, (b) front view in XY plane, (c) side view in YZ plane. - 178 -

Figure 6-26 The reconstructed image for the two targets in one row at $d_{x2}=8$ cm, (a) 2D image of the target, (b) front view in XY plane, (c) side view in YZ plane. - 178 -

Figure 6-27 The two targets in the cross position in the bag, (a) front view of the two targets in the bag, (b) side view of the two targets in the bag..... - 179 -

Figure 6-28 The reconstructed image for the two targets in the cross position, $d_{x2}=6$ cm and $d_{z2}=15$ cm, (a) 2D image of the target, (b) front view in XY plane, (c) side view in YZ plane..... - 180 -

List of Tables

Table 3-1	The dimensions of the circular-edge antenna	- 71 -
Table 4-1	The pulse fidelity of the received signals for different antennas and different input signals.....	- 122 -
Table 5-1	The specification of each RF component	- 137 -
Table 5-2	Dynamic range analysis of the UWB imaging system	- 138 -
Table 6-1	Comparison of reconstructed images and the real one	- 170 -
Table 6-2	Resolution of the UWB imaging system for two targets.....	- 183 -
Table 6-3	Comparison of measured and theoretical down-range resolution and cross-range resolution	- 183 -

Abbreviations and Glossary

ALIS	Advanced Landmine Imaging System
ARC	Active Reflection Coefficient
BAVA	Balanced Antipodal Vivaldi Antenna
CW	Continuous-Wave
CWSA	Constant Width Slot Antenna
CMI	Confocal Microwave Imaging
CMP	Common Middle-point
DAS	Delay and Sum
DMAS	Delay Multiply and Sum
EC	European Commission
EM	Electromagnetic
FCC	Federal Communications Commission
FDTD	Finite Difference Time Domain
FM	Frequency Modulation
GPR	Ground Penetrating Radar
HPBW	Half Power Beam Width
ITU-R	International Telecommunications Union Radio Sector
LDC	Low Duty Cycle
LNA	Low Noise Amplifier
LPF	Low Pass Filter
LTSA	Linear Tapered Slot Antenna
LOS	Line of the Sight
MAMI	Multi-static Adaptive Microwave Imaging
MHV	Mine Hunter Vehicle
MICs	Microwave Integrated Circuits
MIST	Microwave Imaging via Space-time
PCB	Printed Circuit Board
PSD	Power Spectral Density
RCB	Robust Capon beam forming

RCS	Radar Cross Section
RF	Radio Frequency
RFID	Radio Frequency Identification
RVD	Resistively loaded Vee Dipole
RX	Receiving Antenna
SAR	Synthetic Aperture Radar
SNR	Signal-to-Noise Ratio
TSA	Tapered Slot Antenna
TG	Task Group
TX	Transmitting Antenna
TWI	Through-Wall Imaging
UWB	Ultra Wideband
VCO	Voltage Controlled Oscillator
VNA	Vector Network Analyser
VSWR	Voltage Standing Wave Ratio

Chapter 1 Introduction

Ultra-wideband (UWB) system can operate in very large bandwidth by utilising the signals in short pulse duration. According to the First Report and Order defined by Federal Communications Commission (FCC) in United States, the UWB signal or system mainly covers the frequency band from 3.1-10.6 GHz at a limited transmit power of -41.3 dBm/MHz in United States [1]. In Europe, European Community (EC) has chosen to make use of only part of the spectrum, which are 3.1-4.8 GHz and 6.0-8.5 GHz [2].

The UWB signal consists of very short pulses with energy separated in time. This very short pulse duration of the UWB signal makes it better in spatial resolution and short-range capability. Thus when it is applied in radar application, the increase in bandwidth actually allows the UWB radar system to obtain more information of the targets. The down-range resolution is related to the wavelength of the pulse. Typically, the UWB pulse is in 1 ns of pulse duration, which is equal to 30 cm of wavelength in free space, so that the down-range resolution is 15 cm. For traditional narrow band radar system, the pulse duration is 1 μ s, which is equal to 300 m of wavelength in free space, so that the down-range resolution is 150 m. Obviously, the reduction of the pulse duration improves the down-range resolution. Meanwhile, the wavelength of pulse in conventional radar is significantly larger than the size of the target of interest. It will have influence on the returned signal, providing little information about the nature of the target [3-5].

The combination of larger spectrum, lower power and pulsed data in UWB technology improves the data transmission speed, allows low probability of intercept and detection, makes multi-path immunity possible, and is suitable for precision ranging and localization. Thus, UWB technology has been regarded as one of the most promising wireless technologies. It has been widely applied in three main fields which are communication systems, vehicular radar systems, and imaging applications. As for the imaging applications, it mainly includes GPR (Ground

Penetrating Radar), through-wall imaging, diagnostic medical imaging, and suitcase scanning for the detection of concealed weapons or explosives [6].

In this chapter, the motivation of this research topic will be presented first. Then the contributions to this project will be given. Finally the organization of the thesis will be described.

1.1 Challenges, motivations and objectives

Security detecting is now attracting attention worldwide. Usually, the environment is perceived through our eyes based on the reflection of light, which is named as LOS (Line of the Sight). However, visible light cannot penetrate every material. In order to locate and acquire the information through opaque obstacles, it is necessary to develop a see-through scanner to detect dangerous objects through plastics, rubbers, dresses or other non-metallic materials at airports, subway stations or exhibition entrances.

Some of these scanners use X-rays, which have a wavelength in the range from 0.01 to 10 nanometres, corresponding to frequencies in the range of 3×10^{16} Hz to 3×10^{19} Hz. It is a type of ionizing radiation that might cause cancer and other health problems. However, microwave imaging is one promising non-ionizing and non-invasive alternative imaging technology. Consequently, UWB technology, which is harmless to human bodies or the environment, can be employed to see-through imaging applications.

The UWB imaging systems, utilising short pulses to provide higher resolution and better object classification, have the transceiver and the signal-processing unit. Most of them are bi-static or multi-static imaging systems. Therefore, individual antennas or antenna arrays are operating in the UWB imaging system. Although some antenna arrays and UWB imaging systems have already been developed during past years, some challenges still need to be overcome. They are listed below.

- The antenna array system must have high gain and directivity with less complicate structure, and less distortion to the reflected signal.

According to the existing UWB imaging system, which will be reviewed in detail in Chapter 2, larger numbers of antenna arrays are applied in order to improve the performance of the imaging system. They can provide more groups of reflected signals from the targets, improving the accuracy of the image. Moreover, they are beneficial to the cross-range resolution of the whole system.

However, more antennas exist in the systems, more noise and bulky size will be introduced. The bunch of switches will definitely introduce the complicity and noise to the system itself. Besides, the unchangeable number of antennas will also restrict to add more antenna elements to the imaging system.

- The multi-reflection and attenuation are caused by the obstacle and the antenna, which needs to be taken into consideration.

When UWB signals propagate through the opaque material, they suffer multiple reflections and material absorption. So when it comes to the application of seeing through the bag, it needs to deal with multi-path reflections, obstructions and antenna effects to avoid severe attenuation and dispersion.

Meanwhile, the antenna will cause distortion to the transmitting and received signal as it is like a filter. So the antenna with less distortion to the signal is a better choice for time domain imaging systems.

- The imaging system which is in a simple structure and of low cost because of the efficient hardware and signal-processing unit, is able to detect and image the concealed targets in bag;

The simple, cheap and efficient UWB imaging system is a good alternative to the X-ray machine. It needs to consist of efficient hardware (antenna array and RF circuits) and the signal-processing unit.

In short, the project aims to develop a novel UWB imaging system for detecting and imaging the metallic targets concealed in bag. It needs to satisfy the features below.

- 1) The system should be simple and work from 3 GHz to 6GHz.
- 2) The UWB antenna should have relatively high gain (above 6 dBi) especially over the lower frequency band (3-6 GHz). Although the current demand of the imaging system is working during 3-6 GHz, the antenna still needs to cover 3.1-10.6 GHz for the purpose of optimization in the future.
- 3) For the purpose of reducing the cost and optimising the number of antennas conveniently, it is better to update the elements in the antenna array conveniently.
- 4) The RF circuit should provide a good dynamic range.
- 5) The two-dimensional image reconstruction method needs to be achieved.

1.2 Contributions

According to the objective of the research project, the novel UWB imaging system with the rotating antenna array has already been developed and implemented. It can detect and image the metallic targets concealed in bag. The main contributions include design of the rotating UWB antenna array, analysis of the antennas' characteristics in the time domain, design of two-dimensional image reconstruction method and implementation of the UWB imaging system. They are presented below in detail.

1. Design of two types of UWB antennas

The circular-edge antipodal Vivaldi antenna and the corrugated balanced antipodal Vivaldi antenna (BAVA) have been designed and studied. Both of them can work across UWB frequency range from 3.1 GHz to 10.6 GHz, and have directional radiation patterns. The corrugated BAVA with smaller physical size has been improved to have a relative high gain around 7 dBi across the operating frequency range, especially the lower frequency band (3-6 GHz), which is the main operating frequency band of the imaging system. It is higher than the circular-edge antipodal Vivaldi antenna.

2. Characteristics analysis of the two antennas in the time domain

Since the proposed UWB imaging system is working in the time domain, it is necessary to analyse the characteristics of the antennas in the time domain. The corrugated BAVA causes less distortion to the signals in the time domain than the circular-edge antipodal Vivaldi antenna. For the modulated rectangular pulse, the pulse fidelity of the corrugated BAVA is around 95%.

3. Design of the rotating antenna array

The corrugated BAVA has better characteristics than the circular-edge antipodal Vivaldi antenna both in the frequency domain and time domain, so that it is used as the element in the antenna array.

The rotating antenna array is composed of one central transmitting antenna and four receiving antennas. The receiving antennas are placed side-by-side on a straight arm, rotating around the central transmitting antenna. With the rotation structure, the linear antenna array achieves the functionality of the two-dimensional array, reducing the limitation of antennas in space and simplifying the system.

4. Design of the two-dimensional image reconstruction method

In terms of each rotating position, the image reconstruction method is based on DAS (Delay-and-Sum) algorithm. When the antenna array is rotating in space, the corresponding coordinate of one-dimensional image is rotating. Thus, the two-dimensional image of the target is then achieved.

5. Design of the RF circuits

The RF transceiver has been designed to achieve a good dynamic range and receiver sensitivity. Finally, the dynamic range is 69 dB and receiver sensitivity is -78 dBm.

6. Implementation of the UWB imaging system

The UWB imaging system contains the rotating antenna array, RF circuits and the signal-processing unit. It can successfully detect and image the single and pairs of metallic targets concealed in bag. The smallest detectable single metallic target is

with the size of 4 cm × 4 cm × 1 cm, placed at maximum distance of 30 cm away from the imaging system. The metallic target with the size of 10 cm × 10 cm × 1 cm can be detected and imaged at maximum distance of 50 cm. The system has 15 cm in down-range resolution and 6 cm in cross-range resolution.

1.3 Organization of the thesis

The rest of the thesis is organized as follows:

Chapter 2: This chapter gives an introduction to the UWB imaging applications. First it presents the basic UWB radar technology, including the detecting method, frequency domain and time domain imaging techniques. Then it reviews the state-of-the-art of UWB imaging applications, especially the existing UWB imaging systems.

Chapter 3: This chapter describes two own designed UWB antennas, which are the circular-edge antipodal Vivaldi antenna and the corrugated balanced antipodal Vivaldi antenna. The characteristics of the two antennas in the frequency domain are discussed in detail. It is successful to find out that the corrugated structure can improve the gain of the antenna in lower frequency and make the antenna have relative high gain across the operating frequency range.

Chapter 4: This chapter presents the study of characteristics in the time domain for the circular-edge antipodal Vivaldi antenna and the corrugated balanced antipodal Vivaldi antenna described in Chapter 3. The distortion of the signal caused by the antenna has been investigated, which is an important consideration for the use of the antenna in the UWB imaging system.

Chapter 5: This chapter addresses the implementation of the UWB imaging system. It describes the system thoroughly, including the system's architecture, the rotating antenna array, RF circuits and the two-dimensional image reconstruction method based on DAS algorithm.

Chapter 6: This chapter presents the detailed measurements being achieved using the UWB imaging system. Quantities of measurements have been carried out, including the single metallic target and pairs of metallic targets concealed in bag.

The down-range and cross-range resolutions of the UWB imaging system have been investigated.

Chapter 7: This chapter concludes the research work that has been undertaken in this project, and recommends the future work.

Reference

- [1] Federal Communications Commission, *First Report and Order 02-48*, February 14, 2002.
- [2] Draft amended CEPT ECC Decision ECC/DEC/(06)12: “ECC Decision of [1 December 2006] on complementary regulatory provisions for devices using Ultra-Wideband (UWB) technology”, June 2008.
- [3] James D. Taylor, *Introduction to Ultra-Wideband Radar Systems*, 1994.
- [4] E. Perl, “Review of Airport Surface Movement Radar Technology”, *Aerospace and Electronic Systems Magazine, IEEE*, Vol: 21, Issue: 10, Page (s): 24-27, 2006.
- [5] B. Allen, M. Dohler, E.E. Okon, W.Q. Malik, A.K. Brown, D.J. Edwards, *Ultra-wideband Antennas and Propagation for Communications, Radar and Imaging*, John Wiley & Sons, Ltd. 2007.
- [6] B. J. Harker, A. D. Chadwick, G.L. Harris, “Ultra-wideband 3-Dimensional imaging (UWB 3D Imaging)”, *Roke Manor Research Limited, UK*.
<http://www.roke.co.uk/resources/papers/UWB-3D-Imaging.pdf>, 2008.

Chapter 2 UWB Imaging Technology

UWB signal can penetrate a great variety of opaque materials, such as biological tissues, clothes, the ground and concrete walls. It makes the technology be able to detect, identify and image the desired moving or stationary targets in short range [1-2].

UWB technology can be used to measure both distances and positions in GPR applications [3-5] and positioning applications [6-7]. It is now being developed for new types of imaging systems for medical applications, see-through wall applications and security scanning applications. Potential medical applications include breast cancer imaging, cardiac imaging and brain imaging [8-14]. The see-through wall applications or security scanning applications can locate persons or dangerous things hidden behind a wall in crises or rescue situations [15-17]. They can be also applied in home repair industries to improve the safety of the construction by locating steel reinforcements bars, electrical wiring and pipes hidden inside walls [18-19].

Due to the advantages of UWB technology and varieties of applications in imaging area, this chapter will mainly present the UWB imaging technology. Firstly the basic concept of UWB radar technology will be given, including the UWB radar detecting method and typical architectures of the radar system in the frequency domain and time domain. Then the current status of different UWB imaging applications will be reviewed.

2.1 UWB Radar technology

2.1.1 UWB Radar detecting methods

An imaging radar system works similarly to a flash camera but imaging by microwave instead of light to illuminate the target. High power pulses are transmitted towards the target or imaging area. On the target's surface, the energy of the radar pulse is scattered in all directions, some of which are reflected back towards the

antenna. These echoes are converted to digital data and passed to a data recorder for later processing. Based on the echoes, the target can be displayed in an image. Given that the radar pulse travels at the speed of light, it is relatively straightforward to use the measured time for the round trip of a particular pulse to calculate the distance or range to the reflected target.

Radar systems are normally divided into three different types of detecting methods based on the energy transmission way, which are continuous-wave method, the frequency modulation method, and pulse method [20].

The continuous-wave (CW) method uses the Doppler Effect to detect the presence and speed of an object moving towards or away from the radar. The system is unable to determine the range of the target or to differentiate between targets that lie in the same direction and are travelling at the same speed. It is usually used in fire control systems to track fast moving targets at close range.

In the frequency modulation (FM) method, energy is transmitted as RF waves that continuously vary, increase and decrease from a fixed-reference frequency. Measuring the difference between the frequency of the returned signal and the frequency of the radiated signal gives an indication of range. This system works well with stationary or slowly moving targets, but it is not satisfied for locating fast moving targets. It is used in aircraft altimeters that give a continuous reading of the height of the aircraft above the earth.

The pulse modulation method is the most common method in radar modulation. Using this method, the energy of radio frequency in radar is transmitted in short pulses. If the transmitter is cut off before any received pulse which is reflected from a target, the receiver can distinguish between the transmitting pulse and the received pulse. After all reflections have returned, the transmitter can be switched on again. The output of the receiver is applied to an indicator that measures the time interval between the transmission of energy and its return as a reflection. Since the energy travels at a constant velocity, the time interval becomes a measure of the range. It does not depend on the relative frequency of the returned signal, or on the motion of

the target, so this method is used much commonly than other methods in radar applications.

2.1.2 UWB frequency domain imaging technique

When the system is doing the measurements in the frequency domain, the basic architecture of the system is set up as given in Figure 2-1. It consists of VNA (Vector Network Analyser) with swept frequency oscillator. This technique is mainly based on complex transfer function measurement, expressed in terms of magnitude and phase, and performed using VNA. Port 1 of VNA's S-parameter test set is connected to the transmitting antenna, while port 2 is connected to the receiving antenna. The VNA itself can provide the signal source in the measurement and sweep the frequency within the measured band of interest.

Obviously, the wider the chosen swept frequency band is, the longer the measurement will take. Meanwhile, the time of the measurement is related to the data constructed to the imaging resolution. For most modern VNAs, it could use stepping mode instead of sweeping mode to do the measurement, so that it could save more time. But in terms of UWB characterization of the ultra-wide frequency band, it will still be a trade-off between the frequency resolution and the required number of measurements [21]. Thus, it is hard to achieve the real-time imaging with high resolution through VNA, which is the major problem in this kind of frequency domain measurement.

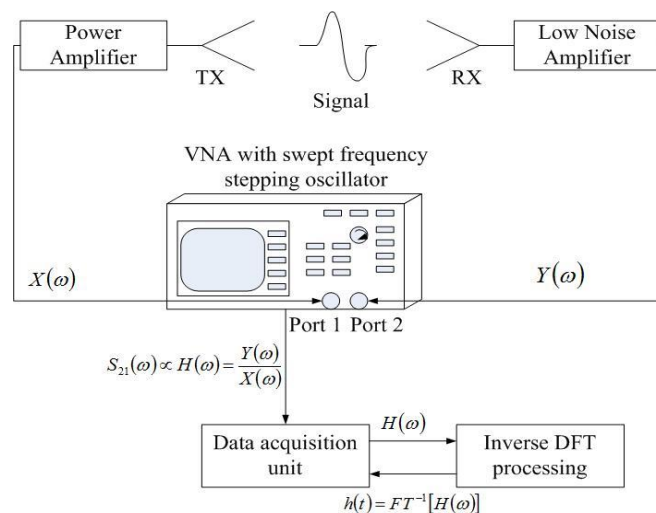


Figure 2-1 UWB imaging system based on frequency domain measurement [21].

As mentioned before, frequency domain measurement through VNA directly measures the phase and magnitude spectrum parameters of the signal. In order to analyse the time domain performance of the signal, it needs to use Inverse Fourier Transform processing unit. The time duration τ is directly proportional to the number of measured points, and is reciprocal to the frequency bandwidth, which is as shown in equation (2-2).

$$\tau = \frac{1}{\Delta f} \quad (2-2)$$

Where, Δf is the frequency bandwidth.

The down-range resolution is proportional to the time duration τ , so that it is necessary to increase the frequency bandwidth. While increasing the bandwidth, the relative number of measured points has to be increased to keep the accuracy over the operating bandwidth, which leads more scanning time to finish the measurement.

Besides the stepping time, another important factor, which may affect the resolution result, is the system loss. In order to reduce the system loss, high-quality RF cables are required to connect the VNA to both transmitting and receiving antennas across UWB frequency range. Furthermore, it is required to shield these cables, avoiding the signals to radiate into the air.

2.1.3 UWB time domain imaging technique

In the time domain technique, a periodic train of very short-duration Gaussian-like pulses separated by sufficiently long quiet intervals is used for measurement of UWB signal propagation. These pulses are radiated by means of a UWB antenna with sufficiently large bandwidth. At the receiving part, the signal is captured by another UWB antenna and sampled by means of a wideband detector such as a digital sampling oscilloscope. The basic UWB imaging system based on time domain measurement is shown in Figure 2-2. It consists of a pair of transmitting and receiving UWB antennas, a pulse generator, a digital sampling oscilloscope, and a triggering signal generator. The pulse generator is connected to the transmitting antenna with a power amplifier to amplify the transmitting power. The receiving

antenna is connected to the digital sampling oscilloscope by means of a wideband coaxial cable. To increase the received signal power, a low-noise amplifier can be used at the output terminals.

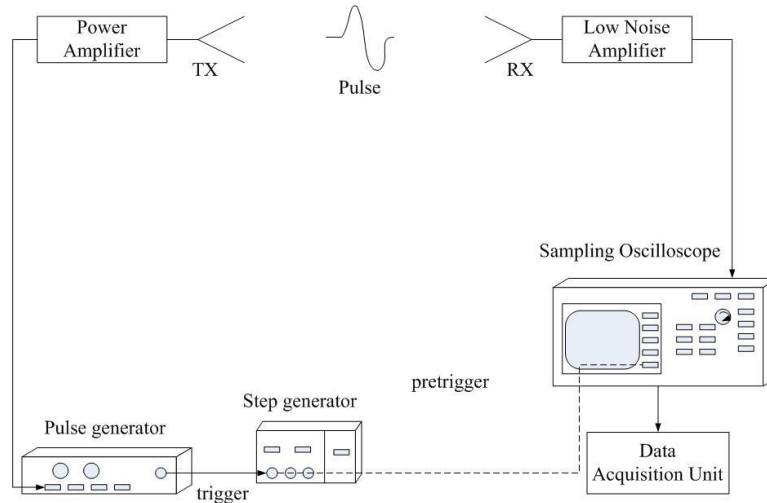


Figure 2-2 UWB imaging system based on time domain measurement.

One of the most important requirements in UWB time domain measurement is synchronization of both transmitting and receiving sides of the propagation channel. To maintain synchronization, a low-jitter triggering signal is established between the pulse generator and the digital sampling oscilloscope. The sampling oscilloscope requires a pre-trigger. This is achieved by using a step generator driver that can supply the required trigger and pre-trigger signals. The time delay introduced by the triggering cables and the propagation path of the pulse can be compensated by adjusting the time delay between the pre-trigger and the delayed trigger signals. This can also be eliminated during the signal processing part.

The other important issues need to be addressed are the calibration and the noise. The purpose of the calibration is to eliminate the effects of non-ideal characteristics of measuring instruments from the measured data. Also, the received UWB signals could suffer degradation due to interference and noise from various sources. Usually, the received signals may contain a narrow band noise in the form of a sinusoidal waveform. This type of noise can be eliminated through band pass filtering. On the other hand, the wideband noise is typically in the form of random short pulses and

can be significantly reduced through multiple signal averaging. Generally it is available in sampling oscilloscopes [22].

In conclusion, the system working in the time domain can acquire bunch of measured data, which is better to have real-time measurement. Without the VNA, it is possible to reduce the cost in the system architecture. Thus, this project plans to develop a UWB imaging system to work in the time domain.

2.2 UWB Imaging applications

2.2.1 Current Status of Medical imaging

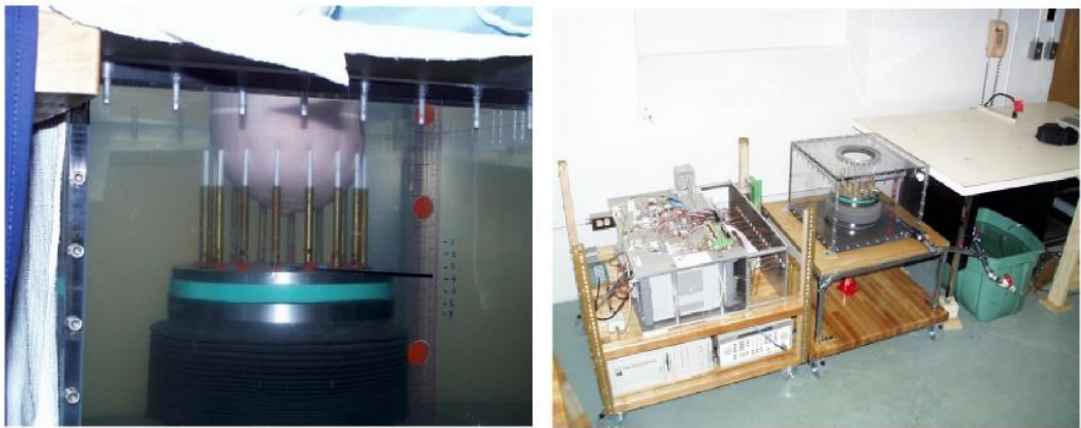
Medical imaging used for exploring interior structures or tissues of human body is a topic of growing interest. Most current clinical imaging technologies are ultrasound scanners, X-ray based on Computed Tomography (CT) and the Radio Frequency (RF) technique of Nuclear Magnetic Resonance Imaging (MRI). As mentioned in the beginning of this chapter, UWB technology has been attracting quite a lot research interest in medical imaging, because it is in advantage of non-ionizing radiation compared to X-ray tomography, making it possible to get accurate information inside the patient's body safely.

Among all medical imaging applications, breast cancer imaging is attracting more interest around the world due to relatively less complicate structure of breast compared with brain and heart. In UWB frequency region, a cancerous tissue shows a considerable dielectric difference to the surrounding healthy breast tissues. Regarding to this contrast, the image for breast tumour could be formed [23].

UWB for breast cancer imaging has been investigated by a number of research groups. Several UWB imaging systems have been reported during past years. The typical ones among them will be reviewed below.

Meaney *et al.* from Dartmouth College developed the initial prototype with a microwave imaging method that actively probed the breast with antenna array elements, as shown in Figure 2-3, which was the first trial to have the clinical tests. The antenna array of 16 monopole antennas operating over a frequency range of 300-

1000 MHz were immersed in 0.9% saline surrounding the pendant breast of a subject positioned prone during the test. The system activated the breast by transmitting the signals from one antenna at a time and sequentially measured the received electric fields at each of opposing antennas. Detection was achieved by down converting the transmitted signal with a reference signal to produce a low-frequency response which was sampled by an analog/digital (A/D) board where the signal amplitudes and phases were extracted using a software-based lock-in amplifier technique [24-26].



(a)

(b)

Figure 2-3 Microwave breast imaging system developed in Dartmouth College. (a) Illumination tank with antenna array during patient examination, (b) integration of electronics cart (top removed) with the illumination tank [25].

Susan Hagness *et al.* from University of Wisconsin presented a mono-static UWB system with an UWB pyramidal horn antenna, as shown in Figure 2-4 (a). This UWB system synthesized an antenna array by scanning the single horn antenna to each array position around the breast phantom, sequentially transmitting a swept-frequency signal and receiving the backscatter, as shown in Figure 2-4 (b) (c). This UWB radar imaging system operating across the frequency band of 1-11 GHz utilised the confocal algorithm based on finite difference time domain (FDTD) method to detect and image the possible breast tumour [27-31].

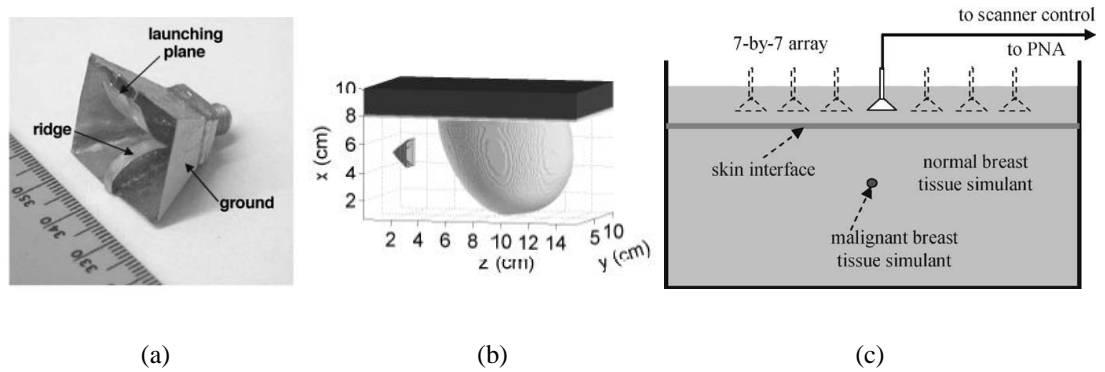


Figure 2-4 UWB mono-static imaging system developed in University of Wisconsin. (a) UWB horn antenna, (b) 3D FDTD model comprised of a breast phantom and an UWB antenna, (c) Schematic showing a cross-sectional side view of the experimental setup [30].

E.C. Fear *et al.* from University of Calgary implemented a mono-static system which was named as tissue sensing adaptive radar (TSAR). They designed three types of UWB antennas, which were TEM horn antenna and two versions of a balanced antipodal Vivaldi antenna (BAVA). At last the UWB radar imaging system used the modified BAVA, which consisted of a profiled dielectric piece with higher permittivity that was placed in the antenna aperture [32], as shown in Figure 2-5 (a). Similar to the one in Dartmouth College, the system also had a tank containing an immersion liquid and sensors located under the table. The sensors included a dielectric BAVA and a laser, which were both attached to an arm. The arm was used to move the sensors in the vertical direction while the entire tank was rotating in a circle in horizontal direction, as shown in Figure 2-5 (b) (c). In this manner, the UWB antenna was able to scan around the breast, sending and receiving microwave signals over the frequency range from 50 MHz to 15 GHz. The recorded data were used to generate 3D images of the breast using a time-shift and sum approach with the volume of interest for imaging defined by the laser data and an adaptive algorithm used to reduce the dominant reflections from the skin [33-35].

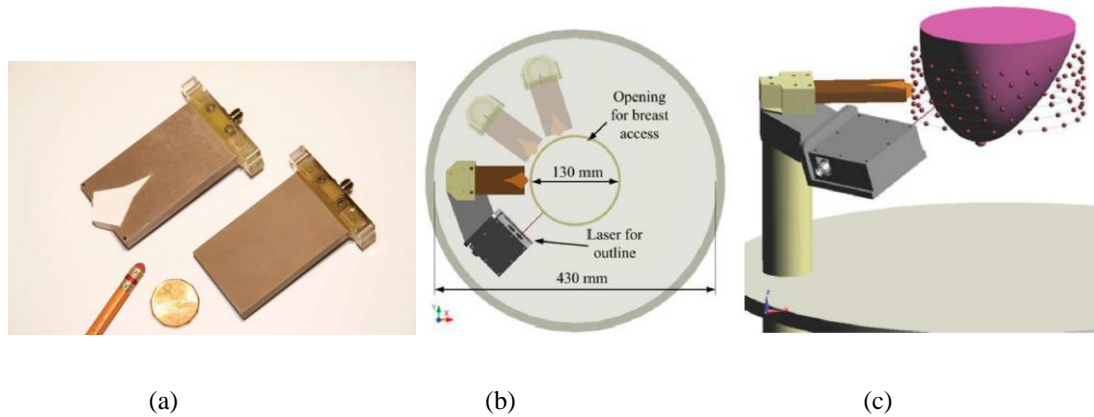


Figure 2-5 UWB mono-static imaging system developed in University of Wisconsin. (a) UWB horn antenna [32], (b) 3D FDTD model comprised of a breast phantom and an UWB antenna [35], (c) Schematic showing a cross-sectional side view of the experimental setup [35].

The research group from University of Queensland set up a microwave imaging system in the X-band with step-frequency synthesized pulse for breast cancer application. The system consisted of a cylindrical scanning mechanical sub-system supporting the movement of a probe antenna, a VNA with time domain processing capability and a breast phantom. The probe antenna was a UWB tapered slot antenna operating in UWB frequency band, as shown in Figure 2-6 (a). Initially the probe antenna was treated as the transmitting antenna, and a horn antenna was treated as the receiving antenna. Then it was optimized to mono-static system, as shown in Figure 2-6 (b). The UWB tapered slot antenna was positioned vertically from the phantom and rotated around the breast phantom [36-38].

Huang *et al.* from University of Liverpool proposed a simulated model to utilise the GPR imaging method to the breast cancer detection. The model in Figure 2-7 (a) contained a group of antennas placed as a straight line to detect the tumour in the phantom. When optimized to image more shape of the object, it proposed a model with a ring of transmitters which were located in a radius of 0.02 m and 20° increments around the target, as shown in Figure 2-7 (b). At each location a transmission was made with the adjacent transmitter location acting as ideal receivers. Thus there were 36 received signals in total [39-41].

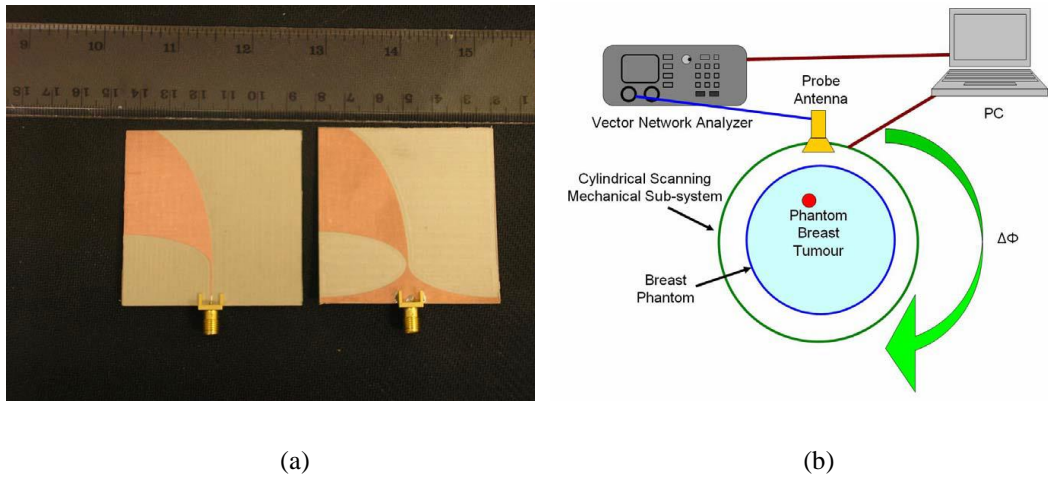


Figure 2-6 UWB mono-static imaging system developed in University of Queensland. (a) UWB tapered slot antenna, (b) Experimental setup [38].

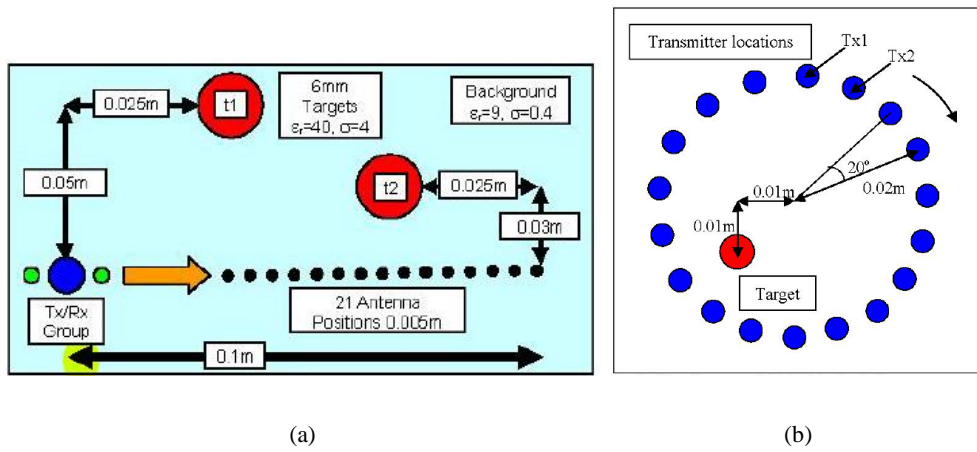


Figure 2-7 The 2D FDTD simulation set up proposed in University of Liverpool; (a) 2D FDTD simulation set up; (b) circular array in this model [41].

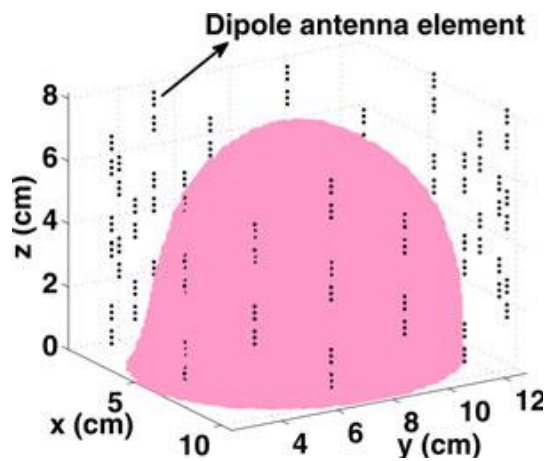


Figure 2-8 The simulated phantom with the dipole antenna array and the skin layer [42].

Kosmas *et al.* from King's College London presented a microwave breast tumor detection based on the use of bio-compatible flagellated magnetotactic bacteria (MTB). A three-element radar array based on the dipole antenna was employed to image possible tumour in the breast phantom. Each antenna element represented both a point source which was assigned an electric field and an observation point. The antennas were immersed in a coupling medium with dielectric property matching the tissue permittivity [42-43].

Benjamin *et al.* from University of Bristol developed a multi-static system using stacked patch antennas arranged on a hemisphere. As shown in Figure 2-9, the system comprised 60 antenna elements as the multi-static structure [46]. These stacked patch antennas were formed as a half spherical structure located on the top of the system, while 60 switches were placed on the bottom of the system to choose each of the antennas to be the transmitter or the receiver. The system had experimentally demonstrated the ability to detect small (4mm and 6mm) tumours using a physical 3D curved breast phantom. But because of the inhomogeneous tissue in breast, the contrast between the cancerous tumour and the healthy tissue was hard to distinguish. According to the large-scale clinical trial carried out at Frenchay Hospital in Bristol in 2008-2009, only 25% of around 200 patients referred to the Breast Care Unit were found to have malignant tumours, using the UWB system developed in University of Bristol [44-46].

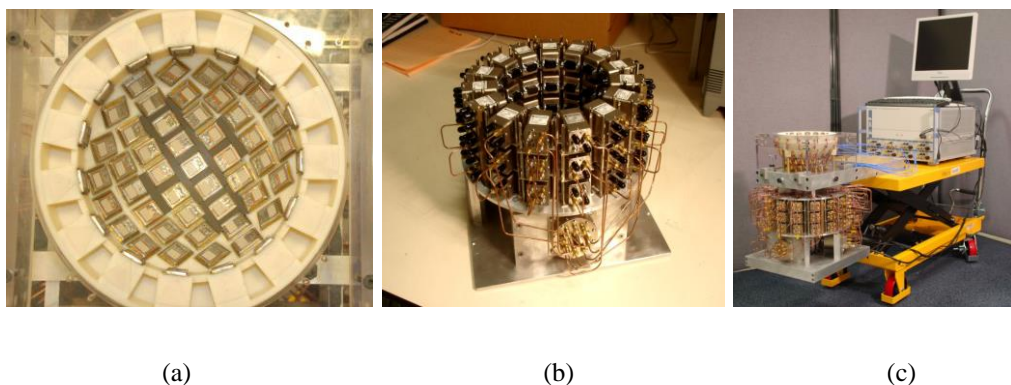


Figure 2-9 Multi-static UWB Radar system for Breast Cancer from University of Bristol; (a) 60-element antenna array; (b) Completed 60-way TX/RX electromechanical switching interface; (c) The whole imaging system including switching interface (below) between VNA and array (top) [46].

2.2.2 Current Status of Ground Penetrating Radar

As stated in [47-49], GPR can provide high-resolution information to a depth of typically 0-10 m, and up to 40 m in some geological environments. It has been developing since it was first taken into practical use in the 1970's for ice sounding in Antarctica. Now GPR is applied to a wide range of inspection tasks, for example to detect buried pipes in the ground, to inspect layers under the roads, or to map steel reinforcing in concrete structures.

When GPR system works in the practical environment, the electrical properties of the ground will influence the input impedance and radiation characteristics of the antenna, because it is close to the ground. Usually the detection time is less than 100 ns. For shallow targets, it can be even a few nanoseconds. Therefore, the antenna must be able to transmit the signal with little distortion or ringing in order to avoid masking of the target echoes and to couple electromagnetic energy into the ground [50].

Different antennas have been studied and designed for GPR systems in different research groups, for example resistively loaded antennas (dipole or bow-tie antenna), TEM horns (dielectric wedge antenna), spiral antennas and Vivaldi antennas. Some typical antennas and GRP systems will be reviewed below.

The resistively loaded Vee dipole (RVD), the conductivity of which is linearly tapered from the feed point to the open end of the antenna, has been proved to greatly reduce clutter related to the antenna and has low backscattering radar cross section (RCS), which makes it easier to distinguish land mines [51-52]. It is lightweight and suitable for an array. But it is poorly matched to the feed line so that the voltage standing wave ratio (VSWR) is large. By curing the arms of the antenna and modifying the resistive profile, the RVD is improved to have better VSWR and gain [53].

Sato *et al.* from Tohoku University developed a dual sensor system, named as Advanced Landmine Imaging System (ALIS), to detect buried landmines in various countries, such as Afghanistan and Croatia [54-55]. In the development of ALIS, two

different antennas were applied, which were the cavity back spiral antenna and the Vivaldi antenna. In the latest hand held ALIS, the cavity back spiral antenna was molded with a metal detector sensor [56], as shown in Figure 2-10, reducing the weight of the sensor head. The cavity spiral antenna was suitable for most normal operation of ALIS. In order to obtain better performance, the Vivaldi antenna was proposed to be used in the vehicle mounted ALIS.



Figure 2-10 ALIS system with the cavity spiral antenna [56]

The Vivaldi antenna has a flat shape, which is easy to construct an antenna array. Meanwhile it possesses a wide bandwidth and a high cross-polarization ratio. In Figure 2-12 (a), the Vivaldi antenna, which was designed in Tohoku University, was used to configure different antenna arrays for different applications. One of the types was the symmetrical CMP antenna array with three pairs of Vivaldi antennas for mine hunter vehicle (MHV), as shown in Figure 2-12. In each pair of antennas, one was used to transmit the signal while the other one was used to receive it [57]. Another type of the arrays was the common-source antenna array with one transmitting antenna and five receiving antennas for non-destructive testing of civil engineering structures. It could greatly improve the accuracy of the velocity and thickness estimations in the laboratory measurements, because the time delay of electromagnetic waves from the antenna feeding point to the point of incident on the ground surface was compensated according to the antenna offset and the estimated phase center position [58].

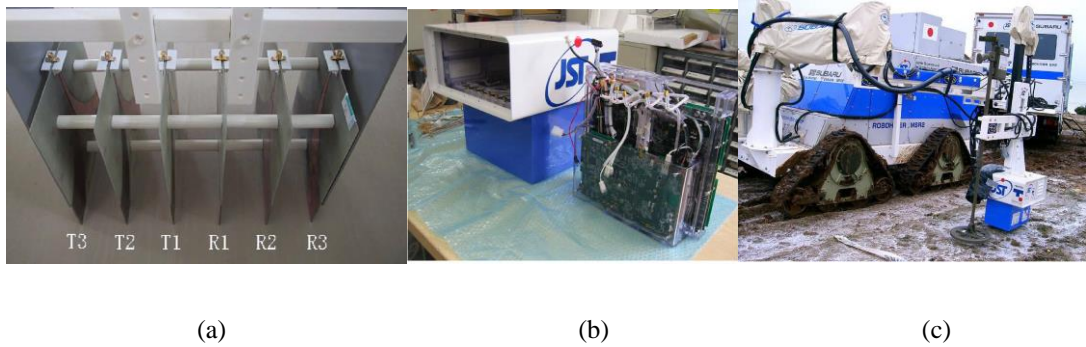


Figure 2-11 ALIS system develop in Tohoku University. (a) The symmetrical CMP antenna array, (b) CMP antenna array GPR system mounted on MHV, (c) Disassemble CMP antenna GPR system [57].

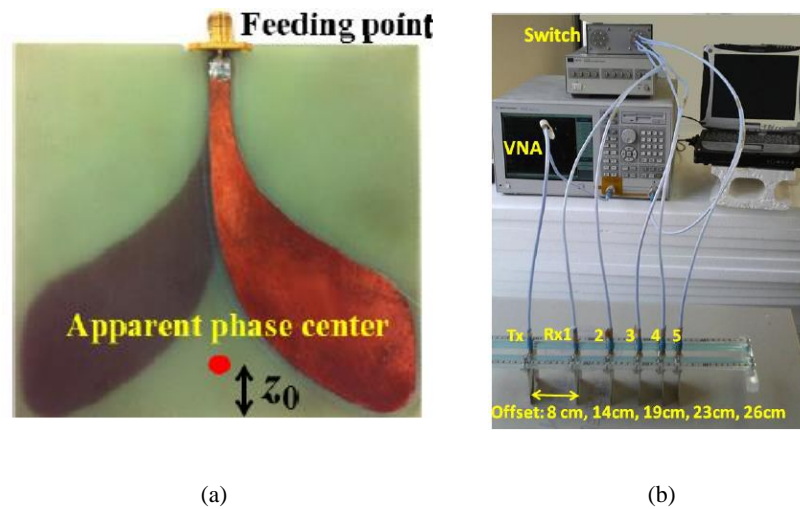


Figure 2-12 The GPR system develop in Tohoku University. (a) the Vivaldi antenna, (b) the developed common-source GPR antenna array system [58].

Yarovoy *et al.* from IRCTR, Delft University of Technology implemented several types of GPR radar for different applications. A multi-channel UWB radar sensor with digital footprint forming has been developed for landmine detection research [59]. The mini-array GPR comprised a pulse generator, an antenna array system, a seven-channel signal conditioner and an eight-channel sampling converter. The radar antenna system consisted of a single dielectric wedge antenna (transmitting antenna) elevated 60 cm above the ground and a linear array of loop antennas (receiving antenna) elevated 20 cm above the ground [60], as shown in Figure 2-13 (a). The whole antenna system was mounted on the TNO Defense test platform and covered with a protective shield, as shown in Figure 2-13 (b) (c). This system operated from 170 MHz, and had a frequency bandwidth of 3.1 GHz. In comparison with

commercially available video impulse GPR system, the developed front-end was larger in operational bandwidth, allocated at lower frequencies, lighter in weight and simplified in block scheme [61].

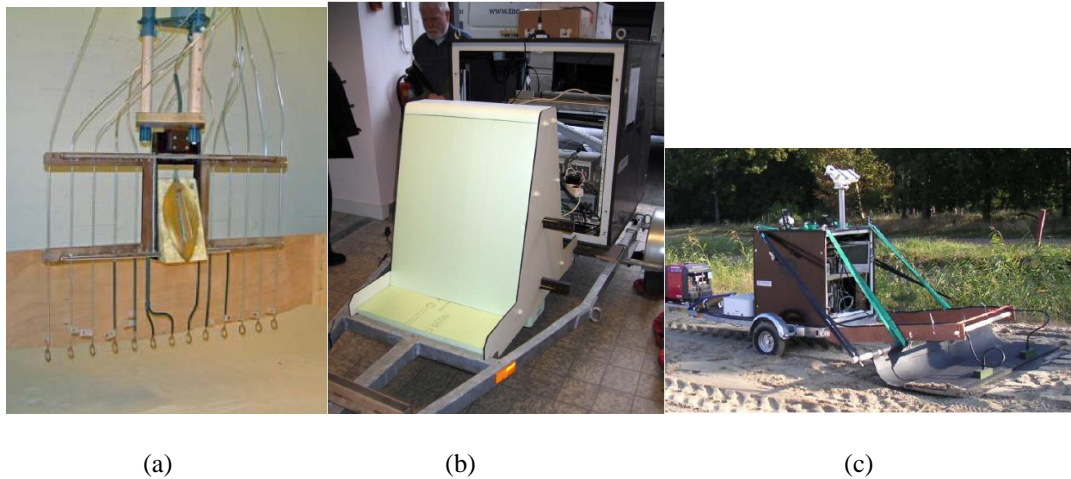


Figure 2-13 IRCTR radar system, (a) The antenna array system [60], (b) Antenna system of the radar mounted at the TNO test platform [61], (c) TNO multi-sensor test trolley for landmine detection research [61].

Another GPR developed in this research group consisted of two cavity-backed resistively loaded bow-tie antennas for detection and location of buried utilities [62-64]. Although the bow-tie antenna was basically the limiting case of bi-conical antennas, it was attractive due to its simplicity and wideband property. For GPR applications, bow-tie antennas with circular ends demonstrated better performance since reflections from the ends occurred at the same time, reducing late-time ringing [65]. The resistive loading of the radiating structure had an ultra-wideband behavior and adequate radiation efficiency. To reduce the volume occupation, this antenna was printed on a high permittivity dielectric substrate.

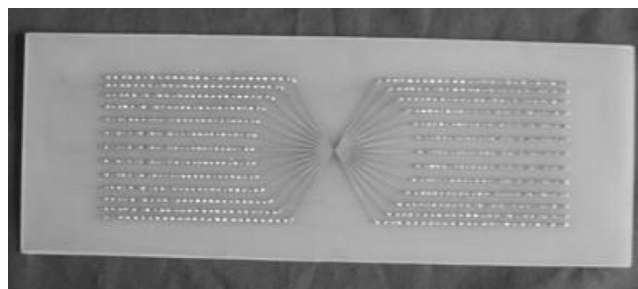


Figure 2-14 The cavity-backed resistively loaded bow-tie antenna [64].

Huang et al. from University of Liverpool also investigated several types of antennas in GPR applications, including the spiral antenna [66] and the monopole antenna. They proposed that the planar monopoles antenna had attracted more attention since its low cost and light weight made it integrated with other devices seamlessly in the system. A coplanar waveguide fed planar UWB monopole antenna was proposed in [67]. It modified the conventional circular disc monopole to a Mickey Mouse shaped radiator, as shown in Figure 2-15, which could not only reduce the size but also offer a broader impedance bandwidth from 0.4-3 GHz.



Figure 2-15 The Mickey Mouse monopole antenna developed in University of Liverpool [67].

2.2.3 Current Status of See-through Wall imaging

Due to the urgent needs of urban warfare, counterterrorism, calamity rescue and so on, UWB imaging systems for see-through wall applications have been developed during past years. Advances in a large variety of UWB see-through wall imaging systems have been reported in research institutes and companies [68-71].

The U.S. Army Research Laboratory (ARL) developed UWB synchronous impulse reconstruction (SIRE) radar to image the interior of an abandoned Army barrack building. The SIRE radar (300 MHz to 3 GHz) employed a physical aperture of 16 tapered slot antennas as the receiving antennas. They were equally spaced across a linear aperture that was approximately 2 m long. Two impulse transmitters were located at either end and slightly above the receiving array, as shown in Figure 2-16. In addition to signal-processing techniques, the SIRE radar achieved enhanced resolution [72-73].



Figure 2-16 The ARL UWB SIRE radar system integrated onto the vehicle [72].

The research group from University of Tennessee has been involved in developing UWB impulse synthetic aperture radar (SAR) prototypes for real-time human imaging and indoor positioning using time-domain techniques, as shown in Figure 2-17 (a). There were two generations of the prototype with two sub-arrays [74-76]. In the first one, the antenna array contained 16 sub-arrays, each of which was a 1×16 antipodal Vivaldi antenna array, covering the usage of 6-10 GHz, as shown in Figure 2-17 (b). This prototype was mainly for seeing through drywall and wooden wall. In the second prototype, the antenna array utilised 8 sub-arrays, each of which was a 1×8 Vivaldi antennas, covering the operation frequency band of 1.99-10.6 GHz, as shown in Figure 2-17 (c). One wideband Vivaldi element was used as transmitting antenna, while a 1×8 linear Vivaldi antenna array was treated as the receiving antenna. This prototype could be mounted on the top of a vehicle for easy deployment and surveillance.

The research group from Universität Duisburg-Essen Germany implemented a 3D bi-static and fully polarimetric UWB imaging system for inspecting a target with weak scattering centres. It was a UWB Maximum Length Binary Sequence (M-Sequence) Radar with an operating band of 4.5-13.5 GHz with an additional quadrature modulator. A pair of directive Teflon embedded two tapered slot line Vivaldi antennas on a single substrate, as shown in Figure 2-18. The antennas, operating from 3.5 GHz to 13.5 GHz, gave a higher gain and saved space compared to an array of two separated antennas. However the sharp focusing characteristic might gather

spatially distributed energy when a target under test was not in the main lobe of the antennas [77-78].

The UWB 3D imager from Manor Research Ltd. was able to image the targets concealed in the suitcase and detect people over a distance. It used four antenna array units, operating as two independent bi-static Radars. They were in co-polar vertical and co-polar horizontal polarisation respectively, as shown in Figure 2-19. Each antenna array unit contained 25 elements, which was total 49 cm in length [79]. Although this system could be applied in multiple applications, it was not in compact size.

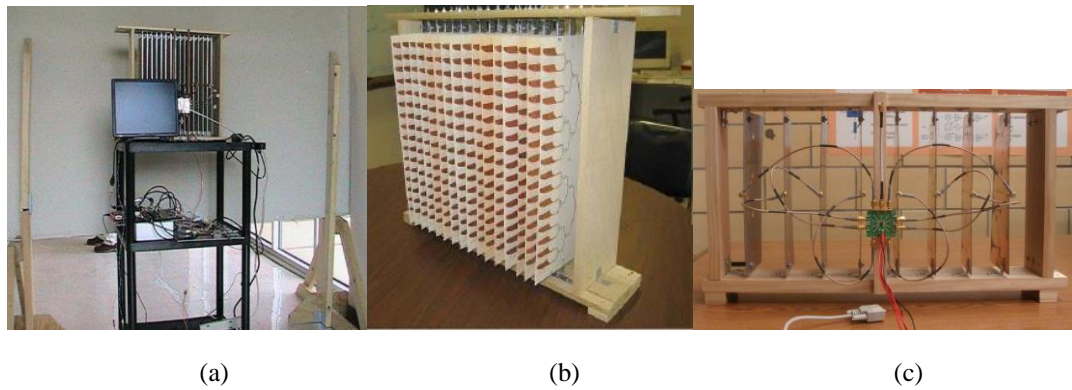


Figure 2-17 UWB through-wall imaging system from University of Tennessee; (a) The first generation of the whole system; (b) 16×16 antenna array (first generation) [74]; (c) 8×8 antenna array (second generation) [76].

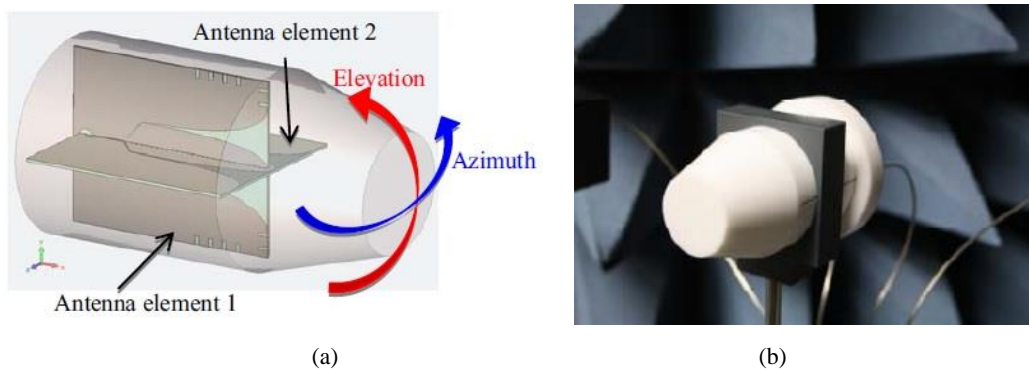


Figure 2-18 The dual-polarimetric antennas used in UWB imaging system from Universität Duisburg-Essen. (a) the model, (b) the manufacture [77].

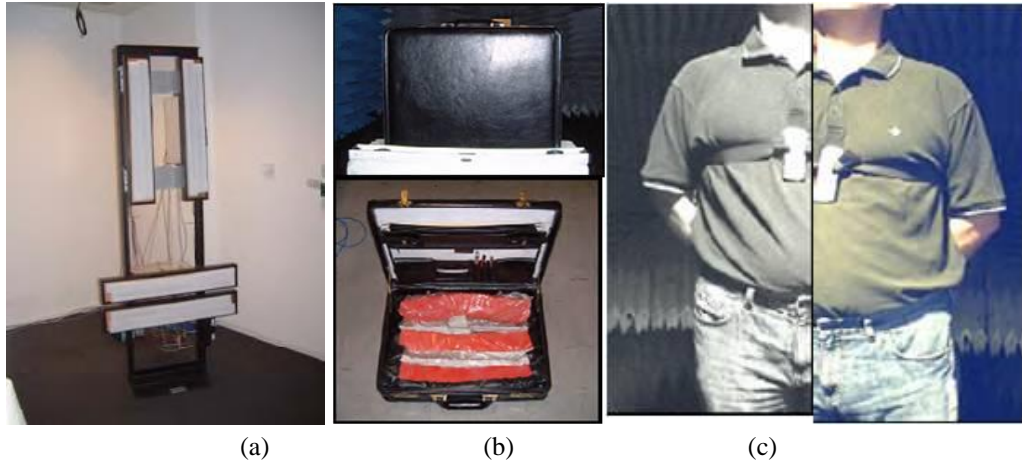


Figure 2-19 UWB 3D Imager from Roke Manor Research Ltd., DTI and Thales Research & Technology (UK) Ltd; (a) The whole system; (b) Suitcase imaging; (c) People scanning [79]

2.3 Summary

This chapter have mainly described the basic concept of UWB imaging technology. First it has presented the basic UWB radar technology, including the detecting method, frequency domain and time domain imaging techniques. Then it has reviewed the state-of-the-art of UWB imaging applications in medical imaging, ground penetrating radar and see-through wall imaging. The typical implemented imaging systems around the world in these applications have been given in a brief description. Among them, it is known that large profile antenna arrays have been applied in the systems. In order to make the system compact, reduce the cost and optimize the number of antennas conveniently, a time-domain UWB imaging system needs to be developed.

References

- [1] I.I. Immoreeve, D.V. Fedotov, “Ultra wideband radar systems: Advantages and disadvantages”, in *Proc. IEEE Ultra Wideband Systems and Technologies Conf.*, Baltimore, MD, Page(s): 201-205, 2002.
- [2] R. Zetik, J. Sachs, R.S. Thoma, “UWB short-range radar sensing”, *IEEE Instrum. Meas. Mag.*, Page(s): 39-45, Apr. 2007.

- [3] D.J. Daniels, "A review of landmine detection using GPR", *European Radar Conference, EURAD 2008*, Page(s): 280-283, 2008.
- [4] D.J. Daniels, "GPR for landmine detection, an invited review paper", *Proceedings of the Tenth International Conference on Ground Penetrating Radar*, Page(s): 7-10, 2004.
- [5] L. Peters, Jr., "Ground penetrating radar (GPR) studies at the Electro Science Laboratory (ESL)", *IEEE Antennas and Propagation Society International Symposium*, Vol. 4, Page(s): 574-577, 2003.
- [6] S. Gezici and H. Poor, "Position estimation via ultra-wide-band signals", *Proceedings of the IEEE*, Vol. 97, No. 2, Page(s): 386-403, Feb. 2009.
- [7] K. Pahlavan, X. Li, and J. Makela, "Indoor geolocation science and technology", *IEEE Communications Magazine*, Vol. 40, No. 2, Page(s): 112-118, Feb. 2002.
- [8] L. E. Larsen and J. H. Jacobi, Eds., *Medical Applications of Microwave Imaging*, Piscataway, NJ: IEEE Press, 1986.
- [9] E.M. Staderini, "UWB radars in medicine", *Aerospace and Electronic Systems Magazine, IEEE*, Vol: 17, Issue: 1, Page(s): 13-18, 2002.
- [10] E. C. Fear, P. M. Meaney, and M. A. Stuchly, "Microwaves for breast cancer detection", *IEEE Potentials*, vol. 22, p. 12, Feb./Mar. 2003.
- [11] I.Y. Immoreev, "Practical Application of Ultra-Wideband Radars", *Ultra wideband and Ultra short Impulse Signals, The Third International Conference*, Page(s): 44-49, 2006.
- [12] I. Immoreev. S. Ivashov, "Remote monitoring of human cardiorespiratory system parameters by radar and its applications", *Ultra wideband and Ultra short Impulse Signals, 4th International Conference on*, Page(s): 34-38, 2008.
- [13] M. Guardiola, L. Jofre, S. Capdevila, J. Romeu, "UWB brain differential imaging capabilities", *2012 6th European Conference on Antennas and Propagations (EuCAP)*, Page(s): 1780-1783, 2012.

- [14] S. Semenov, V. Posukh, A. Bulyshev, T. Williams, "Microwave tomographic imaging of the heart in intact swine", *J. Electromag Waves Applicat.*, vol. 20, no. 7, pp(s): 873-890, 2006.
- [15] Y. Yang, A.E. Fathy, "See-through-wall imaging using ultra wideband short-pulse radar system", *Antennas and Propagation Society International Symposium, 2005 IEEE*, Vol. 3B, Page(s): 334-337, 2005.
- [16] E.J. Baranoski, "Through wall imaging: Historical perspective and future directions", *Acoustics, Speech and Signal Processing, 2008. ICASSP 2008. IEEE International Conference on*, Page(s): 5173-5176, 2008.
- [17] Y. Wang, Y. Yang, A.E. Fathy, "Reconfigurable ultra-wide band see-through-wall imaging radar system", *Antennas and Propagation Society International Symposium, 2009. APSURSI'09. IEEE*, Page(s): 1-4, 2009.
- [18] S. Rahmi, W. Ingolf, "In-Wall Object Recognition based on SAR-like Imaging by UWB-Radar", *Synthetic Aperture Radar (EUSAR), 2010 8th European Conference on*, Page(s): 1-4, 2010.
- [19] X. Zhuge, A.G. Yarovoy, "A Sparse Aperture MIMO-SAR-Based UWB Imaging System for Concealed Weapon Detection", *Geoscience and Remote Sensing, IEEE Transactions on*, Vol: 49, Issue: 1, Part: 2, Page(s): 509-518, 2011.
- [20] B. Sun, Z. Wang, W. Pan, "Method of radar detecting small signal based on adaptive genetic algorithm and neural network", *Chinese Control and Decision Conference, 2009. DDCD'09*, Page(s): 1062-1066, 2009.
- [21] M. Bury, Y. Yashchyshyn, J. Modelski, "Frequency domain measurements for an UWB imaging system", *17th International Conference on Microwaves, Radar and Wireless Communications, 2008. MIKON 2008*, Page(s): 1-4, 2008.
- [22] A.T.S. Ho, W.H. Tham, K.S. Low, "Through-wall radar image reconstruction based on time-domain transient signals in the presence of noise", *Proceeding 2005 IEEE International Geoscience and Remote Sensing Symposium, IGARSS'05*, Vol.6, Page(s): 4271-4274, 2005.

- [23] E.J. Bond, X. Li, S.C. Hagness, B.D. van Veen, "Microwave imaging via space-time beamforming for early detection of breast cancer", *IEEE Trans Antennas and Propagation*, Vol. 51, No. 8, Page(s): 1690-1705, 2003.
- [24] P.M. Meaney, M.W. Fanning, Dun Li, Steven P. Poplack, K.D. Paulsen, "A clinical prototype for active microwave imaging of the breast", *IEEE Transactions on Microwave Theory and Techniques*, Vol: 48, Issue: 11, Part: 1, Page(s): 1841-1853, 2000.
- [25] P.M. Meaney, K.D. Paulse, M.W. Fanning, Steven P. Poplack, Tor D. Tosteson, Dun Li, Navin K.V. Yagnamurthy, "Microwave Breast Imaging with a Non-Contacting, Monopole Antenna Array", *30th European Microwave Conference*, Page(s): 1-4, 2000.
- [26] D. Li, P.M. Meaney, T. Raynolds, S.A. Pendergrass, M.W. Fanning, K.D. Paulsen, "Parallel-detection microwave spectroscopy system for breast imaging", *Review of Scientific Instruments*, Vol: 75, Issue:7, Page(s): 2305-2313, 2004.
- [27] X. Li, S.C. Hagness, "A confocal microwave imaging algorithm for breast cancer detection", *IEEE Microwave Wireless Comp. Lett.*, Vol. 11, Page(s): 130-132, Mar. 2001.
- [28] E.C. Fear, X. Li, S.C. Hagness, M. Stuchly, "Confocal microwave imaging for breast cancer detection: Localization of tumors in three dimensions", *IEEE Trans. Biomed. Eng.*, Vol, 49, Page(s): 812-822, Aug. 2002.
- [29] X. Li, E.J. Bond, SC.C. Hagness, B.D. Van Vee, D. van der Weide, "Three-dimensional microwave imaging via space-time beamforming for breast cancer detection", *IEEE AP-S Int, Symp. And USNC/URSI Radio Science Meeting, San Antonio, TX*, June 2002.
- [30] X. Li, S.K. Davis, S.C. Hagness, D.W. Van Der Weide, B.D. Van Veen, "Mircrowave imaging via space-time beamforming: experimental investigation of tumor detection in multilayer breast phantoms", *IEEE Transactions on*

- Microwave Theory and Techniques*, Vol: 52, Issue: 8, Part: 2, Page(s): 1856-1865, 2004.
- [31] X. Li, E. J. Bond, B. D. Van Veen, S. C. Hagness, “An overview of ultra-wideband microwave imaging via space-time beamforming for early-stage breast-cancer detection”, *IEEE Antennas and Propagating Magazine*, vol. 47, no. 1, pp(s): 19-34, 2005.
- [32] J. Bourqui, M. Okoniewski, E.C. Fear, “Balanced Antipodal Vivaldi Antenna With Dielectric Director for Near-Field Microwave Imaging”, *IEEE Transactions on Antennas and Propagation*, Vol. 58, No. 7, Page(s): 2318-2326, July, 2010.
- [33] T.C. Williams, J. Bourqui, T.R. Cameron, M. Okoniewski, E.C. Fear, “Laser Surface Estimation for Microwave Breast Imaging Systems”, *IEEE Transactions on Biomedical Engineering*, Vol. 58, Issue. 5, Page(s): 1193-1199, 2011.
- [34] B. Maklad *et al.*, “Neighborhood-based algorithm to facilitate the reduction of skin reflections in radar-based microwave imaging”, *PIERB*, Vol: 39, Page(s): 115-139, 2012.
- [35] E.C. Fear, J. Bourqui, C. Curtis, D. Mew, B. Docktor, C. Romano, “Microwave Breast Imaging With a Monostatic Radar-Based System: A Study of Application to Patients”, *IEEE Transactions on Microwave Theory and Techniques*, Vol. 61, No. 5, Page(s): 2119-2128, May 2013.
- [36] W.C. Khor, M.E. Bialkowski, S. Crozier, “Microwave imaging using a planar scanning system with step-frequency synthesized pulse”, *Microwave Conference Proceedings, 2005. APMC 2005. Asia-Pacific Conference Proceedings*, Vol. 1, 2005.
- [37] W.C. Khor, A. Abbosh, N. Seman, S. Crozier, “ An Ultra Wideband Microwave Imaging System for Breast Cancer Detection”, *IEICE Trans. Commun.*, Vol. E90-B, No. 9, Page(s): 2376-2381, 2007.

- [38] W.C. Khor, M.E. Bialkowski, "Investigations into an UWB Microwave Radar System for Breast Cancer Detection", *IEEE Antennas and Propagation Society International Symposium*, Page(s): 2160-2163, 2007.
- [39] B. Cheeseman, Y. Huang, "A study of Detecting Breast Cancer Using Microwave Imaging", *Microwave and Millimeter Wave Technology, 2004. ICMMT 4th International Conference on, Proceedings*, Page(s): 978-982, 2004.
- [40] B. Cheeseman, Y. Huang, "Limited Multi-Static Calibration Technique without a Phantom for the Detection of Breast Cancer", *3rd European Radar Conference, EuRAD 2006*, Page(s): 225-228, 2006.
- [41] B. Cheeseman, Y. Huang, "Comparison of Shape Imaging between Pulse Integration, Correlation and Adaptive Filter". *The Second European Conference on Antennas and Propagation, EuCAP 2007*, Page(s): 1-6, 2007.
- [42] Y. Chen, P. Kosmas, "Detection and Localization of Tissue Malignancy Using Contrast-Enhanced Microwave Imaging: Exploring Information Theoretic Criteria", *IEEE Transactions on Biomedical Engineering*, Vol. 59, No. 3, Page(s): 766—76, Mar. 2012.
- [43] Y. Chen, P. Kosmas, "Microwave Breast Tumor Detection and Size Estimation Using Contrast-Agent-Loaded Magnetotactic Bacteria", *35th Annual International Conference of the IEEE Engineering in Medicine and Biology Society (EMBS)*, Page(s): 5481-5484, 2013.
- [44] I.J. Craddock, M. Klemm, J. Leendertz, A.W. Preece, R. Benjamim, "An Improved Hemispherical Antenna Array Design for Breast Imaging", *The second European Conference on Antennas and Propagation, 2007, EuCAP 2007*, Page(s): 1-5, 2007.
- [45] D. Gibbins, M. Klemm, I.J. Craddock, J.A. Leendertz, A. Preece, R. Benjamim, "A comparison of a wide-slot and a stacked patch antenna for the purpose of breast cancer detection", *IEEE Transactions on Antennas and Propagation*, Vol: 58, Issue: 3, Page(s): 665-674, 2010.

- [46] T. Henriksson, M. Klemm, D. Gibbins, J. Leenderts, T. Horseman, A.W. Preece, R. Benjamin, I.J. Craddock, "Clinical trials of a multistatic UWB radar for breast imaging", *Antennas and Propagation Conference (LAPC), 2011 Loughborough*, Page(s):1-4, 2011.
- [47] J.C. Francke, R. Yelf, "Applications of GPR for surface mining", *Proceedings of the 2nd International Workshop on Advanced Ground Penetrating Radar*, Page(s): 115-119, 2003.
- [48] H.M. Jol, A. Albrecht, "Searching for submerged lumber with ground penetrating radar: Rib Lake, Wisconsin, USA", *Proceedings of the Tenth International Conference on Ground Penetrating Radar*, Page(s): 601-604, 2004.
- [49] R. Yelf, W. Al-Nuaimy, "Classification system for GPR parameters", *Proceedings of the Tenth International Conference on Ground Penetrating Radar*, Page(s): 407-410, 2004.
- [50] M. Soliman, Z. Wu, "Design, Simulation and Implementation of UWB Antenna Array and It's Application in GPR System", *The Second European Conference on Antennas and Propagation, 2007. EuCAP 2007*, Page(s): 1-5, 2007.
- [51] T.P. Montoya, G.S. Smith, "Land mine detection using a ground-penetrating radar based on resistively loaded Vee dipoles", *IEEE Transactions on Antennas and Propagation*, Vol: 47, Issue: 12, Page(s): 1795-1806, 1996.
- [52] W.R. Scott, Kangwook Kim, G.D. Larson, A.C. Gurbuz, J.H. McClellan, "Combined seismic, radar, and induction sensor for landmine detection", *2004 IEEE International Geoscience and Remote Sensing Symposium, 2004. IGARSS'04. Proceedings*, Vol: 3, Page(s): 1613-1616, 2004.
- [53] K. Kim, W.R. Scott, "Design of a Resistively Loaded Vee Dipole for Ultrawide-Band Ground-Penetrating Radar Applications", *IEEE Transactions on Antennas and Propagation*, Vol: 53, Issue: 8, Part: 1, Page(s): 2525-2532, 2005.

- [54] M. Sato, K. Takahashi, J. Fujiwara, "Hand held sensor ALIS and its evaluation test in Cambodia", *IEEE International Conference on Geoscience and Remote Sensing Symposium, 2007. IGARSS 2007*, Page(s): 18-21, 2007.
- [55] M. Sato, "Dual Sensor ALIS for Humanitarian Demining and its Evaluation Test in Mine Fields in Croatia", *IEEE International Conference on Geoscience and Remote Sensing Symposium, 2008. IGARSS 2008*, Vol: 2, Page(s): II-181-II-184, 2008.
- [56] M. Sato, K. Takahashi, J. Fujiwara, "Development of the Hand held dual sensor ALIS and its evaluation", *2007 4th International Workshop on Advanced Ground Penetrating Radar*, Page(s): 3-7, 2007.
- [57] X. Feng, M. Sato, Y. Zhang, C. Liu, F. Shi, Y. Zhao, "CMP Antenna Array GPR and Signal-to-Clutter Ratio Improvement", *IEEE Geoscience and Remote Sensing Letters*, Vol: 6. No: 1, Page(s): 23-27, Jan. 2009.
- [58] H. Liu, M. Sato, "Design of a GPR antenna array for asphalt pavement inspection", *2013 Asia-Pacific Conference on Synthetic Aperture Radar (APSAR)*, Page(s): 133-136, 2013.
- [59] A. Yarovoy, P. Aubry, P. Lys, L. Ligthart, "UWB Array-Based Radar for Landmine Detection", *3rd European Radar Conference, 2006. EuRAD 2006*, Page(s): 186-189, 2006.
- [60] A.G. Yarovoy, T.G. Savelyev, P.J. Aubry, L.P. Ligthart, "Array-Based GPR for Shallow Subsurface Imaging", *2007 4th International Workshop on Advanced Ground Penetrating Radar*, Page(s): 12-15, 2007.
- [61] A. Yarovoy, T. Savelyev, Xiaodong Zhuge, P. Aubry, L. Ligthart, J. Schavemaker, P. Tettelaar, E. den Breejen, "Performance of UWB array-based radar sensor in a multi-sensor vehicle-based suit for landmine detection", *European Radar Conference, 2008. EuRAD 2008*. Page(s): 288-291, 2008.

- [62] A.A. Lestari, A.G. Yarovoy, L.P. Ligthart, E.T. Rahardjo, "A UWB Antenna for Impulse Radio", *IEEE 63rd Vehicular Technology Conference 2006. VTC 2006-Spring*. Vol: 6, Page(s): 2630-2634, 2006.
- [63] D. Caratelli, A. Yarovoy, L.P. Ligthart, "Full-wave analysis of cavity-backed resistively loaded bow-tie antennas for GPR applications", *European Radar Conference, 2008. RuRAD 2008*. Page(s): 204:207, 2008.
- [64] A.A. Lestari, E. Bharata, A.B. Suksmono, A. Kurniawan, A.G. Yarovoy, L.P. Ligthart, "A modified Bow-Tie Antenna for Improved Pulse Radiation", *IEEE Transactions on Antennas and Propagation*, Vol: 58, Issue: 7, Page(s): 2184-2192, 2010.
- [65] A.A. Lestari, A. G. Yarovoy, L.P. Ligthart, "Numerical and experimental analysis of circular-end wire bow-tie antennas over a lossy ground", *IEEE Transaction on Antennas and Propagation*, Vol: 52, Page(s): 26-35, Jan. 2004.
- [66] H.R. Lenler, P. Meincke, A. Sarri, V. Chatelee, B. Nair, I.J. Craddock, G. Alli, J.Y. Dauvignac, Y. Huang, D. Lymperopoulos, R. Nilavalan, "Joint ACE ground penetrating radar antenna test facility at the Technical University of Denmark", *2005 IEEE Antennas and Propagation Society International Symposium*, Vol: 4A, Page(s): 109-112, 2005.
- [67] P. Cao, Y. Huang, J. Zhang, "A UWB monopole antenna for GPR application", *2012 6th European Conference on Antennas and Propagation (EuCAP)*, Page(s): 2837-2840, 2012.
- [68] F. Ahmad, Y. Zhang, M.G. Amin, "Three-dimensional wideband beamforming for imaging through a single wall", *IEEE Geoscience Remote Sens. Letter*, Vol: 5, No: 2, Page(s): 176-179, Apr. 2008.
- [69] M. Dehmollaian, K. Sarabandi, "Refocusing through building walls using synthetic aperture radar", *IEEE Transactions on Geoscience Remote Sensing*, Vol: 46, No: 6, Page(s): 1589-1599, Jun. 2008.

- [70] S. Kidera, T. Sakamoto, T. Sato, "High-resolution 3-D imaging algorithm without derivative operations for UWB through-the-wall radars", *2008 IEEE Antennas and Propagation Society International Symposium (APSURSI)*, Page(s): 1-4, San Diego, CA, Jul. 2008.
- [71] K.M. Yemelyanov, N. Engheta, A. Hoorfar, J.A. McVay, "Adaptive polarization contrast techniques for through-wall microwave imaging applications", *IEEE Transactions on Geoscience Remote Sensing*, Vol: 47, No: 5, Page(s): 1362-1374, May 2009.
- [72] L. Nguyen, "Signal and Image Processing Algorithms for the U.S. Army Research Laboratory Ultra-wideband (UWB) Synchronous Impulse Reconstruction (SIRE) Radar", *ARL-TR-4784*, April 2009.
- [73] A. Martone, R. Innocenti, K. Ranney, "Moving Target Indication for Transparent Urban Structures", *ARL-TR-4809*, May 2009.
- [74] Y. Yang, A.E. Fathy, "Development and Implementation of a Real-Time See-Through-Wall Radar System Based on FPGA", *IEEE Transactions on Geoscience and Remote Sensing*, Vol: 47, Issue: 5, Page(s): 1270-1280, 2009.
- [75] Y. Wang, A.E. Fathy, "Three-dimensional through wall imaging using an UWB SAR", *2010 IEEE Antennas and Propagation Society International Symposium (APSURSI)*, Page(s): 1-4, Jul. 2010.
- [76] Y. Wang, A.E. Fathy, "Advanced System Level Simulation Platform for Three-Dimensional UWB Through-Wall Imaging SAR Using Time-Domain Approach", *IEEE Transactions on Geoscience and Remote Sensing*, Vol: 50, No: 5, Page(s): 1986-2000, May 2012.
- [77] R. Salman, I. Willms, L. Reichardt, T. Zwick, W. Wiesbeck, "On Polarization diversity gain in short range UWB-Radar object imaging", *2012 IEEE International Conference on Ultra-Wideband (ICUWB)*, Page(s): 402-406, 2012.
- [78] R. Salman, I. Willms, T. Sakamoto, T. Sato, A. Yarovoy, "3D Imaging of a Manmade Target with Weak Scattering Centres by Means of UWB-Radar", *2013*

IEEE International Conference on Ultra-Wideband (ICUWB), Page(s): 109-112, 2013.

- [79] B. J. Harker, A. D. Chadwick, G.L. Harris, “Ultra-wideband 3-Dimensional imaging (UWB 3D Imaging)”, *Roke Manor Research Limited, UK*. <http://www.roke.co.uk/resources/papers/UWB-3D-Imaging.pdf>, 2008.

Chapter 3 The Antenna for the Imaging System

The antenna plays a very important role in both UWB communication and imaging systems. Unlike UWB communication systems, the antenna used in UWB imaging applications should have a directional radiation pattern with high directivity and be able to transmit UWB short pulses with minimal distortion [1-2]. The antenna must be compact in size and light in weight as well, considering its portability and practicality.

Usually, single UWB antenna is not suitable for UWB imaging application, because the aperture of one receiving antenna is too limited to achieve a good cross-range resolution. Therefore, an array-based sub-system is developed. The antenna array can be composed of individual antennas or antenna sub-arrays, depending on the required radiation power for different applications. For medical imaging purpose, individual antennas in the array can work as a bi-static or multi-static system. For see-through wall imaging application, antenna sub-arrays should be used for higher radiation power and larger array aperture. The antenna sub-arrays can increase the gain and directivity compared with the single antenna, which is useful for long-range detection application. In conclusion, when designing the UWB imaging system for a particular application, a trade-off needs to be determined among the physical structure of the antenna array, the number of antennas used in the array and the achievable resolution in the system.

At first, this chapter will give an overview of typical antennas used in the UWB imaging system. Then, the tapered slot antenna will be reviewed specifically, as well as its feeding technique. On top of it, a circular-edge antipodal Vivaldi antenna will be proposed and lastly a corrugated balanced antipodal Vivaldi antenna will be presented to show an improvement in its directivity and gain. The frequency-domain analysis will be provided for these two antipodal Vivaldi antennas, including the

simulated and measured results of reflections, current flow changes, gain estimations and radiation patterns.

3.1 Overview of the antennas in UWB imaging systems

Until now, many UWB antennas used in UWB imaging systems have been developed. Among them, four types of antennas are utilised in the typical UWB imaging systems, which are horn antenna, stacked-patch antenna, bow-tie antenna and tapered slot antenna (TSA).

A ridged pyramidal horn antenna has been designed for mono-static UWB breast cancer imaging system at University of Wisconsin. Its VSWR is less than 1.5 across the frequency range from 1 GHz to 11 GHz. The fidelity of the radiated signal ranges between 0.92 and 0.96 over an angular span of 180° centred on bore-sight [3]. A dielectric wedge horn has been designed at Delft University of Technology for GPR system. This horn antenna uses a dielectric wedge to decrease the coupling and the sensitivity to external, reducing the late-time ringing effect by choosing the dielectric permittivity of the wedge as close as possible to the dielectric permittivity of a typical ground. This kind of horn antenna is possible for GRP application, but the size is not small. The height of the wedge in horn antenna is about 25.25 cm with the antenna's aperture of $16\text{ cm} \times 16\text{ cm}$ [4]. A dielectrically scaled double-ridged horn antenna has been developed at Ilmenau University of Technology in Germany for breast cancer imaging [5-6]. This dielectric scaling horn antenna leads to a significant size reduction of the radiating elements at the cost of being immersed into the phantom material. Although the horn antenna has high gain and directivity, it is not easy to form a compact antenna array.

Stacked-patch and wide slot antennas have been designed at University of Bristol. They are mounted on a hemispherical surface and formed as a multi-static UWB breast cancer imaging system. This antenna is compact and radiates effectively into a high permittivity ($\epsilon_r \approx 9$) dielectric medium over the desired frequency bandwidth 1.5 to 7 GHz [7-8].

A modified wire bow-tie antenna has been developed in Delft University of Technology for GPR application. It has 25 cm wires on each arm and 10^0 angular separations between the neighbouring wires. It has been indicated that such a wire structure is a good approximation for a solid bow-tie antenna with respect to its radiation characteristics and moreover allows simple implementation of resistive loading using lumped resistors when the antenna is realized as a printed antenna on a dielectric substrate [9]. It has omni-directional radiation patterns, which are suitable for GPR application, but less in advantage of medical imaging or see-through imaging applications.

An eight-element tapered slot sub-array has been designed for UWB through-wall imaging system which operates from 2 GHz to 4 GHz at University of Tennessee. The overall size of the sub-array, including the impedance matching feeding structure, is about 48 cm \times 21 cm. Meanwhile a sixteen-element antipodal Vivaldi sub-array has been designed for 8-12 GHz UWB imaging system. The overall size of the sub-array is about 17.8 cm \times 40.6 cm including the feeding structure. Both of them used for through-wall imaging application have more than 12 dBi gain over the respective operating band [10]. A tapered slot antenna with flare width and length of 20 mm and 34 mm respectively has been designed to operate over the 20 GHz to 40 GHz region for through-slab imaging system at Michigan State University [11], which has achieved between 10 dBi and 12 dBi bore sight gain over the operating frequency. Balanced antipodal Vivaldi antenna has been implemented at University of Calgary for the breast cancer imaging system. This antenna balances the E-field distribution in the flared slot and provides a lower reflection from the feeding structure. As the feeding structure is followed by a gradual transition from a stripline to a tri-strip transmission line, the conductor width increases linearly while the ground width decreases exponentially to keep constant impedance [12]. A triplate-structured TSA element with the Marchand balun is developed at Queen Mary, University of London [13]. It performs good ARC (Active Reflection Coefficient) and better scanning directivity when forming an infinite planar array.

In all, from the current utilizations in the present UWB imaging systems, these antennas are all have high directivity and gain to the advantage. Considering the

physical size to form an array, rigid horn antenna unfavourably has a solid structure, relatively high cost and a heavy weight. Moreover, due to its large physical aperture it suffers multiple reflections between the aperture of the antenna and the detecting target. The radiated impulse towards the target may bounce back to the antenna and re-radiated. Although the dielectric loaded horn antenna can improve this problem, the radiation efficiency is lowered. So it is not a good candidate.

Stacked-patch antenna is a planar structure which is more desirable than horn, however its worse directivity and gain compared with tapered slot antenna limit its ability in many UWB systems.

Bow-tie antennas exhibit wide bandwidth and simple structure. It has been modified over the years by adding resistive or resistive-capacitive loading for proper radiation as the single transmit antenna for GPR applications. However the omni-directional radiation characteristic reduces its possibility to be used in this bag imaging application.

The tapered slot antenna can provide ultra wide frequency band and maintain high radiation directivity. It is simple in structure, low in fabrication cost and easy to form an array. Therefore, the tapered slot antenna is considered to be the optimal choice for the proposed UWB imaging system in the thesis.

3.2 Tapered Slot Antenna

3.2.1 Principle of operation

The Tapered Slot Antenna (TSA) is widely used as the radiation element for broadband arrays. This antenna was first proposed by Gibson in the late 1970's in [14]. It is a class of end fire, travelling wave antenna. An electromagnetic (EM) wave propagates through the surface of the antenna substrate with a phase velocity less than the speed of light. Elements with phase velocity greater than the speed of light are referred to as leaky wave antennas, which do not typically exhibit end fire radiation. The EM wave moves along the increasingly separated metallization tapers until the separation and radiates into free space from the end of the substrate. The E-

plane of the antenna is the plane containing the electric field vectors of the radiated EM waves [15]. The H-plane, containing the magnetic component of the radiated EM wave, runs perpendicular to the substrate, orthogonally to the electric field.

TSA has several types of taper profiles, as shown in Figure 3-1. The most common types are linear tapered (LTSA), constant width (CWSA) and Vivaldi. Experiments conducted by Lee and Simons have shown that the curvature of the tapered profile has a significant impact on the gain, beam width and bandwidth of tapered slot antennas. The half-power beam width (HPBW) on the E-plane increases with a decrease in the radius of curvature while it is opposite on the H-plane [16].

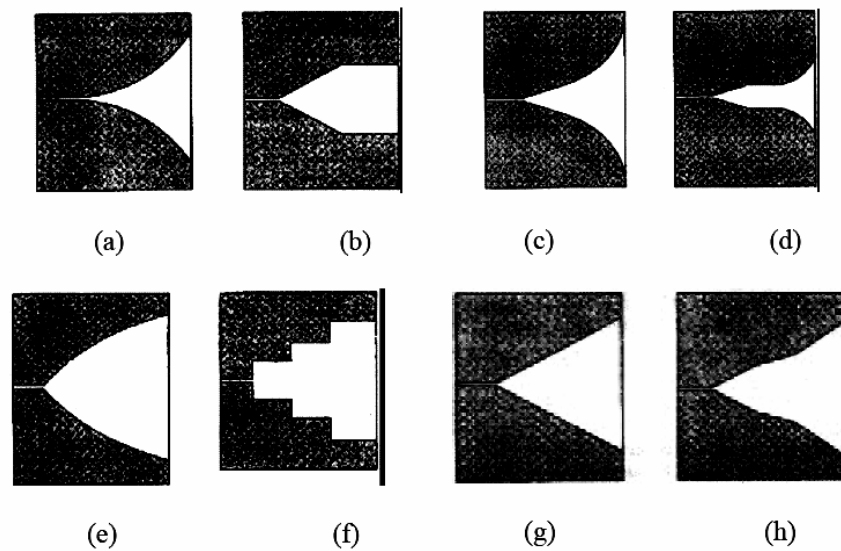


Figure 3-1 Types of TSA: (a) Vivaldi, (b) Linear-Constant, (c) Tangent, (d) Vivaldi-Constant, (e) Parabolic, (f) Stepped-Constant, (g) Linear, (h) Broken-Linear [17].

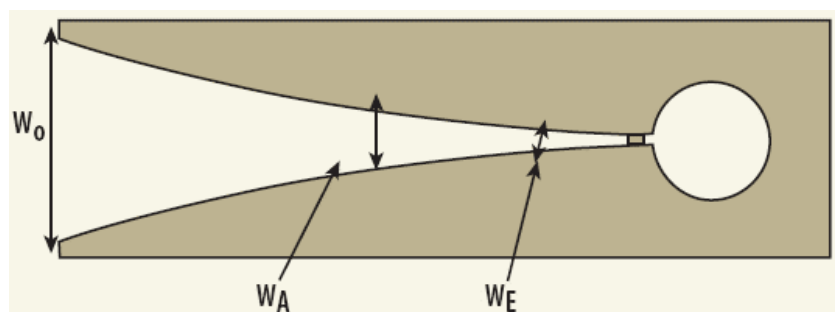


Figure 3-2 Geometry of the tapered slot antenna.

Among all these types of TSA, Vivaldi antenna is a typical ultra-wide band antenna constructed on a PCB (Printed Circuit Board), which has been developed for many years. It is a tapered slot antenna characterised by an exponential flare shape, producing directive radiation pattern with 8-10 dBi gain and side lobe levels of -10 dBi to -15 dBi. The Vivaldi antenna is easy to fabricate, having no highly sensitive dimensional tolerances. The dielectric substrate of the printed antenna slows the travelling wave in the slot, producing enhanced end-fire gain for a band of frequencies.

A conventional Vivaldi antenna is shown in Figure 3-2. W_E , W_A and W_o are the width of the input slot, radiating area slot and output slot respectively. It has two areas for propagation and radiation. The propagation area is the one between W_E and W_A , while the radiation area is defined between W_A and W_o . The EM waves travel down the curved path of the flare along the antenna. In the region where the separation between the conductors is small compared to the free-space wavelength, the waves are tightly bound. As the separation increases, the bond becomes progressively weaker and the waves are radiated away from the antenna. This occurs when the edge separation is greater than one-half wavelength. To achieve a wider bandwidth, it is imperative to consider two aspects, 1) the transition from the main input transmission line to the slot line for feeding the antenna; 2) the dimensions and shape of the tapered slot.

3.2.2 Feeding technique

A proper feeding structure is essential to maximize the impedance match bandwidth, which determines the low and high frequency limits [18].

Most microwave integrated circuits (MICs) are realized in microstrip transmission medium. The best feed suited for the TSA is a slotline. In order to couple microwave signals to the antenna from a planar microstrip circuit, a transition is needed. These transitions should be very compact and have low loss. The commonly used methods are the coaxial line feed and microstrip line feed.

The coaxial line feed provides a direct path for coupling of fields across the slot [19]. The transition consists of a coaxial line placed perpendicular at the end of an open circuited slot. The output conductor of the cable is electrically connected to the ground plane on one side of the slot while the inner conductor of the coaxial line forms a semicircular shape over the slot. However, designing slotlines with very stable characteristic impedances is difficult because the width is too narrow, which leads to inaccurate errors in fabrication.

The microstrip is an unbalanced transmission line while the slotline feeding the tapered slot antenna should be a balanced medium. So, it is necessary to design a balun that would work over a wide frequency range or ideally be frequency independent.

A microstrip to slot transition consists of a slot, etched on one side of the substrate, crossing an open circuited microstrip line, located on the opposite side, at a right angle. The major drawback for this kind of a transition is that it could reduce operating bandwidth. A number of ways have been suggested in the literature to improve this microstrip slotline transition. They will be described in detail below.

(1) Microstrip-slotline

Schuppert has proposed the use of circular quarter-wave stubs in the design of microstrip-slotline transitions to obtain a more wideband transition than from the transitions with straight stubs [20]. Sloan et al has used radial stubs instead of the circular ones [21]. The stripline is used as a connection to the transmitter circuitry, while the slotline is flared outwards from the feed. In [22], a triplate-structured TSA element for array with the Marchand balun has been designed, the geometry of which is shown in Figure 3-3. This kind of antenna has three layers, the top and the bottom of which are identical exponential tapered slotlines acting as ground planes, the middle of which is the stripline plane used as the connection to the signal input. The input signal is fed to the stripline input and is then coupled to the slotline on either side of the substrate. Such a double-sided structure is symmetrical in terms of dielectric loading and field distribution, so that it will be less dispersive.

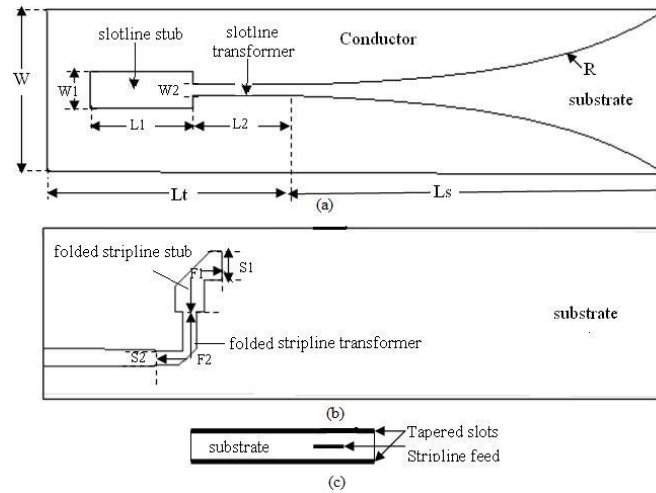


Figure 3-3 Structure of the stripline-fed Vivaldi element (a) top view, (b) middle layer-stripline feed structure, (c) side view [22].

(2) Antipodal slotline

The antipodal antenna, as shown in Figure 3-4, has two flared radiation shape printed on both sides of the dielectric substrate and fed by using a tapered microstrip to symmetric double-sided stripline transition. The smooth transition removes the bandwidth limitation of the original TSA design. However, because of the dielectric spacing between the flares of the antenna, antipodal tapered slot antenna has a relatively high level of cross polarisation.

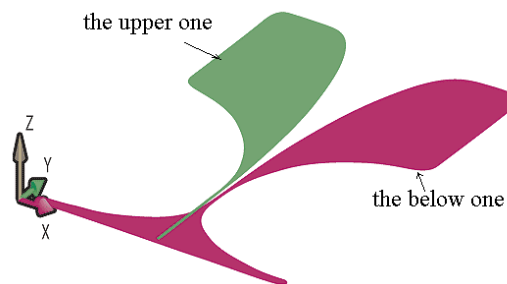


Figure 3-4 The antipodal Vivaldi antenna.

(3) Balanced antipodal slotline

In order to improve the cross polarization of the antipodal slotline, an optimized one named as balanced antipodal Vivaldi antenna is developed. It converts the usual antipodal Vivaldi into a triplate-based structure, adding an additional dielectric and

metallization layer that balances the E-field distribution in the flared slot. The antenna starts in a stripline. One side of the board has the input track that is then flared to produce one half of a conventional Vivaldi antenna. On the other side, the ground planes are reduced to a balanced set of lines that are flared-out in the opposite direction to form the overall balanced structure. This kind of antenna as shown in Figure 3-5 has been developed at University of Calgary for their breast cancer imaging system.

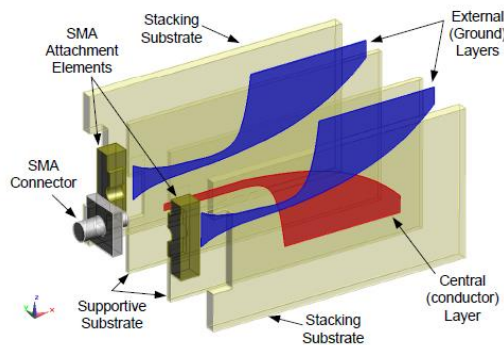


Figure 3-5 Balanced antipodal Vivaldi antenna [23].

All in all, TSA has advantages of light weight, narrower beam width and high gain, which makes it a good candidate for imaging applications. In the following sections, two antennas based on antipodal Vivaldi antenna and balanced antipodal Vivaldi antenna have been developed for our imaging system.

3.3 The circular-edge antipodal Vivaldi antenna

3.3.1 Structure of the antenna

As mentioned in Chapter 1, the antenna for this UWB imaging system should have high gain over the main operating frequency band. It should be in compact and simple structure, which is easy to form an array. Then the antipodal Vivaldi antenna is proposed firstly.

The traditional antipodal antenna, as shown in Figure 3-6 (a), uses two exponentially tapered lines to form as inner and outer edges of the radiation part. The radiation flare and the mirrored one are placed on both sides of the substrate. It is a slow leaky end-fire travelling wave antenna. The electromagnetic wave travels down the

gradually curved path of the flares. As the separation between the flares increases, the EM wave radiates into free space.

Here, a kind of modified antipodal Vivaldi antenna is proposed for our UWB imaging system, as shown in Figure 3-6 (b). It mainly consists of radiation flares and microstrip lines. The microstrip line on the front side of the substrate is a parallel stripline, while the one on the back side is a dual circular stripline. They are on different sides of the substrate and gradually flare out in opposite directions to form the tapered slot. The radiation flare is composed of three curves, which are the inner and outer edges defined by exponential lines, and a circular line connected to them. The exponential line is defined in the following equation (3-1). The circular line connects the two exponential lines. It can provide a smooth path to the surface current and reduce the reflection from the straight edges of the substrate.

$$y = c_1 e^{qx} + c_2 \quad (3-1)$$

Where c_1 and c_2 are determined by the coordinates of the first and last points of the exponential line. q is the opening rate [24].

The antipodal Vivaldi antenna operates as a resonant antenna at the lower end of frequency band. The slot aperture W_0 is determined based on the lowest frequency f_{min} and effective dielectric constant ε , following the equation (3-2).

$$W_0 = \frac{c}{2f_{min}\sqrt{\varepsilon}} \quad (3-2)$$

The impedance match is influenced by the width of the microstrip line Wl . The performance at the lower end of the operating frequency band is determined by the width of the antenna, the size of the ground plane, the flare rate q and the radius R of the circular line. The relative size parameters of the antenna are listed in Table 3-1. They are optimized in the commercial simulation software CST Microwave Studio. The substrate is FR4 with the permittivity of 3. The antenna uses a SMA connector at the bottom side of the substrate. The front and back views of the fabricated antenna are shown in Figure 3-7 (a) and (b). The slot aperture W_0 of the antenna is 30 mm,

equivalent to 0.35λ . λ is the wavelength of 2 GHz. The size of the substrate is $60 \text{ mm} \times 70 \text{ mm}$.

Table 3-1 The dimensions of the circular-edge antenna

Parameter	Length of the substrate, L	Width of the substrate, W	Thickness of the substrate, h	Radius of the circular edge, R	Length of the microstrip line, L1	Width of the microstrip line, W1
Value (mm)	70	60	1.6	16	26	4

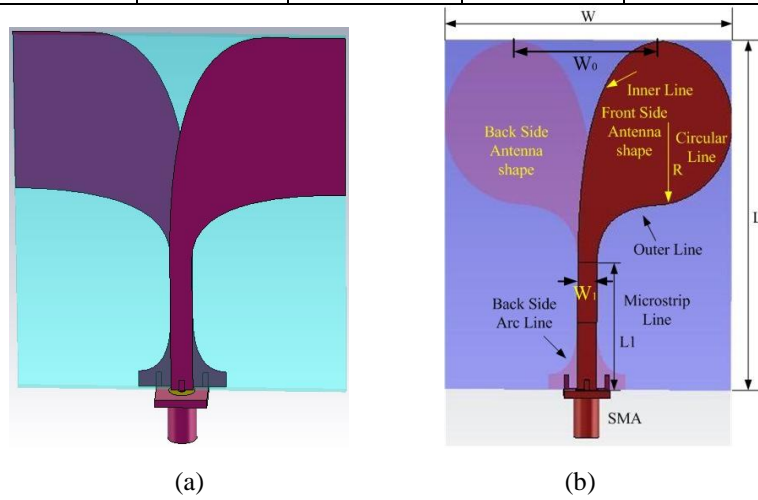


Figure 3-6 The structure of the antipodal Vivaldi antenna; (a) the traditional one; (b) the circular-edge one.

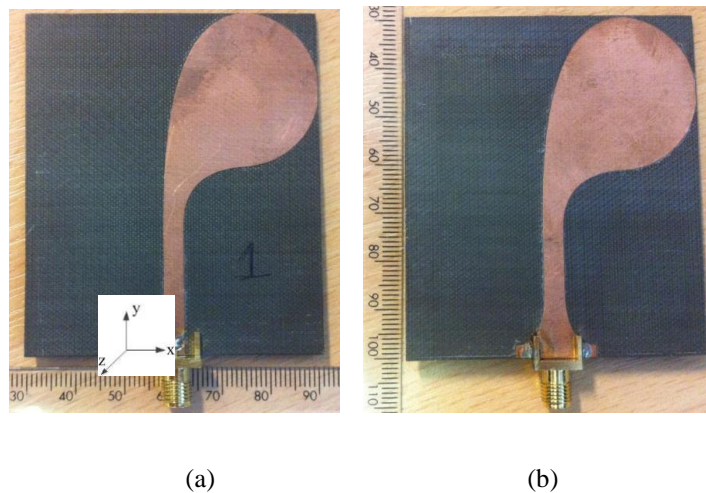


Figure 3-7 The fabricated antipodal antenna; (a) the front view; (b) the back view.

3.3.2 Simulated and measured results

The antenna is simulated in CST microwave studio. The simulated and measured results of S_{11} are shown in Figure 3-8. The -10 dB frequency bandwidth of the circular-edge antipodal Vivaldi antenna is from 2 GHz up to 12 GHz. Such an ultra-wide band is capable enough for the UWB imaging system.

The modified circular-edge antipodal Vivaldi antenna has the same size of the substrate and the same exponential inner and outer edges of the radiation flare as the traditional antipodal antenna, but it has better S_{11} performance especially in lower frequency. The simulated S_{11} for both antennas are plotted in Figure 3-9. The blue dash curve and the red solid curve refer to S_{11} parameters of the traditional antipodal Vivaldi antenna and the circular-edge antipodal Vivaldi antenna, respectively. It can be observed that the circular-edge antipodal Vivaldi antenna operates at lower end of the frequency band than the traditional one.

The reason is that the circular-edge extends the equivalent width of the radiation flare W_o as marked in Figure 3-6 (b). The parameter W_o is proportional to the wavelength of lower operating frequency. Thus when the equivalent width W_o is increasing, the operating frequency is shifting to lower frequency. By increasing the radius R of the circular edge, the extension of the equivalent width W_o is increasing correspondingly. The operating frequency is shifting to lower frequency, which can be obtained from Figure 3-10.

It is also evident from the current distribution on the surface of the antenna shown in Figure 3-11. The current distribution on the circular-edge antipodal Vivaldi antenna covers more area at the edge of the inner radiation flare than the traditional one in 2.2 GHz. This makes the antenna work properly in the lower frequency.

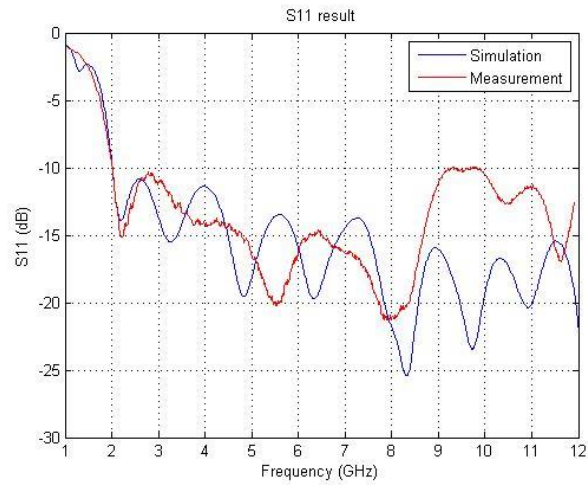


Figure 3-8 S_{11} performance of the simulated and measured results for the circular-edge antipodal Vivaldi antenna.

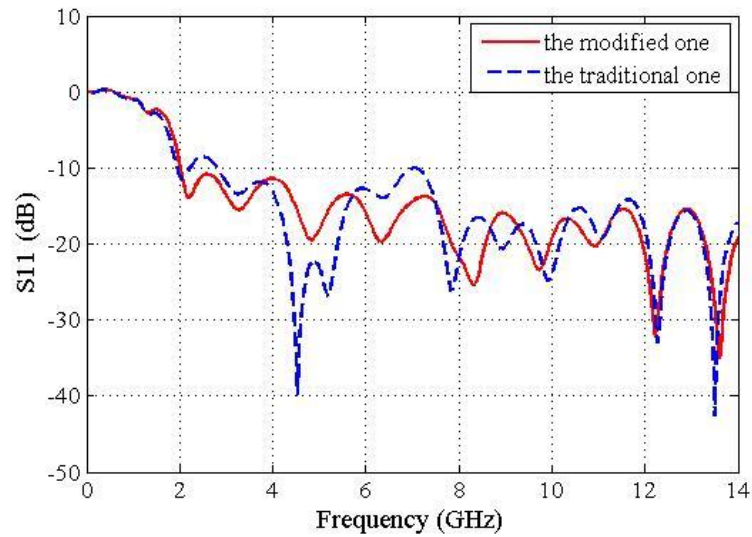


Figure 3-9 The comparison of S_{11} simulated results between the traditional one and the proposed modified one.

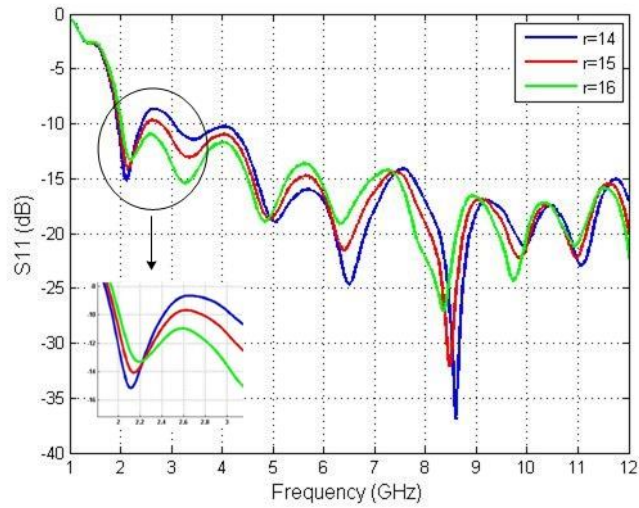


Figure 3-10 The simulated S_{11} when varying the radius of circular edge.

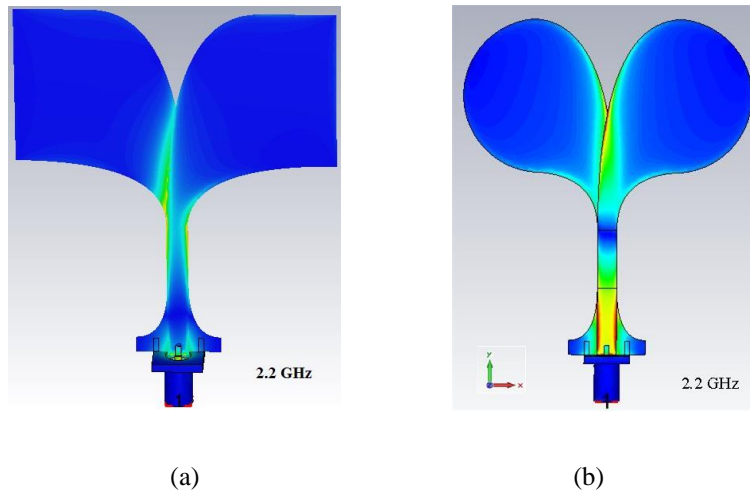


Figure 3-11 The current distribution on the surface of the antenna; (a) the traditional antipodal Vivaldi antenna; (b) the circular-edge antipodal Vivaldi antenna.

The simulated result of the gain is shown in Figure 3-12, which is from 2.04 dBi to 6.25 dBi across the frequency bandwidth of 2-10 GHz. But the gain is not high over the lower frequency band (3-6 GHz). It is the main working frequency band of the system, which will be described in Chapter 5.

The simulated results of radiation patterns at different frequencies are shown in Figure 3-13. The simulated and measured radiation patterns for E-plane and H-plane are respectively shown in Figure 3-14 and Figure 3-15. The 3 dB beam width for the

single antipodal antenna at 4 GHz, 5 GHz, 6 GHz and 7 GHz is respectively 60.7° , 67.8° , 87.7° and 89.1° in E-plane.

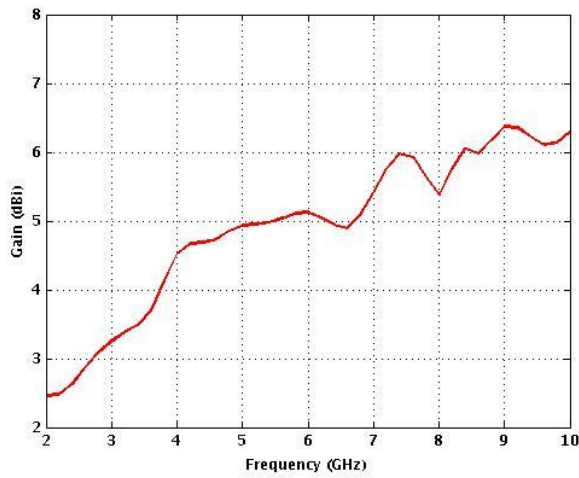


Figure 3-12 The simulated result of gain.

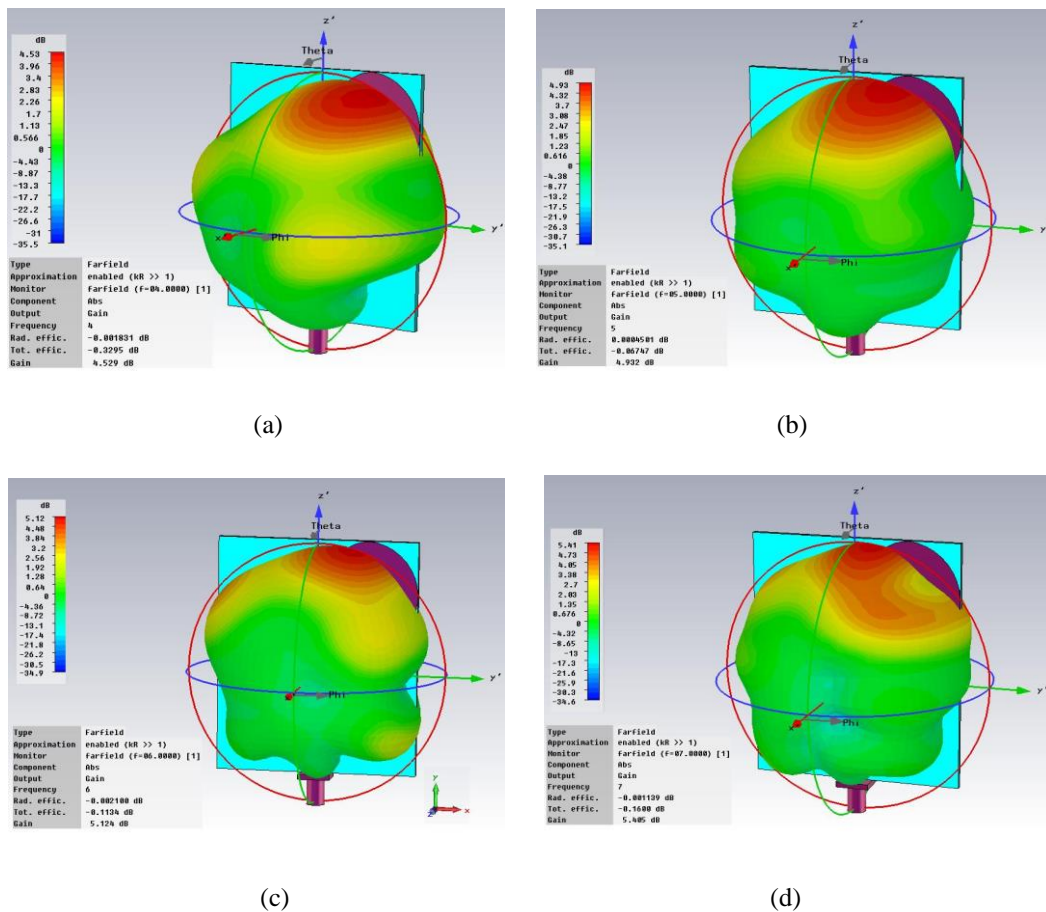


Figure 3-13 3D simulated radiation patterns at different frequencies; (a) 4 GHz; (b) 5 GHz; (c) 6 GHz; (d) 7 GHz.

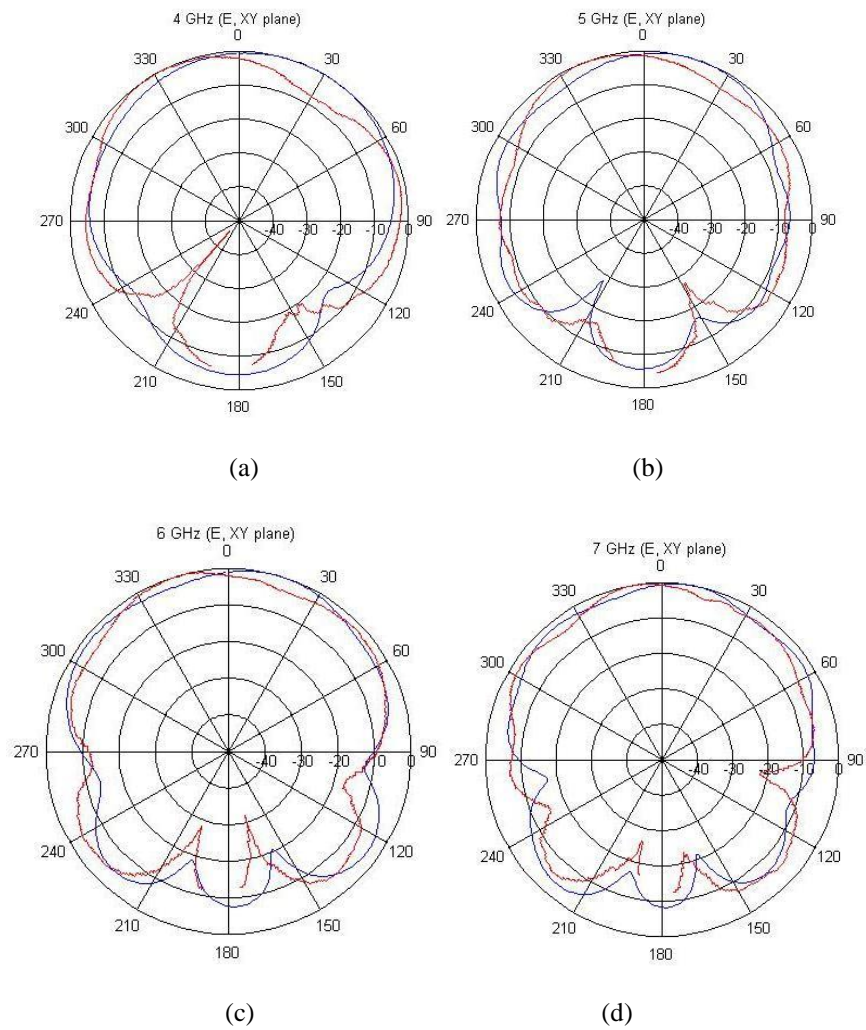
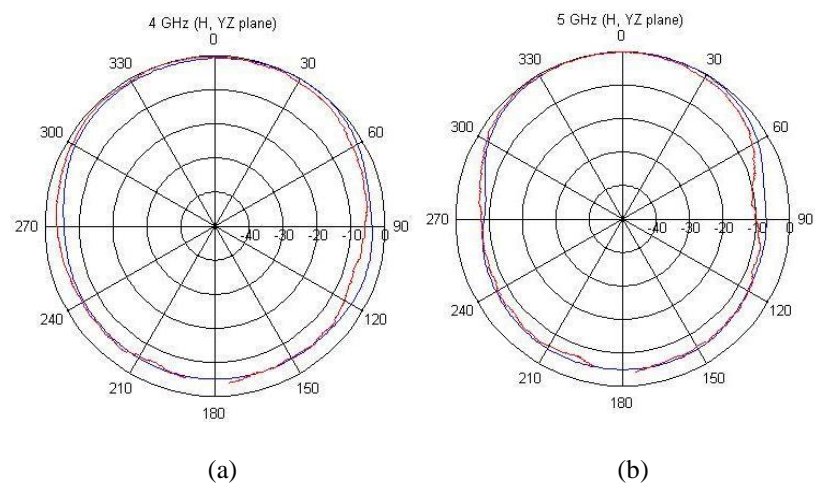


Figure 3-14 E-plane of simulated (blue) and measured (red) results at different frequencies; (a) 4 GHz, (b) 5 GHz, (c) 6 GHz, (d) 7 GHz.



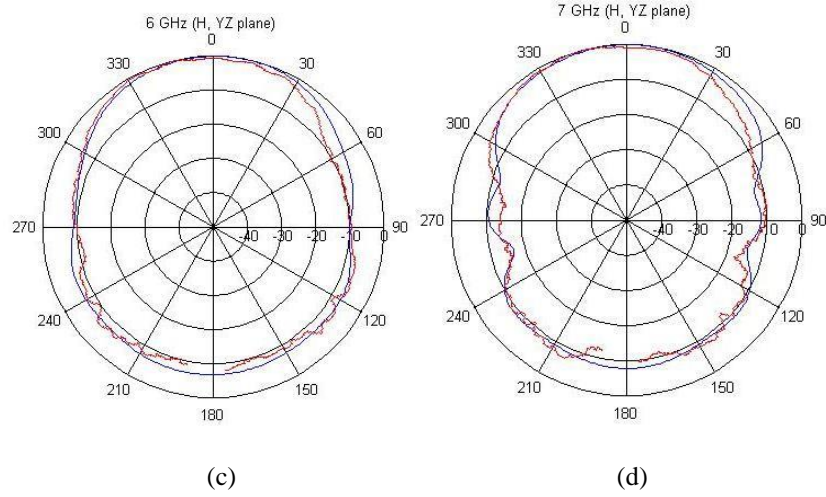


Figure 3-15 H-plane of simulated (blue) and measured (red) results at different frequencies; (a) 4 GHz, (b) 5 GHz, (c) 6 GHz, (d) 7 GHz.

For the linear array with N identical elements, each of which has the same radiation pattern $\bar{f}(\theta, \varphi)$, the overall radiation pattern of the array can be calculated as

$$\bar{F}(\theta, \varphi) = \frac{e^{-jkr}}{r} \bar{f}(\theta, \varphi) AF \quad (3-3)$$

Where r is the distance of elements from the observation point. AF is the array factor. For the normalized array factor, it is given as

$$AF_n = \frac{1}{N} \left[\frac{\sin\left(\frac{N}{2}\psi\right)}{\sin\left(\frac{\psi}{2}\right)} \right] \quad (3-4)$$

$$\psi = pd \cos \theta + \delta \quad (3-5)$$

Where δ is the phase difference between the feed of the array elements. ψ is the required phase shifting along X-axis to control the beam. d is the element spacing.

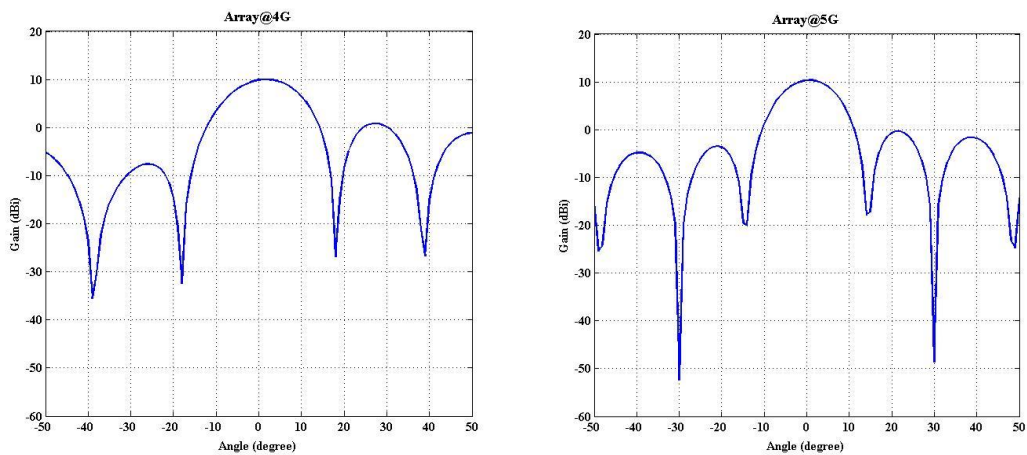
In order to compute the *HPBW* (Half Power Beam width) for the major lobe in addition of the first maximum θ_m , the half-power point θ_h is also required. The *HPBW* can be given as

$$HPBW = 2|\theta_m - \theta_h| \quad (3-6)$$

It is known that the *HPBW* of the antenna array is related to the array factor, which is determined by the element number, element spacing and the excitation phase of each element. The directivity of the antenna array increases with the number of elements and element spacing. But the element spacing should not exceed a half wavelength to avoid the grating lobes. Therefore, it is necessary to choose proper array element to satisfy the requirement.

When this antenna is used as the receiving antenna in the imaging system, a four-element linear antenna array is formed. The 2D radiation patterns in E-plane of the array at different frequencies are simulated in CST Microwave Studio and plotted in Matlab, as shown in Figure 3-16. The antenna gain can go up to 10 dB, and 3 dB beam widths of this array at 4 GHz, 5 GHz, 6 GHz and 7 GHz are respectively 15.8° , 12.9° , 10.8° and 9.1° . The antenna array has been improved in directivity and gain so that it is suitable for the imaging application compared with the single one.

In conclusion, the circular-edge antipodal Vivaldi antenna can work from 2 GHz up to 12 GHz. The linear array based on four antenna elements improves the directivity and the gain. In order to improve the gain in lower frequency, especially from 3 GHz to 6 GHz, the following balanced antipodal Vivaldi antenna has been investigated.



(a)

(b)

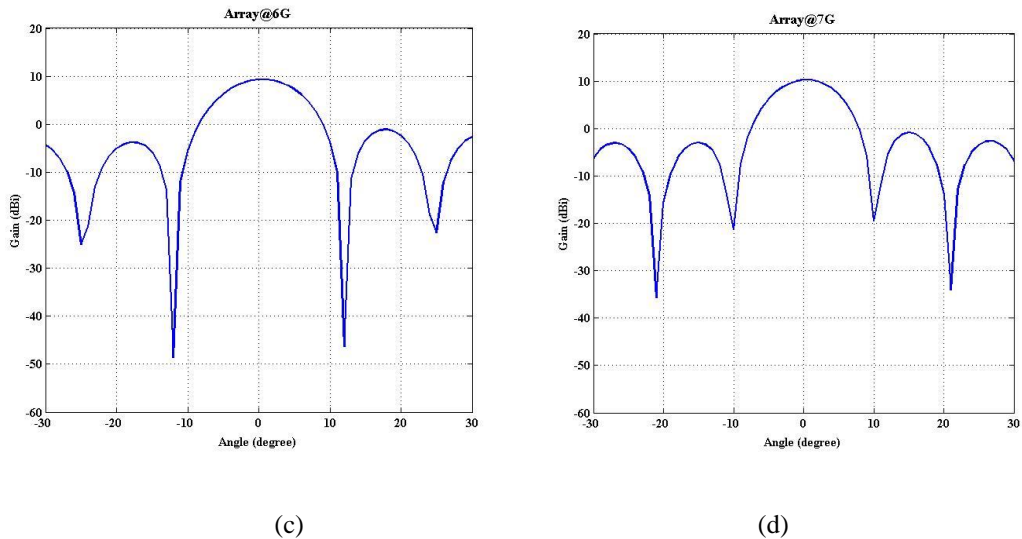


Figure 3-16 The simulated radiation pattern in E-plane of four elements array at different frequencies; (a) 4 GHz, (b) 5 GHz, (c) 6 GHz, (d) 7 GHz.

3.4 The Corrugated Balanced Antipodal Vivaldi Antenna

3.4.1 Structure of the antenna

In order to improve the directivity and gain of the antenna in the lower frequency band, the corrugated structure has been suggested to increase the directivity to the tapered slot antenna in [25-26]. Thus it will be applied to the traditional balanced antipodal Vivaldi antenna.

The corrugated balanced antipodal Vivaldi antenna has been designed. It has three metallic layers and two supporting substrates. The structure of three layers is shown in Figure 3-17. Like a sandwich structure, the radiated antenna layer is in the middle of the two supporting FR4 substrates, while the front and back metallic layers, which can be treated as the ground layer, are attached on the outermost side of these two substrates. The front and back ground layers are in the same shape, while the central radiated one is in the mirrored shape. The radiation flare is shaped of inner and outer exponential edges, and cut with linear slot lines. These slot lines are all in the same length d_s in Y-axis, with the same distance d between them. They reduce the width along X-axis linearly from lower side to up side of the radiation flare. The

dimensions of the radiation flare are similar to the one when designing previous antipodal Vivaldi antenna. The values of the dimensions are also simulated and optimized in CST Microwave Studio to achieve impedance match over the frequency band of 3.1-10.6 GHz. They are listed in Table 3-2.

The width of the corrugated BAVA is reduced remarkably compared with the circular-edge antipodal Vivaldi antenna, mainly due to the effort of these slot lines. The slot lines can enlarge the equivalent size of the radiated area and make the antenna more compact. The fabricated antenna is shown in Figure 3-18.

Table 3-2 The dimensions of the corrugated BAVA

Parameter	W	L	w _m	L ₁	L ₂	d _s	d
Value (mm)	35	75	1.5	10	32	0.7	0.9

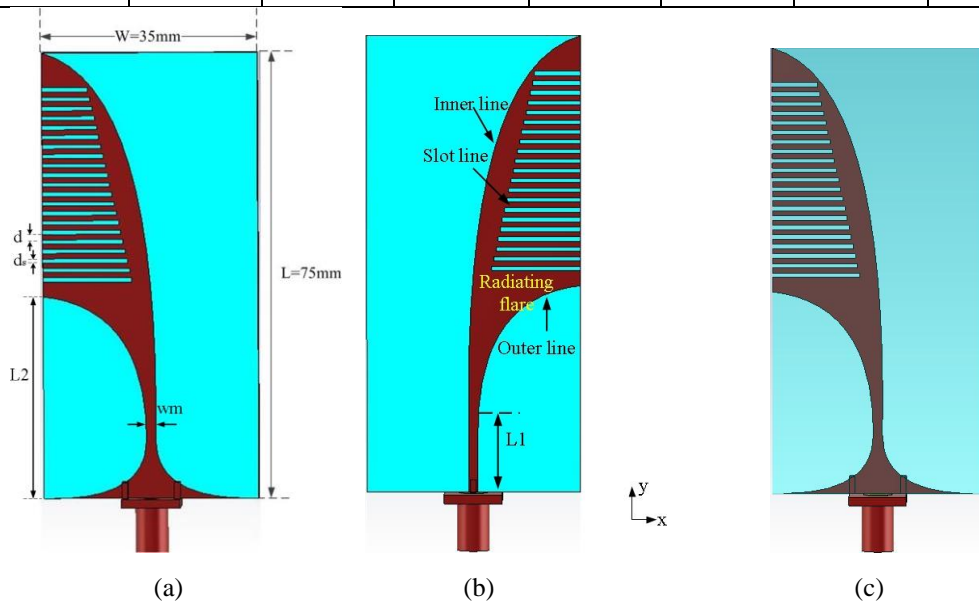


Figure 3-17 The physical structure of the corrugated BAVA; (a) the front layer view; (b) the middle layer view; (c) the back layer view.

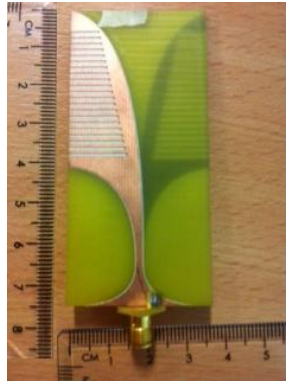


Figure 3-18 The fabricated corrugated BAVA.

3.4.2 Simulated and measured results

This antenna operates from 2.8 GHz to 12 GHz in the simulation and from 3 GHz to 12 GHz in the measurement. The simulated and measured S_{11} are plotted in Figure 3-19. The red curve is the measured result while the blue curve is the simulated one. There is a deep attenuation around 4 GHz in the measured S_{11} , mainly because the gap between the two substrates. This antenna has two substrates, which are connected by the SMA connector at the bottom side. Therefore there is a thin gap of air between them. It may influence the S_{11} performance. In order to verify this possibility, the simulated model of this antenna with a gap of air is carried out in CST Microwave Studio. The thickness of gap is 0.18mm. The simulated S_{11} is shown as the green curve in Figure 3-19. It matches well with the measured result.

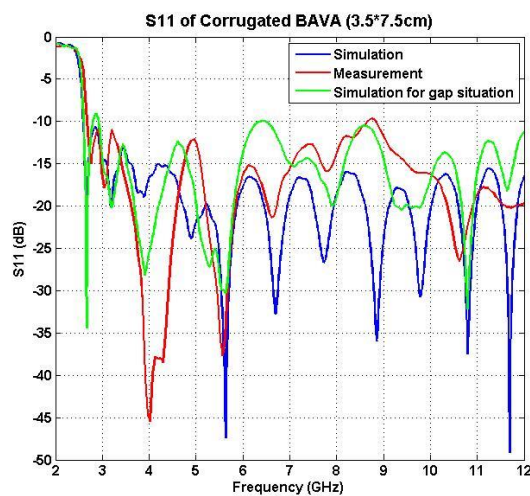


Figure 3-19 The simulated and measured S_{11} of corrugated BAVA.

The corrugated structure can make the antenna operate in lower frequency. As shown in Figure 3-20, the corrugated BAVA has lower end of the operating frequency band compared with the one without corrugated structure.

In BAVA, travelling wave propagates along the inner edge of the flares, which is the main mechanism of the radiation. Normally, the current is flowing along the edge of the radiation flare. For the BAVA without corrugated structure, the wavelength of the wave is relatively long in lower frequency. When the current travels to the end edge of the radiation flare, it will cover most area and flow back on the radiation flare, as shown in Figure 3-21 (a). But in higher frequency, due to the short wavelength, it focuses on travelling along the edge, as shown in Figure 3-21 (b). In this case, the radiation intensity will be reduced by the returned current in lower frequency, so the gain of the antenna is lower compared to the one in higher frequency.

For the corrugated BAVA, the corrugated structure can change the current distribution on the radiation flare, especially in lower frequency. As described above, the current travels on most area of the end edge of the radiation flare and then flows back. Using the corrugated structure, it will be forced to travel along the edge of the flare, and be suppressed to flow back. But in higher frequency, the current is hardly influenced by the corrugated structure, because it originally travels along the edge of the radiation flare. It is evidently shown in Figure 3-21 (c) and Figure 3-21 (d) that the current distribution has changed much at 4 GHz than at 7 GHz. In this case, radiation intensity will not be restrained in lower frequency. Therefore the gain of the antenna in lower frequency will be higher than usual. As illustrated in Figure 3-22, the simulated gain of the corrugated BAVA is higher than the one without corrugated structure, especially remarkable in lower frequency. Compared with the circular-edge antipodal antenna, the gain of the corrugated BAVA has also been improved across the frequency range of 3-6 GHz, while there is only slight difference from 7.5 GHz to 10 GHz, as plotted in Figure 3-23. The blue curve represents the corrugated BAVA, while the red curve is related to the circular-edge antipodal Vivaldi antenna.

Since the corrugated structure suppresses the current to flow back in lower frequency, it can also improve the radiation efficiency. The comparison of the total radiation efficiency for two BAVAs is listed in Table 3-3. It is known that the corrugated

structure makes the antenna have relatively better radiation efficiency than the one without corrugated structure in lower frequency, e.g. 4 GHz and 5 GHz, although it doesn't change much in higher frequency, e.g. 6 GHz and 7 GHz.

Therefore, the corrugated BAVA has been achieved to operate from lower frequency, have better radiation efficiency and have relatively higher gain from 3 GHz to 6 GHz.

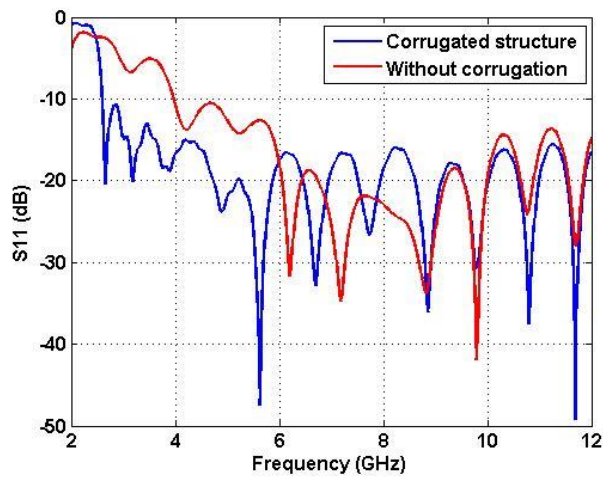
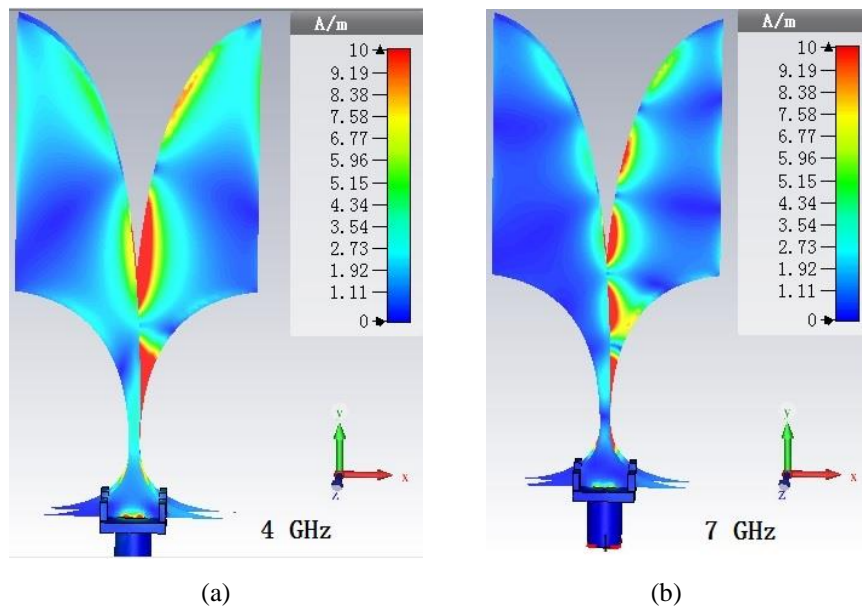


Figure 3-20 The comparison of with and without corrugation in simulated S_{11} .



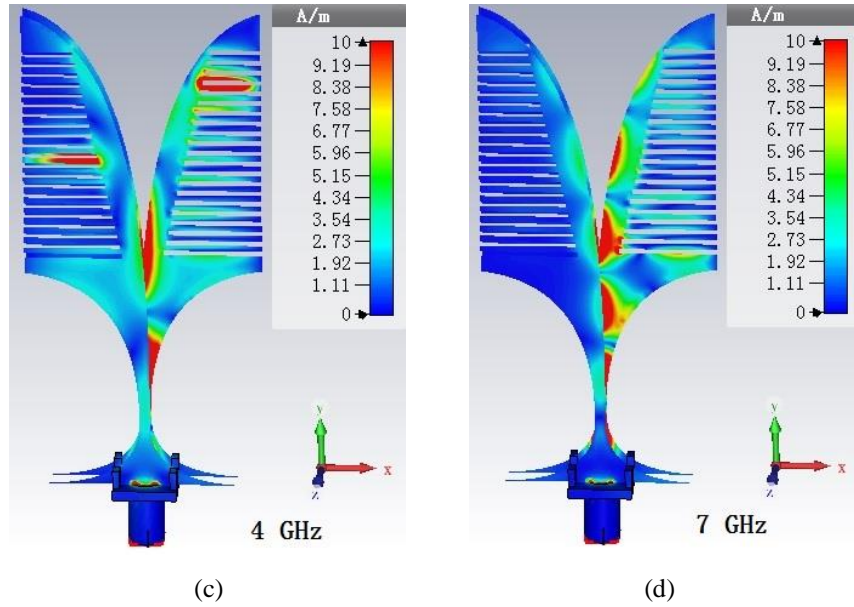


Figure 3-21 The current distribution on the surface of the antenna at 4 GHz and 7 GHz for different BAVAs; (a) the BAVA without corrugation at 4 GHz; (b) the BAVA without corrugation at 7 GHz; (c) the corrugated BAVA at 4 GHz; (d) the corrugated BAVA at 7 GHz.

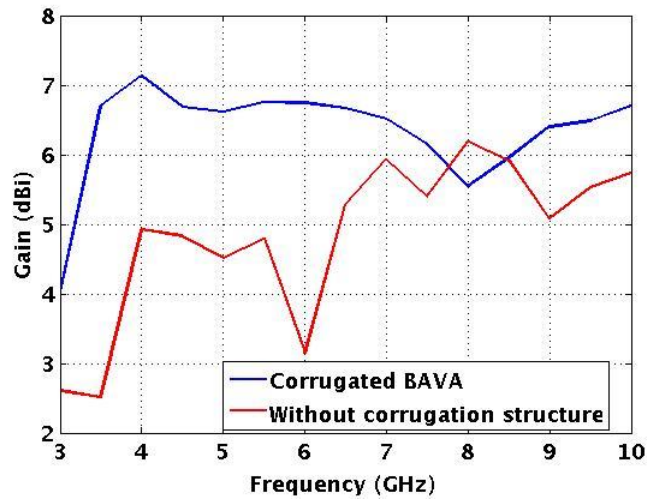


Figure 3-22 The comparison of gain for corrugated BAVA and the one without corrugated structure.

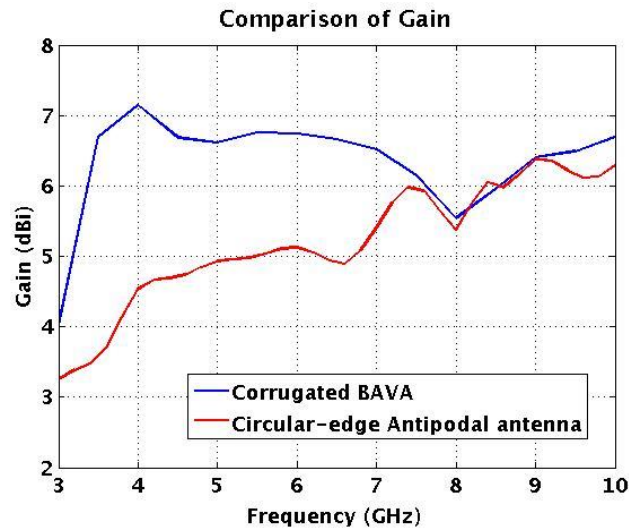


Figure 3-23 The comparison of gain for corrugated BAVA and circular-edge antipodal Vivaldi antenna.

Table 3-3 The total radiation efficiency for two BAVAs at different frequencies.

Frequency (GHz)	Total radiation efficiency (dB)	
	The corrugated BAVA	BAVA Without corrugation
4	-1.1	-1.3
5	-1.2	-1.4
6	-1.6	-1.7
7	-1.9	-1.9

The simulated results of 3D radiation patterns at different frequencies are shown in Figure 3-24. Compared with the circular-edge antipodal Vivaldi antenna, the corrugated BAVA is higher in directivity across the whole operating frequency range especially in lower frequency band. The simulated and measured radiation patterns for E-plane and H-plane are shown in Figure 3-24 and Figure 3-25 respectively. Very good agreement has been met between the measured radiation patterns and the simulated ones. The 3 dB beam widths of the single corrugated BAVA are 68.6° , 62.2° , 62.0° and 61.3° at 4 GHz, 5 GHz, 6 GHz and 7 GHz in the E-plane respectively.

When E-plane array is built by four corrugated BAVAs, the radiation patterns at different frequencies which are simulated in CST Microwave Studio are plotted in Matlab, as shown in Figure 3-26. The 3 dB beam widths of this array are 14.7° , 11.7° , 10.3° and 8.1° at 4 GHz, 5 GHz, 6 GHz and 7 GHz respectively. It is narrower in the beam width than the previous circular-edge antipodal Vivaldi antenna.

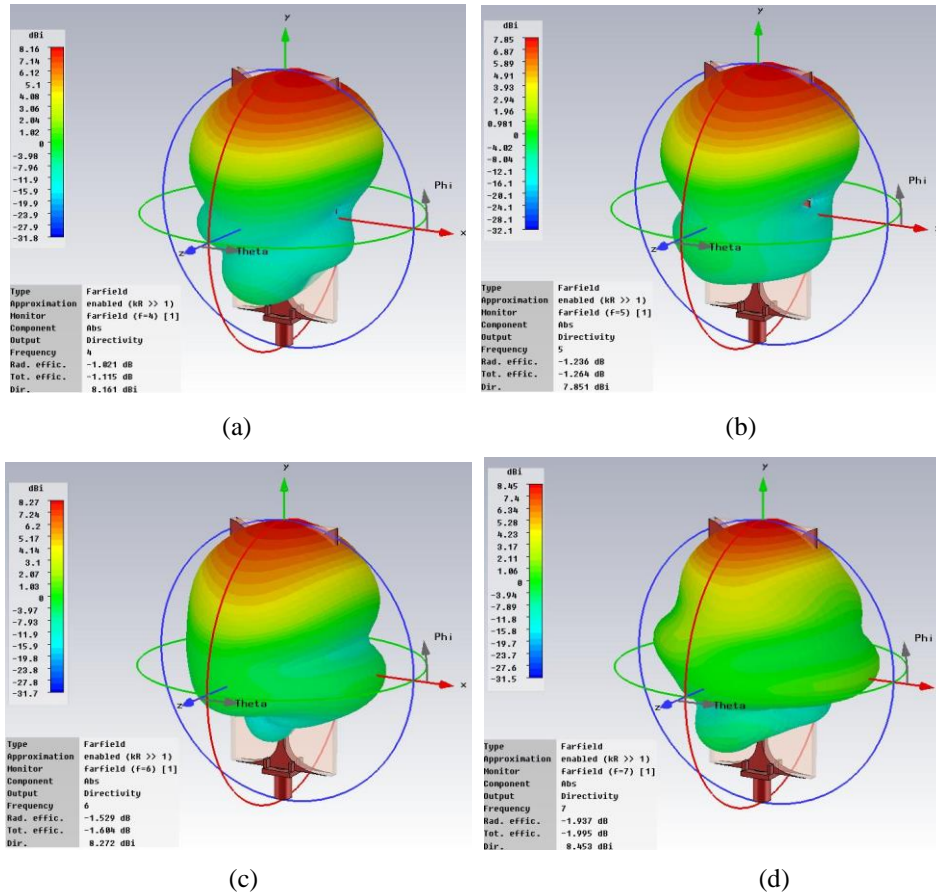
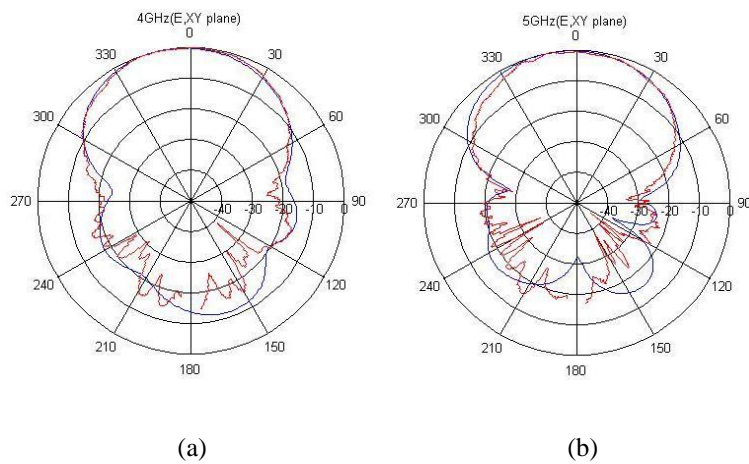


Figure 3-24 3D simulated radiation patterns for Corrugated BAVA; (a) 4 GHz; (b) 5 GHz; (c) 6 GHz; (d) 7 GHz.



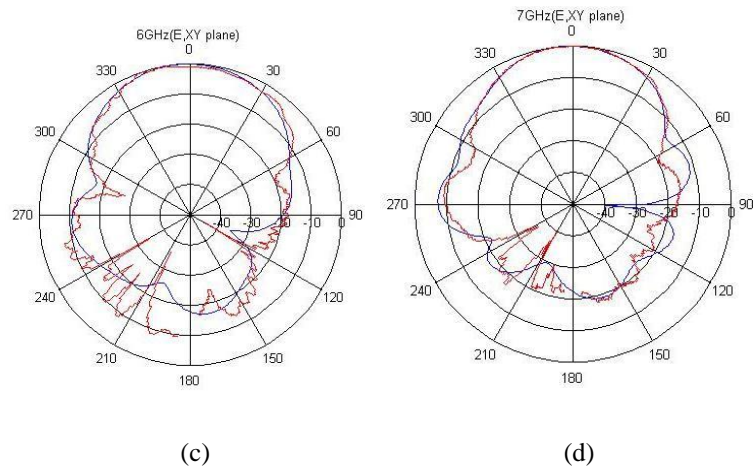


Figure3-25 The simulated (blue) and measured (red) radiation patterns in E-plane; (a)At 4 GHz, (b) At 5 GHz, (c) At 6 GHz, (d) At 7 GHz.

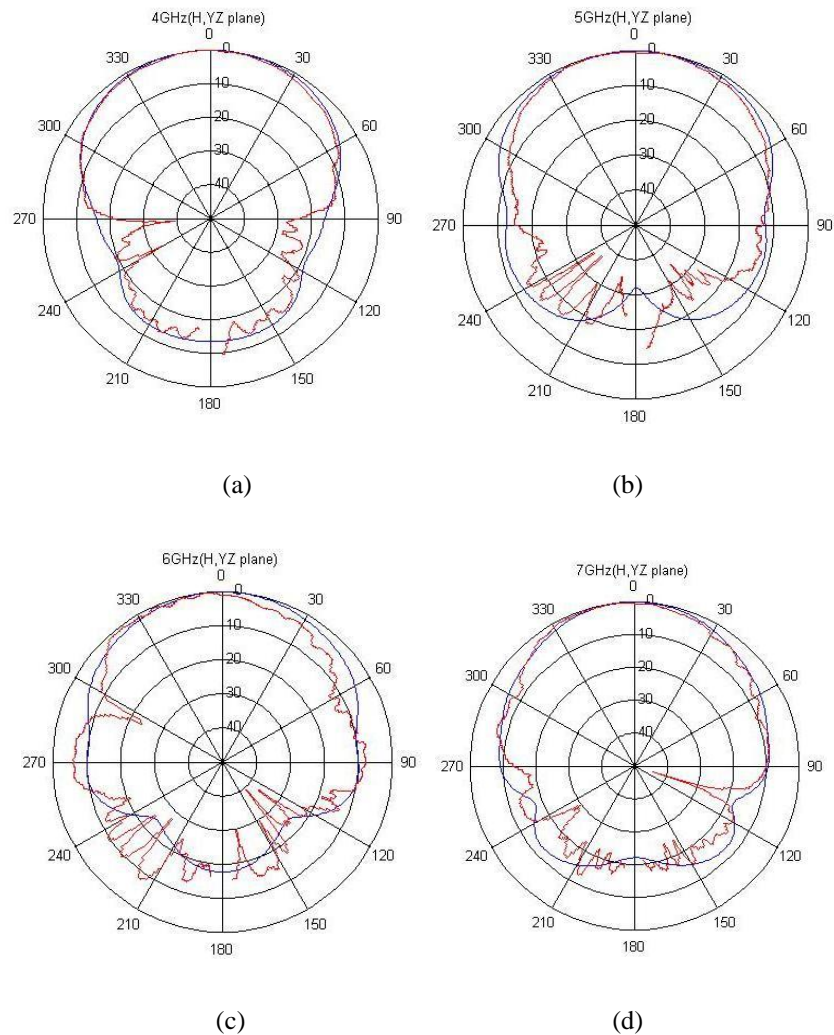


Figure 3-26 The simulated (blue) and measured (red) radiation patterns in H-plane; (a)At 4 GHz, (b) At 5 GHz, (c) At 6 GHz, (d) At 7 GHz.

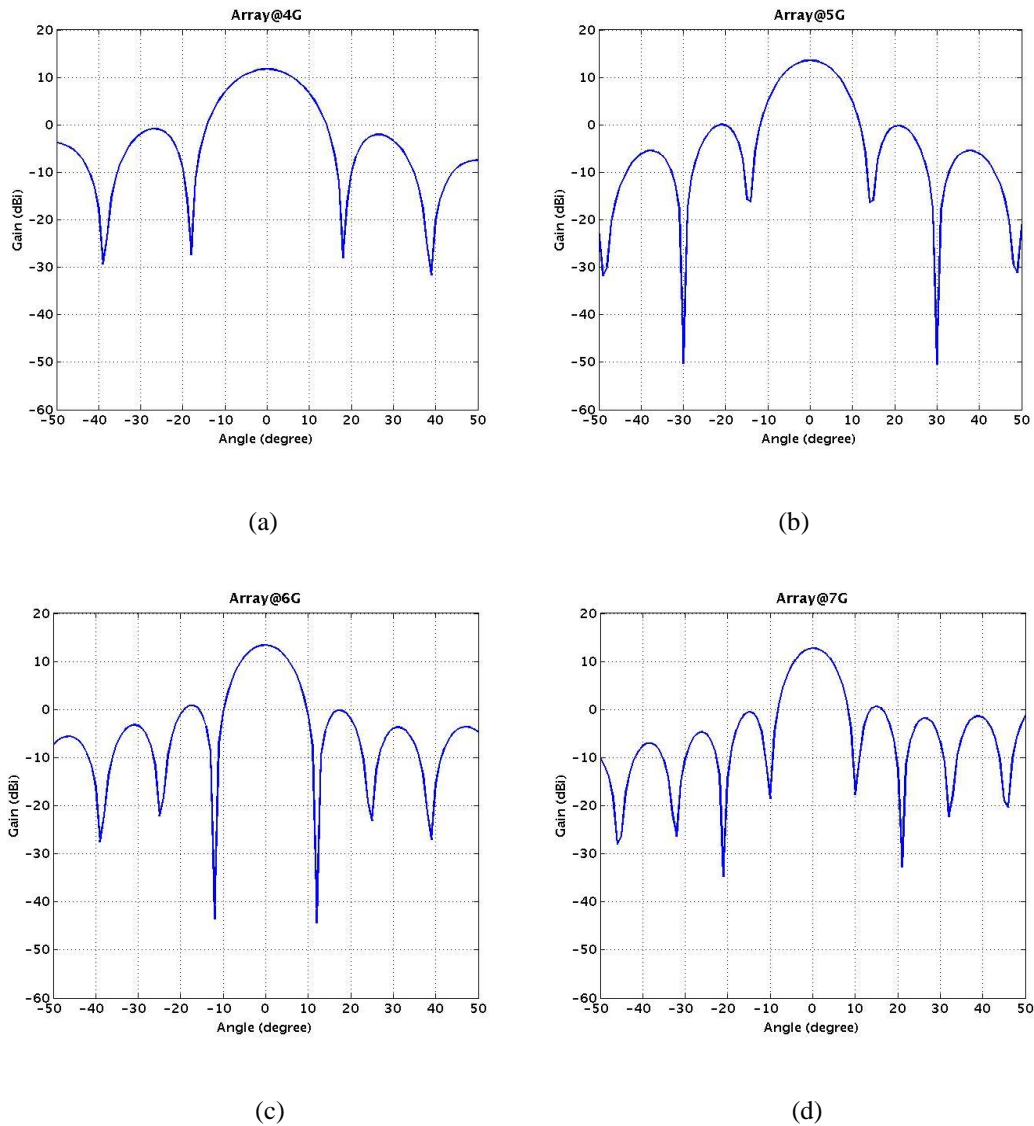


Figure 3-27 The simulated radiation pattern in E-plane of four elements array at different frequency; (a) 4 GHz, (b) 5 GHz, (c) 6 GHz, (d) 7 GHz.

3.5 Summary

This chapter has mainly presented the antennas developed for the UWB imaging system. Two types of antennas, which are the circular-edge antipodal Vivaldi antenna and the corrugated balanced antipodal Vivaldi antenna, have been designed and investigated in the frequency domain. Both antennas can work from 3 GHz to 12 GHz, while the width of the corrugated BAVA is reduced almost as half as that of the circular-edge antipodal Vivaldi antenna. The BAVA with corrugated structure is smaller in size. It has high gain and directivity in lower frequency band. The gain of

the corrugated balanced antipodal Vivaldi antenna has been greatly improved to be relatively 7 dBi, especially in lower frequency, which is better than the circular-edge antipodal Vivaldi antenna.

Based on the characteristic analysis in the frequency domain, both antennas can be good candidates for the UWB imaging system. However, since the proposed imaging system will work in the time domain, characteristics for both antennas in the time domain need to be investigated. This will be described in detail in Chapter 4.

Reference

- [1] F.J. Wang, and J.S. Zhang, "Time domain characteristics of adouble-printed UWB dipole antenna", *Progress In Electromagnetics Research Letters*, Vol. 3, Page(s): 161-168, 2008.
- [2] A. Mehdipour, K. M. Aghdam, and R. Faraji-Dana, "Completed dispersion analysis of Vivaldi antenna for ultrawideband applications", *Progress In Electromagnetics Research, PIER 77*, Page(s): 85-96, 2007.
- [3] X. Li, S.C. Hagness, M.K. Choi, and D.K. van der Weide, "Numerical and experimental investigation of an ultra wideband ridged pyramidal horn antenna with curved launching plane for pulse radiation", *Antennas and Wireless Propagation Letters, IEEE*, vol. 2, Page(s): 259-262, 2003.
- [4] A.G. Yarovoy, L.P. Ligthart, "Dielectric wedge antenna for ground penetrating radars", *Antennas and Propagation Society International Symposium, IEEE*, Vol.2, Page(s): 247-250, 2003.
- [5] U. Schwarz, M. Helbig, J. Sachs, F. Seifert, R. Stephan, F. Thiel, M.A. Hein, "Physically small and adjustable double-ridged horn antenna for biomedical UWB radar applications", *IEEE International Conference on Ultra-Wideband (ICUWB 2008)*, Vol.1, Page(s): 5-8, 2008.
- [6] U. Schwarz, M. Helbig, J. Sachs, F. Seifert, R. Stephan, F. Thiel, M.A. Hein, "Design and application of dielectrically scaled double-ridged horn antennas for

- biomedical UWB radar applications”, *IEEE International Conference on Ultra-Wideband (ICUWB 2009)*, Vol.1, Page(s): 150-154, 2009.
- [7] R. Nilavalan, I.J. Craddock, A. Preece, J. Leendertz, R. Benjamin, “Wideband microstrip patch antenna design for breast cancer tumour detection”, *IET Microwaves, Antennas & Propagation*, Vol.1, Issue:2, Page(s): 277-281, 2007.
- [8] D. R. Gibbins, M. Klemm, I.J. Craddock, G.S. Hilton, D.L. Paul, “The Design of a Wide Slot Antenna for the Transmission of UWB Signals into the Human Body using FDTD Simulation”, *The Second European Conference on Antennas and Propagation, 2007. EuCAP 2007*, Page(s): 1-5, 2007.
- [9] A.A. Lestari, E. Bharata, A.B. Suksmono, A. Kurniawan, A.G. Yarovoy, L.P. Ligthart, “A modified Bow-Tie Antenna for Improved Pulse Radiation”, *IEEE Transactions on Antennas and Propagation*, Vol: 58, Issue: 7, Page(s): 2184-2192, 2010.
- [10] Y. Wang, A.E. Fathy, “Design of a compact tapered slot Vivaldi antenna array for see through concrete wall UWB applications”, *Proceedings of the XXIXth URSI General Assembly in Chicago, USA, 7-16 August, 2008*.
- [11] J.J. Fisher, “Design and Performance Analysis of a 1-40 GHz Ultra-Wideband Antipodal Vivaldi Antenna”, *Proceedings of German Radar Symposium, GRS 2000, Berlin, Germany*, Page(s): 237-244, 2000.
- [12] J. Bourqui, M. Okoniewski, E.C. Fear, “Balanced Antipodal Vivaldi Antenna for Breast Cancer Detection”, *The Second European Conference on Antennas and Propagation, 2007. EuCAP 2007*, Page(s): 1-5, 2007.
- [13] S. Wang, L. Guo, X. Chen, C. G. Parini, J. McCormick, “Analysis of Mutual Coupling in Broadband Arrays”, *2008 IEEE AP-S International Symposium on Antenna and Propagation*, San Diego, U.S.A, July 5-12, 2008, Page(s): 1-4, 2008.
- [14] P. J. Gibson, “The Vivaldi aerial,” in *Proc. 9th European Microwave Conf.*, pp. 101-105, Brighton, U.K., June 1979.

- [15] C. A. Balanis, *Antenna Theory: Analysis and Design*, Mississauga: John Wiley and Sons Canada LTD, 2005.
- [16] R.Q. Lee, R.N. Simons, "Effect of Curvature on Tapered Slot Antennas", *Antennas and Propagation Society International Symposium*, 1996, AP-S, Digest, Vlo. 1, Page(s): 188-191, 1996.
- [17] K.F. Lee, W. Chen (Eds), *Advances in Microstrip and Printed Antennas*, New York: John Wiley and Sons, 1997.
- [18] J.P. Weem et al, "Vivaldi antenna arrays for SKA", *Antennas and Propagation Society International Symposium*, July 2000, Vol.1, Page(s): 174-177, 2000.
- [19] J.P. Weem et al, "Vivaldi antenna arrays for SKA", *Antennas and Propagation Society International Symposium*, vol.1, July 2000, pp. 174-177, 2000.
- [20] Schuppert, "Microstrip/slotline transitions: Modeling and experimental investigations", *IEEE Trans.*, vol. MTT-36, pp. 1272-1282, 1988.
- [21] Sloan et al, "A broadband microstrip-to-slotline transition", *Microwave and optical technology letters*, vol. 18, No. 5, August 1998, pp. 339-342, 1998.
- [22] S. Wang, "Design of Tapered Slot Element for Broadband Arrays", *Thesis for the degree of Doctor of Philosophy*, Queen Mary, University of London, September 2009.
- [23] J. Bourqui, M. Okoniewski, and E. C. Fear, "Balanced Antipodal Vivaldi Antenna with Dielectric Director for Near-field Microwave Imaging", *Transaction On Antennas and Propagation*, vol. 58, issue 7, pp(s): 2318-2316, 2010.
- [24] T.H. Chio, D.H. Schaubert, "Parameter study and design of wide-band widescan dual-polarized tapered slot antenna arrays", *IEEE Transaction on Antennas and Propagation*, Vol: 48, Page(s): 879-886, 2000.
- [25] V. Mikhnev, P. Vainikainen, "Wideband Tapered-Slot Antenna with Corrugated Edges for GPR Applications", *33rd European Microwave Conference*, Page(s): 727-729, 2003.

- [26] M.E. Bialkowski, Yifan Wang, "A size-reduced exponentially Tapered Slot Antenna with corrugations for directivity improvement", *Asia Pacific Microwave Conference, 2009. APMC 2009*. Page(s): 2482-2485, 2009.

Chapter 4 The Antenna's characteristics in the Time Domain

The definition of the UWB antennas indicates that they should be able to operate in an ultra-wide frequency band. The analysis in the frequency domain mainly concerns their S-parameters, gains and radiation patterns.

From the prospective of time-domain analysis, UWB systems can be often achieved by impulse-based technologies: transmitting extremely narrow pulses on the order of 1 ns or less and resulting in bandwidth in excess of 1 GHz. To quantify the time domain performance of UWB antennas, the impulse response is of particular interest and importance. The distortion of the pulse propagation needs to be investigated as well, by analysing the pulse fidelity of the antenna system.

In this chapter, the input modulated Gaussian pulse will be proposed firstly, which has less distortion and more practical possibility than the normal Gaussian pulse. Secondly, the modulated truncated sine function signal will be investigated, as it will be used in the measurement. Thirdly, the time domain analysis are applied to the circular-edge antipodal antenna and corrugated balanced antipodal Vivaldi antenna, respectively. Lastly, a study on the pulse fidelity for two antennas will be conducted.

4.1 The input UWB pulse

4.1.1 Gaussian pulse

Gaussian pulse is usually the common choice for the ultra-wideband communication due to its short duration in the time domain and ultra-wideband spectrum. Different pulse widths of the Gaussian pulse will have different spectral bandwidths.

Following the equations (4-1), the Gaussian pulses with different pulse widths are plotted in Figure 4-1 (a). As increasing the pulse parameter b , the spectral bandwidth will decrease, as shown in Figure 4-1 (b). Although the bandwidth covers several

Gigahertz, the PSD (Power Spectral Density) doesn't satisfy the FCC's regulation especially from 0.96 GHz to 1.61 GHz. Meanwhile if the pulse parameter $b = 450ps$, the peak value of the PSD will access above -41.3 dBm/MHz, which is also beyond the requirement.

$$f_0(t) = e^{-\left(\frac{t-d}{b}\right)^2} \quad (4-1)$$

$$f_1(t) = -\frac{2(t-d)}{b^2} e^{-\left(\frac{t-d}{b}\right)^2} \quad (4-2)$$

$$f_2(t) = \left[-\frac{2}{b^2} + \frac{4(t-d)^2}{b^4} \right] e^{-\left(\frac{t-d}{b}\right)^2} \quad (4-3)$$

$$f_3(t) = \left[\frac{12(t-d)}{b^4} - \frac{8(t-d)^3}{b^6} \right] e^{-\left(\frac{t-d}{b}\right)^2} \quad (4-4)$$

$$f_4(t) = \left[\frac{12}{b^4} - \frac{48(t-d)^2}{b^6} + \frac{16(t-d)^4}{b^8} \right] e^{-\left(\frac{t-d}{b}\right)^2} \quad (4-5)$$

Where, pulse parameter b is related to the pulse width. d is the delay in time.

While increasing the derivation of the Gaussian pulse following the equations from (4-2) to (4-5) in which the pulse parameter $b = 100ps$, the spectrum of these pulses will shift to higher frequency, and be more satisfied to FCC's regulation in PSD. As shown in Figure 4-2 (b), the fourth-order of Gaussian pulse almost satisfies the FCC's regulation even for UWB outdoor application.

In the same principle with Gaussian pulse, the pulse duration is reciprocal of the frequency bandwidth, which can be seen from Figure 4-3. When the pulse parameter b is bigger than 100 ps, the bandwidth in the frequency domain will still beyond the regulation especially from 0.96 GHz to 1.61 GHz. Considering the implementation, it is not easy to generate a pulse in such short pulse duration less than 100 ps. Another thing is that the fourth-order of Gaussian pulse is generated after the fourth derivation of the Gaussian pulse, which means it needs to pass through at least four

filters. It will introduce more noise and distortion when passing through more filters. Due to these reasons, this fourth-order of Gaussian pulse will not be the best choice when using it in the measurement.

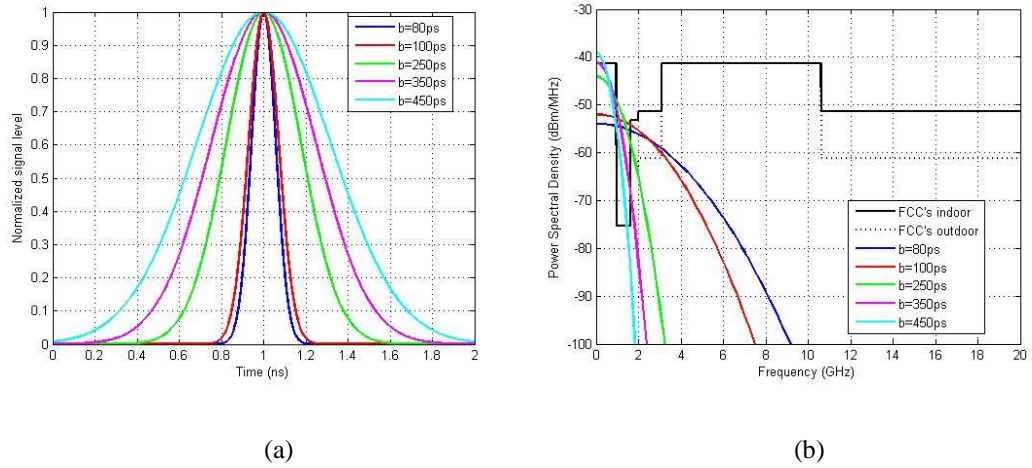


Figure 4-1 The Gaussian pulse with different pulse width; (a) the pulse in the time domain; (b) PSD with FCC's regulation.

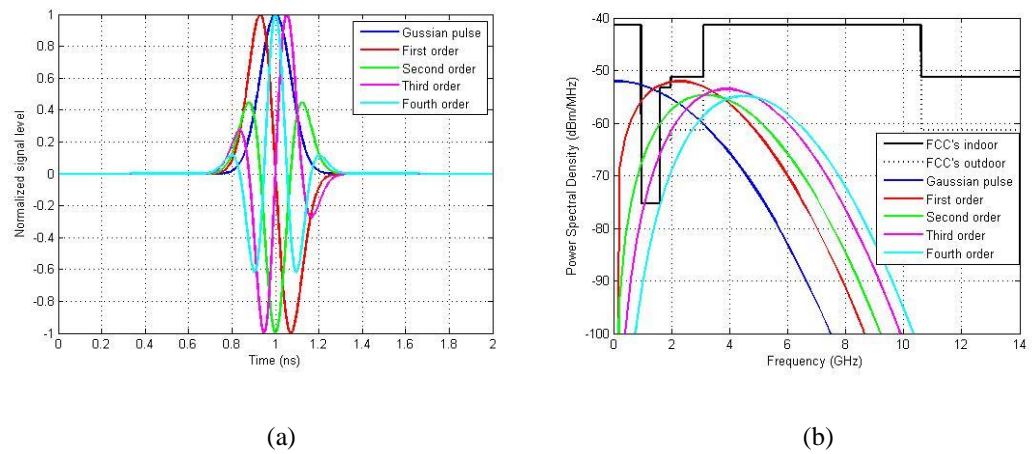


Figure 4-2 The different derivations of Gaussian pulse; (a) the pulse in the time domain; (b) the PSD with FCC's regulation.

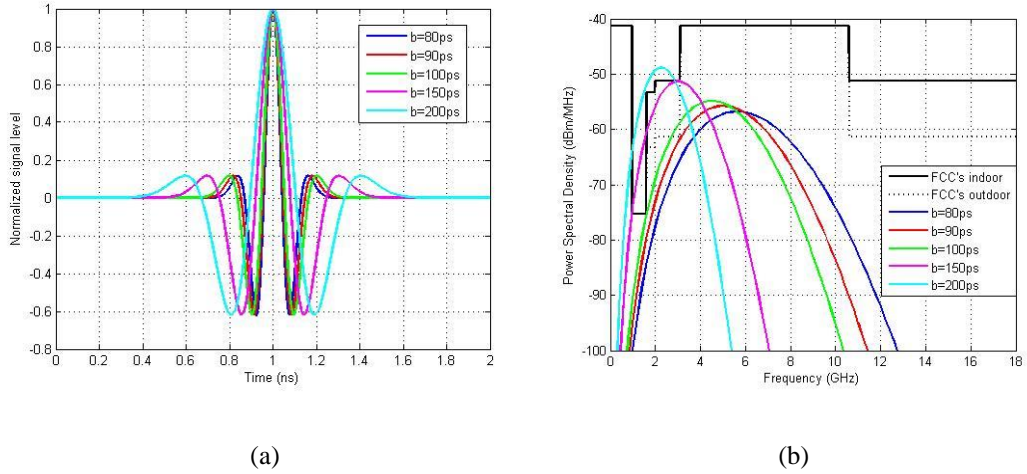


Figure 4-3 The fourth order of Gaussian pulse; (a) the pulse in the time domain; (b) the PSD with FCC's regulation.

4.1.2 Modulated pulse

In order to satisfy the PSD regulation and be easy to implement, a modulated Gaussian pulse is proposed here by modulating the sine function signal and the Gaussian pulse. The sine function signal is following the equation (4-6).

$$f_{\sin}(t) = \sin(2\pi at) \quad (4-6)$$

Where, a is the signal repetition frequency.

Thus, the modulated Gaussian pulse is following the equation (4-7), and plotted in Figure 4-4 (a) with Gaussian pulse width in different values.

$$f_{\text{modu}}(t) = \sin(2\pi at) \cdot e^{-\left(\frac{t-d}{b}\right)^2} \quad (4-7)$$

Where a is equal to 4.5, and d is equal to 1.

The PSD of this modulated signal matches well with the FCC's regulation, as shown in Figure 4-4 (b). Across the UWB frequency band, the power spectral density is below -41.3 dBm/MHz. It shows the advantages of low energy density and covering ultra-wide frequency band. Meanwhile, this modulated Gaussian pulse can be generated easily via modulating signals from VCO (Voltage Controlled Oscillator) and Gaussian pulse generator. Two different values of pulse parameter b are chosen

in Figure 4-4, which will be discussed in the following paragraphs to compare the performances of the antenna when exciting different pulse widths of this modulated signal.

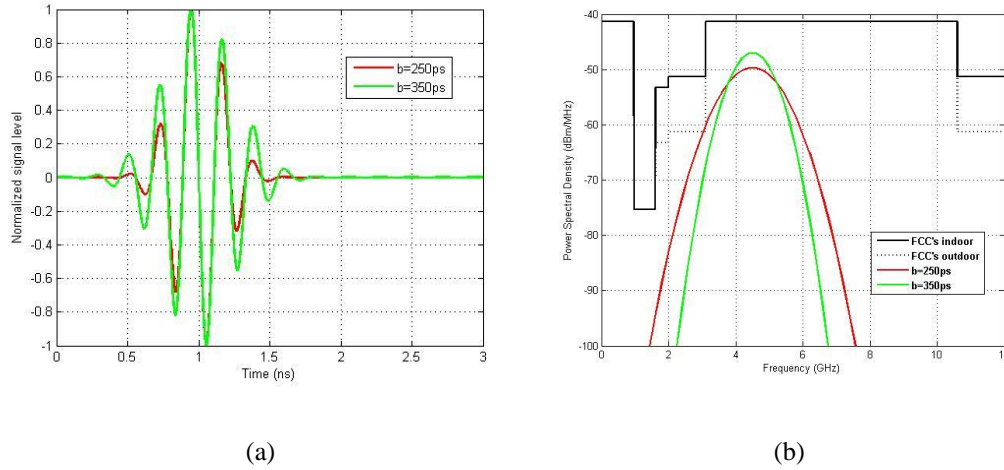


Figure 4-4 The modulated Gaussian pulse; (a) the pulse in the time domain; (b) the PSD with FCC's regulation.

When doing the measurement, because such narrow Gaussian pulse is not available in our lab at the moment, the rectangular signal directly generated from Picosecond Pulse Generator Model 10060A will be used instead. After modulated with the Sine function signal given in equation (4-6), the modulated rectangular signal is fed to the antenna, which is given in formula (4-8)

$$f_{TruncatedSine}(t) = \begin{cases} \sin 2\pi f_c t & qT \leq t \leq qT + \tau \\ 0 & qT + \tau \leq t \leq (q+1)T \end{cases} \quad (4-8)$$

Where q is the periodic time. T is the signal repetition period of 10 μ s. τ is the signal duration of 1 ns. f_c is the centre frequency of 4.5 GHz.

Then one period of this modulated rectangular signal is plotted in Figure 4-5 (a). It is a pulse train of sine signal in rectangular envelope. From its PSD performance, this modulated rectangular signal almost satisfies FCC's regulation across the UWB frequency range.

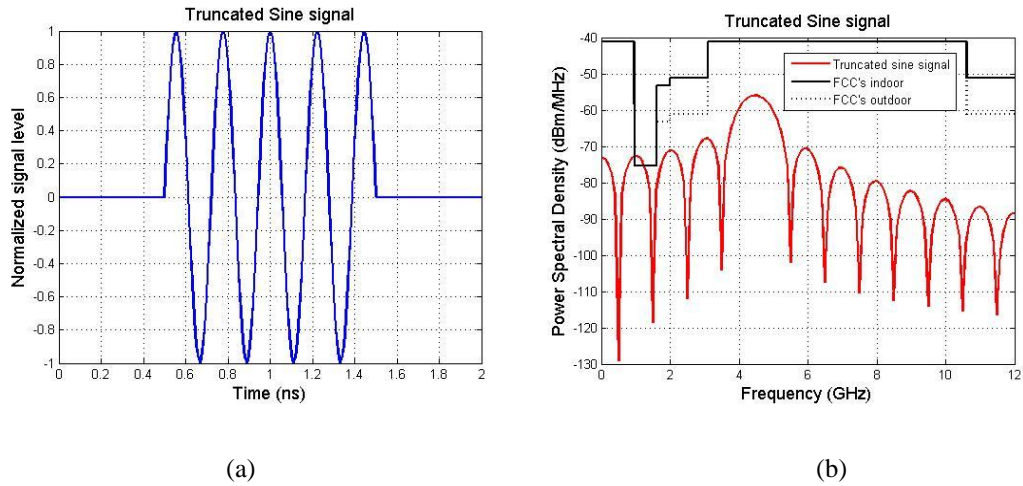


Figure 4-5 The modulated rectangular signal; (a) the signal of one period in the time domain; (b) the PSD of one period with FCC's regulation.

4.2 Impulse response

4.2.1 Fundamental analysis

A simple system is considered, which comprises a transmitting antenna, a receiving antenna and the corresponding propagation environment, as shown in Figure 4-6. The behaviour of the antenna and the system in the frequency domain is usually described in transfer function $H(f)$ from system level [1]. The impulse response can be derived from transfer function by using Inverse Fast Fourier Transform (IFFT). This method also can be realized from the measurement easily.

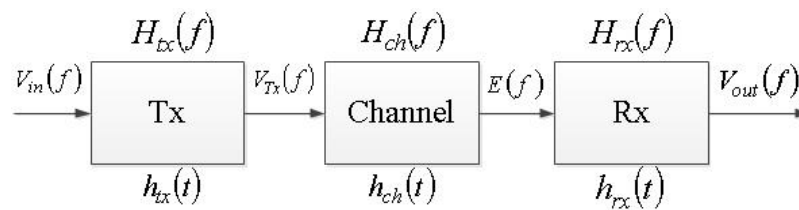


Figure 4-6 A simple communication UWB antenna system [1].

The transfer function of the Tx and the channel are defined as the ratio of the electric far field at the desired direction and the input voltage at the terminal of the Tx, which is expressed in equation (4-9).

$$\vec{H}_{txch}(f) = \vec{H}_{tx}(f) \vec{H}_{ch}(f) = \frac{\vec{E}(f)}{V_{in}(f)} \quad (4-9)$$

Where $\vec{E}(f)$ and $V_{in}(f)$ are the frequency domain expression of the electric field $\vec{e}(t)$ and the input voltage $v_{in}(t)$.

Similarly, a vector transfer function for the Rx is then defined through the following expression.

$$\vec{H}_{rx}(f) = \frac{V_{out}(f)}{\vec{E}(f)} \quad (4-10)$$

$\vec{E}(f)$ is substituted from (4-9) into (4-10) to establish a relationship between the excitation voltage to the Tx and the received voltage at the Rx. This relationship can be treated as the transfer function of the antenna system, which is given by

$$\vec{H}(f) = \vec{H}_{tx}(f)\vec{H}_{ch}(f)\vec{H}_{rx}(f) = \frac{V_{out}(f)}{V_{in}(f)} = \vec{S}_{21}(f) = |S_{21}(f)|e^{-j\varphi(f)} \quad (4-11)$$

This system transfer function is also known as $\vec{S}_{21}(f)$ when doing the measurement. $|S_{21}(f)|$ is the amplitude of the transfer function while φ is the phase of the transfer function.

In this simple UWB radio channel, Kunisch and Pump [2] describe that the antennas generally exhibit different shaped transmission and reception impulse responses to the same stimulus. For a given antenna the temporal impulse responses in transmission and reception are related by a time derivative. In other words, for the same UWB antenna, the ratio of the transmitting antenna transfer function to the receiving antenna transfer function is proportional to the operating frequency [3]. So it can be assumed that the relationship between them is given by equation (4-12).

$$\vec{H}_{tx}(f) = \frac{j \cdot f}{c_0} \vec{H}_{rx}(f) \quad (4-12)$$

Using the conclusion from [4], the free space transfer function is expressed as the following equation.

$$\vec{H}_{ch}(f) = \frac{\lambda}{4\pi d} e^{-jkd} \quad (4-13)$$

Where λ is the wavelength related to the operating frequency. d is the distance between the transmitting antenna and the receiving antenna. k is the propagation constant defined as $k = \frac{2\pi}{\lambda}$.

As the transfer function $\bar{S}_{21}(f)$ can be measured from the network analyzer, the transfer function for the Tx and Rx can be related to the system's transfer function by using the equations above, given by equation (4-14) and (4-15).

$$\bar{H}_{rx}(f) = \sqrt{4\pi d |S_{21}(f)|} \cdot e^{-j\left(\frac{\varphi}{2} - \frac{\pi d f}{c_0} + \frac{\pi}{4}\right)} \quad (4-14)$$

$$\bar{H}_{tx}(f) = \frac{f}{c_0} \sqrt{4\pi d |S_{21}(f)|} \cdot e^{-j\left(\frac{\varphi}{2} - \frac{\pi d f}{c_0} - \frac{\pi}{4}\right)} \quad (4-15)$$

The UWB antennas operate over a huge frequency range so that the performances of the antenna are frequency-dependent. According to the Friis Transmission equation [5], the relationship between the power of the Tx and Rx can be expressed as equation (4-16).

$$\frac{P_r(f)}{P_t(f)} = \left(1 - |\Gamma_t(f)|^2\right) \left(1 - |\Gamma_r(f)|^2\right) G_t(f) G_r(f) |\hat{\rho}_t(f) \hat{\rho}_r(f)|^2 \left(\frac{\lambda}{4\pi d}\right)^2 \quad (4-16)$$

Where $P_t(f)$, $P_r(f)$ are the power of the transmitting antenna and receiving antenna respectively. $\Gamma_t(f)$, $\Gamma_r(f)$ are the reflection coefficient at the input of the transmitting antenna and the output of the receiving antenna. $G_t(f)$, $G_r(f)$ are the gain of the transmitting antenna and the receiving antenna respectively. $|\hat{\rho}_t(f) \hat{\rho}_r(f)|^2$ is the polarisation matching factor between the transmitting and receiving antennas.

If two antennas match well in reflection and polarisation, the equation (4-16) can be simplified in the form of equation (4-17).

$$\frac{P_r(f)}{P_t(f)} = G_t(f) G_r(f) \left(\frac{\lambda}{4\pi d}\right)^2 \quad (4-17)$$

Due to the relationship between the power and the voltage, expressed as equation (4-18), the transfer function of the antenna system can be given by equation (4-19).

$$\left[\frac{V_{in}(f)}{2} \right]^2 = P_t(f)Z_0$$

$$\frac{V_{out}(f)^2}{2} = P_r(f)Z_L \quad (4-18)$$

$$S_{21}(f) = \frac{V_{out}(f)}{V_{in}(f)} = \sqrt{\frac{P_r(f) \cdot 2Z_L}{P_t(f) \cdot 4Z_0}} e^{-j\varphi(f)} \quad (4-19)$$

From the equations, the transfer functions in the frequency domain of the Tx, Rx and the system are determined by the characteristics of both transmitting antenna and receiving antenna, including impedance matching, gain, polarisation matching and the distance between them. The behaviour of the Tx, Rx and the system can be analysed via the transfer function.

When obtaining the transfer function, the impulse responses of the Tx, Rx and the system can be derived easily from IFFT, which are given by

$$\begin{aligned} h(t) &= \text{Re}\{IFFT[\bar{S}_{21}(f)]\} \\ h_{tx}(t) &= \text{Re}\{IFFT[\bar{H}_{tx}(f)]\} \\ h_{rx}(t) &= \text{Re}\{IFFT[\bar{H}_{rx}(f)]\} \end{aligned} \quad (4-20)$$

To reduce the distortion in the received signals, the transfer function should have a relative flat magnitude and a linear phase over the operating frequency [6], which results in a relative sharp and narrow pulse width in the time domain for the impulse response.

As known from the definition of transfer function S_{21} , given by equation (4-11), it is related to the amplitude $|S_{21}(f)|$ and the phase $\varphi(f)$. The amplitude $|S_{21}(f)|$ permits to describe the impact of the antenna in the incoming signal. The phase $\varphi(f)$ introduces another parameter group delay $\tau_g(f)$ to describe how the antenna impacts transmitting or received signals. The group delay is defined as [7]

$$\tau_g(f) = -\frac{d\varphi(f)}{2\pi \cdot df} \quad (4-21)$$

It gives the total propagation delay from the input terminal of the transmitting antenna to the output terminal of the receiving antenna and free space propagation between antennas. This parameter can estimate the signal's distortion when it transmits through the antennas and multiple reflections in the antennas. A non-distorted structure is characterized by a constant group delay, implying that the phase changes linearly with frequency. The nonlinearities of the group delay indicate the resonant character of the structure to store energy. It results in ringing effect of the antenna's impulse response $h(t)$ [8].

The ringing τ_r is undesired and results in oscillations of the pulse after the main peak. It is defined as the time during which the envelope of the waveform has fallen from the peak value p to a certain lower bound $\alpha \cdot p$, following the calculation by the equation (4-22). It should be negligibly small. The energy contained in ringing is of no use at all, which can therefore be eliminated by absorbing materials [7].

$$\tau_r = t_1 \Big|_{h(t_1)=\alpha p} - t_2 \Big|_{t_2 < t_1 \wedge h(t_2)=p} \quad (4-22)$$

4.2.2 Impulse response of the circular-edge antipodal Vivaldi antenna

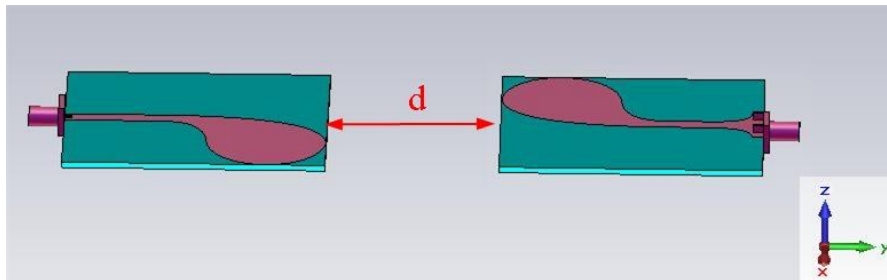


Figure 4-7 The model of antenna system in head-to-head orientation.

By using the method mentioned in the previous section, the circular-edge antipodal Vivaldi antenna is studied in this section. The antennas are put in head-to-head position to do the following analysis. The Gaussian pulse is used in the following model of the antenna system.

Two antennas in head-to-head position are simulated in CST Microwave Studio, as shown in Figure 4-7. It is a simple antenna transmission system. The transfer

function is related to the antenna's radiation performance. Different distances d between the antennas are taken into consideration to check the validity of the model.

The simulated S_{21} in amplitude and phase of this head-to-head antenna system is shown in Figure 4-8. The blue curve is represented for the situation that the antennas are separated by 41 cm, while the red curve is represented for the one that they are separated by 20 cm. Both of them have smooth amplitude of S_{21} and linear phase across the operating frequency range of 2-12 GHz. If the received waveform has less distortion, the transfer function should feature a flat magnitude and linear phase response across the operating frequency band.

When the antennas are spacing from 20 cm to 41 cm, the tendency in amplitude keeps the same. As explained in section 4.2.1, antenna gain is one of the parameters which will influence S_{21} . When the amplitude $|S_{21}(f)|$ has deep resonance over the certain frequency range, i.e. 3 GHz to 5 GHz and 7 GHz to 9 GHz, which are shown in Figure 4-8 (a), the gain varies obviously over the same frequency range, as shown in Figure 4-9. The gain of Tx and Rx have a relatively flat gain from 5 GHz to 7 GHz compared to the other frequency parts.

Using the equation (4-21), the group delays of this antenna system are plotted in Figure 4-10. The blue curve is represented for the situation that the antennas are separated by 41 cm, while the red curve is represented for the one that they are separated by 20 cm. The figure shows that across the operating frequency range, the circular-edge antipodal antenna has a slow variation over the operating frequency range. It will lead the ringing effect in the impulse response $h(t)$ of the antenna or the antenna system.

The normalized impulse responses of the antenna system, Tx and Rx are derived from $S_{21}(f)$, $H_{tx}(f)$ and $H_{rx}(f)$ using IFFT according to the equation (4-20), as shown in Figure 4-11 respectively. $H_{tx}(f)$ and $H_{rx}(f)$ can be calculated from the measured $S_{21}(f)$ based on equation (4-15) and (4-14). The solid line is represented for the distance $d = 41cm$ while the dash line is for the distance $d = 20cm$. It is evident that the impulse responses of the antenna system, Tx and Rx have the same waveform shape in two situations. Due to the non-constant group delay, the impulse

responses have the ringing after the peak value, which have been marked in Figure 4-11. This ringing effect proves that the group delay is related to the ability of the antenna or the antenna system in energy storage. When the group delay is not constant, the antenna or antenna system will store some energy so that the impulse response is going to keep oscillation.

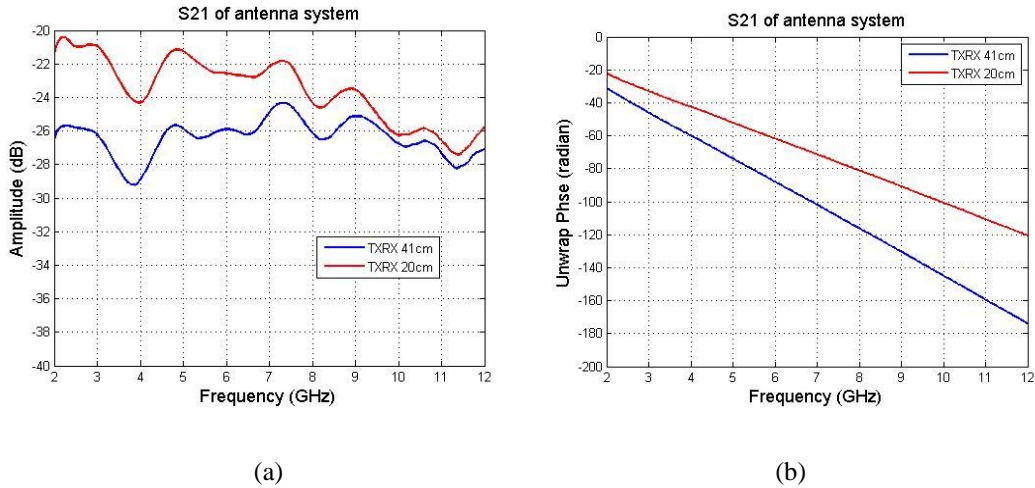


Figure 4-8 The measured S_{21} of the head-to-head antenna system; (a) the amplitude of S_{21} ; (b) the phase of S_{21} .

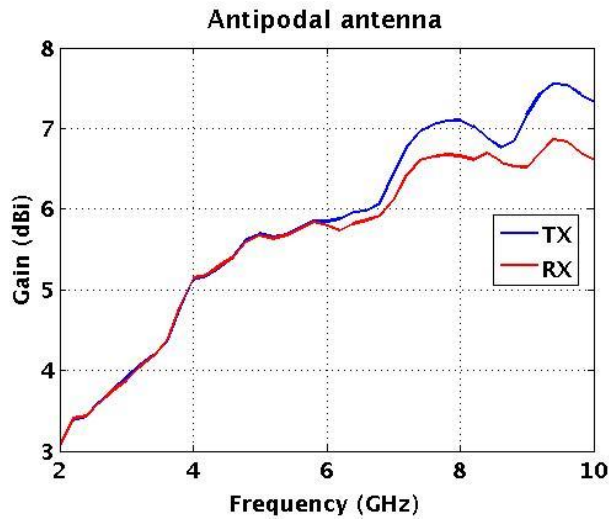


Figure 4-9 The simulated gain of Tx (blue) and Rx (red).

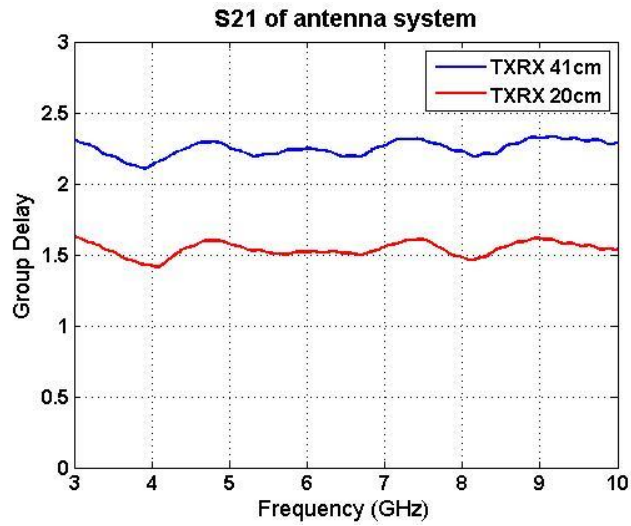
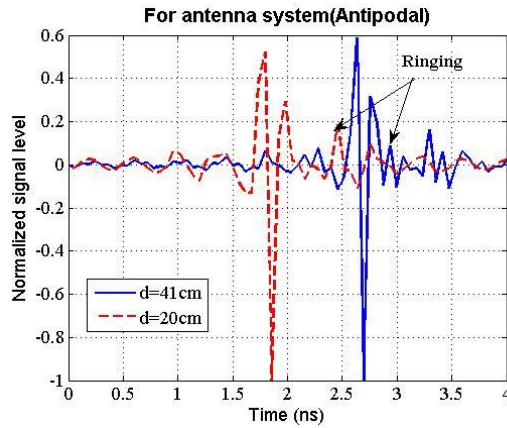
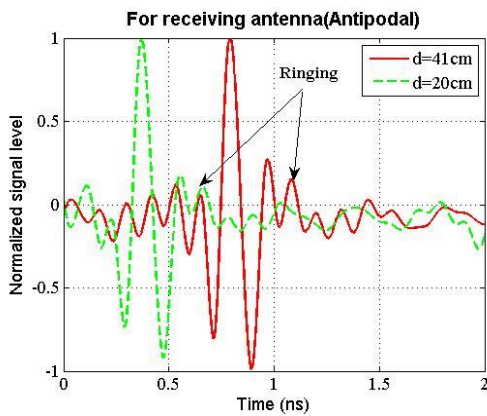


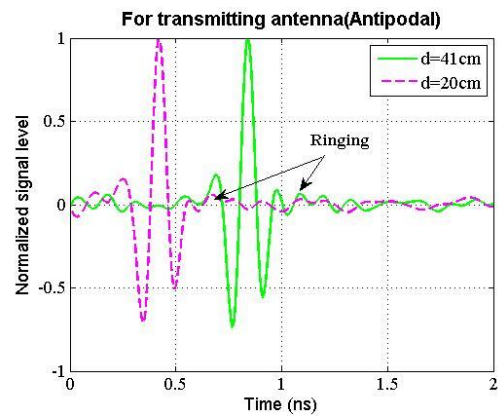
Figure 4-10 The group delay of the head-to-head antenna system for different distances between the two antennas.



(a)



(b)



(c)

Figure 4-11 The impulse responses for the head-to-head antenna system; (a) for the antenna system; (b) for the receiving antenna; (c) for the transmitting antenna.

4.2.3 Measurements for the circular-edge antipodal Vivaldi antenna

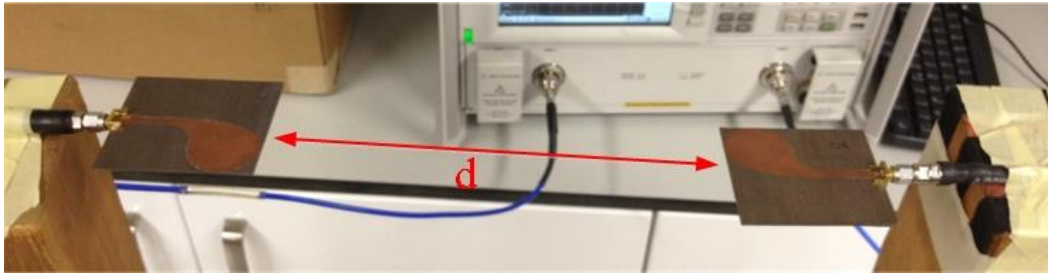


Figure 4-12 The measurement for the transmission of the two antennas (head-to-head).

In order to verify the simulated results for the impulse response, the measurement in the frequency domain of this antenna has been achieved using the vector network analyser (VNA). The measurement is set up as shown in Figure 4-12. Connect the two antennas to the two ports of the VNA, and then the transfer function S_{21} will be acquired. The distance d between the two antennas is chosen to be 20 cm and 41 cm respectively.

The measured amplitudes and phases of S_{21} for two head-to-head antennas separated by 20 cm (red) and 41 cm (blue) are plotted in Figure 4-13. The measured amplitudes in Figure 4-13 (a) (solid curves) match well with the simulated ones (dash curves) over the frequency band except the area around 9 GHz. In reality, the antennas are placed on the holder made of wood to complete the measurement. The influence between the holder and the antennas needs to be verified in CST software using the model shown in Figure 4-14. The permittivity of the wood ϵ_{wood} is chosen to be 2.5 [9]. The simulated S_{21} for this model is plotted in green and black dash curves in Figure 4-15. There is a drop down in the amplitude of S_{21} around 9 GHz, similar to the measured results. When checking the performance of gain, it is found that the gain of the antipodal Vivaldi antenna in the model with the wood has an obvious variation around 9 GHz, as plotted in Figure 4-16. As explained before, the amplitude of S_{21} will change according to the power of the antenna, which is related to the gain in terms of the equation (4-17). Therefore, the difference of the amplitude of S_{21} between the simulation and the measurement is related to the variation of gain introduced by the wood holder, which has been verified in the simulation.

The measured phases (solid curves) across UWB frequency range are linear and keep the same tendency with the simulated ones (dash curves) as shown in Figure 4-13 (b). They also vary a little around 9 GHz, which is in the same reason above.

The group delays derived from the measured phase of S_{21} are then plotted in Figure 4-17. This figure shows that the measured group delay (solid curves) matches well with the simulated result (dash curves) except the frequency around 9 GHz, which is related to the non-linear performance of the phase of S_{21} around 9 GHz.

The normalized impulse responses of the antenna system and the antenna itself are derived from the measured S_{21} , as shown in Figure 4-18. The measured impulse responses (solid curves) are in the same waveform shape as the simulated ones (dash curves). The ringing effect after the peak value of the impulse responses are also in the similar pattern with the simulated results.

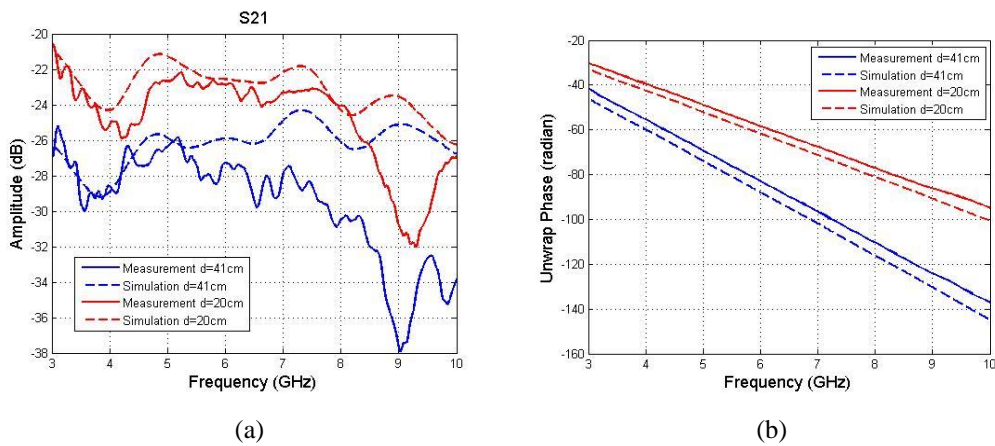


Figure 4-13 The measured (solid curves) S_{21} of the head-to-head antennas in the frequency domain compared with the simulated (dash curves) result for $d=41$ cm (blue) and $d=20$ cm (red); (a) Amplitude of S_{21} ; (b) Phase of S_{21} .

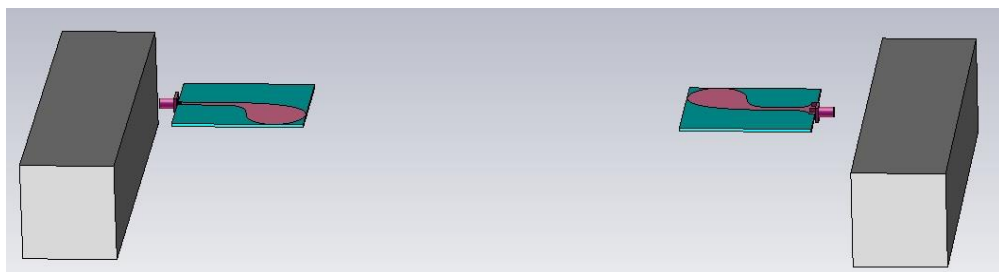


Figure 4-14 The simulated model with the wood behind each antenna in CST.

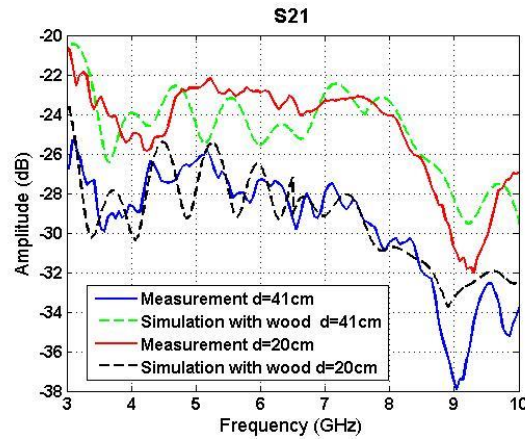


Figure 4-15 The simulated S_{11} for the model with the wood behind each antenna.

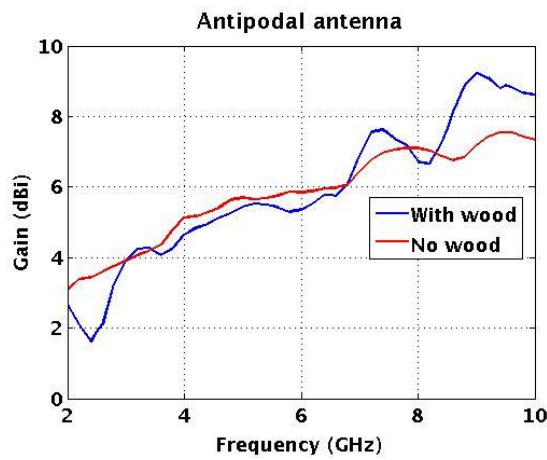


Figure 4-16 The simulated gain of the antipodal antenna in the models with and without woods.

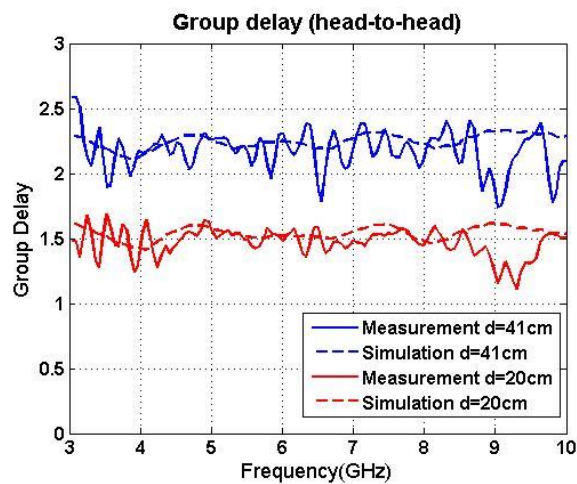


Figure 4-17 The measured (solid curves) and simulated (dash curves) group delay for the head-to-head antennas separated by 41 cm (blue) and 20 cm (red).

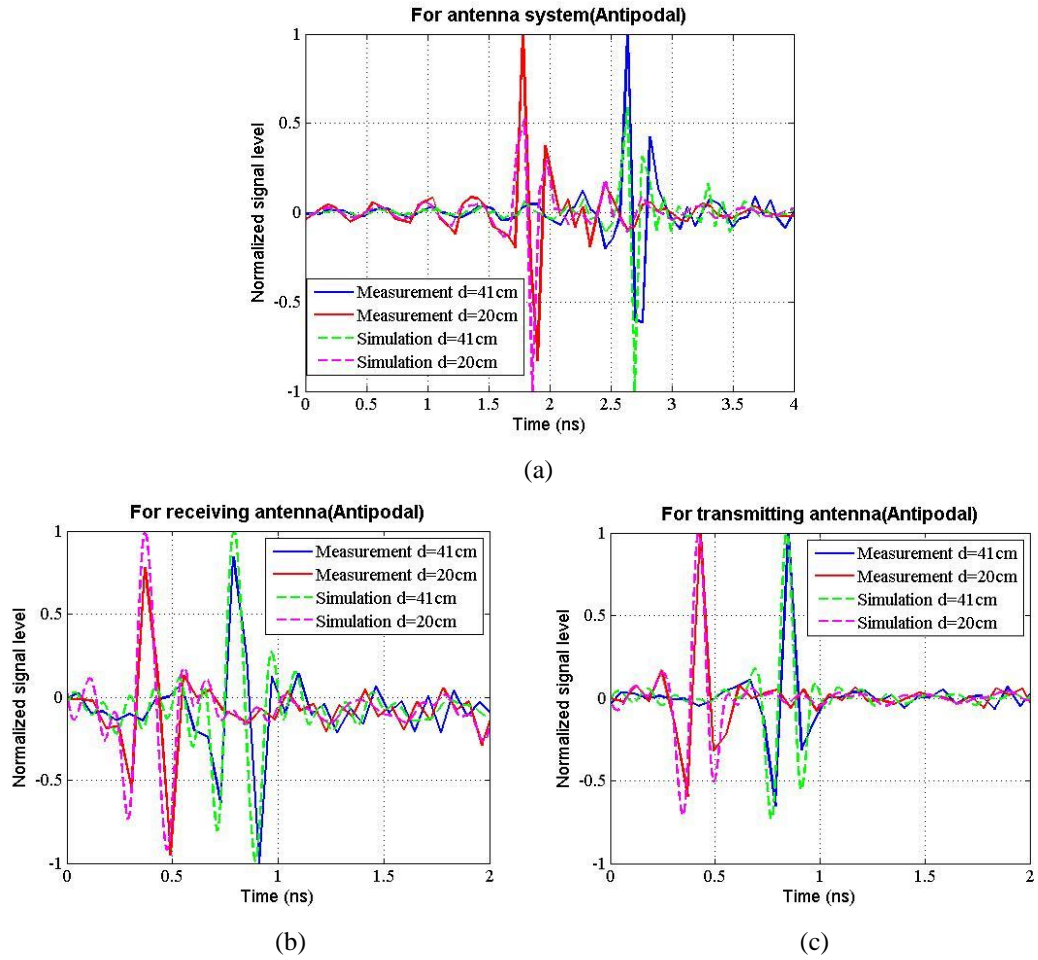


Figure 4-18 The impulse responses for the head-to-head antenna systems in situations of different distances between Tx and Rx; (a) for the antenna system; (b) for the receiving antenna; (c) for the transmitting antenna.

4.2.4 Impulse response of the corrugated balanced antipodal Vivaldi antenna

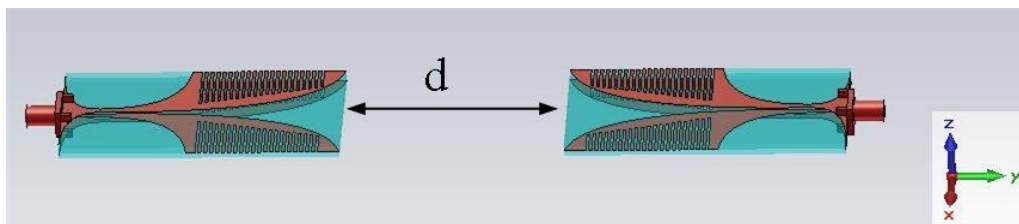


Figure 4-19 The model of the head-to-head antenna system using BAVA.

Similar to the simulation for the circular-edge antipodal Vivaldi antenna in section 4.2.2, the simulated model for the balanced antipodal Vivaldi antenna shown in Figure 4-19 is in the same head-to-head position. One of them is treated as the

transmitting antenna Tx and the other one is the receiving antenna Rx. The distance between them noted as d is chosen to have two different values for the purpose of model validation.

The simulated amplitudes of S_{21} are shown in Figure 4-20 (a). When the amplitude of the corrugated BAVA has a strong resonance over the certain frequency range, i.e. 3 GHz to 4.5 GHz and 7 GHz to 9 GHz, the gain varies obviously over the same frequency range, as shown in Figure 4-21.

The phases of S_{21} shown in Figure 4-20 (b) are linear from 3 GHz to 10 GHz, so that there is a weak variation in the group delay, as illustrated in Figure 4-22.

The normalized impulse responses of the corrugated BAVA and the system are shown in Figure 4-23. The solid curve in this figure represents the situation that the antennas are separated by 41 cm, while the dash curve is represented the one that they are separated by 20 cm. As well as the circular-edge antipodal Vivaldi antenna, due to the non-ideal constant group delay, the normalized impulse response of the corrugated BAVA also has ringing effect after the peak value of the impulse response.

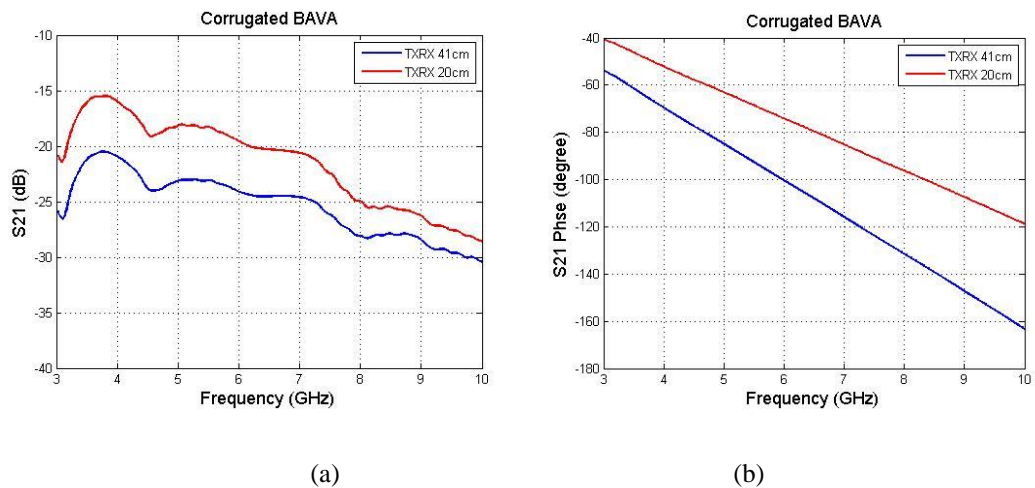


Figure 4-20 The transfer function of the antenna system in the frequency domain; (a) Amplitude of S_{21} ; (b) Phase of S_{21} .

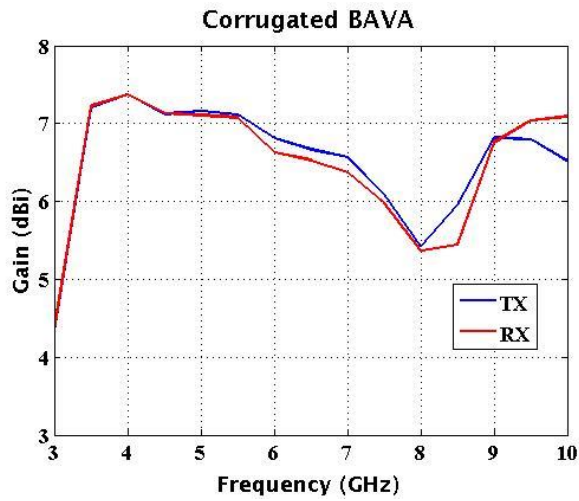


Figure 4-21 The simulated gain of Tx (blue) and Rx (red).

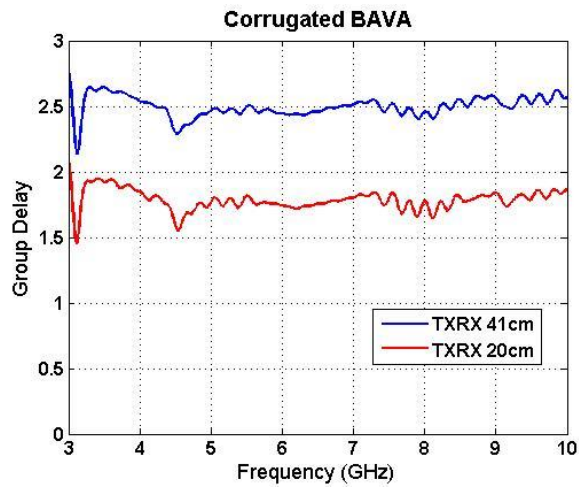
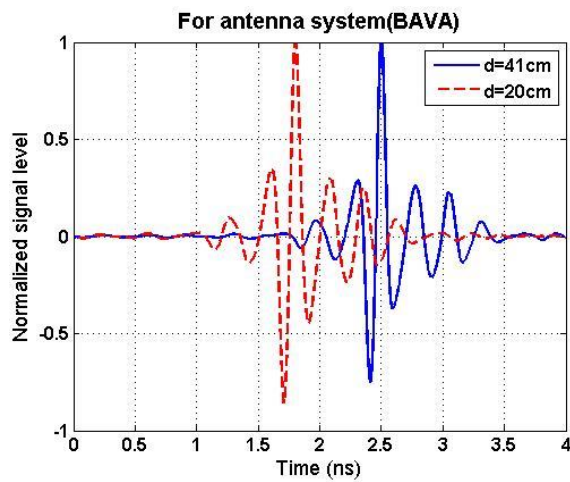


Figure 4-22 The group delay of the head-to-head antenna system when they are separated by 41 cm (blue) and 20 cm (red).



(a)

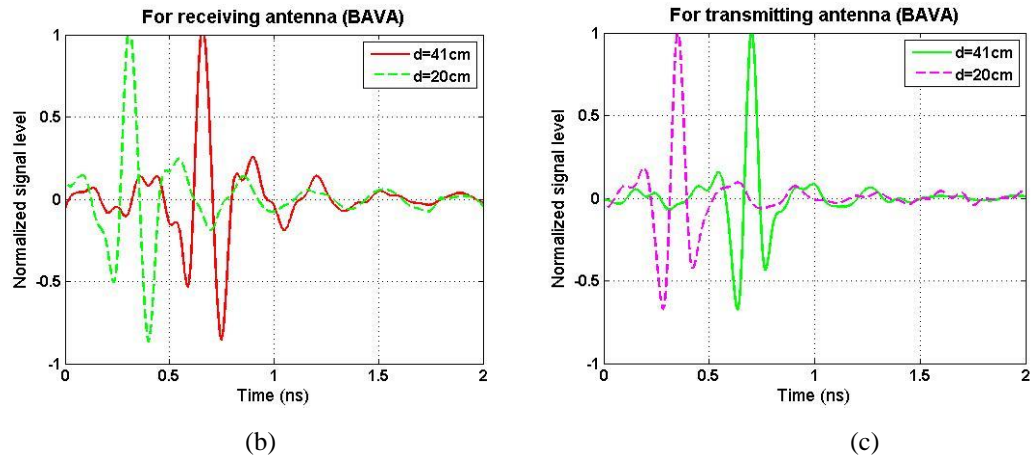


Figure 4-23 The impulse responses for the head-to-head antenna system; (a) for the antenna system; (b) for the receiving antenna; (c) for the transmitting antenna.

4.2.5 Measurements for the corrugated balanced antipodal Vivaldi antenna

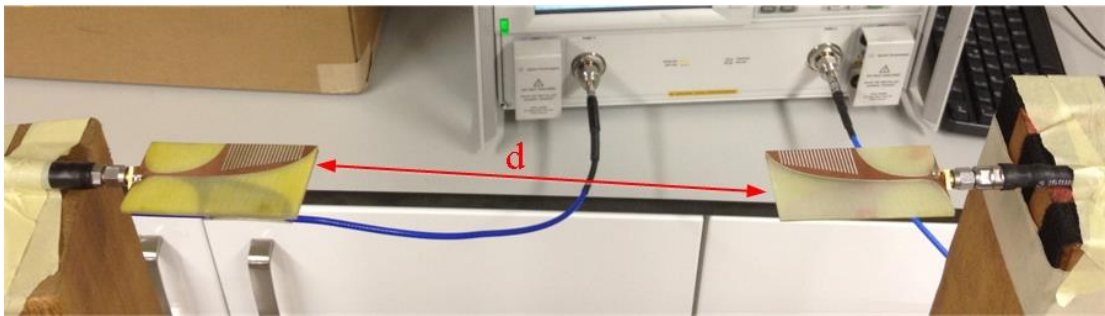


Figure 4-24 The measurement for the transmission of the two antennas (head-to-head).

The transfer function S_{21} for the corrugated BAVA has been measured in free space as shown in Figure 4-24. Same as the simulation, the distance d between the two antennas has also been set as two different values of 20 cm and 41 cm.

The measured amplitudes of S_{21} , which are shown as the solid curves in Figure 4-25 (a), match well with the simulated results (dash curves).

The measured phases of S_{21} are shown in Figure 4-25 (b) (solid curves) also keep the same tendency with the simulated results (dash curves). Both of the measured phases vary linearly across the most part of operating frequency band, except a kink at 5 GHz and 8 GHz, leading to obvious variations at these two frequency ranges in the group delay, as shown in Figure 4-26 (a). Compared with the measured result of the

circular-edge antipodal antenna, the group delay of the corrugated BAVA shows weaker oscillations over the whole frequency range, as known in Figure 4-26 (b).

The normalized impulse responses of the antenna system and the antenna itself are derived from the measured S_{21} , as shown in Figure 4-27. The solid curves are the calculated results from the measured data, while the dash curves are the one from the simulated data. It is noticed that the measured results match well with the simulated ones.

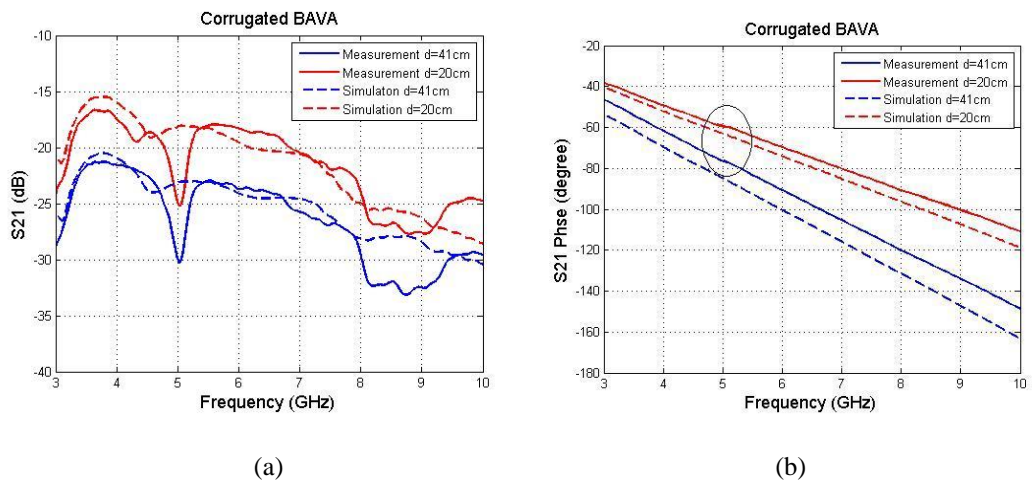


Figure 4-25 The measured S_{21} of the head-to-head antenna system in the frequency domain for different antenna spacing ranges; (a) Amplitude of S_{21} ; (b) Phase of S_{21} .

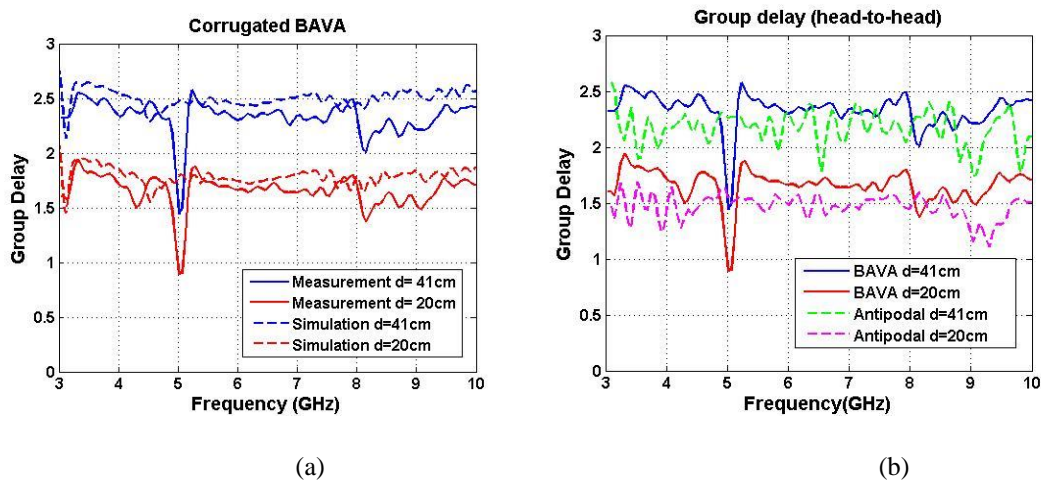


Figure 4-26 The measured group delay for the head-to-head antenna system; (a) the corrugated BAVA separated by 41 cm (blue solid curve) and 20 cm (red solid curve) compared with the simulated results (dash curves); (b) the comparison of the corrugated BAVA (solid curves) with the circular-edge antipodal antenna (dash curves).

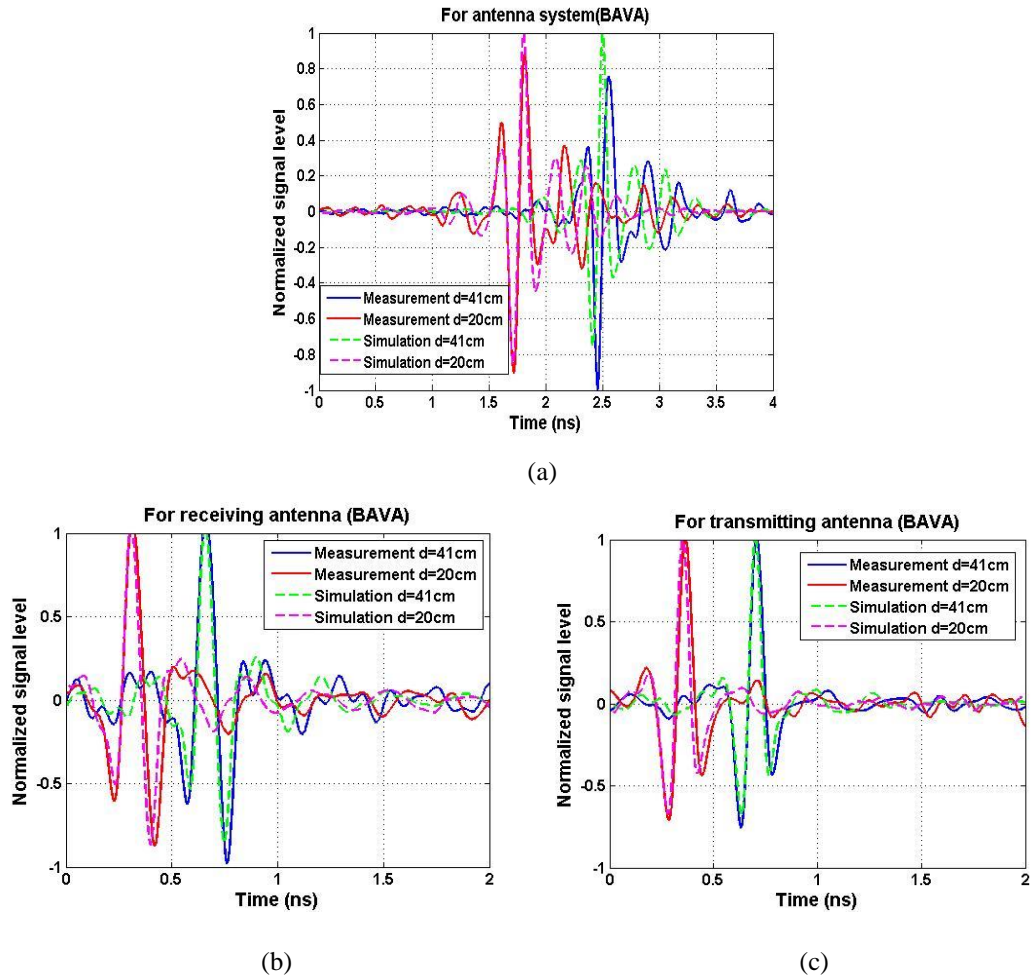


Figure 4-27 The measured impulse response for the head-to-head antenna system spacing at 41 cm (blue solid curve) and 20 cm (red solid curve) compared with simulated ones (dash curves); (a) for the antenna system; (b) for the receiving antenna; (c) for the transmitting antenna.

4.3 Fidelity analysis

4.3.1 Performances of current bow-tie antennas for GPR

In some imaging applications such as impulse GPR, the antenna needs to transmit the signal with minimal ringing effect, since such ringing effect may obstruct reflections from the targets. The commonly-used UWB antenna for short-range impulse GPR applications is resistively-loaded bow-tie antennas due to their relatively simple and practical geometry, as well as their ability to transmit UWB transient pulses properly.

The impulse GPR generally requires the antenna to have sufficient large bandwidth and a constant phase centre. The large bandwidth allows the UWB pulses with

suppressed ringing effect to avoid masking of targets, while the constant phase centre avoids widening of the pulse over time. In order to enlarge the bandwidth, the resistively-load structure is usually introduced to bow-tie antennas. For example, the modified bow-tie antenna developed in [10], had the ringing duration less than 0.6 ns (3 times the pulse duration). It set the potential limit of data rate at more than 1 Gbit/s.

But the resistively-load structure also introduces the disadvantage of low radiation efficiency. It has been indicated that antenna radiation efficiency might drop to as low as 30%, since a large portion of the energy supplied to the antenna was dissipated by the resistive load [11].

Meanwhile the ringing effect is also related to the distortion of the signal. Obviously, larger ringing effect makes the signal distorted in shape. In order to evaluate the amount of distortion introduced by the antenna to the radiated or received signals, the pulse fidelity is directly used to describe. As analysed in [12], the distortion of the signals transmitted by a bow-tie antenna and a Vivaldi antenna respectively has been investigated. Both of them showed a high pulse fidelity to the transmitted signal, which was above 0.8. The Vivaldi antenna developed in [13] had high peak value and short FWHM (Full Width at Half Maximum) (115 ps) of the transient responses envelope. The research work in [14] explained that the Vivaldi antenna had constant phase centre in E-plane, which would lead less dispersion of the signal in the time domain. Thus, it has been verified that the Vivaldi antenna is well suitable for the transmission of good pulses.

In this project, the transmitting and received signals are desired to maintain their original shapes. Therefore, the following analysis is focused on the pulse fidelity for different signals transmitted by the circular-edge antipodal Vivaldi antenna and the corrugated balanced antipodal Vivaldi antenna which are designed for the imaging system.

4.3.2 Fundamental analysis

The mathematical basis for the correlation analysis in the time domain is given below.

When analysing the signal's performance, the pulse fidelity F is used to quantify the variation of the output signal $s_2(t)$ with respect to a reference signal, e.g. the input signal $s_1(t)$. It is the maximum correlation value with the normalized output signal $s_2(t)$ and the input signal $s_1(t)$, mathematically expressed as (4-23) [15].

$$F = \max_{\tau} \left[\frac{\int_{-\infty}^{+\infty} s_1(t) s_2(t + \tau) dt}{\sqrt{\int_{-\infty}^{+\infty} s_1^2(t) dt} \sqrt{\int_{-\infty}^{+\infty} s_2^2(t) dt}} \right] \quad (4-23)$$

Where τ is the time delay between the two signals.

Consequently, from this expression, it can be inferred that when pulse fidelity between the two signals has its maximum value, the minimum distortion will be obtained.

In section 4.1, different pulses have been analysed in terms of the UWB's frequency band regulation. In the following sections, different pulses are transmitted to the antenna system to evaluate the characteristics of the antenna, assessing the distortion of the received signal in the simple UWB antenna system.

4.3.3 The results for the circular-edge antipodal Vivaldi antenna

The simulated model of the head-to-head antenna system shown in Figure 4-7 is still used to evaluate the pulse fidelity in the antenna system. Four different pulses are fed to the transmitting antenna, which are Gaussian pulse (pulse parameter $b = 40ps$), modulated Gaussian pulse $f_{m1}(t)$ (pulse parameter $b = 250ps$), modulated Gaussian pulse $f_{m2}(t)$ (pulse parameter $b = 350ps$) and modulated rectangular signal.

When a broadband impulse is fed to a less broadband antenna, the effect of the antenna band-pass filtering will add zero-crossing or lobes to the waveform. This yields a signal waveform qualitatively similar to differentiations of the original signal. When it is fed by Gaussian pulse, the normalised received signal from Rx as shown in Figure 4-28 (a) is distorted a lot compared with the input one. The normalised received signal filtered by the antenna is more like the second order of Gaussian pulse, the one that is generated in Matlab and plotted in green curve in Figure 4-28 (b). Besides the band-pass filtering, the received signal also has ringing effect introduced by the antenna.

When the excitation signal fits within the antenna bandwidth, the received signal will suffer less antenna's filtering effect as well as attenuation and ringing effect to the signal. As shown in Figure 4-4 (b), the modulated Gaussian pulse is more compatible with the antenna's bandwidth. So when it is fed to the antenna, the distortion to received signal is not too much. The normalised received signals from Rx when fed by the modulated Gaussian pulses ($b=250$ ps and $b=350$ ps) are respectively shown in Figure 4-29 (a) and Figure 4-30 (a). They are in the same envelope as the first-order of corresponding input signals generated in Matlab, which are plotted as the green curves in Figure 4-29 (b) and Figure 4-30 (b).

As seen from Figure 4-5 (b), the modulated rectangular signal is less broadband than the antipodal antenna. When it is fed to Tx, the normalised received signal from Rx, shown in Figure 4-31 (a) also suffers one differentiation. It is in the same envelope as the first-order of the modulated rectangular signal generated in Matlab, as shown in Figure 4-31 (b). The ringing effect is introduced by the antenna.

When transmitting these four pulses, the pulse fidelities of the received signals in the antenna system are listed in Table 4-1. It is known that when fed by the modulated Gaussian pulse, the pulse fidelity is obviously higher than the one fed by Gaussian pulse. When the frequency bandwidth of the signal is more compatible with the antenna's operating frequency band, the fidelity is becoming higher. This is the reason why the fidelity of the modulated Gaussian pulse ($b=350$ ps) is better than the one of pulse parameter ($b=250$ ps). Although the fidelity of the modulated rectangular signal is not as high as the modulated Gaussian pulse, it is still as good as

0.92. In this case, the circular-edge antipodal Vivaldi antenna will not distort the signal much so that it is suitable for the time domain imaging application.

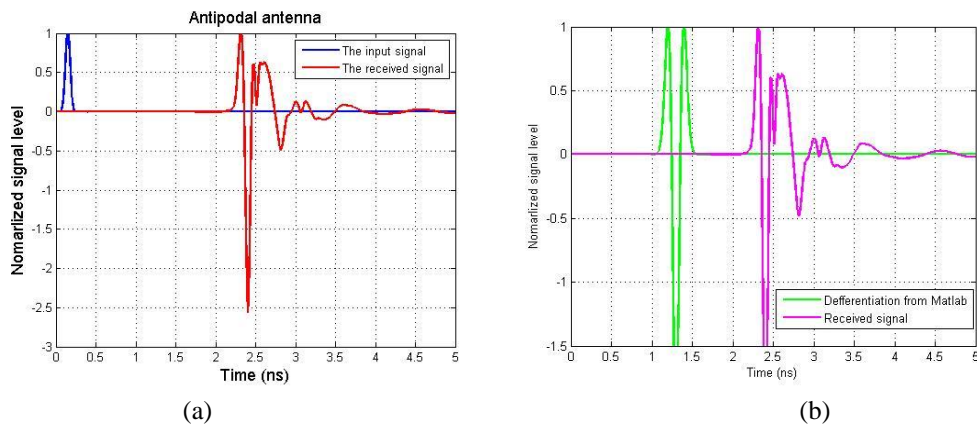


Figure 4-28 The comparison of the signals; (a) the input Gaussian pulse VS the received signal; (b) the double differentiation of Gaussian pulse from Matlab VS the received signal from the antenna.

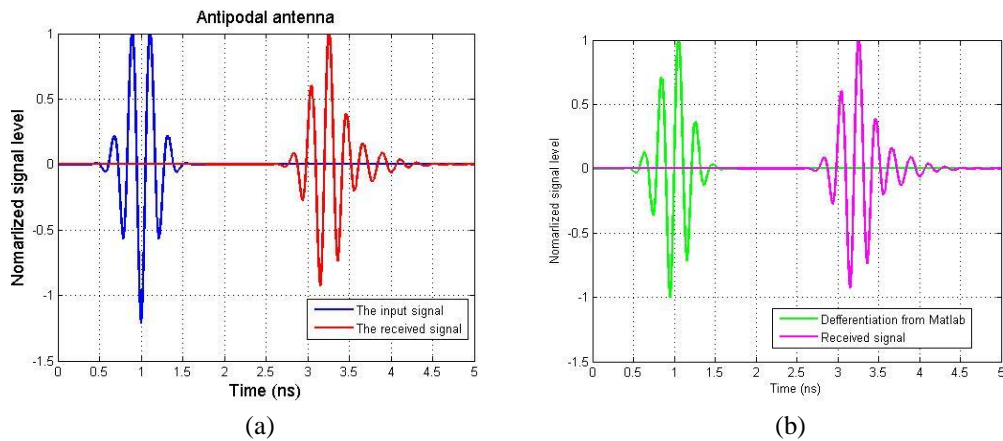


Figure 4-29 The comparison of the signals; (a) the input Modulated Gaussian pulse ($b=250\text{ps}$) VS the received signal; (b) the First-order of Modulated Gaussian pulse ($b=250\text{ps}$) from Matlab VS the received signal from the antenna.

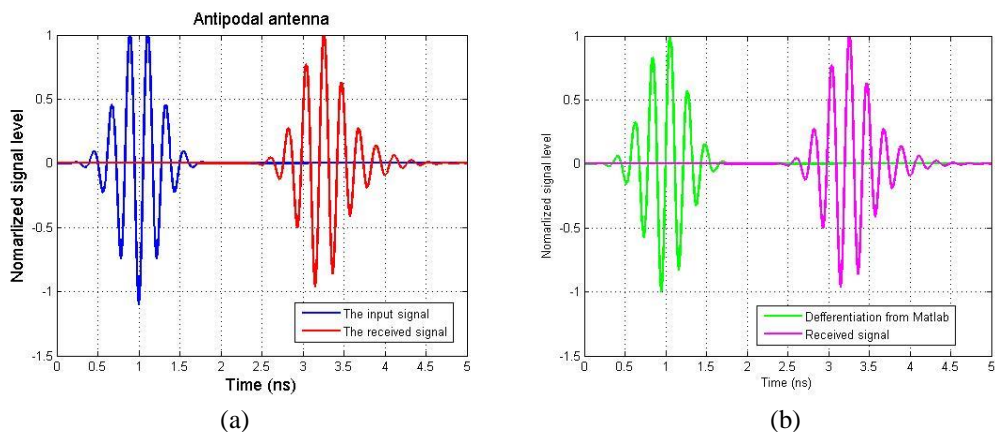


Figure 4-30 The comparison of the signals; (a) the input Modulated Gaussian pulse ($b=350\text{ps}$) VS the received signal; (b) the First-order of Modulated Gaussian pulse ($b=350\text{ps}$) from Matlab VS the received signal from the antenna.

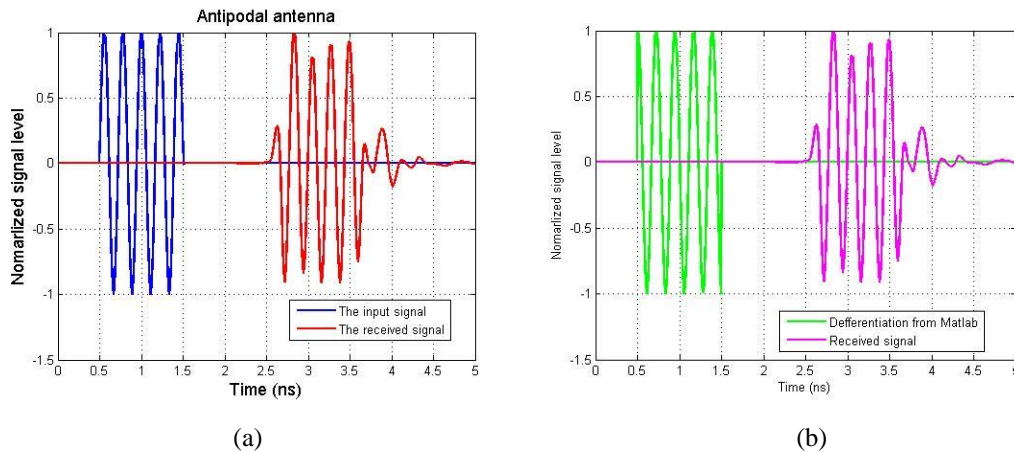


Figure 4-31 The comparison of the signals; (a) the input modulated rectangular signal VS the received signal; (b) the First-order of the modulated rectangular signal from Matlab VS the received signal from the antenna.

4.3.4 The results for the corrugated balanced antipodal Vivaldi antenna

Distortion to the received signal introduced by the corrugated BAVA will be discussed in this section. The antenna system is the same model shown in Figure 4-19. Similar to the analysis in the previous section, four different pulses are fed to the antenna.

When a Gaussian pulse is fed to the antenna, the normalised signal received by the corrugated BAVA is plotted in Figure 4-32 (a). As the same explanation in section 4.3.3, the received signal suffers antenna's band-pass filtering, attenuation and ringing effect. The corrugated BAVA antenna system filters the received signal more like the third-order of Gaussian pulse, as shown in Figure 4-32 (b).

When the modulated Gaussian pulses with different pulse parameters are fed to the BAVA, the signals received from Rx, as shown in Figure 4-33 (a) and Figure 4-34 (a), suffer less distortion because the bandwidth of them matches with the bandwidth of the BAVA better than the Gaussian pulse. They are more like the inversed first-order of Gaussian pulse, as plotted in the green curve in Figure 4-33 (b) and Figure 4-34 (b).

When the modulated rectangular signal is fed to the BAVA, the normalised received signal from Rx as shown in Figure 4-35 (a) also suffers the band-pass filtering and

ringing effect. The received signal is in the same envelope as the inversed first-order of the modulated rectangular signal, shown as the green curve in Figure 4-35 (b).

The pulse fidelities of the received signals in the system of the corrugated BAVA are listed in Table 4-1. The tendency of the pulse fidelity for each antenna is the same when fed by different pulses. Among the different types of the input signals, the modulated signal is obviously better than the normal Gaussian pulse. The pulse fidelity for the modulated ones is higher than 90%. When using the same input signal, compared two types of antennas, the corrugated BAVA is a little better than the antipodal one. When using the modulated rectangular signal, the pulse fidelity of the BAVA is up to 94.7%, which is sufficient for the imaging application.

In general, the distortion to the signal introduced by the antenna's band-pass filtering does not hold a fixed form (derivative, double derivative, etc.). It is dependent on several parameters including the antenna geometry, antenna's polarization matching, the gain and so on [16]. The pulse fidelity drops with larger variations of the gain. It has already been investigated that the corrugated BAVA is more flat in gain than the antipodal one over the operating frequency range. Thus it will produce less distortion to the received signals. This feature makes the corrugated BAVA more suitable for the UWB imaging system.

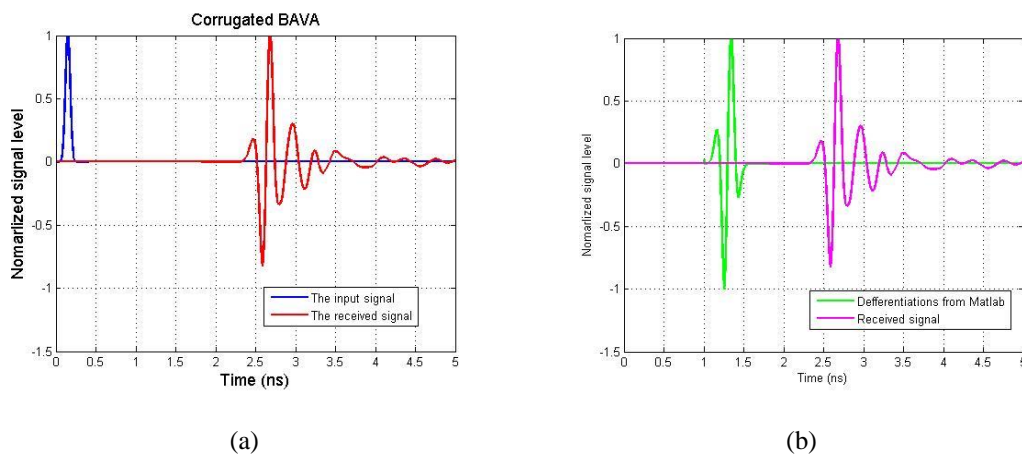


Figure 4-32 The comparison of the signals; (a) the input Gaussian pulse VS the received signal; (b) the Third-order of Gaussian pulse from Matlab VS the received signal from the antenna.

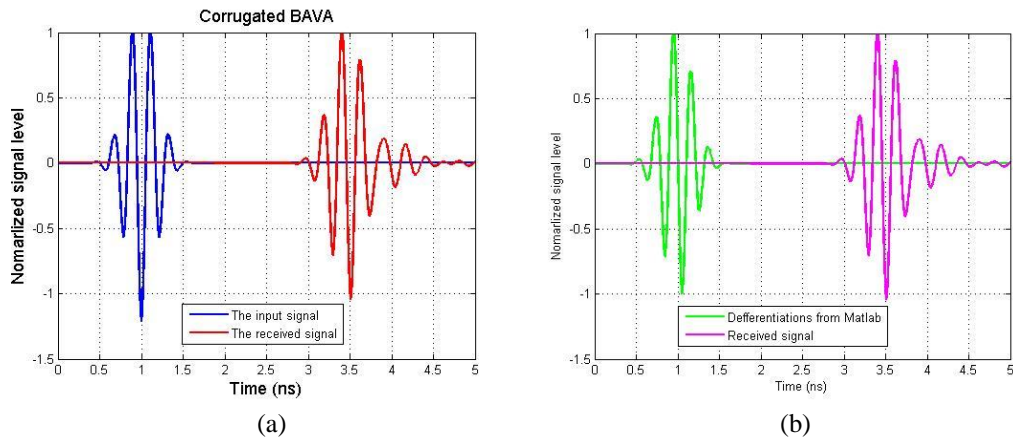


Figure 4-33 The comparison of the signals; (a) the input modulated Gaussian pulse ($b=250\text{ps}$) VS the received signal; (b) the inversed first-order of Modulated Gaussian pulse ($b=250\text{ps}$) from Matlab VS the received signal from the antenna.

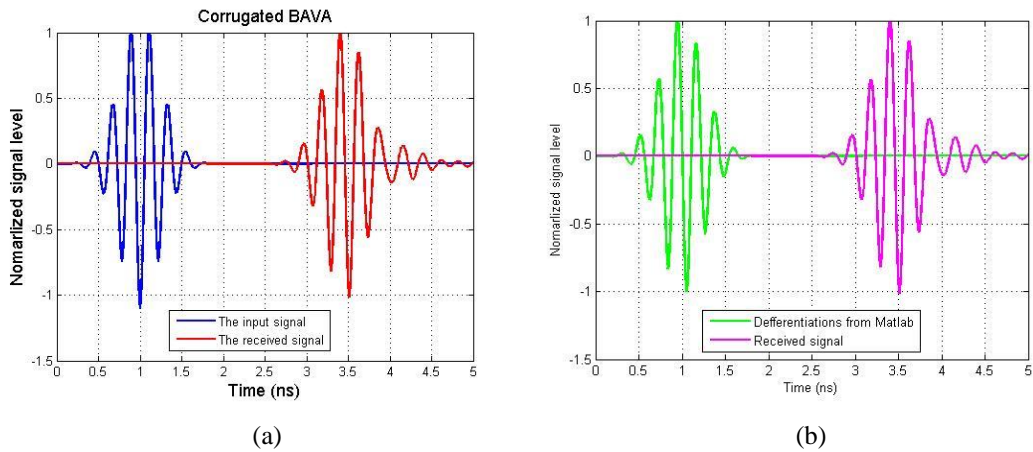


Figure 4-34 The comparison of the signals; (a) the input modulated Gaussian pulse ($b=350\text{ps}$) VS the received signal; (b) the inversed first-order of Modulated Gaussian pulse ($b=350\text{ps}$) from Matlab VS the received signal from the antenna.

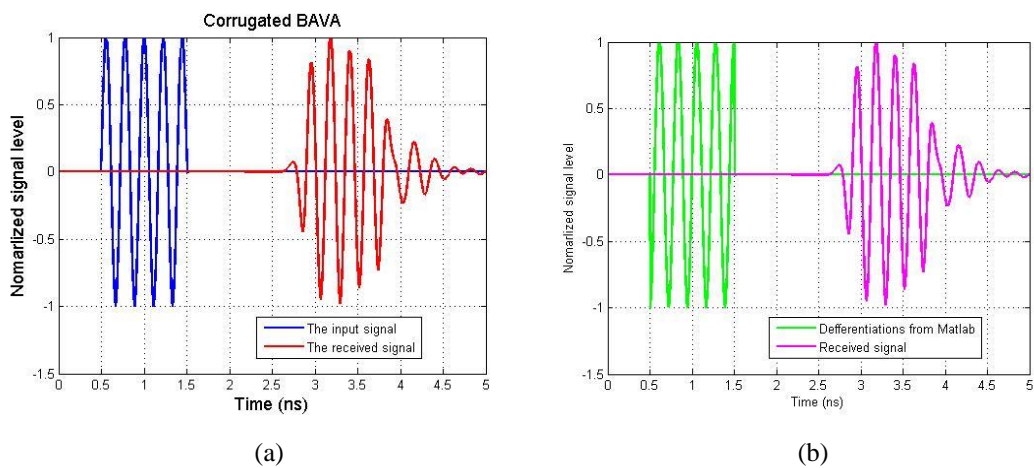


Figure 4-35 The comparison of the signals; (a) the input modulated rectangular signal VS the received signal; (b) the inversed first-order of the modulated rectangular signal from Matlab VS the received signal from the antenna.

Table 4-1 The pulse fidelity of the received signals for different antennas and different input signals

	Gaussian pulse ($b=40\text{ps}$)	Modulated pulse ($b=250\text{ps}$)	Modulated pulse ($b=350\text{ps}$)	Modulated rectangular signal
Circular-edge antipodal Vivaldi antenna	0.324	0.943	0.961	0.920
Corrugated balanced antipodal Vivaldi antenna	0.612	0.959	0.966	0.947

4.4 Summary

This chapter has mainly described the time domain characteristics of the antennas and the antenna system, including the impulse response and the pulse fidelity. Considering transmitting different types of the signals to the antennas, the modulated ones are better in pulse fidelity to the normal Gaussian pulse. Compared with the two antennas, the corrugated balanced antipodal Vivaldi antenna is more suitable for the UWB imaging system since it has shown better characteristics in pulse fidelity than the circular-edge antipodal Vivaldi antenna.

Reference

- [1] A.H. Mohammadian, A. Rajkotia, S.S. Soliman, "Characterization of UWB Transmit-Receive Antenna System", *IEEE Conference on Ultra Wideband Systems and Technologies*, pp. 157-161, 2003.
- [2] J. Kunisch, J. Pamp, "Considerations Regarding the Correlation between Transmit and Receive Response of UWB Antennas", *Proc. URSI EMT-S, Pisa, Italy*, 2004.

- [3] X. Qing, Z.N. Chen, M.Y.W. Chia, "Network Approach to UWB Antenna Transfer Functions Characterization", *2005 European Microwave Conference*, vol. 3, 2005.
- [4] S. Promwong, W. Hachitani, J.-I. Takada, "Free Space Link Budget Evaluation of UWB-IR Systems", *2004 International Workshop on Joint UWBST&IWUWBS*, Page(s): 312-316, 2004.
- [5] C. Balanis, *Antenna Theory Analysis and Design*, © 2005, by John Wiley & Sons, INC, 2005.
- [6] L. Guo, "Study and Miniaturisation of Antennas for Ultra Wideband Communication Systems", *Thesis for the degree of Doctor of Philosophy*, Queen Mary, University of London, 2009.
- [7] W. Wiesbeck, "Basic Properties and Design Principles of UWB Antennas", *Proceedings of the IEEE*, Vol. 97, No. 2, Page(s): 372-385, February 2009.
- [8] G. Quintero, J.-F. Zurcher, Anja K. Skrivervik, "System Fidelity Factor: A New Method for Comparing UWB Antennas", *IEEE Transactions on Antennas and Propagation*, Vol. 59, Issue. 7, Page(s): 2502-2512, July 2011.
- [9] G. Brodie, B.M. Ahmed, Mohan V. Jacob, "Detection of decay in wood using microwave characterization", *2011 Aisa-Pacific Microwave Conference Proceedings (APMC)*, Page(s): 1754-1757. 2011.
- [10] A.A. Lestari, A.G. Yarovoy, L.P. Ligthart, E.T. Rahardjo, "A UWB Antenna for Impulse Radio", *IEEE 63rd Vehicular Technology Conference 2006. VTC 2006-Spring*. Vol: 6, Page(s): 2630-2634, 2006.
- [11] A.A. Lestari, Y.A. Kirana, A.B. Suksmono, A. Kurniawan, E. Bharata, A.G. Yarovo, L.P. Ligthart, "Compact UWB radiator for short-range GPR applications", *Proceedings of the Tenth International Conference on Ground Penetrating Radar, 2004. GPR 2004*, Page(s): 141-144, 2004.

- [12] E. Pancera, T. Zwick, W. Wiesbeck, "Spherical Fidelity Patterns of UWB Antennas", *IEEE Transactions on Antennas and Propagation*, Vol: 59, Issue: 6, Part:2, Page(s): 2111-2119, 2011.
- [13] W. Sorgel, C. Waldschmidt, W. Wiesbeck, "Transient Responses of a Vivaldi Antenna and a Logarithmic Periodic Dipole Array for Ultra Wideband Communication", *Antennas and Propagation Society International Symposium*, Vol. 3, Page(s): 592-595, 2003.
- [14] Q. Wu, Q.S. Jin, L. Bian, Y.M. Wu, L.W. li, "An approach to the determination of the phase centre of Vivaldi-based UWB antenna", *IEEE Antennas and Propagation Society International Symposium 2006*, Page(s): 563-566, 2006.
- [15] D. Lamensdorf, L. Susman, "Baseband-pulse-antenna techniques", *IEEE Antennas and Propagation Magazine*, vol. 36, Issue. 1, Page(s): 20-30, Feb. 1994.
- [16] D.H. Kwon, "Effect of Antenna Gain and Group Delay Variations on Pulse-Preserving Capabilities of Ultrawideband Antennas", *IEEE Transactions on Antennas and Propagation*, Vol: 54, Issue: 8, Page(s): 2208-2215, 2006.

Chapter 5 UWB Imaging System

UWB technology has been widely used for communications, localization and imaging applications. Among them, “See-through” microwave imaging has gained much more attention in the past decades due to its varied applications. For instance, “See-through” the human tissue enables doctors to detect tumors; “See-through” the wall allows security team or police force to deal with unconventional scenarios; “See-through” bags and luggage can help airport and railway staff to distinguish the contraband from permitted items. This project is mainly focused on detecting and imaging of metallic targets concealed in bag.

In this chapter, reflections in the imaging application for targets concealed in bag will be presented in the beginning. Then, the link budget will be calculated to demonstrate the possibility of the proposed UWB imaging system. The construction of the UWB microwave imaging system based on time domain will be illustrated next. The rotating antenna array can greatly enhance the performance of the system, which will be described in detail in this section. Lastly, a two-dimensional image reconstruction method based on DAS (Delay and Sum) algorithm will be discussed in theory.

5.1 Reflections in UWB bag imaging application

As UWB signals propagate through the opaque material, they suffer multiple reflections and the material absorption. So when it comes to “see-through” the bag application, it needs to deal with multi-path reflections, obstructions and antenna effects to avoid severe attenuation and dispersion.

First to mention is the multi-path reflection effect. In general, UWB signals are inherently immune from multi-path effect. However, when the transmitter and the receiver are very close to the obstacle, the multi-path reflection can overlap the received signal, reducing the localization capability of the system [1].

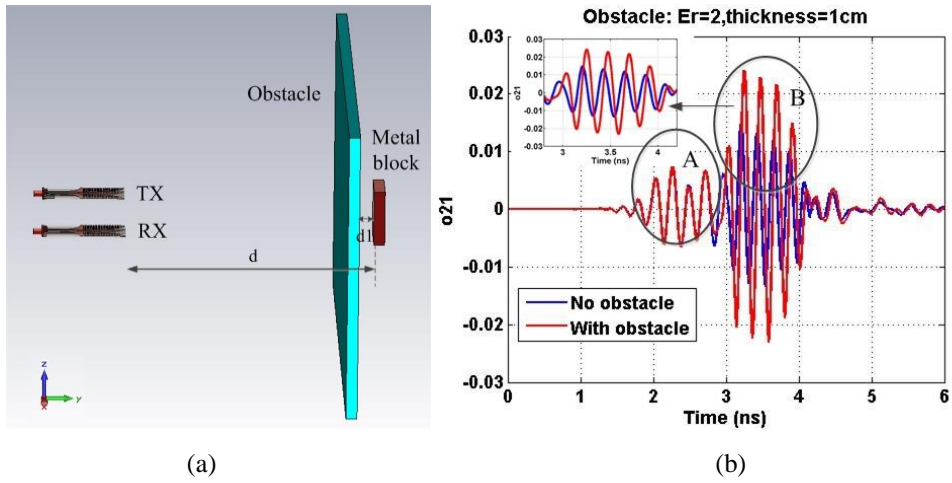
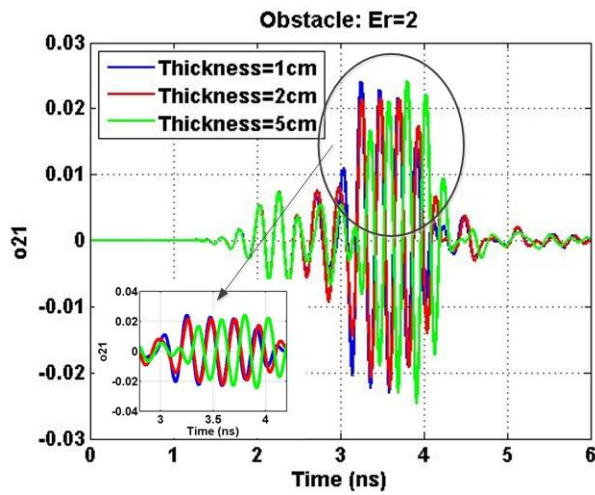
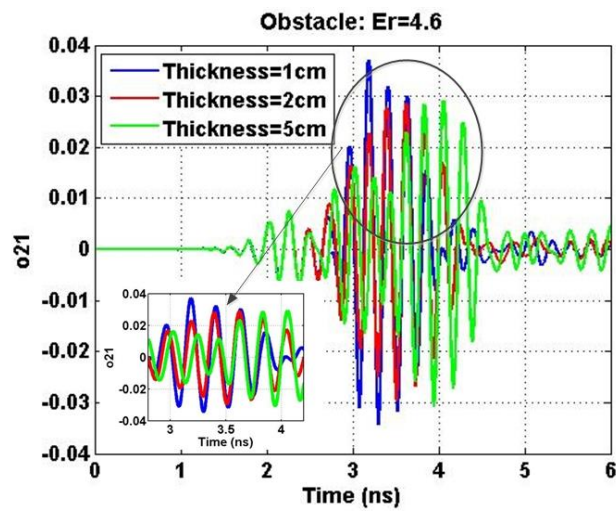


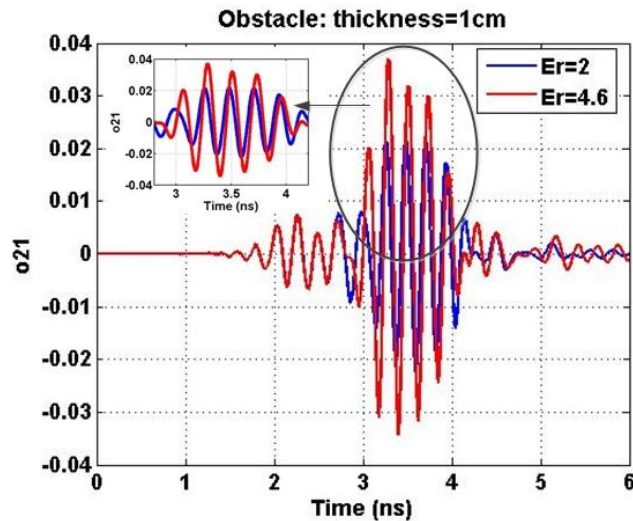
Figure 5-1 The effect on the received signal introduced by the obstacle; (a) the simulation model in CST; (b) the received signals from Rx without (blue) and with (red) the obstacle.



(a)



(b)



(c)

Figure 5-2 The effect on the received signal introduced by obstacles; (a) Permittivity=2, thickness is chosen to be 1 cm , 2 cm and 5 cm; (b) Permittivity=4.6, thickness is chosen to be 1 cm , 2 cm and 5 cm; (c) Thickness=1 cm, permittivity is chosen to be 2 and 4.6.

Apart from multiple reflections, the obstacle may also affect the signal energy level. In order to investigate the cause and extent of this influence, a model is built up as shown in Figure 5-1 (a), including two side-by-side corrugated balanced antipodal Vivaldi antennas, one obstacle and one metallic target. The modulated rectangular signal is deployed because of its ease of sensitivity and less distortion caused by the antennas. The spacing between Tx and Rx is about 11.5 cm. The obstacle is with the size of 52 cm (width) \times 26 cm (height) \times D cm (thickness) (D is adjustable), while the metallic target is with the size of 5 cm (width) \times 5 cm (height) \times 1 cm (thickness). The metallic target is 20 cm ($d=20$) away from the antennas, and 2 cm ($d1=2$) away from the obstacle. Different thicknesses and permittivities of the obstacle are applied in the simulation.

The received signals from Rx with and without the obstacle are plotted in Figure 5-1 (b). The first bunch of fluctuation noted as signal A is the signal directly transmitted from Tx to Rx, and the second fluctuation of signal B is the received signal which is reflected from the metallic target. Signal B is the one which would be analysed in the signal processing unit. The blue solid line is the received signal when there is no obstacle in the model, while the red one is the received signal when there is an obstacle in the model. The thickness of the obstacle is 1 cm ($D=1$) and its relative

permittivity is 2 ($\epsilon_r=2$). The obstacle introduces the time delay to the reflected signal, as well as multi-reflections, which increases the amplitude of the signal, as shown in Figure 5-1 (b).

The thickness of the obstacle is now under investigation. The received signals which are reflected from the metallic targets are plotted in Figure 5-2 (a) and Figure 5-2 (b). There are three different values for the thickness of the obstacle used in the simulation, which are set to be $D=1$ cm, $D=2$ cm and $D=5$ cm respectively. When the permittivity of the obstacle is 2, the increase of the thickness of the obstacle causes little delay in time and attenuation in amplitude of the reflected signal, which are plotted in Figure 5-2 (a). The same effect can be observed when the permittivity of the obstacle is increased to 4.6, as shown in Figure 5-2 (b).

By fixing the thickness of the obstacle, the change of the permittivity can also have great impact on the transmission of the signal. Higher permittivity causes stronger reflection and more ringing effect to the received signal, as shown in Figure 5-2 (c).

Another challenge in UWB imaging system is the antenna design. The radiation pattern, directivity and time domain characteristics of the chosen antenna would directly affect the final imaging results. The antenna with a high directivity and a narrow beam width can focus the energy on the direction of the target so as to reduce the multi-path effect. Besides, it should also own excellent time domain characteristics against any possible distortion to the signal, especially in the time domain imaging system.

In conclusion, all the underlying problems are needed to be taken into account when implementing the proposed UWB imaging system.

5.2 Link budget

As explained in Chapter 3 and Chapter 4, the corrugated BAVA is considered to be the antenna element for the proposed UWB imaging system. According to the equation (5-1), the far field region R_{far} of the corrugated BAVA is more than 3.2 cm. Because the proposed UWB imaging system is designed for bag imaging, it scans the bag at a certain distance more than 10 cm. So it is a far-field imaging system.

$$R_{far} = \frac{2D^2}{\lambda} \quad (5-1)$$

Where D is the linear dimension of BAVA. λ is the wavelength of 3 GHz.

The theoretical link budget has been discussed to investigate the relationship between the antenna gain and SNR , in order to demonstrate the practicability of the proposed UWB imaging system.

According to the Radar equation [2], the received power of the signal at the receiving end P_r and the Signal-to-Noise Ratio SNR can be expressed respectively by equation (5-2) and (5-3).

$$P_r = \frac{P_t G_t G_r \sigma \lambda^2}{(4\pi)^3 R^4 L_s} \quad (5-2)$$

$$SNR = \frac{P_r}{N} = \frac{P_t G_t G_r \sigma \lambda^2}{(4\pi)^3 R^4 k T_0 F B L_s} \quad (5-3)$$

Where, P_t is the transmitting power. G_t and G_r are the gain of the transmitting and receiving antennas respectively. σ is the Radar Cross Section. λ is the wavelength of the electromagnetic wave. R is the distance between Tx and Rx. $k = 1.38 \times 10^{-23} JK^{-1}$ is Boltzmann's constant. T_0 is the system temperature, generally which is 290K. F is the noise figure, usually assumed as $F = 3dB$ [2]. B is the bandwidth of the signal. L_s is the loss through the whole system. Thus, the thermal noise floor is $-84 dBm (kT_0B)$.

Radar cross section σ is different according to the shape of the target. In terms of the definition and summary in [2], for the square flat plate target, σ is given by

$$\sigma = \frac{4\pi A^2}{\lambda^2}. \text{ Here, } A \text{ is the surface area of the target and } \lambda \text{ is the wavelength.}$$

Thus, substituting σ into equation (5-2) and equation (5-3), they can be rewritten in

$$P_r = \frac{P_t G_t G_r A^2}{(4\pi)^2 R^4 L_s} \quad (5-4)$$

$$SNR = \frac{P_t G_t G_r A^2}{(4\pi)^2 R^4 k T_0 FBL_s} \quad (5-5)$$

As discussed in Chapter 4, the antenna would introduce the distortion to the signal in shape and the attenuation in amplitude. In order to find out the approximate loss to the received signal introduced by the corrugated BAVA, a model of one metallic target placed behind an obstacle is simulated in CST Microwave Studio which is shown in Figure 5-3.

There is one transmitting antenna (Tx), one receiving antenna (Rx), one obstacle and one metallic target in this model. Both of Tx and Rx use the corrugated BAVA, which is the type used in the proposed UWB imaging system. Practically, there are four receiving antennas placed as a straight arm, but they work independently. In this case, only one receiving antenna is studied here in order to investigate the performance of the system. The distance between Tx and Rx in the model is 11.5 cm, which is the same with the practical one between Tx and the closest Rx in the UWB imaging system. The obstacle with the size of 52 cm (width) \times 26 cm (height) \times D cm (thickness) (D is adjustable), keeps the same as the front surface of the practical bag used in the imaging application, which will be described in Chapter 6. The permittivity of the obstacle is assumed as 2, which is also determined according to the material of the practical bag used in the measurements. The metallic target with the size of 5 cm (width) \times 5 cm (height) \times 1 cm (thickness) is one of the targets concealed in bag. In the simulations, it is placed behind the obstacle, which is equivalent to the practical situations. The spacing between the antenna line and the target d is 20 cm, while the distance between the obstacle and the target d_1 is 2 cm. It is one of the situations in the practical measurements.

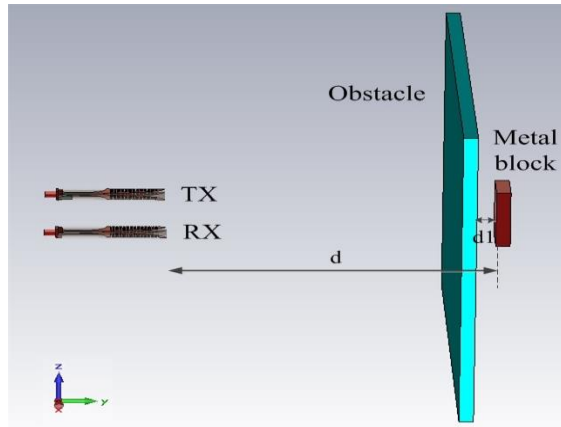
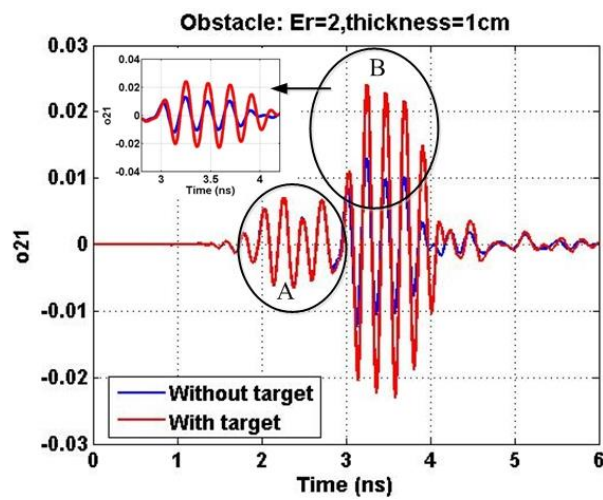
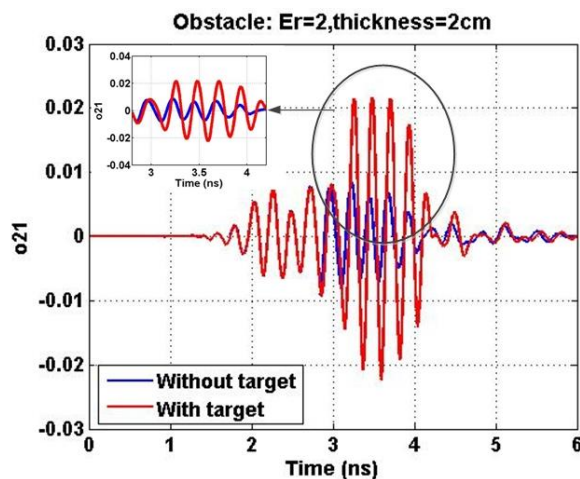


Figure 5-3 Model of detecting metal block behind the obstacle.



(a)



(b)

Figure 5-4 The received reflected signals without metallic target (blue) and with metallic target (red); (a) the thickness of the obstacle is 1 cm; (b) the thickness of the obstacle is 2 cm.

Two scenarios have been considered. The first one only includes the obstacle and the antennas, while the other one adds a target, placed behind the obstacle.

Considering the thickness of the obstacle to be 1 cm, the received reflected signals in two scenarios are shown in Figure 5-4 (a). The blue curve represents the first situation, while the red curve is for the second one with the presence of the target. The energy of the reflected signal with the presence of the metallic target is larger than the one without target, because the metallic target has full reflectivity. Considering the system-loss, the power of the signal without the presence of the metallic target in the system will be accounted for. In this model the input power of the signal is 29.1 dBm. According to the results in Figure 5-4 (a), the reflected power of the signal without the target is -18.9 dBm. Then the total loss is 47 dB.

As demonstrated in section 5.1, the power of the reflected signal is proportional to the thickness and the permittivity of the obstacle. By increasing the thickness of the obstacle to 2 cm, the simulated results are shown in Figure 5-4 (b). The power of the received reflected signal from the obstacle without the target is -20.9 dBm. Then the loss becomes to be 50 dB. Therefore, the loss is dependent on the characteristics of the obstacle. In the discussion below, the loss will be chosen to be 40 dB and 50 dB respectively.

In this UWB imaging system, the maximum transmitting power P_t to the transmitting antenna is 29 dBm, which is the maximum output power of the power amplifier. The power of the minimum noise level is about 0.1 mW (-10 dBm), which can be acquired from the measured results in Figure 6-2. The minimum power of identified received signal is no less than 0.2 mW (-7 dBm). Thus, SNR is considered to be above 3 dB.

When the transmitting power P_t to the transmitting antenna is 29 dBm, and the loss of the system is 40 dB or 50 dB, the relationships between SNR and antenna gain for different targets are plotted in Figure 5-5. To detect smaller target, the antenna gain needs to be higher. If the antenna gain is 6 dBi, the system can detect the target as small as 4 cm \times 4 cm.

When the transmitting power P_t to Tx is reduced to 250 mW (24 dBm), the relationships between SNR and antenna gain are plotted in Figure 5-6. When the loss is 50 dB, the target with a size of 6 cm \times 6 cm can be detected in the system if the antenna gain is above 6 dBi, as shown in Figure 5-6 (b).

In the following discussion, consider the transmitting power to the transmitting antenna is 24 dBm. When the target is of 6 cm \times 6 cm, the relationships between SNR and antenna gain in different detecting ranges with loss of 40 dB and 50 dB are plotted in Figure 5-7. When the loss is 50 dB, the system can detect the target up to 40 cm away if the antenna gain is 6 dBi.

When the size of the target increases to 10 cm \times 10 cm, the relationships between SNR and antenna gain in different detecting ranges with loss of 40 dB and 50 dB are plotted in Figure 5-8. In this case, the antenna gain of above 6 dBi is suitable for both situations.

Therefore, the antenna gain of 6 dBi is suitable for the proposed UWB imaging system.

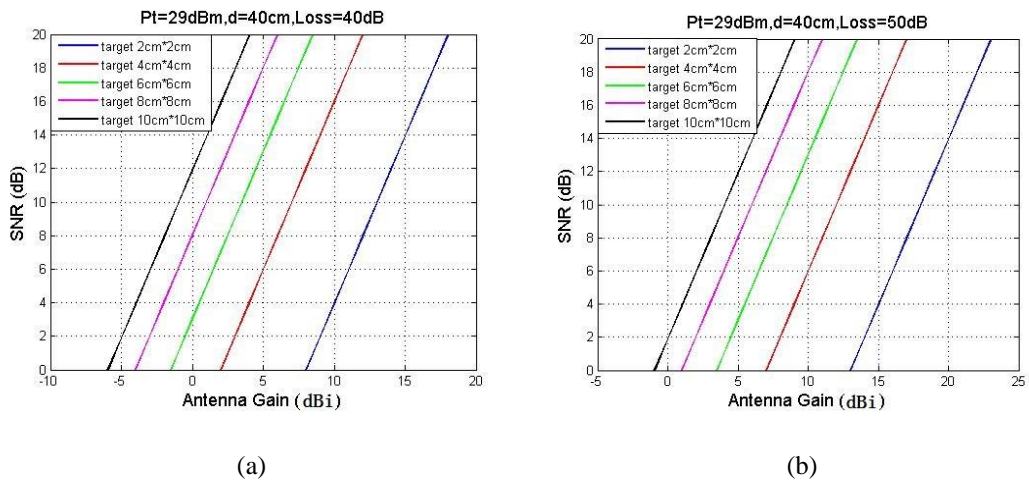


Figure 5-5 The relationship between the antenna gain and SNR for different sizes of the detected target when $P_t = 29$ dBm and $d = 40$ cm; (a) Loss=40 dB; (b) Loss=50 dB.

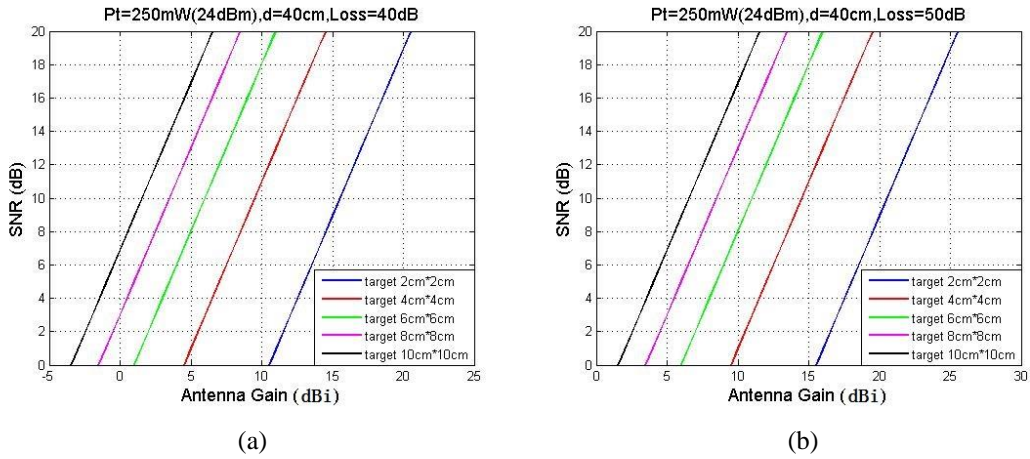


Figure 5-6 The relationship between antenna gain and SNR for different sizes of the detected target when $P_t=24$ dBm and $d=40$ cm; (a) Loss=40 dB; (b) Loss=50 dB.

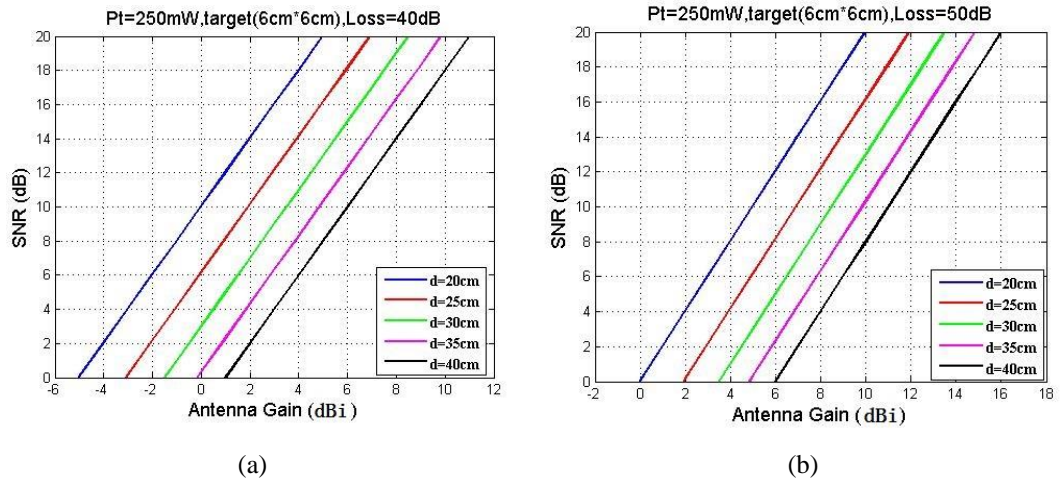


Figure 5-7 The relationship between the antenna gain and SNR for the target of 6 cm × 6 cm in different detecting ranges when $P_t=29$ dBm; (a) Loss=40 dB; (b) Loss=50 dB.

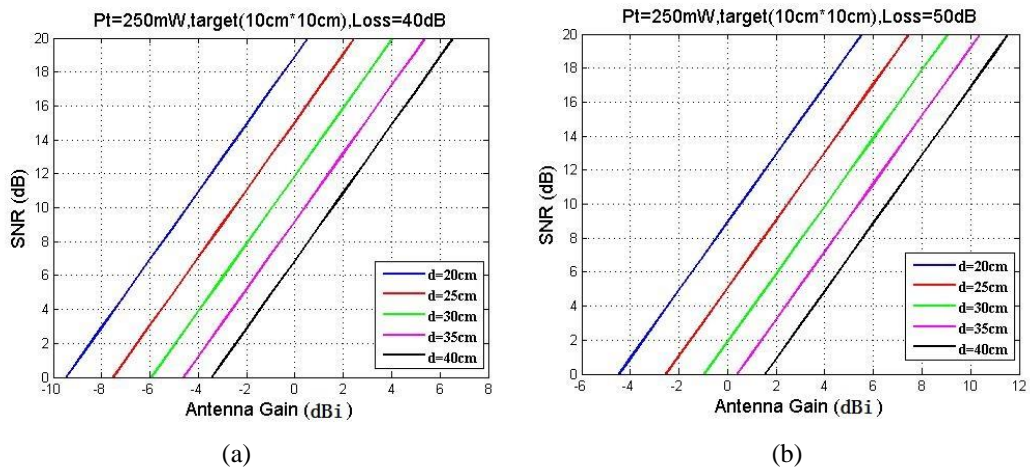


Figure 5-8 The relationship between the antenna gain and SNR for the target of 10 cm × 10 cm in different detecting ranges; (a) Loss=40 dB; (b) Loss=50 dB.

5.3 The UWB imaging system

This project mainly aims to detect, locate and image the target concealed in bag. In order to acquire the fine resolution with a compact testing structure, we have proposed a UWB imaging system with the rotating antenna array. This UWB imaging system has been implemented, and will be described in detail in the following sections.

5.3.1 Architecture of the system

The implemented UWB imaging system consists of the RF circuit, the rotating antenna array and the signal-processing unit. The modulated rectangular signal goes through RF transceiver path and is radiated by the transmitting antenna. It penetrates through the bag, and is reflected by the concealed target. Then it penetrates through the bag again, and is received via the receiving antenna array. After the signal is received by the receiving antenna, it will travel through RF receiver path to Lecroy SDA 11000 serial data analyser and be analysed by the signal processing unit. Finally the images will be reconstructed and shown on PC. The whole architecture of the imaging system with the path of the signal is shown in Figure 5-9.

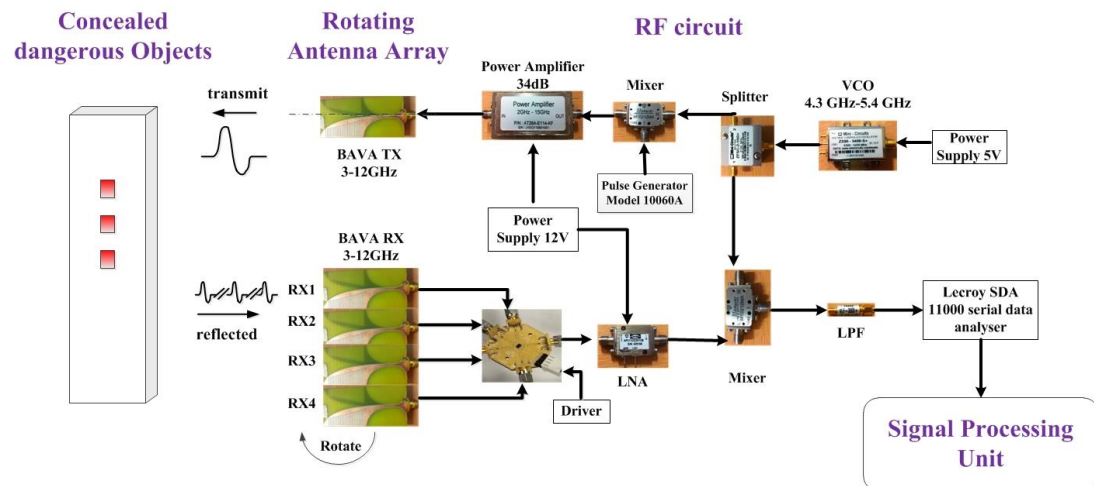


Figure 5-9 The UWB imaging system architecture.

5.3.2 The signal and RF circuit

In this system the signal generated from the Picosecond Pulse Generator Model 10060A is the periodic rectangular pulse. The time period T_p is 10 μ s and time duration τ_p is 1 ns. The LO (Local Oscillator) signal generated from VCO is a sine function signal, the time period of which is 0.22 ns, operating at 4.5 GHz. When they are mixed by Marki mixer M1-0212, the modulated rectangular pulse is following the equation (5-6), and fed to the transmitting antenna.

$$f_{TruncatedSine}(t) = \begin{cases} \sin 2\pi f_c t & pT \leq t \leq pT + \tau \\ 0 & pT + \tau \leq t \leq (p+1)T \end{cases} \quad (5-6)$$

Where p is the periodic times. T is the signal repetition period of 10 μ s. τ is the signal duration of 1 ns. f_c is the centre frequency of 4.5 GHz.

As discussed in Chapter 4, the modulated rectangular signal will keep higher pulse fidelity when transmitted and received via the corrugated BAVA, so it can be used as the input signal in this UWB imaging system.

The link of RF circuit in the UWB imaging system is the own designed link using the commercial RF components, including one VCO (Voltage Controlled Oscillator), one splitter, two mixers, one power amplifier, one LNA (Low Noise Amplifier), one LPF (Low Pass Filter) and one switch, which are shown in Figure 5-10. The detailed specification of each component is listed in Table 5-1.

The transmitting power level of this imaging system is mainly determined by the power amplifier. The commercial component AAREN AT26A-E114-KF provides the maximum output power of 29 dBm. Considering that there is loss of 5 dB when driving the amplifier and inefficient output power from the pulse generator, approximately total output power of 24 dBm is finally transmitted to the transmitting antenna. At the receiver side, the VNA has minimum 1 dB output compression of 13 dBm and gain of 22 dB, so that the theoretical minimum received power at VNA port is -9 dBm. The estimated antenna isolation between Tx and Rx is around 33 dB.

The thermal noise floor of the receiver is -84 dBm, as calculated in section 5.2. The noise figure F is 3 dB. Meanwhile, as described in section 5.2, the minimum SNR is 3 dB. Subsequently the receiver sensitivity is -78 dBm. Because the minimum received power is -9 dBm, the dynamic range of this UWB imaging system is 69 dB. The values of these parameters of the RF circuit are listed in Table 5-2.

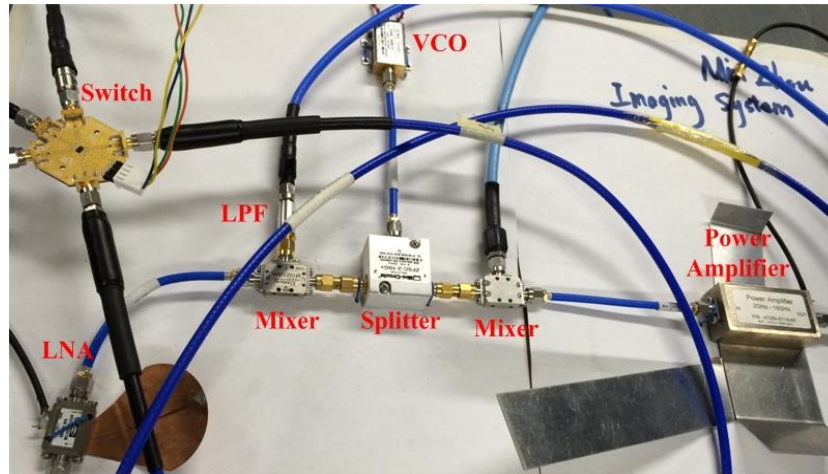


Figure 5-10 The RF circuit in the UWB imaging system.

Table 5-1 The specification of each RF component

Item	Model	Specification
VCO	Mini Circuits ZX95-5400+	Linear tuning 4.3 to 5.4GHz
Splitter	Mini Circuits ZFSC-2-10G+	Low insertion loss 0.5 dB typ.
Mixer	Marki M1-0212	Input 1 dB Compression: 8 dBm
Power Amplifier	AAREN AT26A-E114-KF	Gain: 34 dB, P_{omax} : 29 dBm
Switch	SKY13322-375LF SP4T	Low insertion loss: 0.45 dB @ 1 GHz
LNA	AF0112223013B	Gain: 22 dB @ 0.1-12 GHz

Table 5-2 Dynamic range analysis of the UWB imaging system

Parameters	Values
Transmitter total power (dBm)	24
Tx-Rx isolation (dB)	33
Thermal noise floor (dBm)	-81
Noise figure (dB)	3
Required SNR	3
Receiver sensitivity (dBm)	-78
Receiver minimum received power (dBm)	-9
Receiver dynamic range (dB)	69

5.3.3 The rotating antenna array

An antenna array at the receiver end is always preferable to the single receiving antenna in the UWB imaging system, because it has a much wider effective aperture. Based on the discussion in Chapter 3 and Chapter 4, the corrugated balanced antipodal Vivaldi antenna is a better candidate to the proposed UWB imaging system.

Usually, a receiving antenna array needs to scan the space in both horizontal and vertical planes to produce two-dimensional images of the target. The advantage is that more data can be provided for image reconstruction algorithm. However more severe mutual coupling effect is brought in between the antennas. The system becomes much more complicated. To solve this dilemma, a rotating antenna array has been proposed.

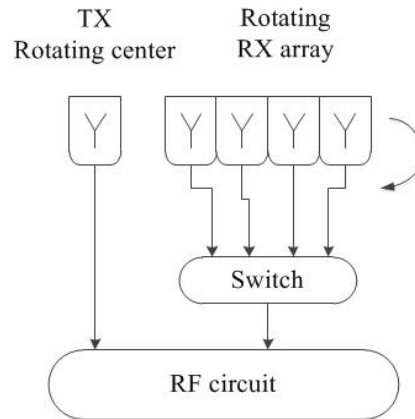


Figure 5-11 The transmitting and receiving antennas part.

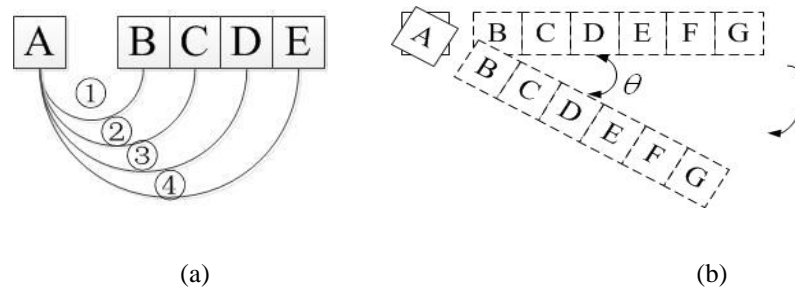


Figure 5-12 The operation principle of antenna part; (a) the measured order in each rotating position; (b) the rotating way of the receiving antenna array.

The rotating antenna array comprises one central transmitting antenna and four receiving antennas. The four receiving antennas are placed side-by-side to form a straight arm, which rotates around the central single transmitting antenna at a sampling angle increment θ . The structure of this rotating antenna is shown in detail in Figure 5-11.

In this rotating antenna array, the receiving antenna element chosen by a switch works individually to provide four groups of received data in total. To explain it more clearly, the central transmitting antenna is named as A, while each element in the receiving antenna array is named as B to E. The switch chooses one antenna from B to E in the array to receive the reflected signals each time, as represented in Figure 5-12 (a). For the four elements antenna array, there will be four groups of measured results in each rotating position. Then, the receiving antenna array will rotate the angle of θ around the central transmitting antenna, as shown in Figure 5-12 (b), to

acquire another four groups of measured data. After one rotation of a circle, all the numbers N of the measured data will be

$$N = n \cdot \frac{360^\circ}{\theta} \quad (5-7)$$

Where, n is the number of receiving antenna elements, which is equal to 4.

The developed rotating antenna array is shown in Figure 5-13. The distance d_{txrx} between TX and RXA is 11.5 cm. Because the corrugated BAVA is in width of 3.5 cm and the receiving antenna elements are placed side-by-side, the total length L of the rotating antenna array is 29 cm.

Although four receiving antenna elements are close to each other, the return loss S_{11} for each receiving antenna element does not change much. As shown in Figure 5-14, each receiving antenna can still work across the operating frequency band from 3 GHz to 12 GHz. Meanwhile, the mutual coupling between the receiving antennas is below -15 dB, as shown in Figure 5-15, which means the receiving antenna will not influence the other received reflected signals. For the imaging application, higher directivity will be beneficial to have better imaging resolution. As shown in Figure 5-16, the four receiving antenna elements array has a higher directivity compared with the single one, which will improve the cross-range resolution of the imaging system.

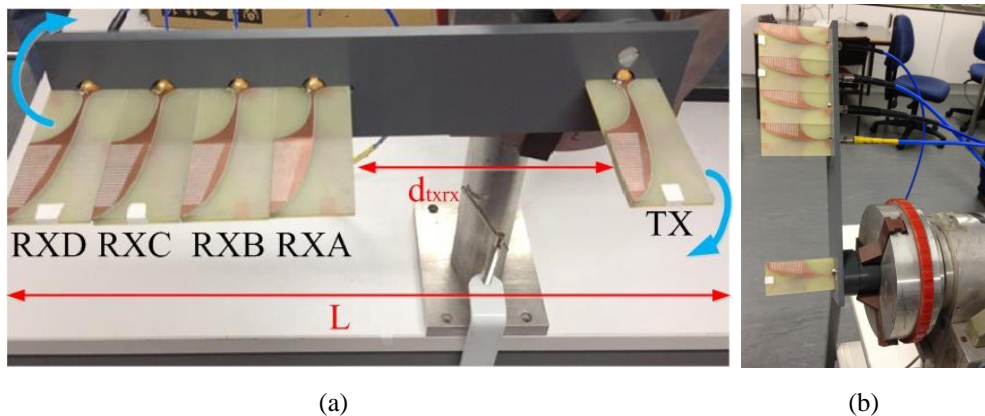


Figure 5-13 The UWB imaging system implemented in the lab.

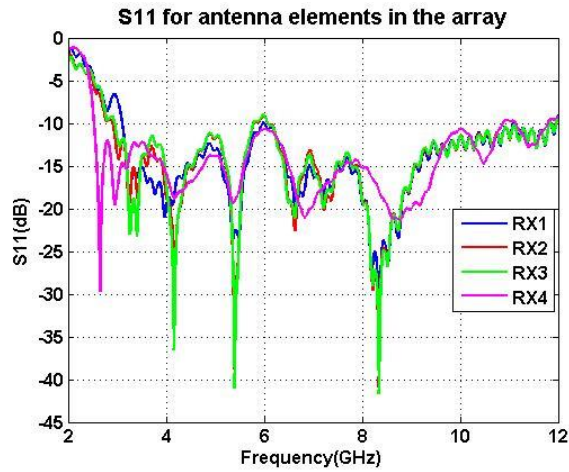


Figure 5-14 The simulated S_{11} for each receiving antenna element.

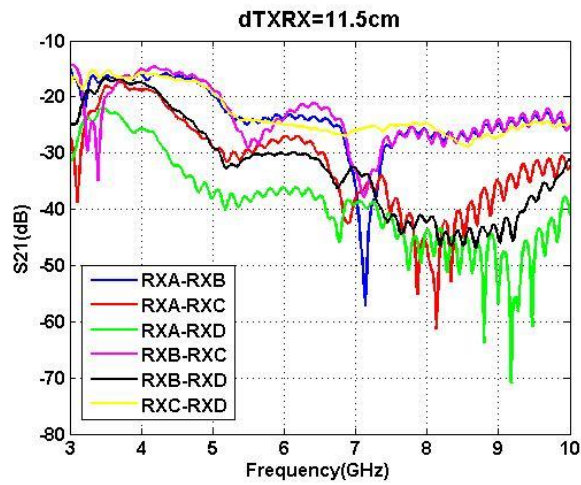


Figure 5-15 The mutual coupling S_{21} between the receiving antenna elements.

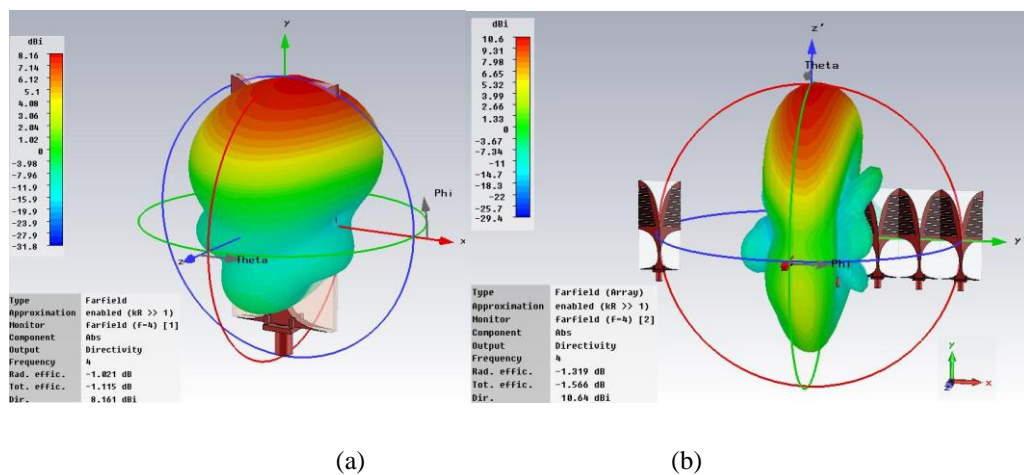


Figure 5-16 The radiation pattern (a) the single receiving antenna, (b) four Rx elements array.

The mutual coupling between Tx and Rx is changing correspondingly to the distance d_{txrx} between two antennas. Four different distances d_{txrx} are chosen to evaluate the performance between Tx and each Rx, which are 8 cm, 11.5 cm, 15 cm and 18.5 cm. The simulated results are plotted in Figure 5-17. When d_{txrx} is 8 cm, S_{21} between Tx and each Rx are all below -35 dB, which means the isolation Tx and Rx is at least 35 dB. When the distance between them is increasing, the relative S_{21} is decreasing. The coupling between each Rx is not influenced by d_{txrx} , because the spacing between each Rx keeps the same. Practically the antenna array is placed in front of the step motor, as shown in Figure 5-13 (b). The radius of the front panel of the motor step is 9 cm. The cable connected to RXA will be influenced by the step motor if RXA is too close to Tx. The final antenna array is expected to be compact and relatively small in size, so smaller distance d_{txrx} will be considered. According to these two points, the distance $d_{txrx}=11.5$ cm is chosen to be the better choice.

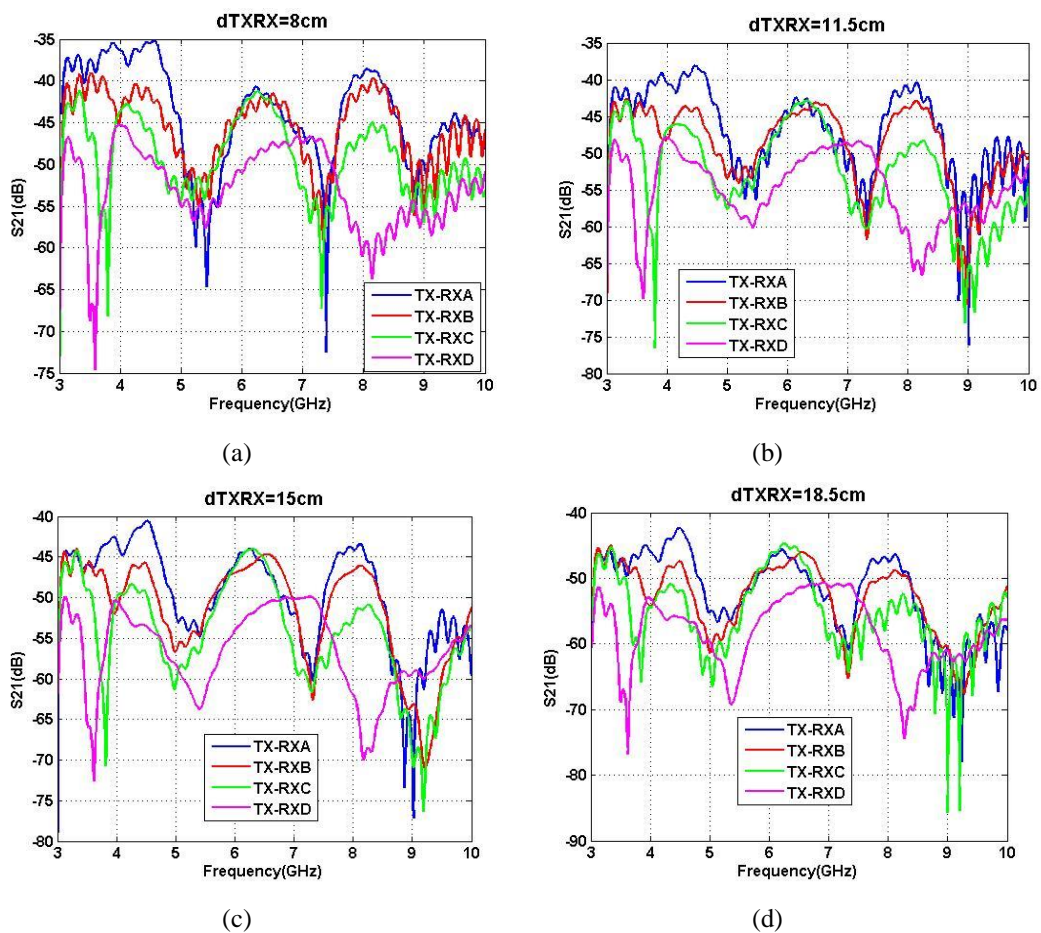


Figure 5-17 S_{21} between Tx and each Rx for different distances between them; (a) $d_{txrx}=8$ cm; (b) $d_{txrx}=11.5$ cm; (c) $d_{txrx}=15$ cm; (d) $d_{txrx}=18.5$ cm.

The receiving antenna array of the straight arm becomes a two-dimensional antenna array when it rotates around the central transmitting antenna. It is equivalent to place the antenna elements in the number of N in space. Thus it is possible to obtain N groups of measured data when the antenna array is rotating. If the sampling angle increment θ is smaller, the total number of N will become bigger. More groups of measured data are acquired, more accurate the image results will be.

From the view of architecture, by reducing the number of antenna elements from N to n , fewer switches and the cables would be used. Thus the whole system will be more compact and less noise would be introduced. Meanwhile, the mutual coupling between the antennas will be smaller.

It can be concluded that the rotating antenna array makes it possible to have an equivalent large number of antennas in space by using fewer antenna elements in the array. Meanwhile, the rotating structure of the linear one-dimensional antenna array can reduce unwanted mutual coupling and make the system much more compact than other reviewed UWB imaging systems.

5.4 The Imaging Algorithm

5.4.1 The existing imaging algorithms

Different image reconstruction algorithms have been developed for varied applications. Among them, the synthetic aperture radar (SAR) technique is the typical synthetic method in the UWB radar imaging system, especially in GPR applications. It mainly applies the phase difference between each element of the antenna array to create a synthetic array aperture. Several modifications and improvements have been introduced to this algorithm to optimize the imaging results. The algorithm proposed in [3] was implemented as a non-linear waveform based on signal processor integrated with a SAR focusing procedure. It constructed a SAR-like image of the subsurface using the outputs of the signal processor, and was suitable for GPR to image plastic cased antipersonnel landmines.

The reconstructed image which is the result of the beam-forming process, is known as the delay and sum (DAS), considering the time domain analysis. After collecting

all the data in free space and applying the conventional delay and sum beam-forming algorithm, the image of the target could be obtained from fine spatial sampling of the received signals [4]. To improve the resolution, larger aperture of the antenna array is generally demanded, which has been proved quite successfully in some numerical models [5-6]. Besides that, several advanced methods based on DAS algorithms have also been investigated. A confocal microwave imaging (CMI) techniques that employed simple DAS beam-forming algorithm was first proposed in [7-9] for breast cancer imaging. In this algorithm, UWB microwave pulses were transmitted from antennas at different locations near the surface of the breast. The backscattered responses from the breast were recorded, and then the backscattered energy distribution was calculated coherently. The advantages of UWB CMI included high resolution resulting from ultra-wide band signal, as well as simple and effective signal processing algorithms for image reconstruction. However, this algorithm did not account for dispersive propagation effects and offered limited capability for discriminating against artifact and noise. An alternative CMI technique, termed as microwave imaging via space-time (MIST) beam forming, used filters that compensated for dispersion and other limitations of the earlier DAS algorithm [10]. A delay-multiply-and-sum (DMAS) algorithm was developed for breast cancer detection. In this algorithm, the backscattered signals received from numerical breast phantoms which were simulated using the finite-difference time-domain (FDTD) were shifted in time, multiplied in pair, and summed to form a synthetic focal point [11].

Other imaging reconstruction approaches include time-reversal technique, multi-static adaptive microwave imaging (MAMI), tomography and the inverse scattering, etc. The time-reversal technique refers to the inverse manipulation of the signals in time domain, which equals to the signal phase conjugation in the frequency domain [12]. It is beneficial in the non-uniform and complex medium in the environment or the scene with a moving target. MAMI employs the data-adaptive Robust Capon beam forming (RCB) in two stages for a 3D breast model. Firstly, the data-adaptive RCB algorithm is used spatially to obtain a vector of multiple backscattered waveforms for each probing signal. Secondly, RCB is employed to recover a scalar waveform based on the estimated vector of waveforms obtained in first stage [13].

The research group at King's College employed a method of 3D microwave tomography for imaging the varied and complex dielectric spatial profiles of realistic breast tissue structure [14]. It was based on a multiple frequency inverse scattering method from computational electromagnetic simulations and could be applied in the dispersive dielectric model.

The algorithms presented above are some common imaging methods used in the UWB imaging system. Each of them has been evolved in different numerical models to suit their purposes.

5.4.2 Two-dimensional image reconstruction method

In this UWB imaging system, the imaging scheme is based on DAS algorithm.

The fundamental of the method is shown in Figure 5-18. Assuming the transmitting antenna is placed at $X_t = (x_t, z_t)$, the reflected signal from the target T is received by m -th receiving antenna located at $X_{r_m} = (x_{r_m}, z_{r_m})$. The target is located at $X_j = (x_j, z_j)$. The signal received by the m -th receiving antenna is given by equation (5-8) [15].

$$b_m(t) = w_m a(t - \tau_m) \quad (5-8)$$

Where, $a(t)$ is the transmitted signal. w_m is the weighting factor of the m -th receiving antenna. It is represented that the pulse attenuation determined by antenna influence, system loss and so on. τ_m is the time-delay when the signal travels from Tx to the target and then reflected back to the m -th Rx, which is given by

$$\tau_m = \frac{d(X_t, X_j)}{c} + \frac{d(X_j, X_{r_m})}{c} \quad (5-9)$$

Where c is the speed of the light in free space (m/s) and $d(X, Z)$ is the direct distance between two positions X and Z .

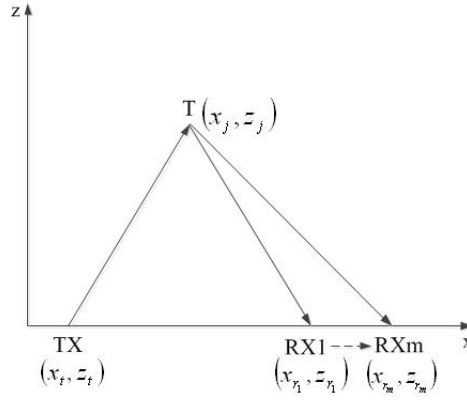


Figure 5-18 The detecting process.

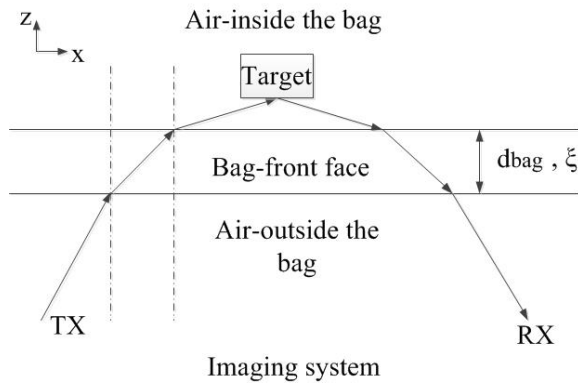


Figure 5-19 The influence introduced by the bag.

In reality, the target is concealed in bag, which is rather thin in thickness (around 0.1cm) and made of denim. The permittivity ϵ_{bag} of the denim is about 2 [16]. Because of its thin thickness and low permittivity, the modulated signal transmitted from the imaging system can penetrate the bag, only introducing a small time delay, as shown in Figure 5-19. The time-delay t_{bag} caused by the bag can be calculated by the equation (5-10) and be eliminated from the time-delay τ_m caused by the target.

$$t_{bag} = \frac{d_{bag} \cdot \sqrt{\epsilon_{bag}}}{c_0} \quad (5-10)$$

The above process is repeated until the M -th receiving antenna. By adding M output signals, shown in Figure 5-20, the processed signal $f(t)$ is given in equation (5-11), which will be used for further analysis to reconstruct the images.

$$f(t) = \sum_{m=1}^M b_m(t + \tau_m) \quad (5-11)$$

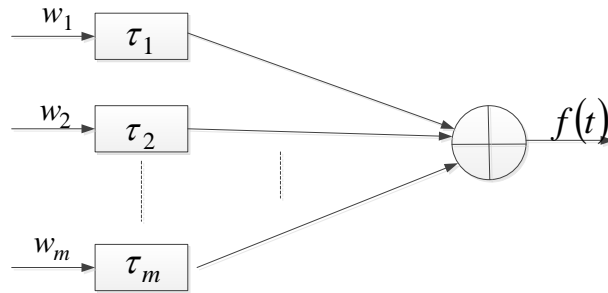


Figure 5-20 Delay-and-summed received signal.

By analysing the processed signal $f(t)$, the time window TW is applied to extract the most useful part, which is defined as

$$\begin{cases} t_{1m} \leq TW_m \leq t_{2m} \\ \frac{t_{1m} + t_{2m}}{2} = t_{pm} \end{cases} \quad (5-12)$$

Where t_{pm} is the time of peak value P_m for $b_m(t)$, as shown in Figure 5-21 (a).

Normally, the number of data for the signal $f(t)$ increases with the width of time window TW . But it will also rise the processing time. To balance the number of data and processing time, t_{1m} and t_{2m} are determined in terms of the definition (5-13).

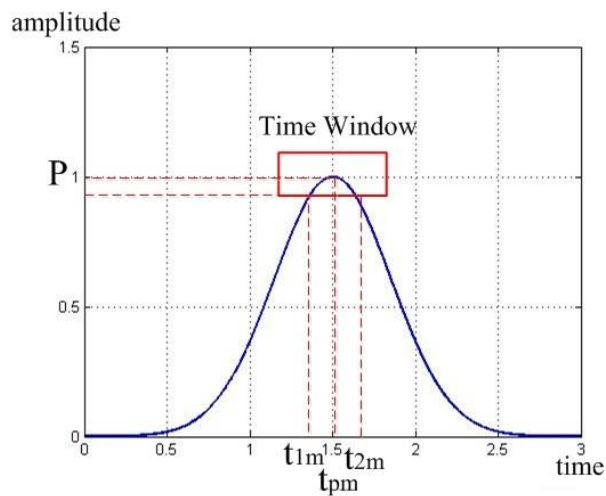
$$\begin{cases} t_{1m} | (p(t_1) = \alpha \cdot P_m) \wedge (t_1 < t_{pm}) \\ t_{2m} | (p(t_2) = \alpha \cdot P_m) \wedge (t_2 > t_{pm}) \end{cases} \quad (5-13)$$

Where $p(t_1)$ and $p(t_2)$ are amplitude for t_{1m} and t_{2m} respectively. α is ratio of the peak value. When α is assumed as 80%, the corresponding image result is good enough for identification.

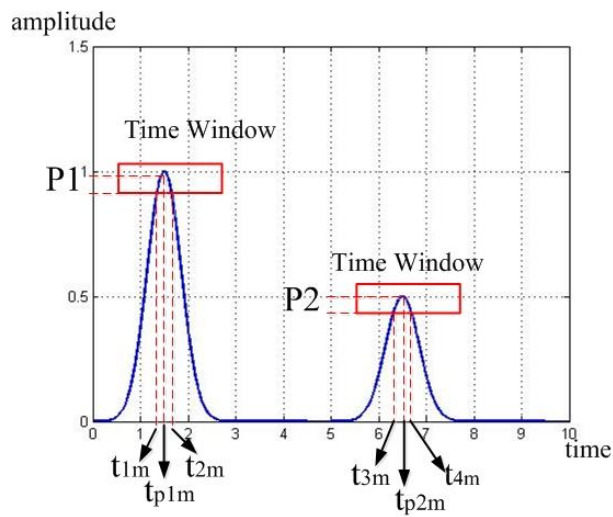
The region of space is divided into a finite number of pixels in small square unit. The imaging value for the j -th pixel (x_j, z_j) is obtained by passing through the processing signal $f(t)$ based on equation (5-9). Then the elliptical slot is obtained for every TW_m .

The overlapped area with the maximum pixel value by M elliptical lines is the position of the target in one-dimensional, as shown in Figure 5-22. The received signal is affected by the multi-path reflection, so the reconstructed target is in elliptical shape instead of the perfect rectangular shape.

For two targets imaging, when the received reflected signals do not overlap, the image reconstruction can be achieved by defining two separated time windows, as shown in Figure 5-21 (b). The process of the image reconstruction for each target follows the same method as the signal one.



(a)



(b)

Figure 5-21 Time window for the received signal; (a) One target; (b) Two targets.

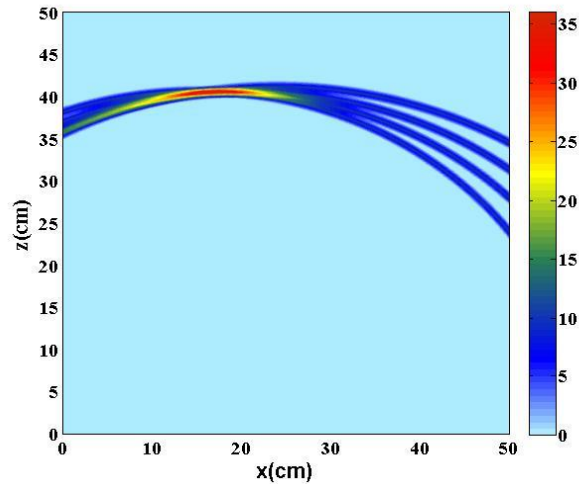


Figure 5-22 The process of image reconstruction

The two-dimensional reconstructed image is based on the combination of each rotation plane of the antenna array. In each plane, the DAS method is put into use once. X-axis is assumed to be the direction along the horizontal width of the target, while Y-axis is along the height of the target and Z-axis is along the down range between the target and the system, as shown in Figure 5-23 (a).

Here the four receiving antenna elements are named as RXA, RXB, RXC and RXD. In XY plane, when receiving antenna elements RXA, RXB, RXC and RXD are at the angle of 0° , the reconstructed image highlighted in red can be achieved as “image1” in Figure 5-23 (b). When rotating the arm of the receiving antenna array to the other different angles, the coordinates X-axis and Y-axis will be considered to rotate at the same angle. Thus the reconstructed image will rotate correspondingly, resulting in an imaging area known as “image m”, “image n” and “image q” in Figure 5-23 (b). After a complete circular rotation, the area highlighted in red will ideally form the final reconstructed images of the desired target.

In conclusion, the 2D reconstructed image of the target can be obtained by rotating the straight-arm of the one-dimensional linear antenna array, which turns out to be a rather straight forward 2D imaging structure.

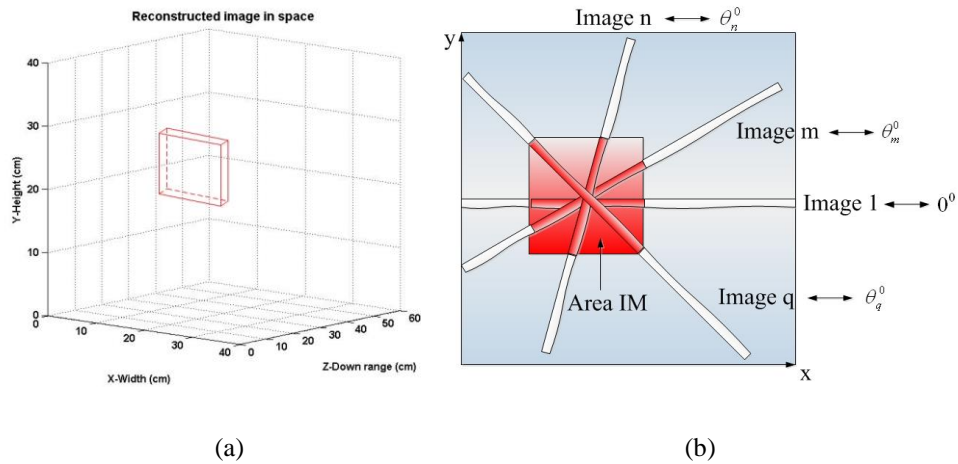


Figure 5-23 The 2D image reconstruction method.

5.5 Summary

The link budget of the UWB imaging system has been calculated, while the practicability of the system has been verified in this chapter. Then the detailed description of the UWB imaging system has been given, including the architecture of the system, the RF circuit characteristics, the rotating antenna array and the 2D image reconstruction method based on DAS algorithm.

Reference

- [1] A. Muqaibel, A. Safaai-Jazi, A. Attiya, B. Woerner, S.M. Riad, “UWB through-the-wall propagation”, *IEEE Proc. On Microwave Antennas Propag.* 152 (6), Page(s): 581–588, 2005.
- [2] S. Kingsley, S. Quegan, *Chapter One Fundamentals, Understanding Radar Systems*, 1992.
- [3] V. Kovalenko, A. Yarovoy, L.P. Ligthart, “A SAR-Based Algorithm for Imaging of Landmines with GPR”, *Proceedings of the 2006 IEEE International Workshop on Imaging Systems and Techniques, 2006. IST 2006*, Page(s): 65-70, 2006.
- [4] H. KKobayashi, M. Inami, Sang-Eun Park, Y. Yamaguchi, G. Singh, Yi Cui, “Radar Imaging by Using GTD Near-field Model and Antenna Array-factor”, *2012 International Symposium on Antennas and Propagation (ISAP)*, Page(s): 616-619, 2012.

- [5] W. Shao, B. Zhou, Z. Zheng, and G. Wang, "UWB microwave imaging for breast tumor detection in inhomogeneous tissue", in *Proceedings of the 27th IEEE Annual International Conference of the Engineering in Medicine and Biology Society (EMBS'05)*, Shanghai, China, Page(s): 1496-1499, 2005.
- [6] Z. Wang, J. Li and R. Wu, "Time-delay and time-reversal-based robust Capon beamformers for ultrasound imaging", *IEEE Transactions on Medical Imaging*, vol. 24, no. 10, Page(s): 1308-1322, 2005.
- [7] X. Li, S.C. Hagness, "A confocal microwave imaging algorithm for breast cancer detection", *IEEE Microwave and Wireless Components Letters*, Vol: 11, No: 3, Page(s): 130-132, Mar. 2001.
- [8] E.C. Fear, X. Li, S.C. Hagness, M.A. Stuchly, "Confocal microwave imaging for breast cancer detection: Localization of tumors in three dimensions", *IEEE Transactions on Biomedical Engineering*, Vol: 49, No: 8, Page(s): 812-822, Aug. 2002.
- [9] R. Nilavalan, A. Gbedemah, I.J. Craddock, X. Li, S.C. Hagness, "Numerical investigation of breast tumor detection using multi-static radar", *Electronics Letters*, Vol: 39, Issue: 25, Page(s): 1787-1789, 2003.
- [10] E. J. Bond, X. Li, S.C. Hagness, B.D. Van Veen, "Microwave imaging via space-time beamforming for early detection of breast cancer", *IEEE Transactions on Antenna and Propagation*, Vol: 5, No: 8, Page(s): 1690-1705, Aug. 2003.
- [11] H.B. Lim, N.T.T. Nhung, E.P. Li, N.D. Thang, "Confocal Microwave Imaging for Breast Cancer Detection: Delay-Multiply-and-Sum Image Reconstruction Algorithm", *IEEE Transactions on Biomedical Engineering*, Vol: 55, Issue: 6, Page(s): 1697-1704, 2008.
- [12] M. Fink, "Time-reversal of ultrasonic fields I: basic principles", *IEEE Trans. On Ultrasonics, Ferroelectrics and Frequency Control*, Vol: 39, Issue: 5, Page(s): 555-666, 1992.

- [13] Y. Xie, B. Guo, L. Xu, J. Li, S. Petre, “Multistatic Adaptive Microwave Imaging for Early Breast Cancer Detection”, *IEEE Transactions on Biomedical Engineering*, Vol: 53, Issue: 8, Page(s): 1647-1657, 2006.
- [14] J.D. Shea, K. Panagiotis, C.S. Hagness, B.D. VanVeen, “Three-dimensional microwave imaging of realistic numerical breast phantoms via a multiple-frequency inverse scattering technique”, *Medical Physics*, Vol. 37, No. 8, Page(s): 4210-4226, 2010.
- [15] L. Chen, O.Y. Shan, “A Time-domain Beamformer for UWB Through-wall Imaging”, *TENCON2007 – 2007 IEEE Region 10 Conference*, Page(s): 1-4, 2007.
- [16] S.W. Harmer, N. Rezgui, N. Bowring, Z. Luklinska, G. Ren, *Determination of the complex permittivity of textiles and leather in the 14-40 GHz millimetre-wave band using a free-wave transmittance only method*, *Microwaves, Antennas & Propagation, IET*, Vol. 2, Issue 6, 2008, Page(s): 606-614.

Chapter 6 Imaging Measurements

The UWB imaging system with the rotating antenna array has been implemented and analysed in the previous chapter. In this chapter, the experiments are conducted to detect and image metallic targets concealed in bag. The measurements are carried out in different scenarios, depending on the varied sizes of the metallic targets and the changing ranges from the antenna array to the domain of detection interest. The down-range and cross-range resolutions are also investigated in the relative measurements for two targets detection.

6.1 Received signals

As described in detail in Chapter 5, the modulated rectangular signal is transmitted to the transmitting antenna. In the UWB imaging system, the input signal is a periodic modulated rectangular pulse with a time-duration of 1 ns and a repetition of 10 μ s. The input signal in blue curve and the received one in red curve within one period are plotted in Figure 6-1. The input signal is obtained at the output port of the pulse generator, and the received signal is acquired at the output port of LPF (Low Pass Filter).

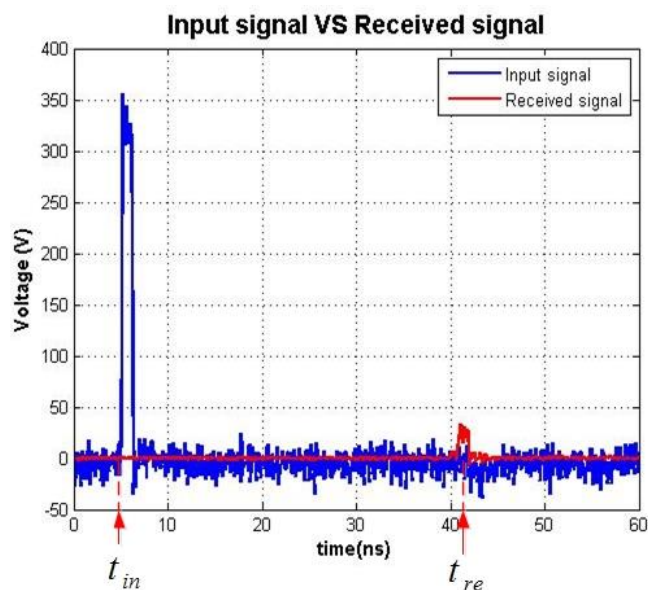


Figure 6-1 The input signal and received signal in one period.

By analysing the received signal in time and amplitude, it can successfully image the desired target. The information in time gives the probable area where the desired target is, while the values in amplitude can help to decide the exact position of this target.

t_{in} and t_{re} are the propagation time of input and received signals respectively. The time delay between them is introduced by the propagation time of t_{system} (travelling through RF circuits and antennas in the system), t_{bag} (travelling through the front surface of the bag) and t_{tar} (travelling from Tx to the target and then back to Rx). Thus the relation between them is as follows:

$$t_{re} = t_{in} + t_{system} + 2 \times t_{bag} + t_{tar} \quad (ns) \quad (6-1)$$

The received signal needs to subtract the propagation time of t_{in} , t_{system} and t_{bag} to obtain the accurate propagation time t_{tar} for the signal travelling from Tx to the target and then back to Rx without interruption of bag.

t_{system} can be calculated in this way. When there is no target in free space, the received signal is the direct signal from Tx to Rx. Its propagation time t_{cali} is the sum of t_{system} and t_{theory} . t_{theory} is following the equation (6-2).

$$t_{theory} = \frac{d_{txrx}}{c} \quad (6-2)$$

Where d_{txrx} is the distance between Tx and Rx. c is the velocity of light ($3 \times 10^8 m/s$).

t_{bag} can also be calculated using the equation (5-10), which is explained in section 5.4.2.

Therefore, when scanning the bag with the concealed metallic target, t_{tar} can be extracted following the above steps.

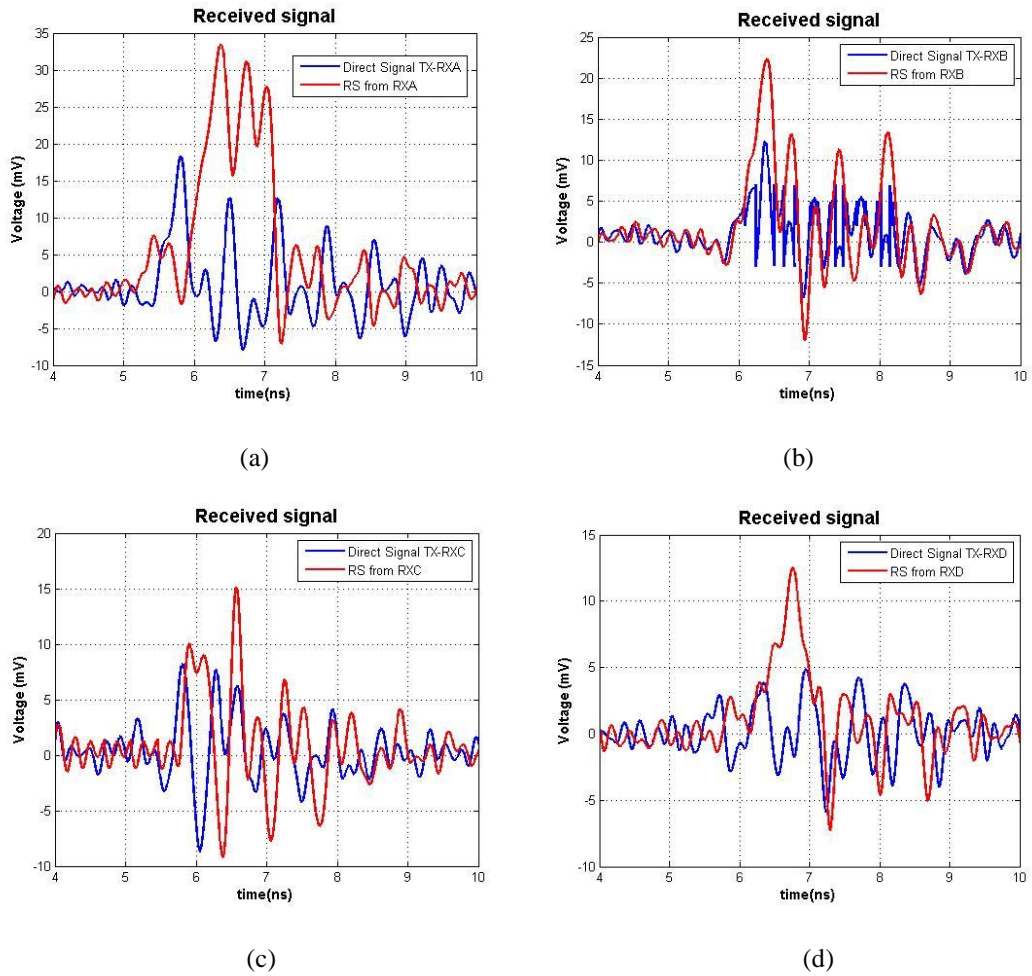


Figure 6-2 Comparison of the direct signal transmitted from Tx to each Rx and the returned signal reflected from the target in one period of time; (a) Received by RXA, (b) Received by RXB, (c) Received by RXC, (d) Received by RXD.

There is no absorber between Tx and Rx in the imaging system, so that part of the signal propagated by Tx will directly transmitted to Rx. It is named as the direct signal $S_{Lrx}(t)$. The received signal, named as $S_{re}(t)$, includes the direct signal $S_{Lrx}(t)$ and the signal reflected from the desired target $S_{tar}(t)$. $S_{re}(t)$ and $S_{Lrx}(t)$ received by each Rx are plotted in Figure 6-2. The blue curve represents the direct signal $S_{Lrx}(t)$, which is obtained by Rx when there is no target in free space. The red curve represents the received signal $S_{re}(t)$ in the situation that there is one metallic target concealed in bag in front of the antenna array. This figure shows that $S_{Lrx}(t)$ is smaller in amplitude than $S_{re}(t)$. $S_{re}(t)$ should minus $S_{Lrx}(t)$ in amplitude to acquire the relatively accurate information of $S_{tar}(t)$.

The above method of signal-processing is named as *Step1*. Following *Step1* the signal of $S_{tar}(t)$ can be finally extracted from the measured received signal $S_{re}(t)$. The results for each Rx channel in one rotating position are plotted in Figure 6-3 (a). As described in section 4.3.3, the antenna acts as a filter, inducing the distortion and attenuation to the propagating signals. Like the simulated received signal shown in Figure 4-35 (a), the modulated rectangular signal shows oscillations in amplitude in one pulse duration. It is distorted by the antenna. When this distorted signal is demodulated with sine function signal again, the envelope will keep oscillations in amplitude of the pulse. That is the reason why the demodulated received signal is not in perfect square shape, as shown in Figure 6-3. Although it has oscillations in amplitude, the time duration of the FWHM τ_{FWHM} remains around 1 ns, which can be analysed to reconstruct the image of the target.

For the situation of two targets concealed in bag, the demodulated signals after *Step1* are plotted in Figure 6-3 (b). It can be found that the demodulated signal from each Rx almost contains two pulses in one period, which stands for the ones reflected from two targets.

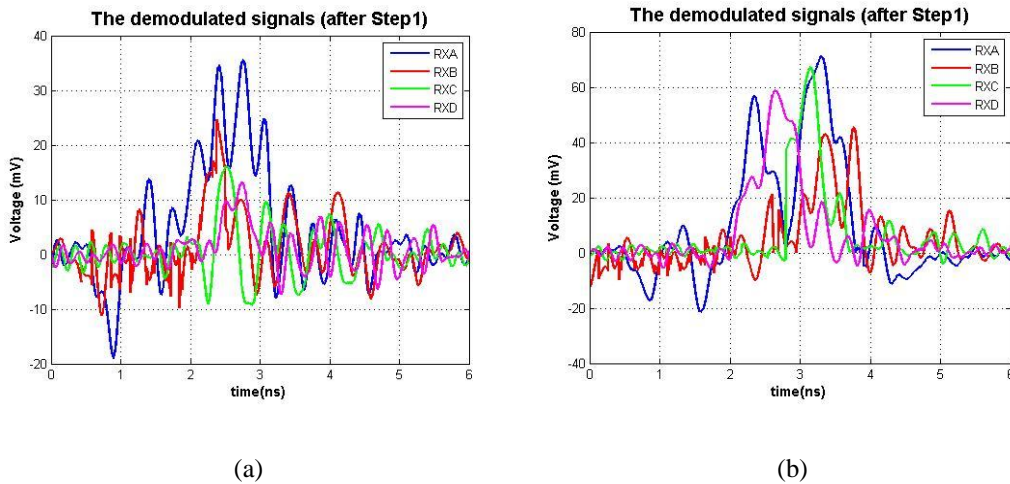


Figure 6-3 The demodulated signal received from different receiving antenna in one rotating position; (a) The situation of one target; (b) The situation of two targets.

6.2 Images for the single concealed target

Based on the demodulated signals after *Step1*, the reconstructed image can be finally achieved using the time window to extract the information for image reconstruction. The two-dimensional image reconstruction method is described in section 5.4.2. The step of reconstructing the image is named as *Step2*.

Using the UWB imaging system, the measurements of the single metallic target concealed in bag are analysed in this section. A bag in cylinder shape is made of denim, which causes less reflection due to its low permittivity, as shown in Figure 6-4. It is with the size of 52 cm (Width) \times 26 cm (Height) \times 26 cm (Depth). The UWB imaging system with the rotating antenna array in the measurement is shown in Figure 6-5. The bag is placed in front of the rotating antenna array with a distance named as d_z along Z-axis. The bag and the central transmitting antenna are almost at the same height along Y-axis, as shown in Figure 6-5 (a). The rotating receiving antenna array rotates around the central transmitting antenna in XY plane, as shown in Figure 6-5 (b). The single metallic target is concealed in bag, as shown in Figure 6-5 (c). Different sizes of the single target have been taken into consideration.



Figure 6-4 The bag used in the following measurements.

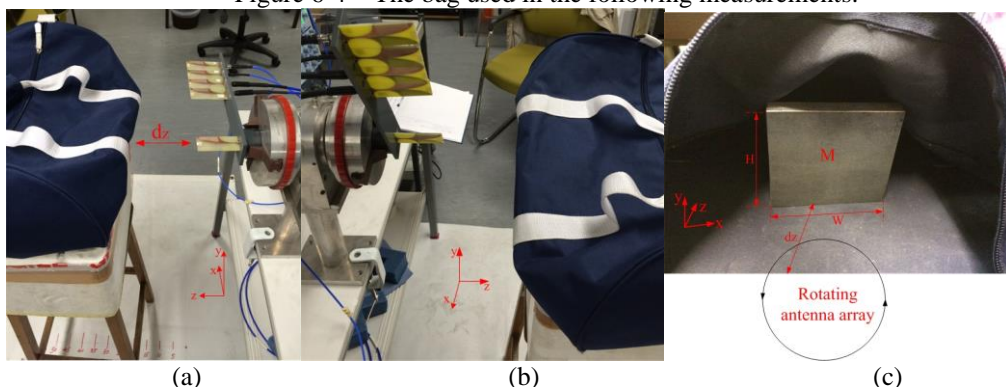


Figure 6-5 The UWB imaging system in the measurement, (a) side view of the bag and the antenna array, (b) side view of the measurement when the antenna array is rotating, (c) the concealed metallic target in the bag.

6.2.1 The results of the measurements

(1) Single target (10 cm × 10 cm × 1 cm)

Firstly, the metallic target with the size of 10 cm (width) × 10 cm (height) × 1 cm (thickness) is concealed in bag, and placed at different ranges from the rotating antenna array. Different distances d_z between the target and the antenna array along Z-axis are set to be 20 cm, 30 cm, 40 cm and 50 cm respectively.

The 2D reconstructed images of the measured target are shown from Figure 6-6 to Figure 6-9. Each of them corresponds to a pre-set detecting distances d_z of 20 cm, 30 cm, 40 cm and 50 cm sequentially. To make it clear, the real target is illustrated as a black square block in the figure, while the coloured area indicates the reconstructed image of the target.

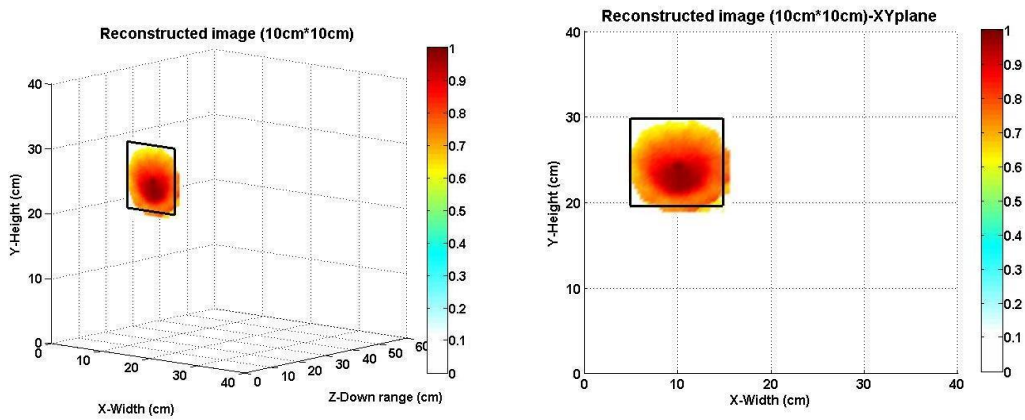
By comparison, the reconstructed images of the target are very close to the real one, as shown in Figure 6-6 (a) (b) to Figure 6-9 (a) (b). When the target is placed closer to the antenna array, e.g. the distance d_z of 20 cm or 30 cm, the reconstructed image of the target is more accurate. When the target is moving further away from the system, such as 40 cm or 50 cm, the highlighted reconstructed area is getting smaller because the received signal becomes smaller when the target is placed further away from the system due to the propagation loss and multi-reflections.

Another inaccuracy issue is the ability to fully recover the shape of the real target. From Figure 6-6 (a) (b) to Figure 6-9 (a) (b), the reconstructed images show some lack of information around the edges of the standard rectangular shape. This is supposed to be caused by the diffusion at these edges during the reflection. As explained in section 5.4.2, the reconstructed image in one-dimensional has an elliptical shape. The two-dimensional reconstructed image is summed by the elliptical shape of image at each rotating position. In this case the edge of the reconstructed area is not an exact rectangular shape.

The reconstructed image of the target has very accurate down range estimation along Z-axis, as shown from Figure 6-6 (c) to Figure 6-9 (c). The reason is that the localization of the target in free space is prominently determined by the propagation time of the reflection from the target. While the arm of the antenna array starts to

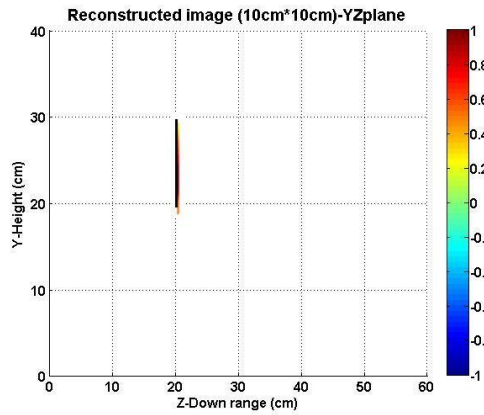
rotate in front of the target, more received data in each scanning position would intrinsically enhance the accuracy of the final reconstructed images. As described in section 5.4.2, the propagation time t_{bag} has already been subtracted in *Step1*, so that the estimated down range d_z is much closer to its real position. A similar tendency is observed that the reconstructed down range result is better when the gap between the target and the antenna array is closer ($d_z = 20$ cm / 30 cm) and slightly worse when the distance d_z is kept longer ($d_z = 40$ cm / 50 cm). Nevertheless, the difference is still acceptable even when the concealed target is placed at the distance of 50 cm. However, when the target is moved beyond 50 cm along Z-axis, the received signal gets obscured among the direct signal $S_{LTX}(t)$ and the noise. It cannot be extracted for effective signal analysis.

Thus it can be concluded that the single target with the size of 10 cm × 10 cm × 1 cm can be detected and imaged successfully at different down ranges in the UWB imaging system. The maximum distance d_z between the target and the antenna array is 50 cm.



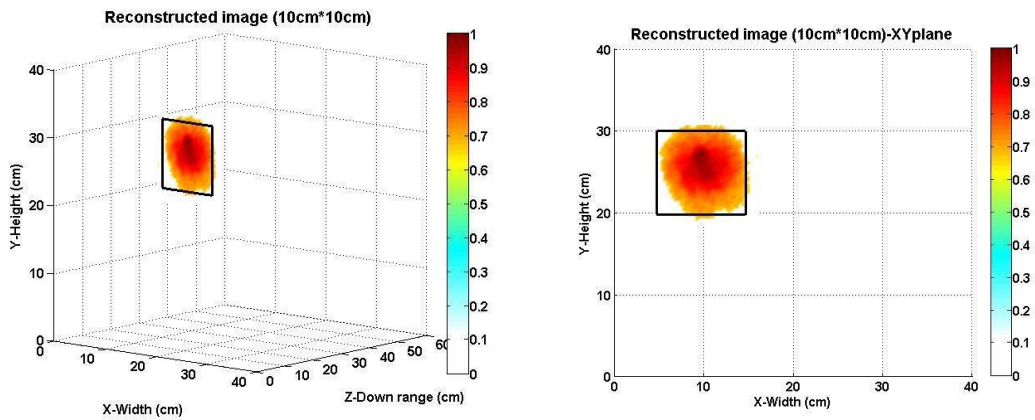
(a)

(b)



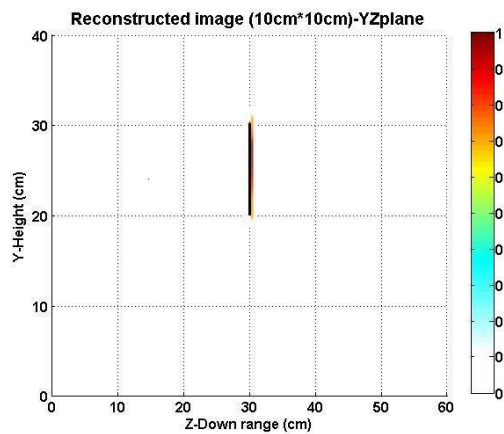
(c)

Figure 6-6 The reconstructed image for the single metallic target with the size of 10 cm × 10 cm × 1 cm at $d_z=20$ cm, (a) 2D image of the target, (b) the reconstructed image of the target in XY plane, (c) side view of the reconstructed image in YZ plane.



(a)

(b)



(c)

Figure 6-7 The reconstructed image for the single metallic target with the size of 10 cm × 10 cm × 1 cm at $d_z=30$ cm, (a) 2D image of the target, (b) the reconstructed image of the target in XY plane, (c) side view of the reconstructed image in YZ plane.

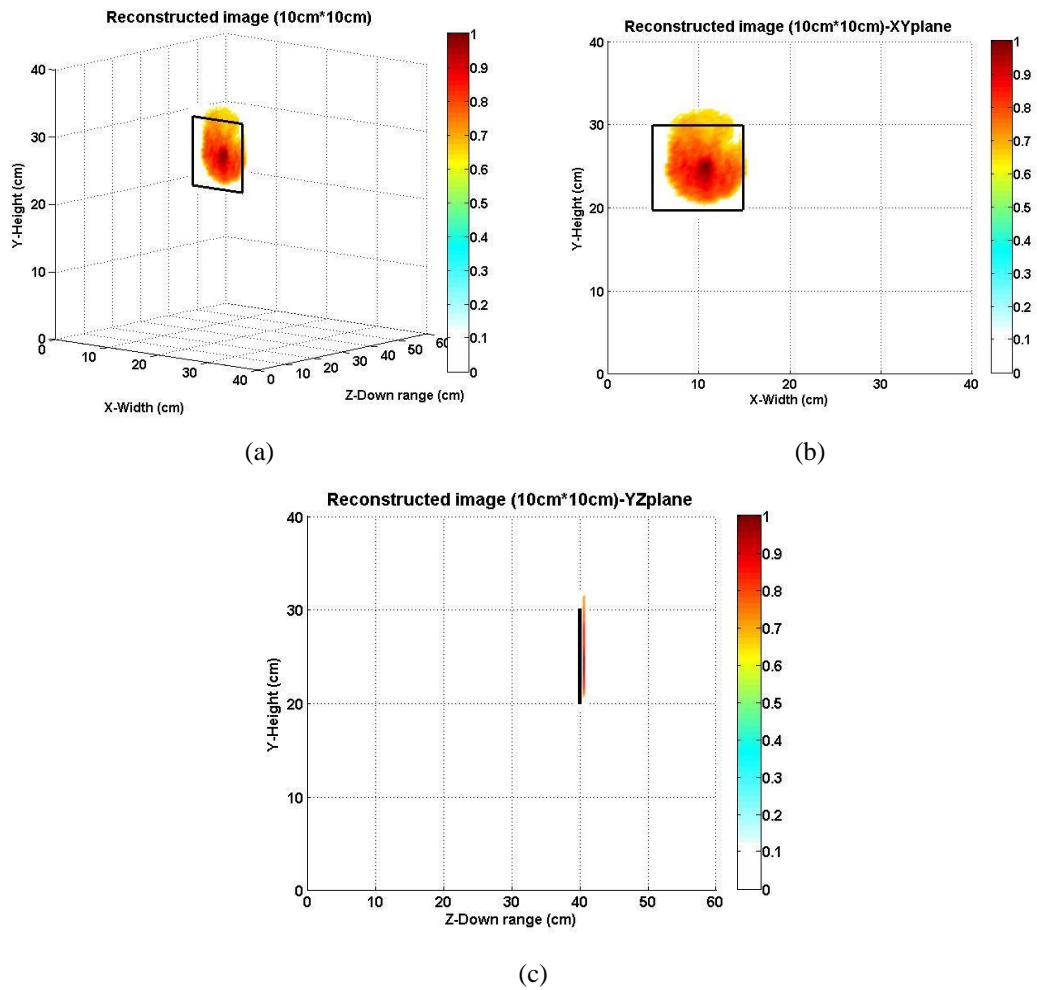
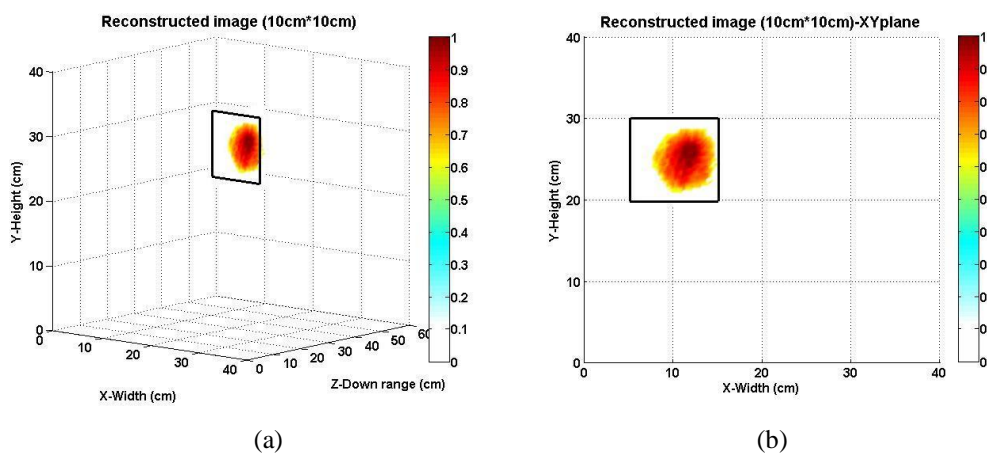
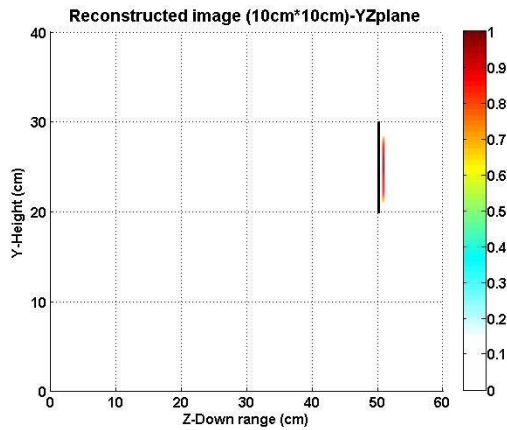


Figure 6-8 The reconstructed image for the single metallic target with the size of 10 cm × 10 cm × 1 cm at $d_z = 40$ cm, (a) 2D image of the target, (b) the reconstructed image of the target in XY plane, (c) side view of the reconstructed image in YZ plane.





(c)

Figure 6-9 The reconstructed image for the single metallic target with the size of 10 cm × 10 cm × 1 cm at $d_z = 50$ cm, (a) 2D image of the target, (b) the reconstructed image of the target in XY plane, (c) side view of the reconstructed image in YZ plane.

(2) Single target (8 cm × 8 cm × 1 cm)

In the second scenario, the metallic target with the size of 8 cm (width) × 8 cm (height) × 1 cm (thickness) is chosen to test the capability of the imaging system. Different distances d_z between the target and the antenna array along Z-axis are set to be 20 cm, 30 cm and 40 cm.

The 2D reconstructed images of the concealed target are plotted from Figure 6-10 to Figure 6-12, each of which corresponds to a down range distances d_z of 20 cm, 30 cm and 40 cm respectively. The reconstructed images for this target show the same tendency as the results of the target with the size of 10 cm × 10 cm × 1 cm. The reconstructed images are more or less the same as the real one, even though the edges of the reconstructed targets are not in perfect shape compared with the real one. The reconstructed images have rather accurate distance estimation along Z-axis. When the bag is moving further away from the antenna array, the imaging results of both shape reconstruction and down range estimation are becoming less accurate, which can be observed from Figure 6-10 to Figure 6-12.

Because the target is smaller, the detectable down range of the imaging is getting closer to the antenna array. The maximum distance d_z is about 40 cm for the single concealed metallic target in bag with the size of 8 cm × 8 cm × 1 cm.

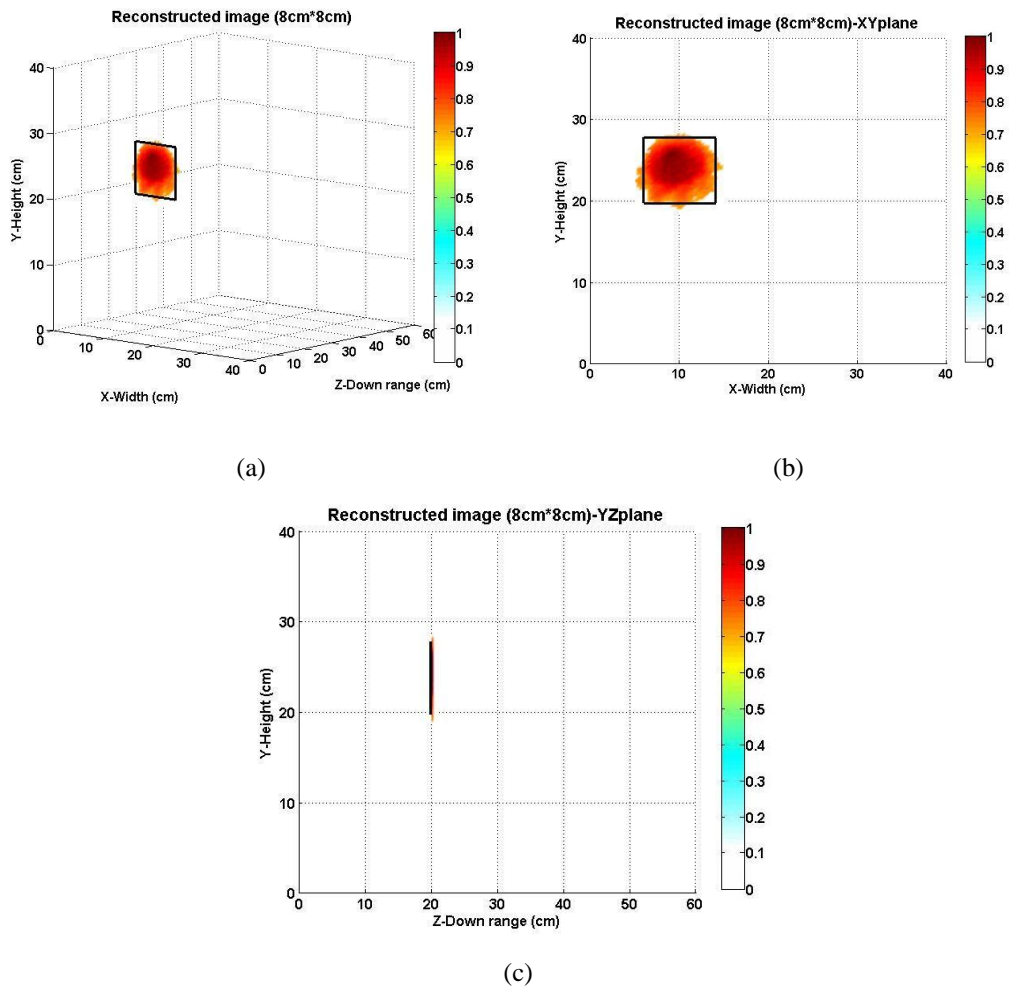
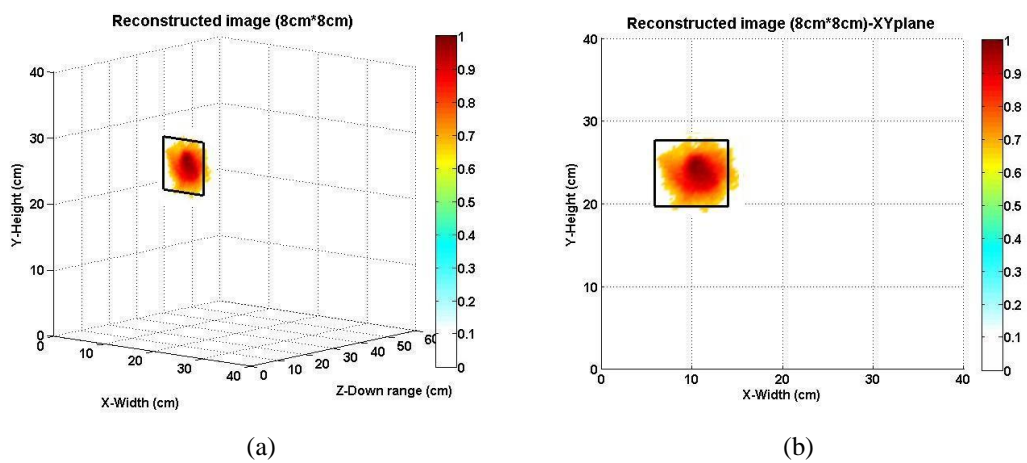
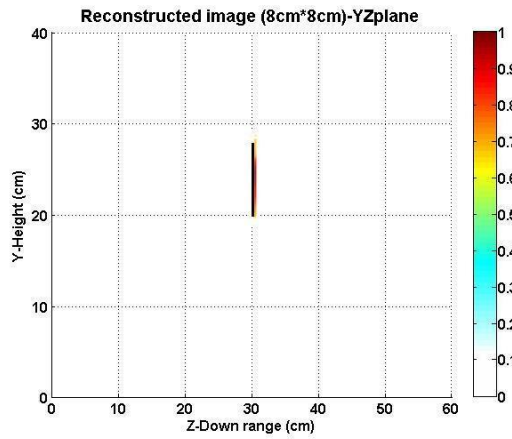


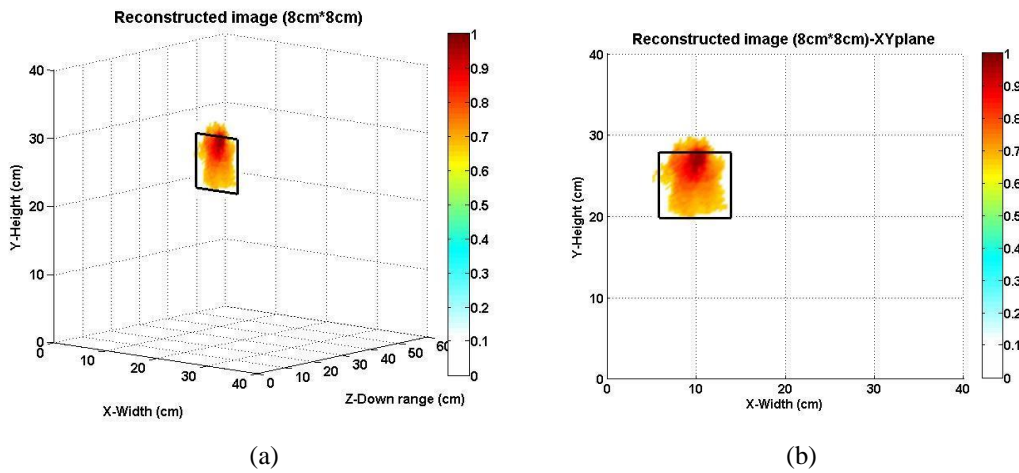
Figure 6-10 The reconstructed image for the single metallic target with the size of 8 cm × 8 cm × 1 cm at $d_z = 20$ cm, (a) 2D image of the target, (b) the reconstructed image of the target in XY plane, (c) side view of the reconstructed image in YZ plane.





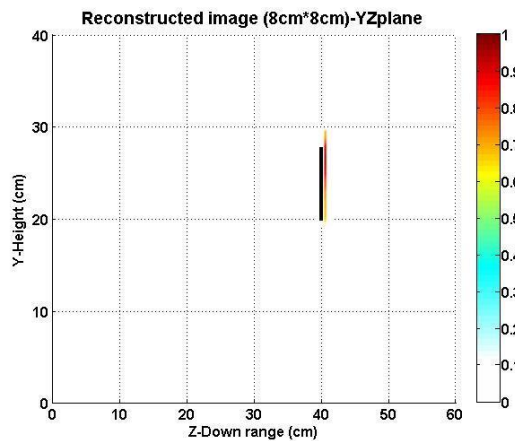
(c)

Figure 6-11 The reconstructed image for the single metallic target with the size of $8\text{ cm} \times 8\text{ cm} \times 1\text{ cm}$ at $d_z=30\text{ cm}$, (a) 2D image of the target, (b) the reconstructed image of the target in XY plane, (c) side view of the reconstructed image in YZ plane.



(a)

(b)



(c)

Figure 6-12 The reconstructed image for the single metallic target with the size of $8\text{ cm} \times 8\text{ cm} \times 1\text{ cm}$ at $d_z=40\text{ cm}$, (a) 2D image of the target, (b) the reconstructed image of the target in XY plane, (c) side view of the reconstructed image in YZ plane.

(3) Single target (5 cm × 5 cm × 1 cm)

Furthermore, the concealed metallic target is decreased to the size of 5 cm (width) × 5 cm (height) × 1 cm (thickness). As the target is becoming smaller, the reflected signals will be weaker to reach the receiver. During the experiment, it is found that when the distance d_z is longer than 30 cm away from the rotating antenna array, the received signal is too weak to derive any useful information. Hence, this target is placed at the distance d_z of 20 cm and 30 cm away from the rotating antenna array.

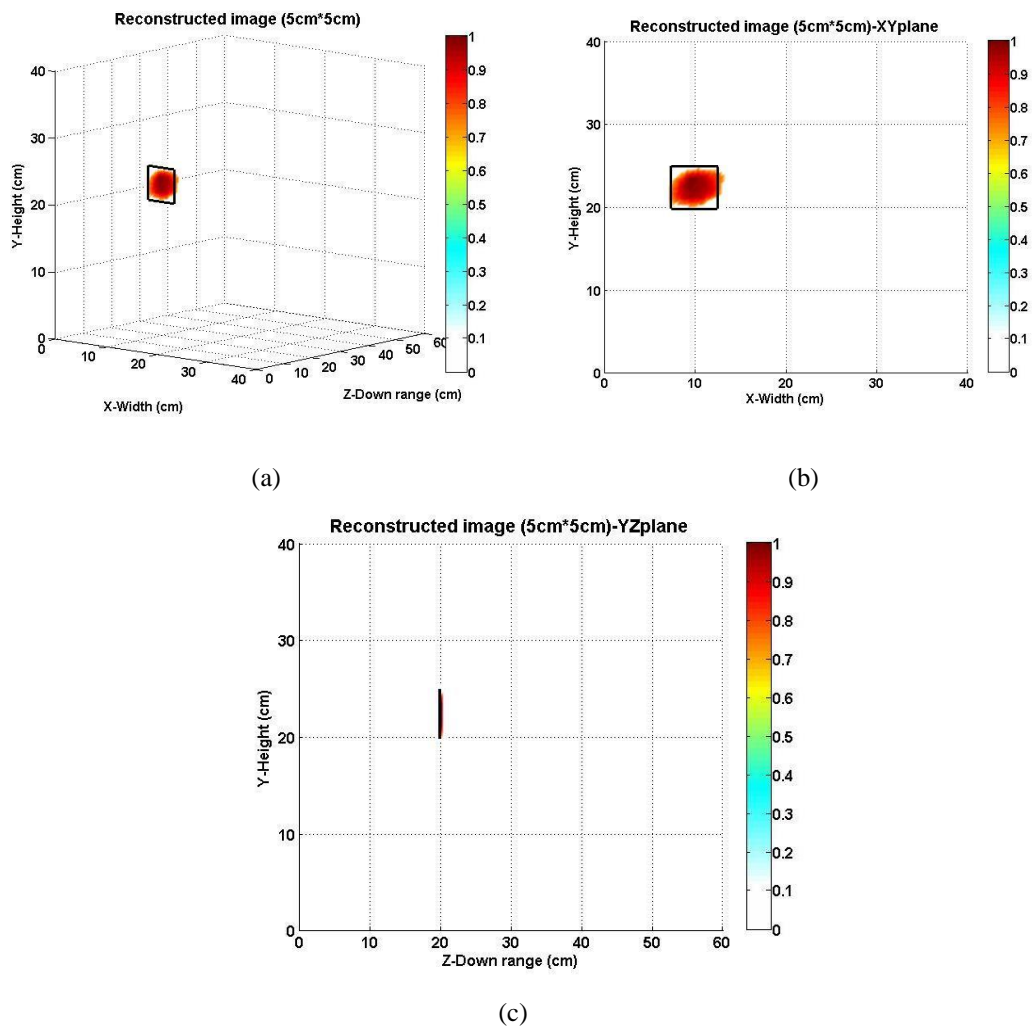


Figure 6-13 The reconstructed image for the single metallic target with the size of 5 cm × 5 cm × 1 cm at $d_z = 20$ cm, (a) 2D image of the target, (b) the reconstructed image of the target in XY plane, (c) side view of the reconstructed image in YZ plane.

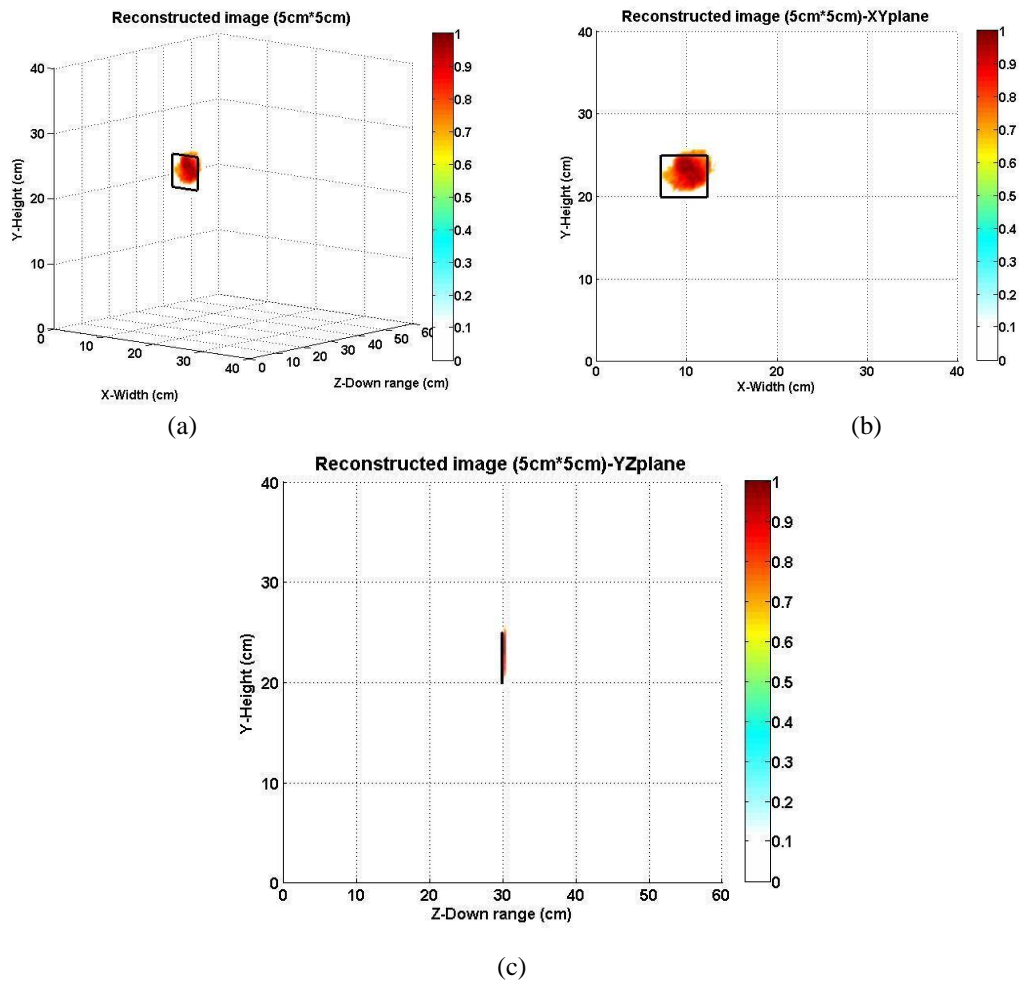


Figure 6-14 The reconstructed image for the single metallic target with the size of 5 cm × 5 cm × 1 cm at $d_z = 30$ cm, (a) 2D image of the target, (b) the reconstructed image of the target in XY plane, (c) side view of the reconstructed image in YZ plane.

The 2D reconstructed images of the concealed target placed at the distance d_z of 20 cm and 30 cm are plotted in Figure 6-13 and Figure 6-14, respectively. The reconstructed images are at the expected positions, with blurred shape at the edges. The reconstructed image of the target at the distance d_z of 20 cm displays much more accuracy than the one at the distance d_z of 30 cm.

(4) Single target (4 cm × 4 cm × 1 cm)

After all the previous measurements with a decreasing size of targets, what the smallest detectable size would be using the UWB imaging system becomes the topic of interest. In theory, when the target is getting smaller, the reflected signal is becoming weaker and can be easily drowned within the noise. After the continuous

tests and trials, the smallest detectable concealed metallic target is found to be the one with the size of 4 cm (width) \times 4 cm (height) \times 1 cm (thickness), placed at the distance d_z of 20 cm and 30 cm away from the antenna array.

The 2D reconstructed images of the target with this size are plotted in Figure 6-15 and Figure 6-16. The reconstructed images of the target are almost at the right position. The same imperfect blurring shape occurs at the edges. The down range distance estimation is rather accurate, indicating the right position away from the antenna array.

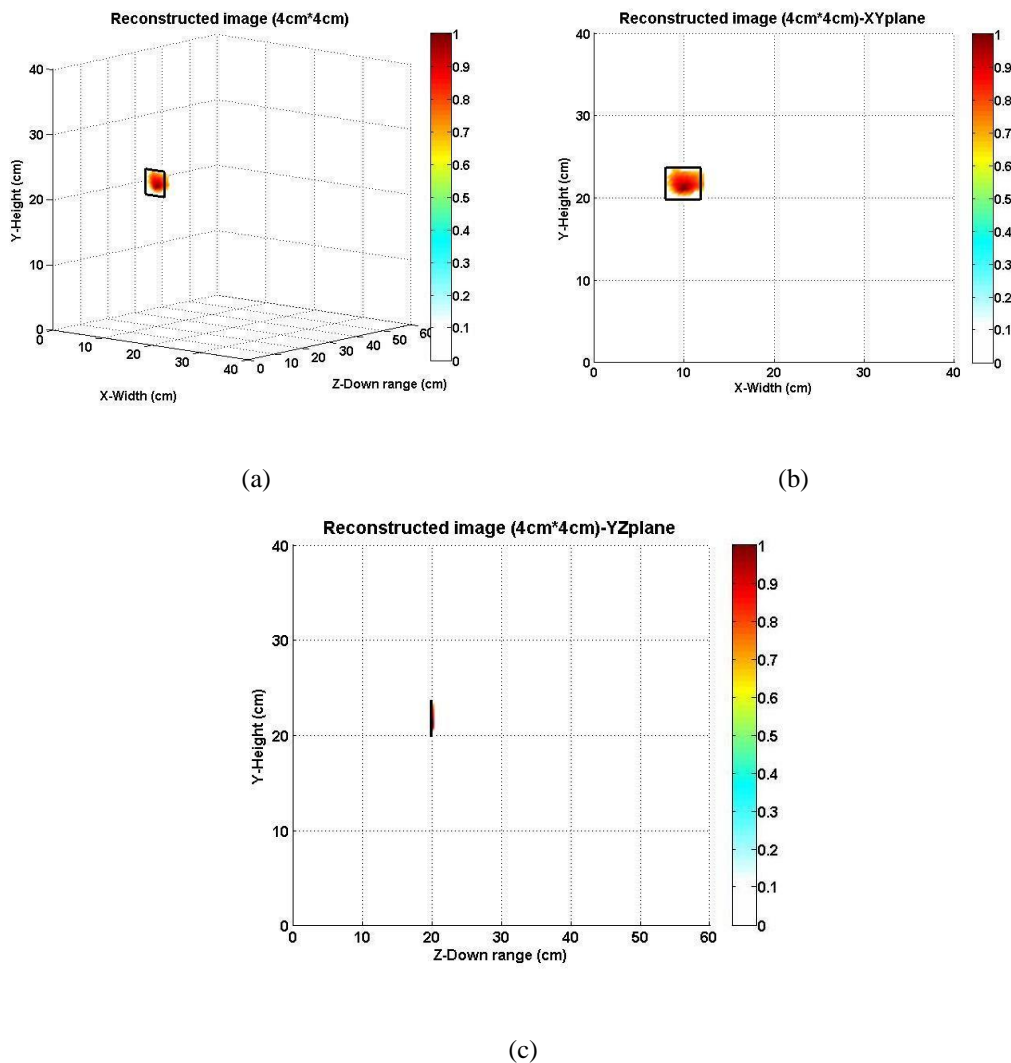


Figure 6-15 The reconstructed image for the single metallic target with the size of 4 cm \times 4cm \times 1 cm at $d_z=20$ cm, (a) 2D image of the target, (b) the reconstructed image of the target in XY plane, (c) side view of the reconstructed image in YZ plane.

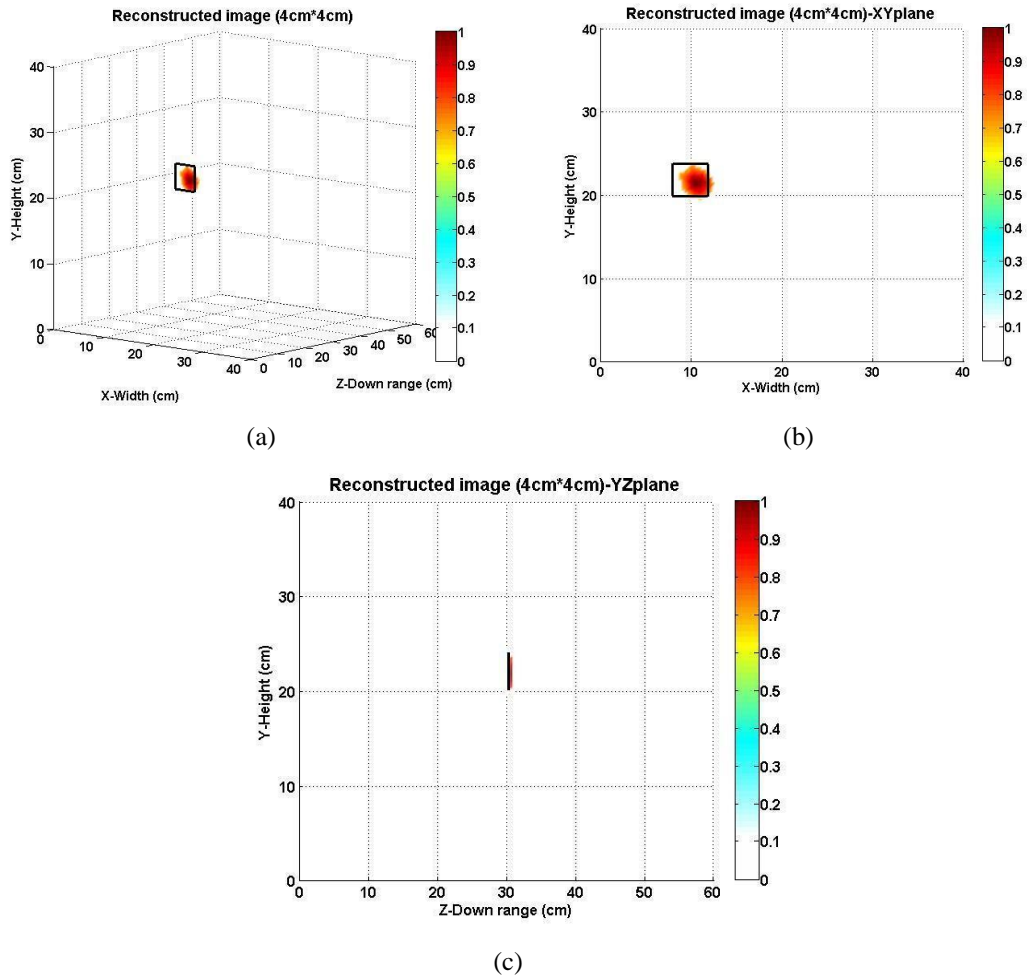


Figure 6-16 The reconstructed image for the single metallic target with the size of 4 cm × 4 cm × 1 cm at $d_z=30$ cm, (a) 2D image of the target, (b) the reconstructed image of the target in XY plane, (c) side view of the reconstructed image in YZ plane.

6.2.2 The analysis on imaging results

As described in the previous section, the UWB imaging system can detect and image the concealed metallic rectangular target in different sizes and at different distances. All the reconstructed images of the targets are almost at the right position. They have similar shapes compared with the real one, but not in perfect shapes.

In order to analyse the accuracy of the reconstructed image, two aspects have been taken into consideration, one of which is the reconstructed surface area of the target in XY plane and the other one is the distance d_z away from the antenna array along Z-axis in YZ plane. The illustrations are shown in Figure 6-17.

As shown in Figure 6-17 (a), the surface area of the real target Tar_M in XY plane is assumed as A_T , while the reconstructed one $Recon_M$ is assumed as A_R . The percentage $A\%$, which is the proportion of the reconstructed area to the real one, following the equation (6-3), is used to qualify the accuracy of the reconstructed surface area in XY plane. Due to the system error in the measurement and the unpredictable error during the rotation of the array arm, the centre of the reconstructed image moves slightly away from the real one to any direction in XY plane. Thus the off-centre distance C_{off} is another indicator, showing the maximum shifting distance around the fixed real centre, as shown in Figure 6-17 (a).

When reconstructing the image of the target, the antenna array is assumed to be at the position where $z=0$. The distance away from the antenna array for Tar_M is named as d_{z0} , while the one for $Recon_M$ is named as d_{zR} . The difference between them is named as Δd .

The range of error between the reconstructed image and the real one is used to compare the quality of the UWB imaging system, which is defined in the equation (6-4).

$$A\% = \frac{A_R}{A_T} \quad (6-3)$$

$$\Delta A\% = \left| \frac{A_T - A_R}{A_T} \right| \cdot 100$$

$$\Delta d_z \% = \left| \frac{d_{z0} - d_{zR}}{d_{z0}} \right| \cdot 100 \quad (6-4)$$

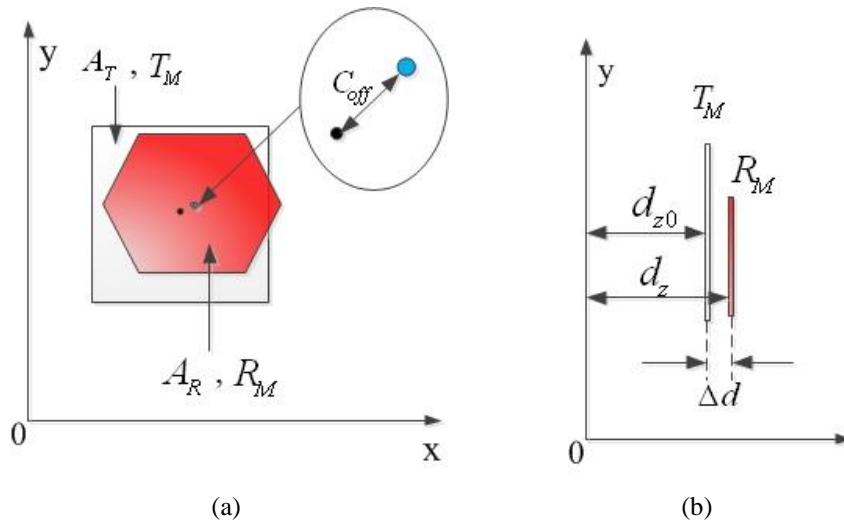


Figure 6-17 The comparison of the reconstructed image with the real one, (a) in XY plane, (b) in YZ plane.

Table 6-1 Comparison of reconstructed images and the real one

Target's size	The real target		Reconstructed images			Error (%)	
	A_T (cm ²)	d_{z0} (cm)	$A\%$	C_{off} (cm)	d_{zR} (cm)	ΔA	Δd_z
10 cm × 10 cm × 1 cm	100	20	98.4%	0.2	20.1	1.6	5.0
	100	30	91.6%	0.2	30.2	8.4	6.7
	100	40	82.5%	0.5	40.3	17.5	7.5
	100	50	43.6%	0.5	50.5	56.4	10.0
8 cm × 8 cm × 1 cm	64	20	94.5%	0.1	20.1	5.5	5.0
	64	30	87.8%	0.3	30.2	12.2	6.7
	64	40	84.2%	0.3	40.3	15.8	7.5
5 cm × 5 cm × 1 cm	25	20	82.0%	0.1	20.2	18.0	10.0
	25	30	78.2%	0.2	30.3	21.8	10.0
4 cm × 4 cm × 1 cm	16	20	79.9%	0.2	20.2	20.1	10.0
	16	30	69.8%	0.3	30.3	30.2	10.0

The comparisons of the results are listed in Table 6-1. The furthest detected distance is about 50 cm away from the antenna array along Z-axis for the concealed target with the size of 10 cm × 10 cm × 1 cm. The smallest concealed metallic target is with the size of 4 cm × 4 cm × 1 cm, placed at the maximum 30 cm away from the antenna array.

When the concealed target is moving further away from the system, the reconstructed image is becoming smaller and the error is getting bigger and unreliable. It is mainly because the returned signal suffers energy loss during the propagation and is drowned in noise. The accuracy in the reconstructed image deteriorates.

At the same distance d_{z0} away from the antenna array, the accuracy of the reconstructed image of the concealed target is decreasing when the size of the target is smaller. The reason is that the received reflected signal from a smaller target is obviously smaller than the one from a bigger one.

The reconstructed image of the target is more accurate and convincing at a closer distance away from the antenna array along Z-axis. The longer the signal is travelling, more losses would suffer, and the poorer the imaging result could be. Generally, all the reconstructed results are good enough for the imaging purpose.

6.3 Images for pairs of concealed targets

6.3.1 Fundamental analysis on resolutions

(1) Down-range resolution

Range resolution, denoted as ΔR , is a metric that describes the ability to detect targets in close proximity to each other as distinct targets along the vertical direction. The pulse with the width of τ , is travelling towards the two targets, separated by the distance of R . When the pulse trailing edge A strikes target 1, part of it will be reflected by target 1 and the other part will penetrate through target 1 and be reflected by target 2. The returned pulse would be composed of returns from both targets. If these two targets are not separated by distinguishable distance, the reflected pulse from them will overlap. In order to acquire two distinct returned

pulses, as shown in Figure 6-18 (c), the minimum distance ΔR needs to be defined as below:

$$ct_{A_{\text{target}1}} + \Delta R = 2c\tau$$

$$ct_{B_{\text{target}2}} - \Delta R = c\tau$$

$$t_{A_{\text{target}1}} = t_{B_{\text{target}2}} \tag{6-5}$$

Therefore,
$$\Delta R = \frac{c\tau}{2} \tag{6-6}$$

From equation (6-6), the minimum distance ΔR is related to the pulse width.

In our measurement, the pulse width is 1 ns, so the theoretical down-range resolution R_{down} is equal to 15 cm.

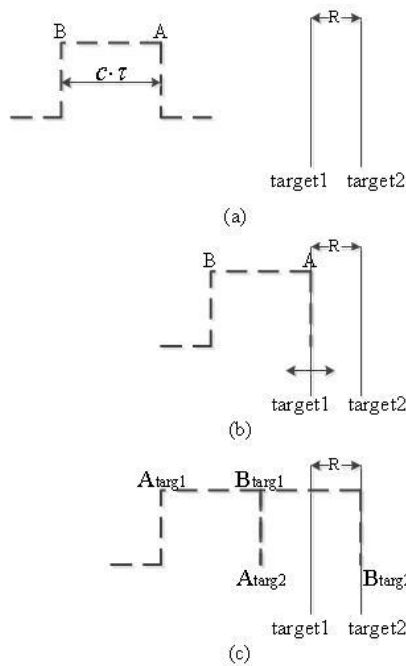


Figure 6-18 Range resolution; (a) pulse towards the target, (b) pulse reflected from the target1, (c) two returned pulse FWHM.

(2) Cross-range resolution

Cross-range resolution is used to distinguish the targets along horizontal direction, which is related to the beam width of the antenna array. As shown in Figure 6-19,

assuming the range from the antenna to the target is at the distance of R , the antenna's beam width is θ_B , the cross-range resolution δ_y is defined as below:

$$\delta_y = 2R \tan \frac{\theta_B}{2} \quad (6-7)$$

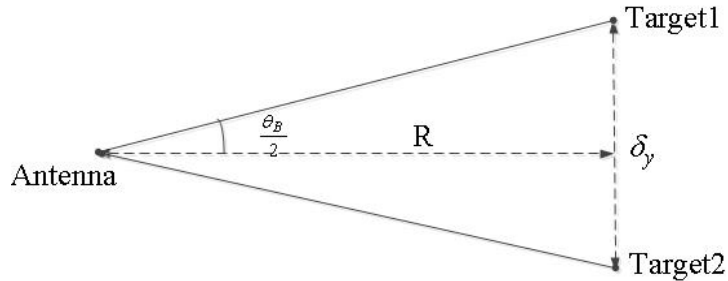


Figure 6-19 Cross-range resolution

The signal generated from VCO operates at 4.5 GHz and the bandwidth of the modulated signal is about 1 GHz, so the UWB imaging system works across this frequency band. The four-element array composed of the corrugated balanced antipodal Vivaldi antennas has 3 dB beam width of 10.3° at 6 GHz, as shown in Figure 3-16 (c). So the distance R_{dis} of 20 cm can theoretically achieve a cross-range resolution 7 cm.

6.3.2 The results of the measurements

The measurements for the down-range resolution and cross-range resolution of the UWB imaging system are introduced. Two targets M1 and M2 are concealed in the bag and placed in front of the antenna array. The size of M1 is 8 cm (width) \times 8 cm (height) \times 1 cm (thickness) and the one of M2 is 10 cm (width) \times 10 cm (height) \times 1 cm (thickness), because targets with bigger sizes are easier to image, as proved in previous chapter.

At first, target M1 will be placed around 20 cm away from the antenna array along Z-axis. Then second target M2 is positioned behind M1 at different locations to find out the resolution both in down-range and cross-range. It is assumed that dx_2 and dz_2 are the distances between these two metal blocks along X-axis and Z-axis. The detailed measurements are described below.

(1) M1 and M2 are in one column

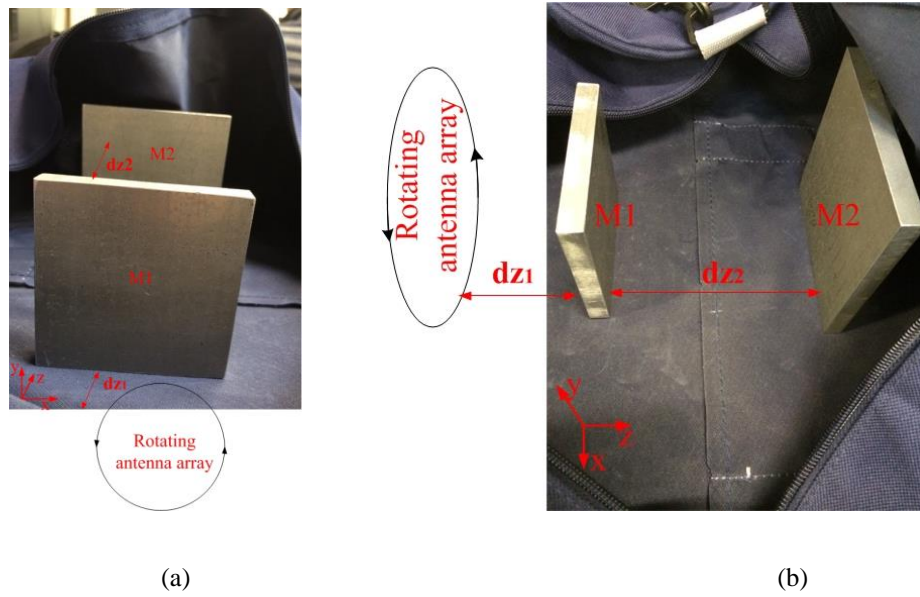
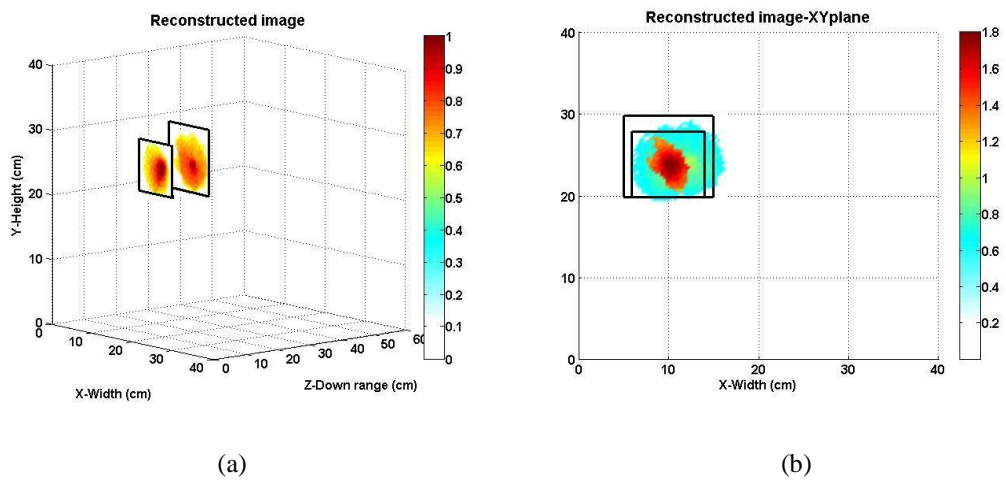
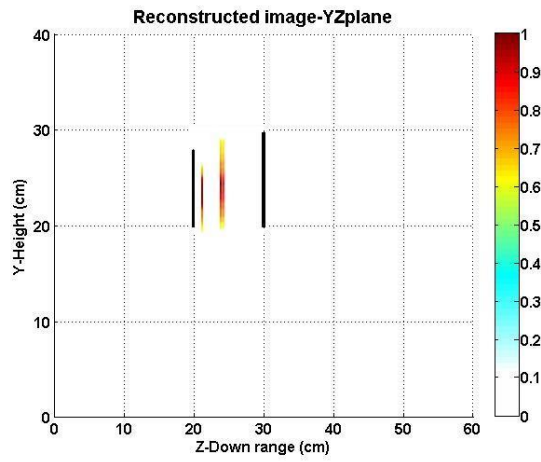


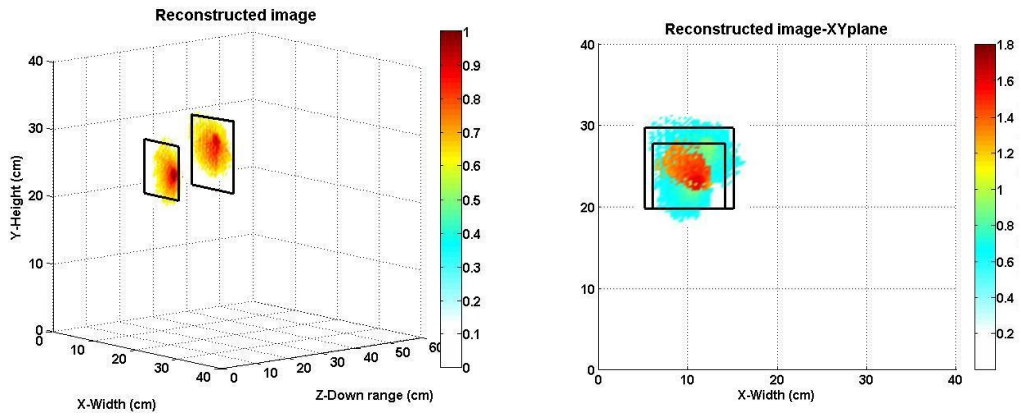
Figure 6-20 The two targets in one column concealed in bag, (a) front view of the two targets in the bag, (b) side view of the two targets in the bag.





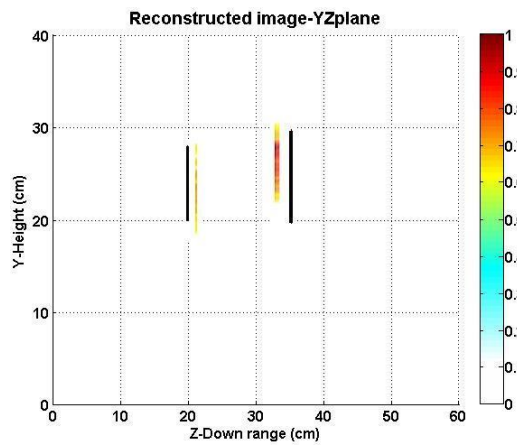
(c)

Figure 6-21 The reconstructed image for the two targets in one column at $d_{z2}=10$ cm, (a) 2D image of the target, (b) front view in XY plane, (c) side view in YZ plane.



(a)

(b)



(c)

Figure 6-22 The reconstructed image for the two targets in one column at $d_{z2}=15$ cm, (a) 2D image of the target, (b) front view in XY plane, (c) side view in YZ plane.

Keeping two targets in one column is the situation that M2 is placed right behind M1 with a certain distance, as shown in Figure 6-20. The target M1 is placed around $d_{z1}=20$ cm away from the antenna array along Z-axis. The distance d_{z2} between M1 and M2 along Z-axis is chosen to be 10 cm and 15 cm.

The reconstructed images for different d_{z2} are shown in Figure 6-21 and Figure 6-22. Reconstructed images of two targets are highlighted in colour and can be very well distinguished. The same blurring at the edges occurs again which makes the reconstructed images of targets smaller than the real ones. If two returned signals are well-resolved, they certainly can be extracted separately and analysed following *Step1*. Because the gap between two targets is small, the time window used in *Step2* is smaller than the one used for the single target, leading to the degradation in the reconstructed image of the target.

From Figure 6-21 (c) and Figure 6-22 (c), it is known that M1 is at the same position along Z-axis as the real one, while M2 has more error in the distance d_{z2} . The reason is that the time duration of the transmitting signal used in the system is only 1 ns, which means that the theoretical down-range resolution is about 15 cm. Therefore, when the space between the two targets is about 15 cm, this error is less severe than the previous one.

(2) M1 and M2 are in one row

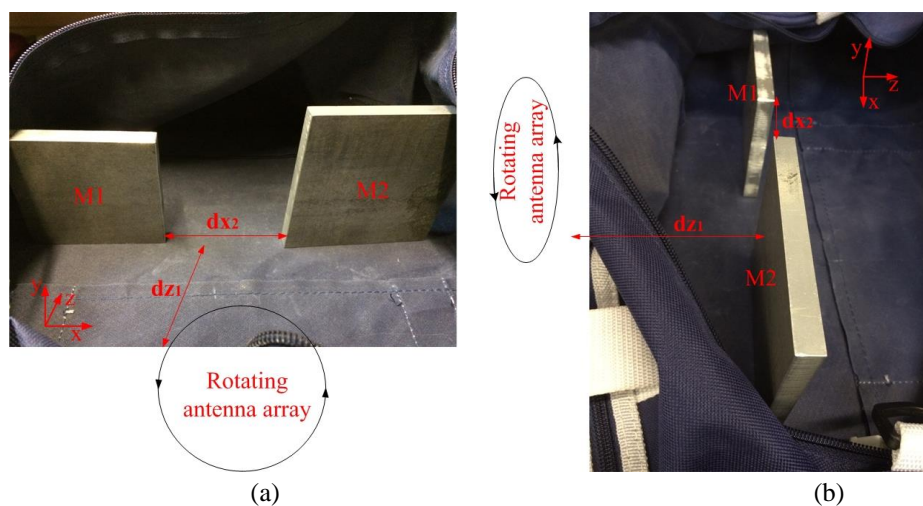


Figure 6-23 The two targets in one row concealed in bag, (a) front view of the two targets in the bag, (b) side view of the two targets in the bag.

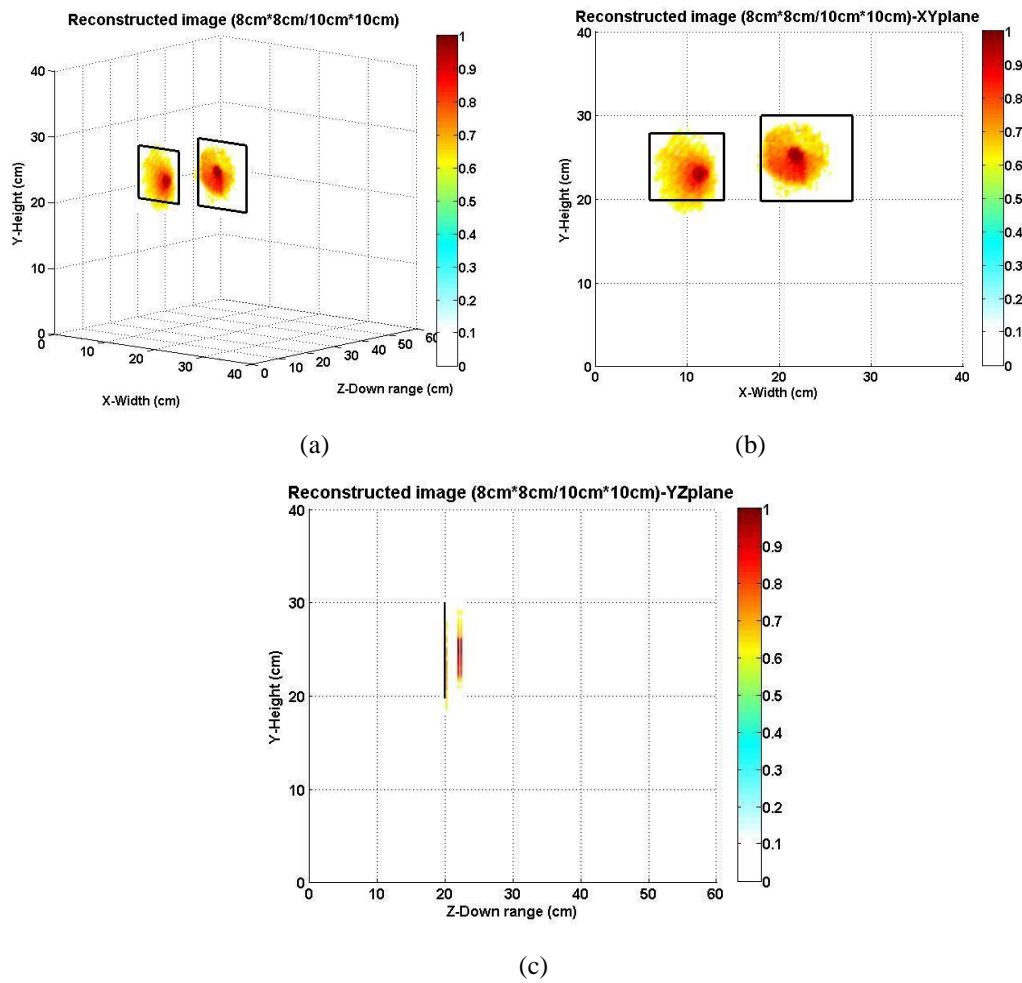
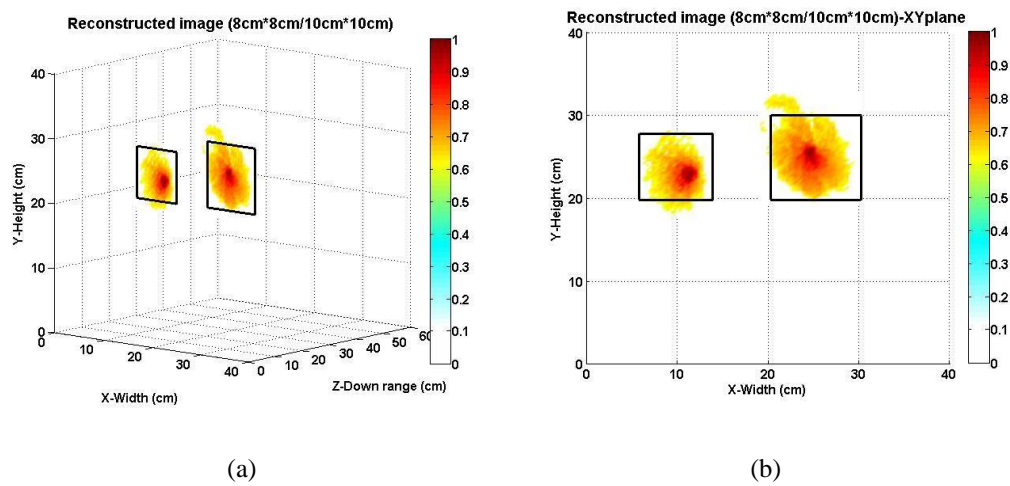
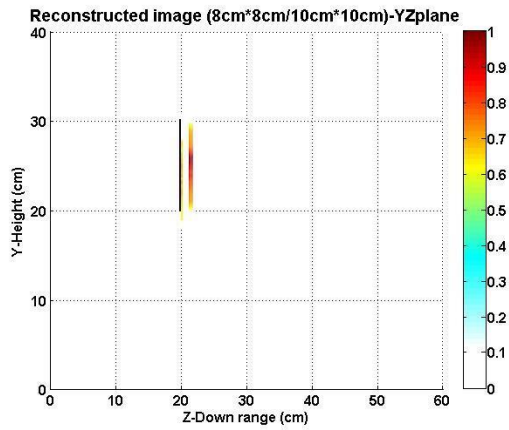


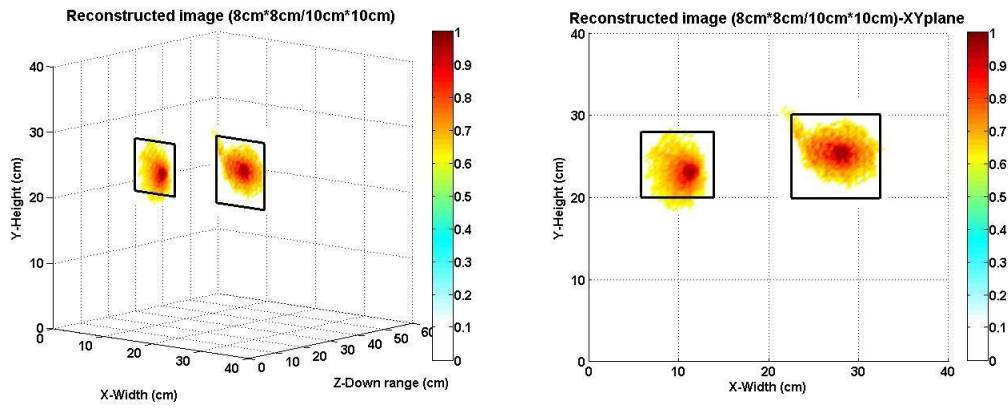
Figure 6-24 The reconstructed image for the two targets in one row at $d_{x2}=4$ cm, (a) 2D image of the target, (b) front view in XY plane, (c) side view in YZ plane.





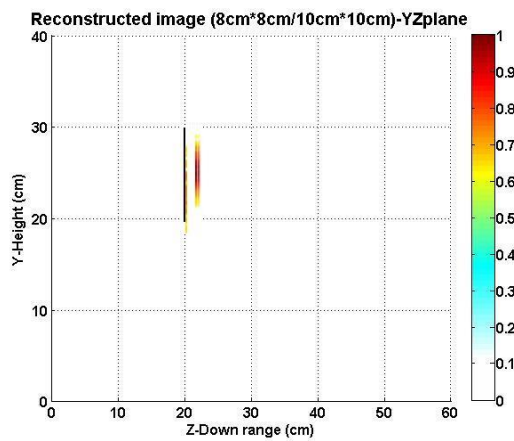
(c)

Figure 6-25 The reconstructed image for the two targets in one row at $d_{x2}=6$ cm, (a) 2D image of the target, (b) front view in XY plane, (c) side view in YZ plane.



(a)

(b)



(c)

Figure 6-26 The reconstructed image for the two targets in one row at $d_{x2}=8$ cm, (a) 2D image of the target, (b) front view in XY plane, (c) side view in YZ plane.

In this measurement, two targets M1 and M2 keep a certain distance dx_2 along X-axis in the bag, as shown in Figure 6-23. The distance dz_1 between the targets and the antenna array is still 20 cm. The target M1 is closer to the transmitting antenna than the target M2.

Different distances dx_2 between M1 and M2 have been measured, which are 4 cm, 6 cm and 8 cm. The reconstructed images are shown from Figure 6-24 to Figure 6-26. The highlighted and coloured areas indicate the shapes and locations of the reconstructed targets. However, 8 cm is the longest range between these two targets in the experiment, because when the target M2 is placed beyond 8 cm away from the transmitting antenna, the reflection at M2 will be too weak. Hence, the reconstructed image of the target M2 will be very unreliable.

For the same reason, when the target M1 is closer to the transmitting antenna, the estimation distance dz_1 is more accurate than the one for M2, as shown in Figure 6-24 (c) to Figure 6-26 (c).

(3) M1 and M2 are in the cross position

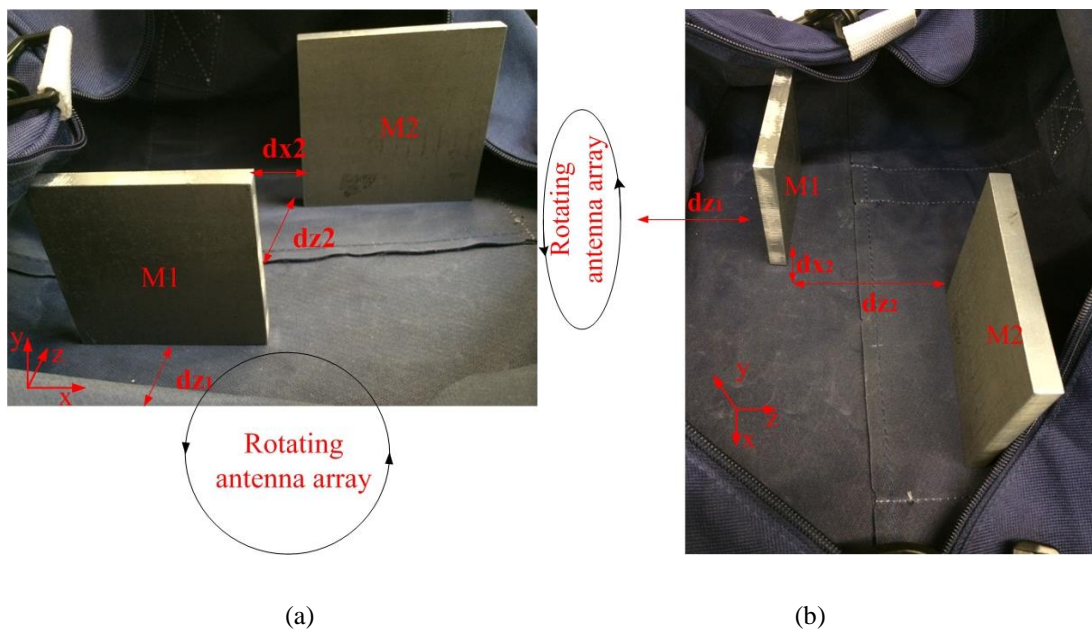


Figure 6-27 The two targets in the cross position in the bag, (a) front view of the two targets in the bag, (b) side view of the two targets in the bag.

The two targets are placed in the cross position in the bag, as shown in Figure 6-27. The smaller target M1 is in front of the target M2 and close to the antenna array. The distances between them, denoted as d_{x2} and d_{z2} , are about 6 cm and 15 cm respectively.

The reconstructed images of the two targets are plotted in Figure 6-28. In the cross position, the two targets can still be distinguished.

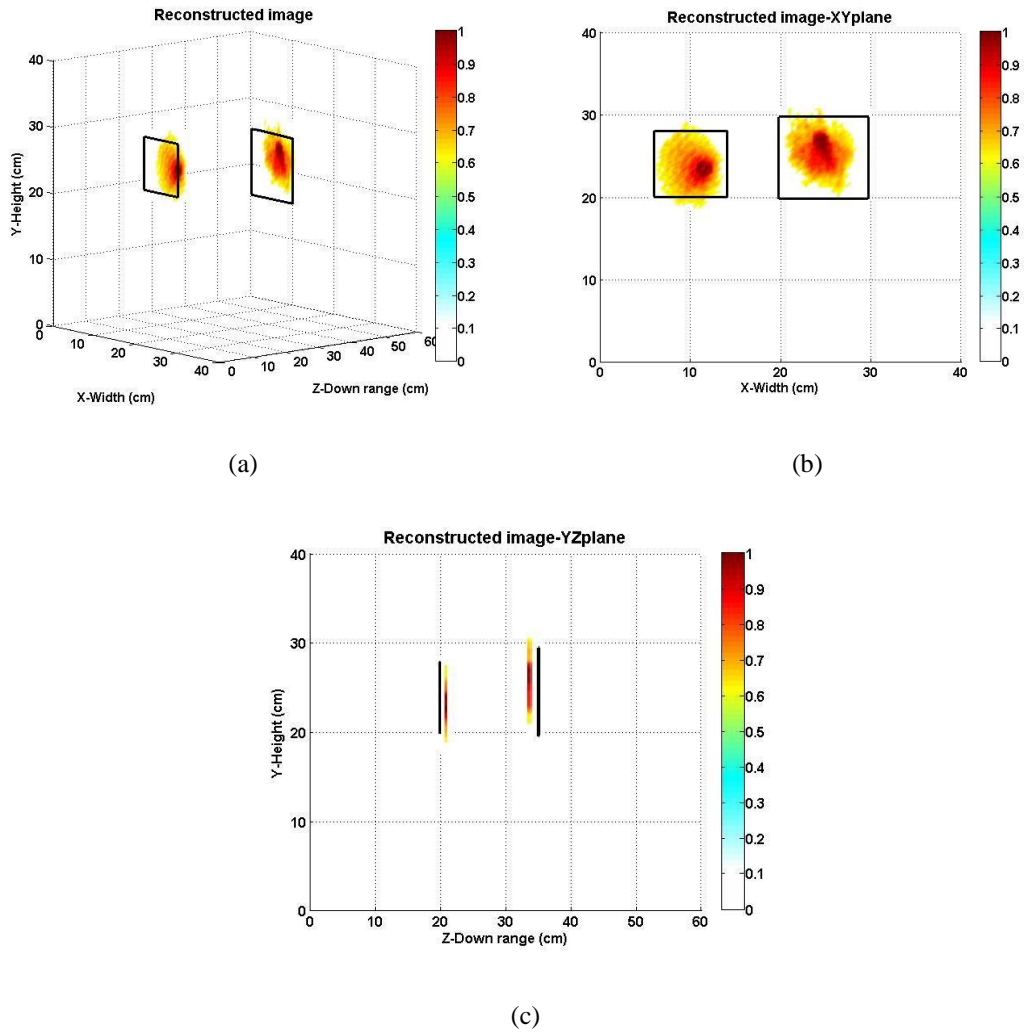


Figure 6-28 The reconstructed image for the two targets in the cross position, $d_{x2}=6$ cm and $d_{z2}=15$ cm, (a) 2D image of the target, (b) front view in XY plane, (c) side view in YZ plane.

6.3.3 The analysis on imaging results

The imaging results from all the three different arrangements of two targets, as illustrated in section 6.3.2, validate that the UWB imaging system can successfully image the two targets with well-maintained accuracy and stability.

In order to analyse the accuracy of the reconstructed images, the surface area in XY plane of the reconstructed target and the space between them have been investigated. Assume A_{TM1} and A_{TM2} are the surface area of the real metallic target in XY plane, while A_{RM1} and A_{RM2} are the surface's area of the reconstructed one. The value d_{x2} and d_{z2} are the distances between the two targets along X-axis and Z-axis, while d_{Rx2} and d_{Rz2} are the ones for the reconstructed targets. The errors for these parameters are calculated by the equation (6-6). Based on it, the measured data are listed in Table 6-2.

$$\begin{aligned}\Delta A_1 \% &= \left| \frac{A_{TM1} - A_{RM1}}{A_{TM1}} \right| \cdot 100 \\ \Delta A_2 \% &= \left| \frac{A_{TM2} - A_{RM2}}{A_{TM2}} \right| \cdot 100 \\ \Delta d_{x2} \% &= \left| \frac{d_{x2} - d_{Rx2}}{d_{x2}} \right| \cdot 100 \\ \Delta d_{z2} \% &= \left| \frac{d_{z2} - d_{Rz2}}{d_{z2}} \right| \cdot 100\end{aligned}\tag{6-6}$$

When two targets are in one column, the reconstructed surface area for M2 is worse than M1 because most of the energy of the input signal is reflected by M1. The time duration of the transmitted signal used in the imaging system is about 1 ns, so the space of 15 cm between M1 and M2 along Z-axis is the limit and any gap shorter than that would not produce better imaging result.

When two targets are in one row, the closer they are to each other, the less distinguishable they would be. As listed in Table 6-2, the difference errors both in the surface area and the spacing along X-axis are much bigger, when d_{x2} is 4 cm

compared to that when it increases to 6 cm and then 8 cm. Interestingly the accuracy of the results is not increasing in the proportion of the spacing distance. If the target M2 is further away, the signal arrived at M2 will get smaller, which affects the accuracy of the reconstructed images. From the measurements, it is found that the accuracy is better when the spacing between two targets is 6 cm along X-axis.

When the distance d_{x2} is 6 cm and d_{z2} is 15 cm, the UWB imaging system can achieve the best imaging results in the previous two groups of measurements. So in the cross range experiment, two targets are arranged based on these two distance values. From Table 6-2, the reconstructed surface area of target M2 is no better than that in the “in-one-row” scenario, because the received reflected signal is weakened when the target M2 is moved much further away from the antenna array, as validated in section 6.2.2. Whereas, the estimation of the distance d_{z2} is better than that in the “in-one-column” scenario, since there are less multi-reflections in the case of the cross position arrangement.

Compared with the theoretical calculation for down-range and cross-range resolutions, although the results are not accurate, the two targets can still be distinguished in the measurement even when the spacing between them is smaller than the theoretical one. The reason is that a small time window is used in *Step2* to process the received signal. Figure 6-3 (b) shows that there are two main peaks in one received signal. The two peaks can easily be distinguished if they are not overlap. Even if parts of the two peaks overlap, a relative small time window can still be used to extract the short duration around the peak for analysis in *Step2*. It is contributed to the practical resolution for distinguishing two concealed targets.

The results in Table 6-2 demonstrate that the UWB imaging system is capable of imaging two metallic targets in down-range and cross-range. The resolutions are close to the theoretical calculation, as shown in Table 6-3.

Table 6-2 Resolution of the UWB imaging system for two targets

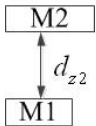
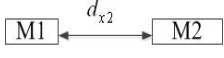
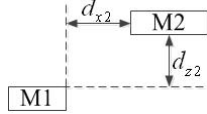
Target's Positions								
The real target	A_{TM1} (cm ²)	64	64	64	64	64	64	
	A_{TM2} (cm ²)	100	100	100	100	100	100	
	d_{x2} (cm)	/	/	4	6	8	6	
	d_{z2} (cm)	10	15	/	/	/	15	
Reconstructed images	A_1 (%)	69.2	71.2	70.9	71.4	71.2	79.6	
	A_2 (%)	56.7	64.1	48.7	78.9	58.2	53.1	
	d_{Rx2} (cm)	/	/	5.1	7	9.7	10.9	
	d_{Rz2} (cm)	3	11.7	3	2.8	3.1	12.6	
Error (%)	ΔA_1	30.8	28.8	29.1	28.6	28.8	49.4	
	ΔA_2	43.3	35.9	51.3	21.1	41.8	51.9	
	Δd_{x2}	/	/	27.5	16.7	21.3		
	Δd_{z2}	70	22	/	/	/	16	

Table 6-3 Comparison of measured and theoretical down-range resolution and cross-range resolution

	Down-range resolution (cm)	Cross-range resolution (cm)
Theoretical results	15	7
Measured results	15	6
$Error\% = \left \frac{Theory - Measurement}{Theory} \right \cdot 100$	0	14.2%

6.4 Summary

The imaging measurements for the targets concealed in bag have been carried out in free space using the UWB imaging system. For single concealed target, the smallest concealed metallic target with the size of 4 cm × 4 cm × 1 cm can be detected at the maximum distance of 30 cm away from the antenna array. In contrast, while the size of the target is chosen to be 10 cm × 10 cm × 1 cm, the maximum detectable distance can reach up to 50 cm. As for imaging pairs of concealed targets, the UWB imaging system can achieve down-range resolution of 15 cm and cross-range resolution of 6 cm.

Chapter 7 Summary and Future work

7.1 Summary

Security detecting problem is now attracting worldwide attention. The UWB technology is an attractive technology in detecting, localization and imaging applications, such as medical imaging, ground penetrating radar and see-through wall imaging. Compared with X-ray machine, UWB imaging system is compact in physical size and relative cheap in cost. The most important advantage is that it is non-ionizing radiation, making it harmless to human body and the environment.

The thesis mainly focuses on the detection of the concealed metallic targets in bag using UWB imaging technology. A time domain UWB imaging system with the rotating antenna array has been successfully proposed, implemented and tested. It is unconstrained to the antenna elements in the scanning space due to the rotating antenna array.

Two types of UWB antennas, the circular-edge antipodal Vivaldi antenna and the corrugated balanced antipodal Vivaldi antenna have been designed and studied. Characteristics of the two antennas in the frequency domain and time domain have been investigated. Both of them can work across UWB frequency range from 3.1 to 10.6 GHz and have directional radiation patterns. The corrugated BAVA has been improved to have a relative high gain around 7 dBi over the lower frequency band of 3-6 GHz, which is the main operating frequency band of the imaging system. It also has a better characteristic in the time domain, causing less distortion to the signal. The pulse fidelity of the BAVA to the modulated Gaussian pulse and modulated rectangular pulse is above 95%. Thus the corrugated balanced antipodal Vivaldi antenna is used as the antenna element for the UWB imaging system.

The implemented UWB imaging system consists of an RF circuit, a rotating antenna array as well as the two-dimensional DAS algorithm for image reconstruction. The rotating antenna array comprises one central transmitting antenna and four receiving antennas. The receiving antennas are placed side-by-side on a straight arm, rotating around the central transmitting antenna.

By scanning the targets concealed in bag, the UWB imaging system can detect and reconstruct the image of single and pairs of metallic targets concealed in bag. For single concealed target, the smallest concealed metallic target with the size of $4\text{ cm} \times 4\text{ cm} \times 1\text{ cm}$ can be detected at a maximum distance of 30 cm away from the antenna array. In contrast, while the size of the target is chosen to be $10\text{ cm} \times 10\text{ cm} \times 1\text{ cm}$, the maximum detectable distance can reach up to 50 cm. As for imaging two concealed targets, the UWB imaging system can achieve down-range resolution of 15 cm and cross-range resolution of 6 cm.

In summary, the key contributions are listed below.

1. Design of two types of UWB antennas

The circular-edge antipodal Vivaldi antenna and the corrugated balanced antipodal Vivaldi antenna (BAVA) have been designed and studied. Both of them can work across UWB frequency range from 3.1 GHz to 10.6 GHz, and have directional radiation patterns. The corrugated BAVA with smaller physical size has been improved to have a relative high gain around 7 dBi across the operating frequency range, especially the lower frequency band (3-6 GHz), which is the main operating frequency band of the imaging system. It is higher than the circular-edge antipodal Vivaldi antenna.

2. Characteristics analysis of the two antennas in the time domain

Since the proposed UWB imaging system is working in the time domain, it is necessary to analyse the characteristics of the antennas in the time domain. The corrugated BAVA causes less distortion to the signals in the time domain than the circular-edge antipodal Vivaldi antenna. For the modulated rectangular pulse, the pulse fidelity of the corrugated BAVA is about 95%.

3. Design of the rotating antenna array

The corrugated BAVA has better characteristic than the circular-edge antipodal Vivaldi antenna both in frequency domain and time domain, so that it is used as the element in the antenna array.

The rotating antenna array comprises one central transmitting antenna and four receiving antennas. The receiving antennas are placed side-by-side on a straight arm, rotating around the central transmitting antenna. With the rotation structure, the linear antenna array achieves the functionality of the two-dimensional array, reducing the limitation of antennas in space and simplifying the system.

4. Design of the two-dimensional image reconstruction method

In terms of each rotating position, the image reconstruction method is based on DAS (Delay-and-Sum) algorithm. When the antenna array is rotating in space, the corresponding coordinate of one-dimensional image is rotating. Thus, the two-dimensional image of the target is then achieved.

5. Design of the RF circuit

The RF transceiver has been designed to achieve a good dynamic range and receiver sensitivity. Finally, the dynamic range is 69 dB and receiver sensitivity is -78 dBm.

6. Implementation of the UWB imaging system

The UWB imaging system contains the rotating antenna array, RF circuits and the signal-processing unit. It can successfully detect and image the single and pairs of metallic targets concealed in bag. The smallest detectable single metallic target is with the size of 4 cm × 4 cm × 1 cm, placed at a maximum distance of 30 cm away from the UWB imaging system. The metallic target with the size of 10 cm × 10 cm × 1 cm can be detected and imaged at a maximum distance of 50 cm. The system has 15 cm in down-range resolution and 6 cm in cross-range resolution.

7.2 Future work

In the future, further optimizations can be carried out to improve the performance of the UWB imaging system:

1. Increase of the capacity of the rotating receiving antenna array

More antenna elements can be added into the rotating receiving antenna array to increase the gain and narrower the beam width, which can help to improve the cross-range resolution of the UWB imaging system.

2. Optimisation of the input pulse generation

A specifically designed pulse generator can be used in the imaging system, offering narrower time duration over the off-the-shelf instrument. This will enhance the down-range resolution of the imaging system.

3. Integration of the RF detector

In order to make the system more compact, an integrated RF detector with the FPGA design greatly improves the sampling ability of the UWB imaging system.

4. The improvement of the signal processing algorithm

More advanced imaging algorithm needs to be developed to enable the non-metallic target detection, as well as adapt to more challenging propagation environments with different obstructions. Doppler effects can also be taken into account in the algorithm to detect and image moving targets.

List of publications

Journal papers

- [1] **Min Zhou**, Xiaodong Chen, Lei Li, Clive Parini, “Implement of the UWB Imaging System with Rotating antenna array for security application ”, *to be submitted to IEEE Transactions on Antennas and Propagation*.
- [2] Bin Yang, Robert S. Donnan, **Min Zhou**, and Ali A. Kingravi, “Reassessment of the electromagnetic reflection response of human skin at W-band”, *Optics Letters*, Vol. 36, Issue 21, pp. 4203-4205, 2011.

Conference papers

- [1] **Min Zhou**, Xiaodong Chen, Lei Li, Clive Parini, “The UWB Imaging System with Rotating Antenna Array for Concealed Metallic Object”, *The 8th European Conference on Antennas and Propagation, EuCAP 2014*, 6-11 Apr. 2014, the Netherlands.
- [2] **Min Zhou**, Xiaodong Chen, Clive Parini, “Development of Rotating Antenna Array for UWB Imaging Application”, *2013 International Symposium On Antennas and Propagation (ISAP 2013)*, Vol.1, Page(s): 172-175, 23-25 Oct. 2013, China. (**Best Student Paper Award**)